Characterisation of Ultra-thin Oxynitride dielectric layers

Jason Roche (B.Sc.)

School of Physical Sciences

Dublin City University

A thesis submitted to

Ollscoil Chathair Bhaile Átha Cliath

For the degree of

Doctor of Philosophy

Research Supervisor

Dr. Greg Hughes

March 2003

Declaration

I hereby certify that this material, which I now submit for assessment on the programme of study leading to the award of doctor of Philosophy is entirely my own work and has not been taken from the work of others save and to the extent that such work has been cited and acknowledged within the text of my own work.

Signed: Jason Rolfe Id Number: 98970577

Date: 23/1/03

Contents

Abstract

This thesis is an investigation of thin oxides formed on Si(100) in a device manufacturing environment. Chemical analysis was performed on SiO_2 and SiON films comprising a sample set with thicknesses spanning 5 to 20 nm. Chemical characterisation, using XPS confirmed film quality through the consistency in stoichiometry, thickness, elemental composition and peak parameters for the as-received wafers. ARXPS measurements provided a qualitative interpretation of the interface and suggest suboxides are localised near the interface. In synchrotron studies using soft X- rays, both tunable photon energy and high resolution revealed precise information on the chemical and spatial distribution of interfacial suboxides and nitrides in the SiO_2 and SiON film respectively. It was possible to identify the presence of hydrides at both interfaces. For the oxynitrides the presence of a nitrogen rich region at the surface and interface is supported by the XPS and synchrotron studies.

X-ray Absorption Spectroscopy XAS and X-ray emission Spectroscopy XES measurements were performed using synchrotron radiation in order to profile the partial density of states of the nitrogen and the oxygen in the valence band and conduction respectively. While the 8.5 eV energy bandgap between the PDOS associated with the oxygen in the valence band and conduction band agrees with the SiO_2 bandgap, the equivalent energy gap for the nitrogen related states is approximately 5.5 eV.

The surface reconstruction of sulphur passivated Si(100) and Ge(100) surfaces were investigated by LEED and synchrotron soft X- ray photoemission spectroscopy. These studies were an attempt to ideally terminate these group IV (100) surfaces by a monolayer of divalent group VI element. Sulphur was deposited onto the atomically clean Si(100) (2x1) from an electrochemical cell. While the resulting surface displayed a (1x1) LEED pattern indicating ideal termination, the core level photoemission spectra reveled the presence both +1 and +2 oxidation states. Analysis of these spectra concluded that the sulphur coverage approximated to ¾ of a monolayer meaning that the surface termination was non-ideal. LEED results from the study of sulphur deposition on the clean Ge(100) surface again revealed the presence of a (1x1) surface reconstruction. The photoemission results from the Ge_{3d} displayed the presence of all four Ge oxidation states again indicating the non-ideal termination of the surface.

The samples examined in this thesis were realised in an industrial fabrication process. Precise knowledge of the nature of the sample history is limited to that which is expressed in the thesis.

Acknowledgements

For patience, encouragement, and understanding I'm indebted to Dr. Greg Hughes who's enthusiasm for and insight into the field of Surface Science will always be a source of inspiration.

On the surface, it's a crazy quantum world out there, but it's made a little easier thanks to Dr. Tony Cafolla.

" To learn is to grow ". To my parents Ann and Bernard, for more than word can say, thank you.

Where would I be without the love and support of my brother Bernard, sister Elaine and nephews Uilliam Caoilfhinn and baby Brannach.

Many thanks also to the lads in the lab both past and present.
"In the beginning there was" Clodagh and me. After four years of scans, coffee, beer, arguments, laughter, tears and a fire, we, "still haven't found what we're looking for". Also, from the Lab a big thanks to Darren, Philippe, and Eilish.

Cheers to "little Phil" Ryan for help at the NSLS . He throws ball like a girl !.

Finally I would like to acknowledge the financial help and support from Intel Ireland and Enterprise Ireland under the applied grants scheme.

Famous last words: "Silicon, that's just like sand?"

Table of Acronyms

AES	Auger Electron Spectroscopy
AFM	Atomic Force Microscopy
FWHM	Full Width Half Maximum
IMFP	Inelastic Mean Free Path
LEED	Low Energy Electron Diffraction
MOSFET	Metal Oxide Semiconductor Field Effect Transistor
NRA	Nuclear Reaction Analysis
PDOS	Partial Density of States
RBM	Random Bonding Model
RBS	Rutherford Back Scattering
SICT	Structure Induced Charge Transfer
SIMS	Secondary Ion Mass Spectroscopy
UHV	Ultra High Vacuum
XAS	X-ray Absorption Spectroscopy
XES	X-ray Emission Spectroscopy
XPS	X-ray Photoelectron Spectroscopy

Chapter 1

Introduction

1.0 Transistor History and the birth of the MOSFET

The modern semiconductor industry was born in the discovery of the bipolar transistor at Bell Labs in 1947 by Shockley, Bardeen and Brattain [1], a solid-state switch that replaced vacuum tubes in the early implementation of binary logic. Continued improvement in material science, computer architecture and device design lead to the emergence of the MOSFET in the sixties [2]. A MOSFET as shown in figure 1.0, it is a high speed switch which works when a voltage applied to the gate terminal (G) giving a potential difference across an insulating oxide, results in an induced channel of accumulated minority charge (n or p type) carrier underneath the oxide facilitating current flow from the source (S) to drain (D) terminal. The evolution of this device from then was envisioned by Gordon Moore, "the number of components on integrated chips

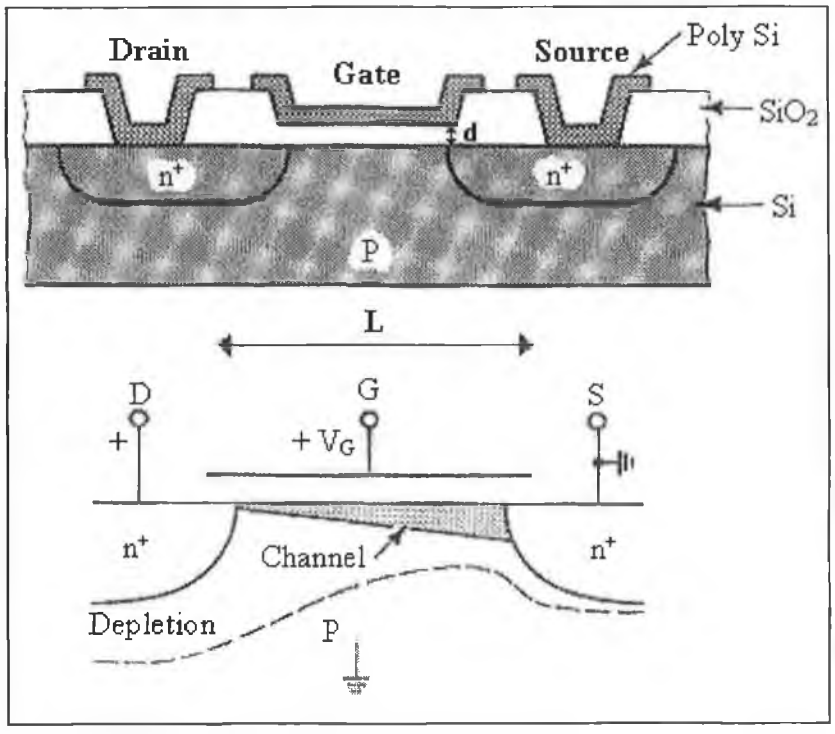

Figure 1.0: A cross section of an enhancement type n-channel MOS transistor [3].

would double every 18 months for the next ten years". MOS technology moved from p to n and then to CMOS through continuous improvements in areas like lithography and contamination control [2]. Despite lower performance, high processing complexity and a tendency to "lock up" in high current mode, lower power dissipation facilitating higher integration allowed CMOS to surpass bipolar technology and become the key "building block" of the modern semiconductor industry [4].

1.1 Si(100) A technologically important surface

In today's global semiconductor device fabrication industry the integrity of silicon's oxide plays a critical role. The oxidation of silicon at high temperature in an oxygen ambient is a remarkable process, resulting in a stoichiometric (O/Si, 2:1) amorphous film in which Si atoms form a tetrahedral diamond-like lattice similar to crystalline silicon but now each silicon is connected to four other silicon atoms not directly, but via linear Si-O-Si bonds. At MOS operating temperatures this protective oxide film is; mechanically stable, electrically insulating (almost a perfect dielectric) and chemically protective. Germanium and gallium arsenide, materials whose inherent electrical properties are superior to silicon's are at a disadvantage because of the inferior properties of their oxides: germanium dioxide is water soluble and the oxidation of gallium arsenide produces metallic precipitates [5]. Figure 1.1 (a) shows a ball and stick model of a Si(100) surface which has been oxidised and whose indigenous state due to two surface dangling bonds has been H passivated.

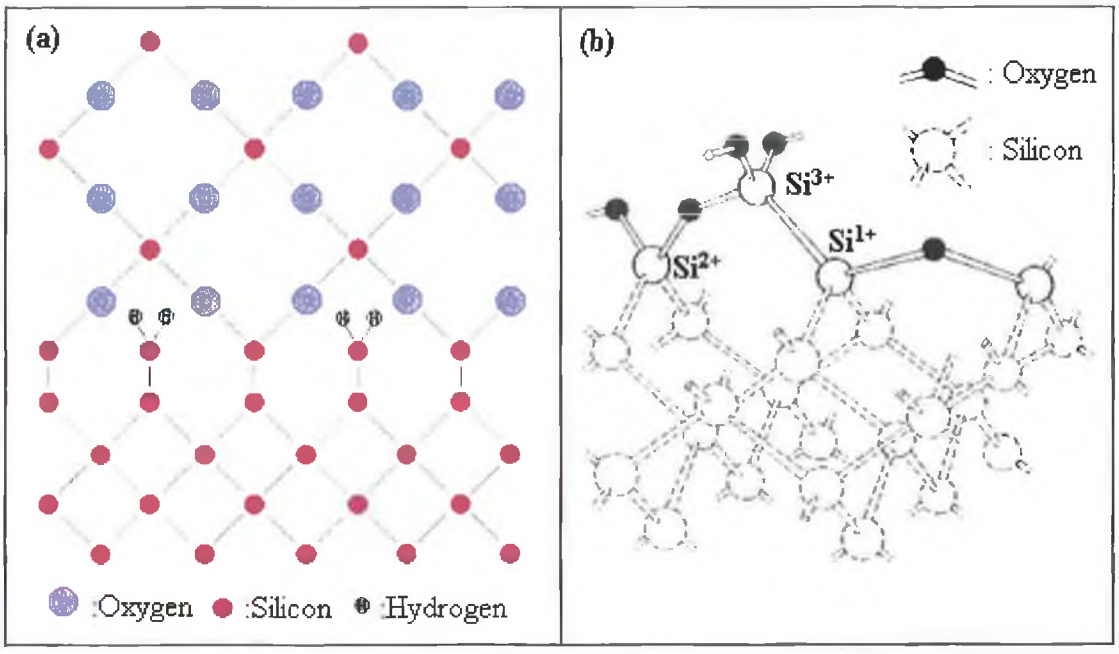

Figure 1.1: (a) Si(100) Ideal Termination, (b) Actual interface (Lu [6])

This represents an ideal interface, as it is atomically abrupt and chemically inert. Si(100) is the preferred substrate orientation for device fabrication due to it's lower defect density and post oxidation suboxide distribution, relative to Si(111) where a rougher, more distributed interface is obtained owing to the greater number of indigenous defect states (Si^{1+} and Si^{3+}).

1.2 Oxidation of silicon

At a clean Si(100) surface, silicon atoms at the lattice boundary have a reduced coordination number and reconstruct to reduce surface energy. Surface passivation with hydrogen terminates the silicon dangling bonds and renders the surface chemically inert. When heated to 1000 °C the silicon lattice, through as many degrees of freedom as possible, violently dissipates the thermal energy. The surface reconstruction is broken.
If oxygen is present, a complex two-stage reaction takes place, which was first described by Deal and Grove [7] where an oxide layer is formed as the underlying silicon is oxidised.

$$Si + O_2 \Leftrightarrow SiO_2$$

Atomic transport during thermal oxidation occurs via interstitial diffusion of molecular oxygen across the growing oxide, without reacting with it, and subsequent reaction with Si at the oxide/Si interface promoting growth [8]. The oxidation kinetics is controlled by "interface reactions" in the initial stages and by "diffusion of the reacting species" once a thick film has been grown. The "marriage" between the oxide and underlying film is not without "strain". The transition from bulk crystalline silicon to bulk amorphous silicon dioxide occurs at an interface where the density of silicon atoms in crystalline Si is twice that in glassy SiO_2, so the silicon "lattice" must expand during oxidation due to the insertion of an O atom into the Si-Si bond [9]. This lattice mismatch makes an epitaxial relationship between the substrate and oxide hard to realise. Both compressive and tensile stress result in the interfacial region consisting of buffer regions in which there are both chemical and structural transitions in Si in terms of its bonding state and geometry.

1.3 SiO_x Chemical transition region

In $Si(100)/SiO_2$ and $Si(111)/SiO_2$ interfaces, the detection by photoemission of the non-indigenous suboxides Si^{2+} and Si^{3+} respectively, indicates the existence of non-ideal interfaces in both systems. By growing the oxides to different thickness and varying the degree of surface sensitivity, photoemission studies can be used to determined the suboxides to be distributed within ~1 nm of the interface. Figure 1.2 (a) and (b) shows the Si_{2p} core level spectra from oxide layers grown in-situ to a thickness of 0.5 nm on Si(100) and Si(111) substrates respectively [10]. The figure shows the presence of all possible suboxide states in both systems but as will be described in chapter 4, the different intensity distributions is related to the surface orientation.

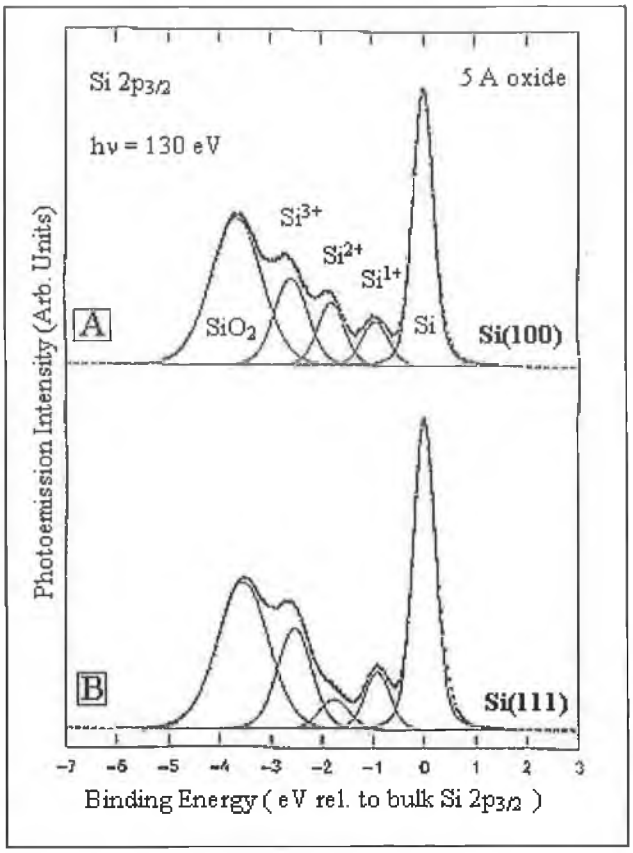

Figure 1.2: The distribution of silicon oxidation states for 0.5 nm dielectric layers grown in UHV on atomically clean Si(100) and Si(111) (Himpsel [10])

1.4 Structural transition region

Thermal oxidation results in an oxide, which is amorphous or glassy. Silicon is bonded to four oxygen atoms in a tetrahedral structure. In high resolution scattering studies Mozzi and Warren [11] have shown that the intra-tetrahedral bond angle $\theta_{O\text{-}Si\text{-}O}$ is essentially preserved in amorphous SiO_2 but the inter-tetrahedral Si-O-Si bond angle $\theta_{Si\text{-}O\text{-}Si}$ has a distribution of values. The individual tetrahedra form an interconnecting ring system of three to eight SiO_4 tetrahedra units that are joined together via bridging oxygens with a range of Si-O-Si bond angles θ. Figure 1.3 (a) and (b) [12] show the basic bonding unit of the oxide with Si tetrahedraly coordinated to four oxygens.

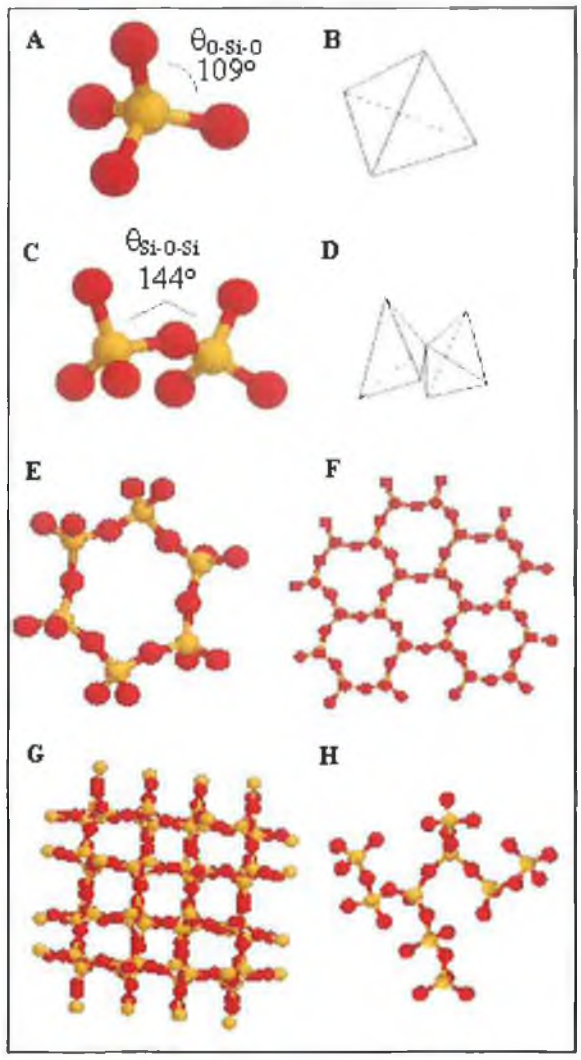

Figure 1.3: The well defined geometric bonding structure of Si and O in the basic SiO_2 tetrahedron and the possible crystalline and amorphous structures formed from inter-tetrahedron bonding through the flexible Si-O-Si bond [12].

However, individual tetrahedra are connected via bridging oxygen atoms as shown in figure 1.3 (c), this bond is flexible and doesn't support any long range order normally found in crystals. Individual tetrahedra link to form ring structures. Figure 1.3 (e) shows a six-member ring, figure 1.3 (f) shows how such rings connect in a plane. The number of tetrahedra in a ring is related to the O bonding angle that connects them. Zachariassen et al [13] described the distribution of these ring structures using a continuous random network in a random bonding model (RBM). Figure 1.3 (g) shows crystalline SiO_2 (α quartz), which has long-range order. The high temperature crystalline forms of SiO_2 are tridymite and cristobalite (not shown). Figure 1.3 (h) shows the amorphous form of SiO_2. Structural transition regions are thought to exist on both sides of the interface.

On the substrate side Haight and Feldman [14] in a non-destructive study of the interface structure and stoichiometry, using ion backscattering channelling methods NRA and RBS found that in the near interfacial region there is a zone with excess Si. This Si corresponds to non-epitaxial layers within the single crystalline substrate. They associated the result with a vertical displacement of two atomic layers of silicon next to the interface. On the oxide side of the interface a structural transition region is thought to exist above the suboxide layer. This SiO_2 layer is stoichiometric but the Si-O-Si bond angle is reduced due to compressive stress associated with the interface. Grunthaner et al [15] considered a structure induced charge transfer (SICT) model in which the charge distribution in the Si-O bond, as well as the in the ring, would be dependent upon the inter-tetrahedral bond angle $\theta_{Si\text{-}O\text{-}Si}$ and the ring size n. Bulk SiO_2 has a distribution of Si-O-Si bond angles centred near 144°, similar to α-quartz and indicative of six Si tetrahedra in a ring structure. In a region within 0.3 nm of the interface, a strained layer induced by lattice mismatch is observed corresponding to a Si-O-Si bond angle distribution centred near 120°, similar to the four-member ring structure of the SiO_2 polymorph coesite. Grunthaner resolved both the O_{1s} and Si_{2p}^{4+} photoemission peaks into components corresponding to the bulk and strained regions. Although the SICT model is well defined and a strained SiO_2 region above the interfacial region has been revealed by both TEM studies and by a reduction in oxide etch rate [16]. Due to the relative insensitivity to the chemical environment beyond the nearest neighbour coordination shell, photoemission has little to say regarding the local or extended structure of the oxide.

1.5 Limitations

As further reduction in MOSFET device dimensions require further reduction in oxide thickness and channel length, the chemical and structural transitions discussed above will constitute a larger fraction of the oxide. With the effect of these regions on device performance not yet fully understood, SiO_2's ability to sustain Moore's law into the future is not certain. Also in optical processing, lithographic improvements have become diffraction limited and the cost of electron beam alternatives may outweigh the gains. In addition, further device scaling is already limited by leakage current through

the oxide and short-channel effects [2]. Solutions have come forth in the form of device design revision, as in (i.e. silicon on insulator SOI) and the re-engineering of the oxide material in the form of high k dielectrics. A material with a higher dielectric constant than SiO_2, can have a thicker oxide (thus reducing the tunnelling problem) while maintaining the same capacitive thickness. Unfortunately many higher k dielectrics Y_2O_3, CeO_2, Ta_2 and TiO_2 have bandgaps smaller than SiO_2 and so the gains from increased thickness are undermined by the exponential dependence of leakage current on the bandgap related barrier height. Also, a number of these materials are not thermally stable on silicon and suffer from a large number of interface density of states [2]. So far N incorporation in SiO_2 either directly during oxidation (N_2O or NO) or in a post oxidation anneal (N_2O, NO or NH_3) has improved device operation by: acting as a barrier to Boron diffusion at the gate/oxide interface, increasing the oxide dielectric constant in the bulk oxide and reducing interface strain at the oxide/substrate interface.

1.6 Thesis Motivation

The pursuit of a complete understanding of the oxide layer resulting from thermal oxidation of silicon encompassing both the interface and bulk film properties has been on going and will continue, for many years. SiO_2 films have been characterised by many different experimental techniques whose results give information on film thickness (Elliposimetry [17], TEM [18], ARXPS [19-25], XPS [26-27], NRA), chemical state (XPS, AES, FTIR), chemical composition (SIMS), micro roughness (AFM, STM) and interface structure (synchrotron radiation photoemission).

The processes used to realise SiO_2 films on Si are diverse and range from; thermal oxidation, wet chemical oxidation, electrochemical anodization, chemical deposition (CVD, PECVD, JVD, ALD), physical deposition (i.e. LEII). Also many oxides are grown in-situ on atomically clean silicon surfaces in ultra-high vacuum. It is not surprising therefore to find discrepancies in the literature among researchers trying to converge on a universal description of the Si/SiO_2 system, for samples with such different sample histories.

The samples studies in this thesis are thermal oxides grown in an oxygen ambient at room temperature in a class 100 clean room (i.e. 1 μm sized contaminant per cubic meter) on a 200 mm hydrogen passivated Si(100) wafer in a 0.18 μm (channel length) fabrication process which is designed to produce high quality oxide films. This provides the confidence that any 1 x 1 cm sample of such a production wafer analysed is identical both chemically and electrically to any other. After all, a 0.1 nm thickness variation in oxide thickness would result in an order of magnitude variation in tunnelling current in a final MOS structure. Within the capabilities of conventional XPS and synchrotron radiation sources, this thesis seeks to characterise the dielectric layer chemically using photoemission.

1.7 Thesis Layout

In chapter 2 both the theory of and implementation details, of the experimental procedures used in this thesis are outlined and discussed.

The aim of chapter 3 is to investigate the quality of dielectric layers spanning the thin (<10 nm) to ultra-thin (<5 nm) thickness regimes chemically. To that end chapter 3 undertakes the chemical characterisation using XPS to gauge the chemical composition, chemical state and thickness of the as received films. Depth profiling using inert ion bombardment and wet chemical etching using weak HF solutions, in conjunction with ARXPS is used to "better illuminate" the interface which is otherwise attenuated by the overlying oxide. Also, from wet chemical profiling of the oxynitrides the spatial distribution and bonding environment of nitrogen is measured.

The large energy window and large sampling depth of XPS allowed the high binding energy peaks (N and O) to be sampled and the substrate to be seen through the thick (6.5 and 5.5 nm) oxide layers allowing values of thickness and stoichiometry to be calculated. The consistency in these values along with the homogeneity of the elemental composition has allowed the high quality of the dielectric layer to be ascertained.

In chapter 4 the chemical state and distribution of interfacial suboxides in both SiO_2/Si and SiON/Si interfacial regions were investigated using the tuneable surface sensitivity and high resolution capabilities of a synchrotron radiation source. A comparison of the interfacial regions in the nitrided and non-nitrided layer was made to elucidate possible interfacial Si-N related bonding. The dielectric layers were thinned wet chemically using dilute HF acid etching in order to realise an oxide thickness comparable to the small sampling depth of the photon energies used in the study. AFM measurements were undertaken in order to gauge the extent of wet chemical etch induced surface roughness.

Chapter 5 was based on a collaboration with Boston University where XES and XAS measurements were performed at a synchrotron (NSLS) on the oxide and oxynitride layers. The layers were etched to thickness comparable to those in chapter 4. The measurements gave information about the element specific partial density of states. From comparison of the partial densities of valence and conduction band states for oxygen and nitrogen in the interfacial region, the role of nitrogen incorporation at the interface and its effect on the band off-sets was investigated.

In Chapter 6 the potential of sulphur to ideally terminate the surface re-constructions of the clean Si(100) and Ge(100) surfaces in-situ using an UHV compatible electrochemical cell was investigated. The surface microstructure and chemical state were interpreted through the surface core level shifts, which were measured using synchrotron soft X-ray core level photoemission and LEED.

In Chapter 7 an overall conclusion and discussion of the thesis work undertaken is presented and possible future work is considered.

1.8 References for Chapter I

1 S. M. Sze, Physics of Semiconductor Devices. New York: John Wiely & Sons 1969.

2 D. A. Buchanan, IBM J. RES. DEVELOP.,**43** (1999),

3 B.G. Streetman, Solid State Electronic Devices: Prentice/Hall International 1980.

4 R. D. Issac, IBM J. Res. Develop., **44** (2000), 369

5 F. J. Feigl, Physics Today, Oct. (1996), 47

6 Z. H. Lu et al, Appl. Phys. Lett. **63** (1993) 2941

7 B. Deal, A. Grove, J. Appl. Phys. **36** (1965) 3770

8 I. J. R. Baumvol, Surf. Sci. Rpts. **36** (1999) 1

9 Z. Lu, S. Tay, R. Cao, Appl. Phys. Lett. **19** (1995) 2836

10 F. Himpsel, F. McFeely, A. Ibramimi, J. Yarmoff, G. Hollinger, Phys. Rev. B**38** (1988) 6084

11 L. Mozzi and B. Warren, J. Appl. Crystallogr. **2** (1969) 164

12 West Virginia University Department of Geography and Geology http://www.geo.wvu.edu/~langv/Geol284/Min8IgFels/tsld030.htm

13 W. H. Zachariassen, J. Am. Chem. Soc. **54** (1932) 3841

14 R Haight, L Feldman, J. Appl Phys. **53** (1982) 4884

15 F. Grunthaner, P. Grunthaner, R. Vasquez, B. Lewis, J. Maserjian, A Madhukar, Phys Rev. Lett. **43** (1979) 1683

16 S. Miyazaki, T. Tamura, m. Ogasawara, H. Itokawa, H. Murkami M. Hirose, Appl. Surf. Sci. **159** (2000) 75

17 E. Irene, Crit. Rev. Solid State Mater. Sci. **14** (1998) 175

18 A. Carim, R. Sinclair, Chemical and Electrochemical Processes **3** (1987) 741

19 S. Spruytte, D. Pantelidis J. Vac. Sci. Technol. A**19** (2001) 603

20 L. Chen, R. W. Hoffman J. Vac. Sci. Technol. A**11** (1993) 2303

21 J. E. Fulghum, Surf. Interface Anal. **20** (1993) 161

[22] T.D. Bussing, P.H. Holloway J. Vac. Sci. Technol. A**3** (1985) 1973

[23] W.A.M Aarnink, Appl. Surf. Sci. **45** (1990) 37

[24] M.F. Ebel, Spectrochimica Acta, **39**B (1984) 637

[25] P. J. Cumpson J. Electron Spectrosc. Relat. Phenom. **73** (1995) 25

[26] D.F. Mitchell, Surf. Interface Anal **21** (1994) 44

[27] Z.H. Lu, S.P. Tay L.c. Feldman B. Brar, Appl. Phys. Lett. 71 (1997) 2764

Chapter 2

Theory of Experimental Techniques

2.0 Photoemission Introduction

In the condensed environment of a solid, the overlap and nature of electron bonds, along with the lattice structure, decide the solid's electronic properties. In a metal, the abundance of de-localized "free" electrons "screen" the effect of the lattice, resulting in a free electron dispersion relation (parabolic E vs. k) for its wavevector. In a semiconductor the "unscreened" periodic lattice diffracts (forbids) certain wavevector values resulting in band gaps. Photoemission's ability to probe electron dispersion by interrogating the momentum of occupied states, and electron bond interactions from binding energies arises from both the quantised and wave like nature of electromagnetic radiation and matter as shown in figure 2.0.

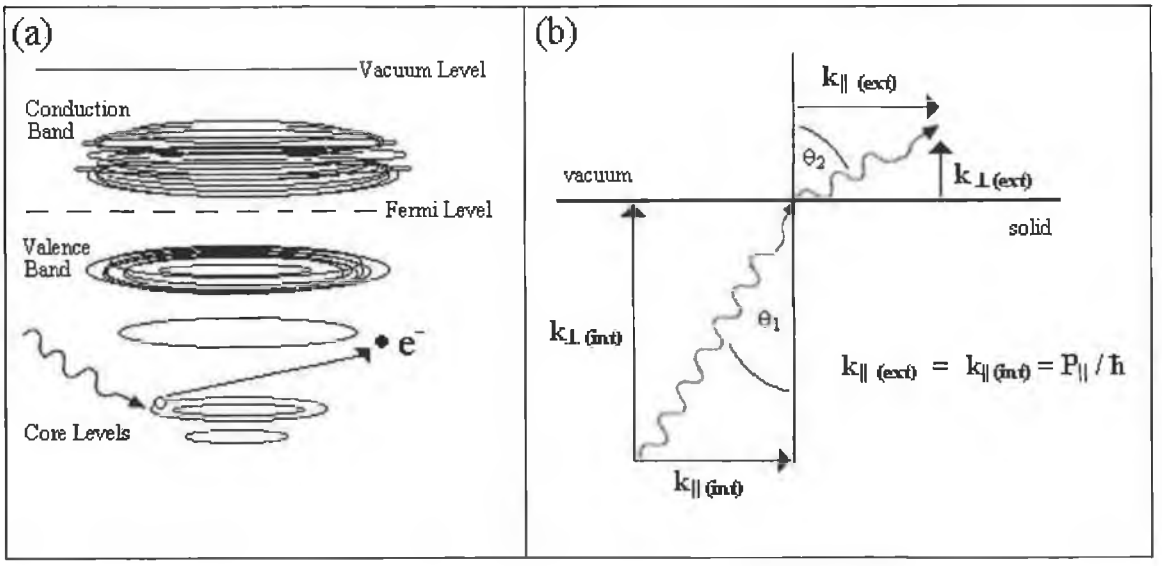

Figure 2.0: a) Simplified representation of the band structure of a semiconductor where adjacent atomic wavefunctions overlap to form bands. b) Absorption of a high-energy photon by a inner core electron can liberate it from the solid. The photoelectron emitted from the sample is refracted by the surface potential step. The parallel component of the momentum is conserved during the transition, but the perpendicular component is not conserved due to the loss of crystal periodicity along the surface normal.

When illuminated with light of suitable photon energy, an electron absorbs the quantised photon energy in an "all or nothing process" in which total energy is conserved, as borne out by the Einstein relation equation 2.0. Its wave nature is conveyed via the de-Brogile relationship by its momentum and associated wavelength. The termination of the solid presents an interface across which the component of the photoelectron's momentum tangential to the surface is conserved. The component of the photoelectrons momentum normal to the surface is not conserved due to the loss of crystal periodicity. In the photoemission process a solid is illuminated with photons, which are energetic enough to excite electrons from filled states below the Fermi level (E_F) to empty states above the vacuum level where they escape the solid [1]. By measuring the kinetic energy and intensity of the emitted electrons integrated over a large number of emission directions, the binding energy and joint density of states can be directly measured. By measuring the momentum of the emitted electron (i.e. it's direction of emission), the k-vector of the occupied electronic state can also be determined. Thus, angle resolved photoemission ARP spectroscopy measures the dispersion of the bands in the solid. ARP typically uses photons with energies < 100 eV. Using higher energy (X-ray) photons, XPS probes the chemical state of "deep" core level electrons by measuring their binding energies [2].

A complete appreciation of the photoemission process embodying both the particle and wave aspects necessitate a rigorous quantum mechanical treatment as undertaken by models such as, the three-step model [3] and the microscopic scattering theory of the dynamic approach. This thesis is not concerned with the momentum of photoelectrons in the SiO_2 dielectric layers. While it does have a band gap and sits on a semiconductor silicon substrate, the dielectric layer is amorphous and doesn't have a band structure. There is local order in the silicon oxygen bonding tetrahedra, but long range "glassy" disorder arises from the flexibility of the Si-O-Si bonds which link these tetrahedra. The pursuit of this thesis is the "Chemical shift" or binding energy change experienced by the photoelectron due to the silicon oxygen bonding interaction.

2.1 Photoemission Process

In the photoelectric effect the absorption of a photon of suitable energy by an electron in a solid can result in photoionisation were the electron is liberated from the solid with a well defined kinetic energy; having "paid off" it's workfunction and binding energy "debt" to the solid and host atom respectively as described by the Einstein relation in equation 2.0.

$$E_k = h\upsilon - E_b - \phi \qquad \textbf{Equation 2.0}$$

A photoelectron which escapes the solid with out being scattered by other electrons or the lattice, "remembers" it's bonding history when it's kinetic energy is analysed because each excited atom (except hydrogen) possesses "core electrons" not directly involved in the bonding. The binding energy of each core electron is characteristic of the elemental atom to which it is bound. Information on the binding energies of core electrons within a sample allows qualitative elemental analysis. In photoemission the number of photoelectrons produced from any given core level for a given photon energy flux per unit time is characterized by a transition probability called the photoionisation cross section. The resulting line shapes (N(E) vs. E) are determined by a convolution of the photon energy (X-ray) distribution, the initial state structure (electron energy distribution in the ground state), the final state structure (electron energy distribution in the photoionised state), lifetime broadening effects, electron energy loss structure acquired during transfer from the atom to the surface, and the spectrometer resolution function.

Figure 2.1 [4] illustrates the photoexcitation process (upper panel) and a typical photoelectron spectrum (lower panel). It shows the narrow core level states which sit below the complex overlapping valence band states. Above the vacuum level there exists an infinite continuum of states. The lower panel shows the corresponding peaks as seen by the analyser. The core level peak sits on a secondary electron tail.

When surface sensitivity is being optimised (chapter 4, section 4.6.1, figure 4.25) by selecting a photon energy which results in a E_k value at the minimum of the Universal curve [5], (shown in figure 2.6) the peak sits quite high on the background making background removal (see figure 4.25) a formidable task. The contributions to the spectrum mentioned above will be discussed next.

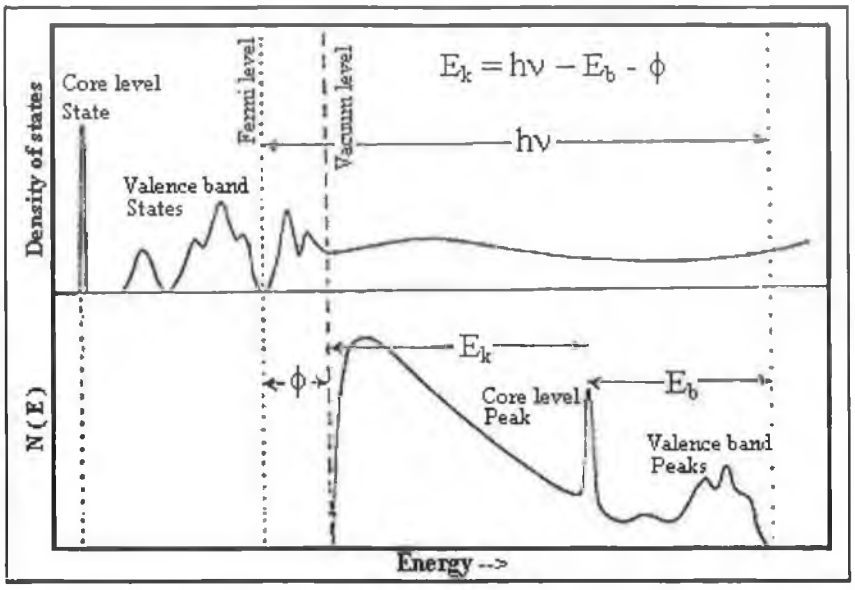

Figure 2.1: In the photoemission process sates below the Fermi level are probed. Above the vacuum level a continuum of states exists. The valence band states are broad and complex; the core level states are narrow and well defined. Analysing the photoelectrons kinetic energy reveals the density of states in the sample. The spectrum sits on a secondary electron tail [4].

2.1.1 X-Ray production

Core level transitions as shown in figure 2.2, of the type 2p–1s, initiated by high energy electron bombardment of conventional X-ray anodes (Al and Mg) result in characteristic emission lines on a continuous Bremsstrahlung background. An improvement in resolution can be made at the cost of intensity by "monochromating" the emission with a Rowland circle, thus removing the Bremsstrahlung and unwanted X-ray line features such as ghost peaks. For non-monochromated systems a thin (μm) Al foil will perform a reasonable "clean up" of the emission but without any improvement in resolution.

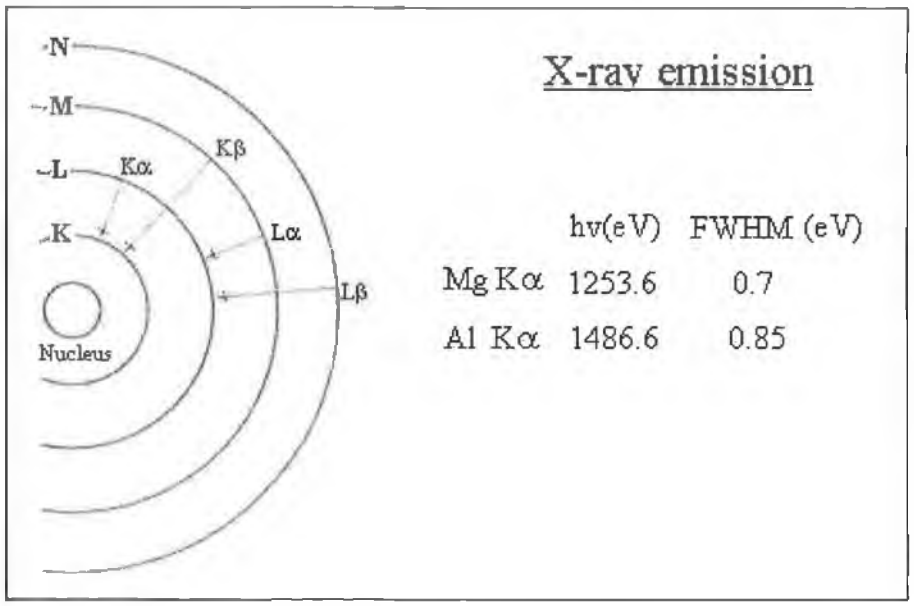

Figure 2.2: Illustration of the atomic transitions associated with the principal X-ray lines.

The emission lines are Lorentzian in shape representing the inherent lifetime broadening in the X-ray excitation process. The fate of the energy contained in X-ray emission can be considered in terms of; initial state effects, final state effects and extrinsic losses; all can contribute to the final spectrum.

1) Absorption and ionisation (initial state effects)
2) Response of atom and creation of photoelectron (final state effects)
3) Transport of electron to surface and escape (extrinsic losses)

2.1.2 Spin-Orbit Splitting (SOS)

For any electron in an orbit with orbital angular momentum, coupling between magnetic fields of spin (s) and angular momentum (l) occurs. The phenomenon is not observed in 's' orbits due to the spherical nature of the orbit (i.e. no net Angular momentum). Spin-orbit splitting is an initial state effect. Figure 2.3 illustrates the coupling possibilities.

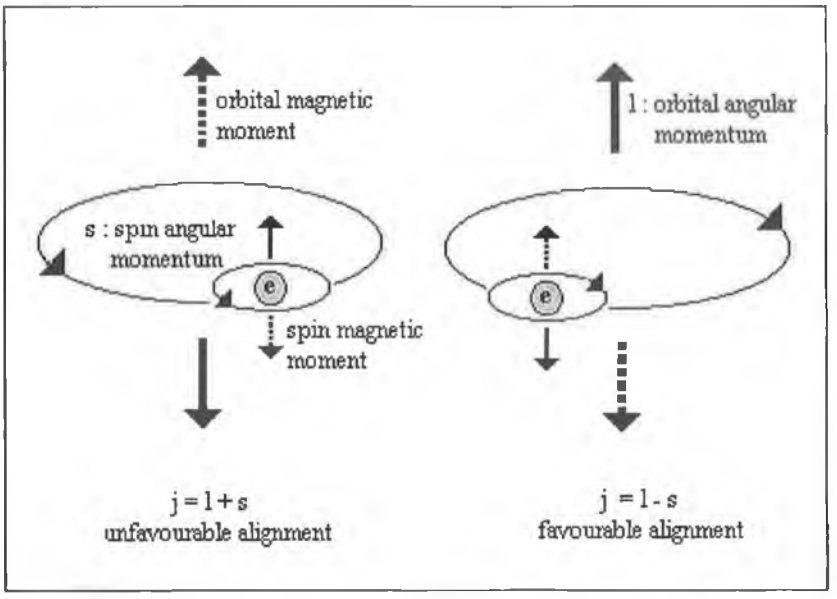

Figure 2.3: Illustration of coupling between orbital and spin magnetic moments which gives rise to degeneracy in the atomic transition.

The total angular momentum is: $j = |l \pm s|$

For the Si_{2p} line :

n	l	s	j	Term
2	1	$+1/2$	$3/2$	$^2{}_{P(3/2)}$
2	1	$-1/2$	$1/2$	$^2{}_{P(1/2)}$

There are 2j+1 spin orbit levels at each j value resulting in a spectral degeneracy of 2:1 for $2_{P(3/2)}$ to $2_{P(1/2)}$. Figure 2.4 shows the presence of the spin-orbit interaction in an experimental spectrum. A high resolution (100 meV) Si_{2p} spectrum (black: raw data, red: fit to data) of a 0.7 nm SiO_2 dielectric layer. Each peak has a spin-orbit split of 0.6 eV, the energy split is resolved by two peaks whose intensity ratio conveys the (3/2:1/2) degeneracy of the state. For clarity the background has been removed, the spectrum has been charge referenced to the $Si_{2p}{}^{0+}{}_{3/2}$ state (at 99.3 eV), and only the $Si_{2p}{}^{0+}$ component is shown (in blue).

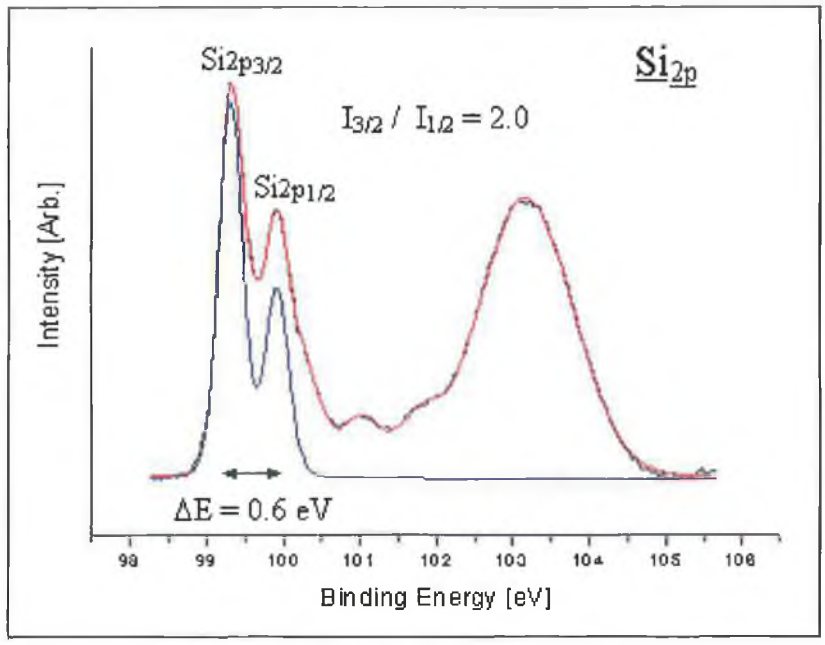

Figure 2.4: A high resolution Si_{2p} spectrum reveals the presence of two spectral components associated with each atomic state as the spin orbit split ($2p_{1/2}/2p_{3/2}$) degeneracy is resolved.

2.1.3 The Chemical Shift

The discovery that the so called 'fixed' binding energies of core level atoms were affected by their chemical environment, leading to detectable (0.1 to 10 eV) shifts in their photoelectron energies was made in the by Siegbahn et al [6], the shifts became known as 'chemical shifts'. Using the high resolution and surface sensitivity of synchrotron radiation Himpsel et al [7] proposed a 'graded' interface model (as discussed in chapter 4) for the SiO_2/Si interface by considering the chemically shifted components in a spectrum similar to ours as shown in figure 2.5. Figure 2.5 is essentially figure 2.4 with all oxidation states present except interfacial hydrides (removed for clarity). The chemical states represented in the ball and stick model of Si(100)/SiO_2 in figure 1.1 are all represented. From comparing the figures, the presence of the interfacial hydrides in the raw data close to the Si^{0+} is dramatic.

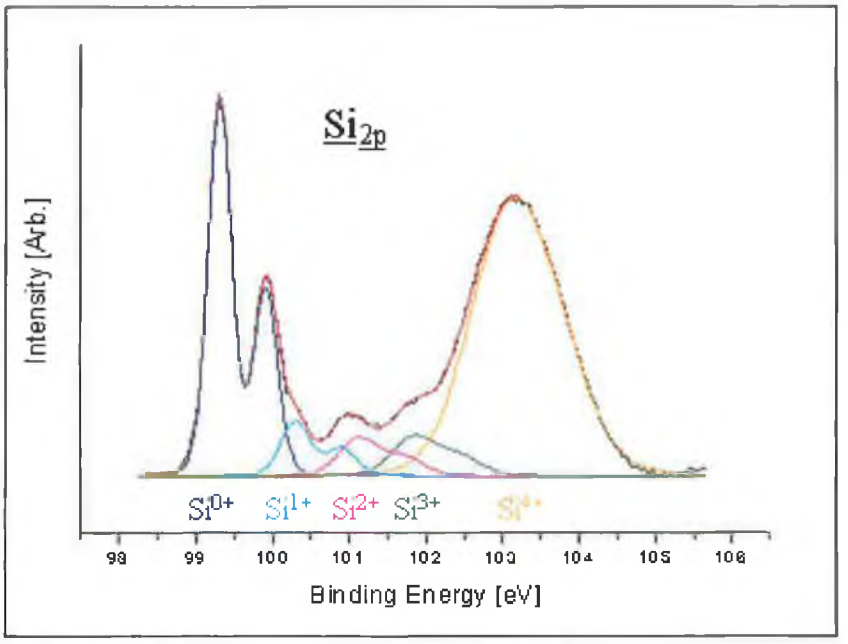

Figure 2.5: A high resolution Si_{2p} spectrum reveals the presence of four chemically shifted oxidation states, which occur at binding energies higher than the substrate due to the increased influence of nearest neighbour oxygen atoms. The chemical shift varies approximately linearly with oxygen coordination number.

The chemical shift which a core level electron experiences arises from the oxidation state its host atom sees within the first oxidation sphere (i.e. from the nearest neighbour oxygen atom). The extent of the shift is linearly proportional to the degree of oxidation (Silicon^{x+} $\Rightarrow$ x Oxygen atoms). The chemical shift is assumed to be an initial state effect if final state effects such as relaxation have similar magnitudes for different oxidation states. However, the changes in chemical environment leading to the chemical shift arise from changes in both, distribution and density of the bonding electrons [8]. For example the full charge implied by the formal oxidation state is only attained when the chemical bonding is completely ionic (i.e. no covalent character). In the charge potential model [3], the observed E_B is related to a reference energy E°_B (neutral atom), the charge q_i, on atom i, and the charge q_j, on surrounding atoms j at distances r_{ij}, with the constant k through:

$$E_B = E^{\circ}_B + kq_i + \sum_{j \neq i} \left(\frac{q_i}{r_{ij}} \right) \qquad \textbf{Equation 2.1}$$

As the positive charge on the reference atom increases by formation of chemical bonds, the binding energy E_B will increase. The last term in equation 2.1 (the Madelung potential) represents the fact that the charge q_i removed or added by formation of a chemical bond is not displaced to infinity, but to surrounding atoms. Thus the chemical shift between states 1 and 2 can be written:

$$E_B = k\Delta q_i + \Delta V_i \qquad \textbf{Equation 2.2}$$

where ΔV_i represents the potential change in surrounding atoms. However, the chemical shift assignment based on charge transfer due to oxidation state is acceptable for the SiO_2 system due to the well known bond length and structure, also this assignment scheme has recently been validated by Car's group [9] after being questioned by Banaszak et al [10] who argued that the chemical shifts also depend on O-Si bond in the second coordination sphere.

2.1.4 Koopmans' Theorem [11]

The photoemission process is extremely rapid (~10^{-6} sec) and the assumption that the other electrons remain "frozen" forms the basis for Koopmans' theorem, which states:

"The binding energy of an emitted photoelectron is simply the energy difference between the (n-1) electron final state and the n electron initial state".

If no relaxation follows photoemission, then the binding energy E_B is equal to the orbital energy which can be calculated from Hartree–Fock calculations. However, other electrons do not remain "frozen" during the photoemission process. The electron response is discussed in section 2.1.7. Despite this, the spectral implications of electron relaxation processes can be catered for during peak fitting and so Koopmans' theorem provides a working basis.

2.1.5 Surface Sensitivity

The penetration depth of X-rays in solids is on of order of several microns due to the low interaction between photons and the material. However, whether or not a photoelectron excited at a certain depth will pass through a solid without scattering after absorbing an X-ray depends on it's kinetic energy and the nature of the material. The average distance an electron with a given energy travels between inelastic collisions is known as the Inelastic Mean Free path (IMFP), whose functional relationship for the elements is described by Seah and Dench [12]:

$$\mathrm{IMFP} = \lambda = 538\frac{1}{E_k^{\,2}} + 0.41\sqrt{aE_k} \qquad \textbf{Equation 2.3}$$

- λ is in units of monolayers
- a monolayer thickness (nm)
- E_k electron kinetic energy (eV)

Therefore photoelectrons with kinetic energies in the 10–1000 eV energy range, above the Fermi energy, must originate very close (<10 nm) to the surface in order to emerge unscattered and make up the primary photoelectron peak. Inelastically scattered electrons contribute to the secondary electron background. Herein lies the surface sensitivity of photoemission. In synchrotron studies the minimum in the 'universal' curve shown in figure 2.6 (IMFP vs. E_k) is exploited when an incident photon with a given energy results in photoelectrons emerging exclusively from the outermost atomic layers due to the strong interaction of low kinetic energy electrons with the sample. Also by considering off angle emission (grazing incidence), the longer path to be travelled by grazing photoelectrons deep in the solid means they are attenuated more, and so the primary peak arises from surface photoelectrons.

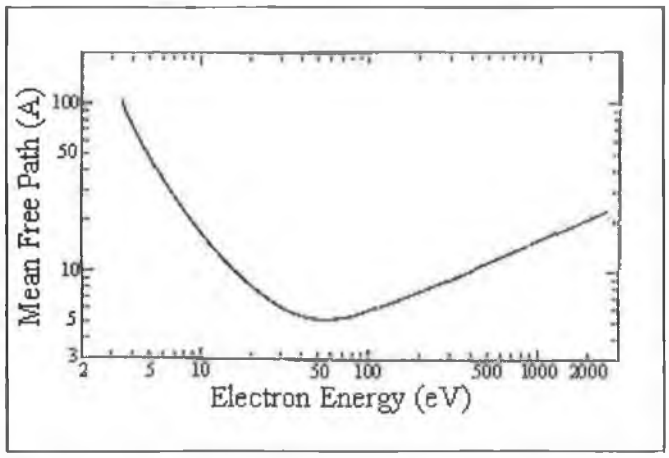

Figure 2.6: The universal trend for a minimum in the IMFP of photoelectrons with a kinetic energy of approximately 50 eV is mapped out by the universal curve [5].

2.1.6 Final state effects

During the photoemission process, other electrons in the sample respond to the creation of a core hole by rearranging to shield, or minimize, the energy of the ionised atom. Relaxation of electrons from the atom containing the core hole is known as atomic relaxation and from electrons on surrounding atoms as extra-atomic relaxation. Most of the atomic relaxation component is due to the rearrangement of outer shell electrons, which have a smaller E_B than the photoelectron. The inner shell electrons who's E_B is larger than the emitted photoelectron, have a small contribution and are neglected. The form of extra-atomic relaxation depends on the material being examined. In metals and highly doped semiconductors, valence band electrons can move from one atom to the next to screen a core hole.

2.1.7 Peak broadening

Ultimately a core level photoelectron signal presents itself as a Voigt peak on a secondary electron background. A core level Voigt peak is a convolution of a Lorentzian and a Gaussian peak. It's FWHM contains contributions from; the X-ray source E_{source}, the electron analyser $E_{analyser}$, and energy uncertainty due to the core hole

lifetime E_{hole}. The sum of the square of these factors is the square of the measured FWHM:

$$(\Delta E_M)^2 = (\Delta E_{source})^2 + (\Delta E_{analyser})^2 + (\Delta E_{hole})^2 \quad \textbf{Equation 2.4}$$

The line shape due to the lifetime of the core hole is Lorentzian. Lifetime broadening results in symmetric broadening. Lifetime broadening can be gauged from the Heisenberg uncertainty principle

$$\Gamma = \frac{h}{\tau} \quad \textbf{Equation 2.5}$$

Γ is the intrinsic peak width in eV

h Planck's constant in eV seconds

τ is the core hole lifetime in seconds

A typical value of Γ is 0.1 eV. The instrumental broadening of the X-ray source and analyser is Gaussian. For non-metallic samples broadening also arises from charging. Asymmetric broadening can occur in metals and highly doped semiconductors where the production of a positive potential site with a final state energy lower than the original surface scatters conduction electrons across the Fermi level, providing a continuous range of allowed one-electron excitation energies, resulting in a asymmetric tailing of the main peak to the high binding energy side, the extent of which depends on the density of states at the Fermi level.

Plasmon losses:

A plasmon peak arises from a collective oscillation of a group of charges or Plasma (i.e. free electrons in a metal or gas). A photoelectron passing through a crystal couples with its longitudinal electric field and electron density fluctuations to create extrinsic plasmons. Intrinsic plasmons are produced during core-hole relaxation. Following the photoelectric excitation of bound electrons, plasmons show up as broad smooth replicas of the photoelectron peaks shifted to lower kinetic energy by an amount equal to the

plasmon energy $\omega_p h/2\pi$. In the free electron approximation, the plasmon energy is related to the valence electron density as

$$\left(\omega_p \frac{h}{2\pi}\right)^2 = \left(\left(\frac{hq}{2\pi}\right)^2 \frac{1}{m\pi}\right) N_v \quad \textbf{Equation 2.6}$$

$\omega_p h/2\pi$ is the plasmon energy

m is the electron mass

q is the electron charge

N_v is the valence electron density

2.2 XPS experimental set-up / Data Acquisition

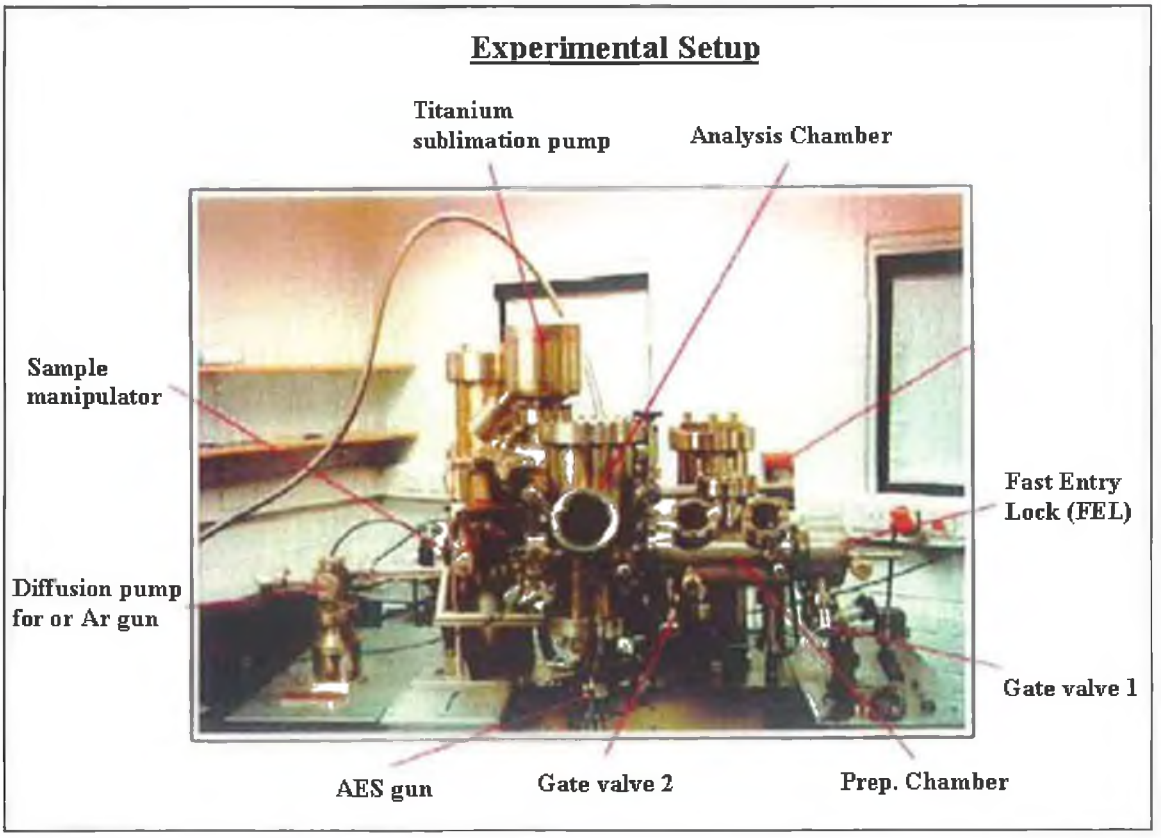

Figure 2.7: Photograph of the XPS system showing principle components; diffusion pumps, preparation and analysis chambers. The X-ray gun and analyser are at the rear of the system.

Figure 2.7 shows a photograph of the XPS system. It is equipped with two rotary backed diffusion pumps, which maintain UHV pressures in both the analysis and preparation chambers. An additional fast entry lock (FEL) chamber allows samples to be introduced from air to UHV quickly. The pressure in the preparation and analysis chamber are isolated from each other and from the FEL via UHV compatible gate valves. Samples are transferred using a trolley system and wobble sticks. The analysis chamber is equipped with a VG clam analyser with electrostatic lens, an Auger electron spectroscopy gun and a differentially pumped ion sputter gun. The X-ray gun is (Mg/Al) twin anode. The system is equipped with a titanium sublimation pump.

Pump down

When the vacuum is "broken" to either repair or replace parts on the system it is vented with nitrogen in order to protect the clean internal walls from excess ambient contamination. From atmospheric pressure UHV is achieved by "roughening" out the system using rotary pumps. The diffusion pumps are used in order to achieve high vacuum (~10^{-5} mbar). However, unavoidable contamination on the inside walls due to loss of vacuum acts as a constant source of pressure and so the system is "baked" at 120 ^{0}C for approximately 12 hours allowing the contamination to desorb from the vessel walls. After degassing cycles and allowing the system to cool to room temperature a pressure of approximately $4x10^{-10}$ mbar is achieved in which an atomically clean surface can be maintained for a reasonable amount of time and a photoelectron signal can traverse macroscopic distances without interacting with other atoms outside the sample being examined.

Analyser

Under the control of a computer the photoelectron flux from the surface is collected through a focusing electrostatic lens where the kinetic energy is interrogated by a hemispherical analyser. The tiny photoelectron current (~nA) is then amplified by a channeltron and undergoes analogue to digital conversion were it is finally presented by the computer as a digital spectrum as shown in figure 2.8 [13]. In XPS the chemical bonding states in the sample are revealed through the chemical shifts of core level peaks.

When chemical states are close in energy, the ability to resolve them is limited by the resolution, which has contributions from the X-ray source (0.7 to 1.0 eV), the natural line width (< 0.1 eV) and the analyser as discussed in chapter 3. The ability of the analyser to discriminate between or resolve two closely lying peaks is known as the resolving power:

$$R = \frac{\Delta E}{E} \qquad \textbf{Equation 2.7}$$

ΔE $\approx$ FWHM (eV)

E kinetic energy of peak (eV)

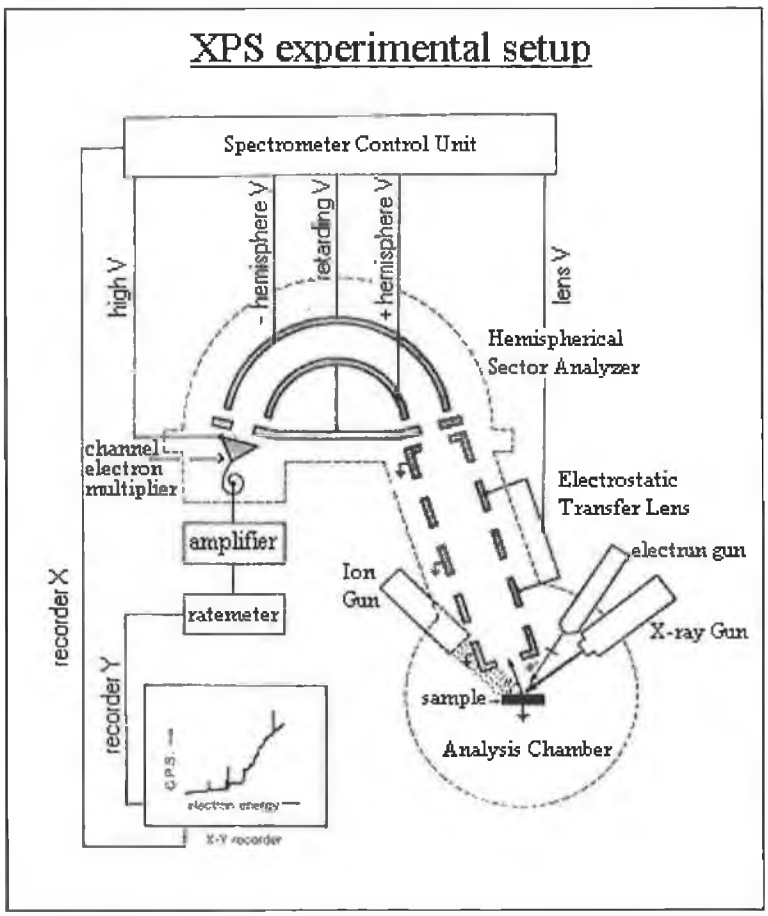

Figure 2.8: Schematic of XPS experimental set-up. The photoelectron signal originates in the analysis chamber under UHV where it is collected and focused by an electrostatic lens onto the entrance slit of the analyser. Through suitable voltages on the hemispherical spheres the analyser can scan a wide energy at constant resolution. The photoelectron signal undergoes amplification before being converted to a digital signal (VG [13]).

For a large energy window as in figure 2.10, the resolving power changes with kinetic energy. In order to analyse all kinetic energies with the same resolution the incident photoelectrons are pre-retarded to a constant pass-energy E_p. Photoelectrons entering on-axis at the input slit of the hemispherical analyser are deflected by an electric field between the two hemispheres in such a way that only those electrons travelling at the pass energy E_p of the analyser follow the path of the mean radius R_0 and arrive at the exit slit for amplification. Figure 2.9 [14] shows a cross-section of the CHA.

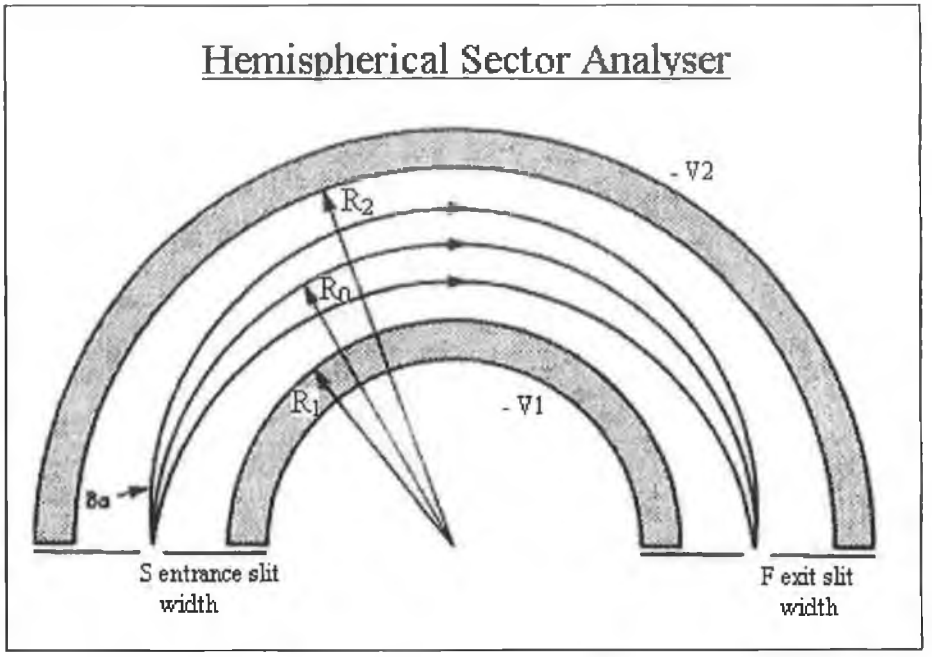

Figure 2.9: Cross-section of a CHA analyser. Photoelectrons entering on-axis at the input slit of the hemispherical analyser are deflected by an electric field between the two hemispheres in such a way that only those electrons travelling at the pass energy E_p of the analyser follow the path of the mean radius R_0 and arrive at the exit slit for amplification [14].

Two hemispheres of radii R_1 (inner) and R_2 (outer) have negative potential of V_1 and V_2 applied to them respectively, where ($V_2 > V_1$). The potential along the mean path V_0 is given by:

$$V_0 = V_1 R_1 + \frac{V_2 R_2}{2R_0} \qquad \textbf{Equation 2.8}$$

Since R_0, R_1, and R_2 are fixed, changing V_1 and V_2 allows the scanning of electron kinetic energies following the mean path through the analyser.

$$\frac{\Delta E}{E_p} = \frac{s}{2R_0} \qquad \textbf{Equation 2.9}$$

s mean slit width

Therefore the resolution can be increased by decreasing the pass energy E_p or slit width or increasing R_0.

Lens

The lens collects photoelectrons from a large angular distribution and focuses them at the entrance slit of the analyser. It also retards the incident photoelectrons to the analyser pass energy E_p.

Channeltron

The channeltron is a small glass trumpet like structure whose inner surface area is large and coated with a film, from which many secondary electrons are emitted per incident electron providing "gain" and thus amplifying the tiny photoelectron current. A channeltron potential difference of around 3 keV accelerates the photoelectrons through the channeltron ensuring many collisions with its surface.

Scan Parameters

Due to different concentrations and photoionisation cross-sections associated with an elemental atomic transition, an XPS scan of a particular chemical state has individual requirements. Typically a survey scan is performed as shown in figure 2.10 using a wide energy window in order to reveal all elements present. Full elemental detection is more important than resolution here, so a large pass energy for greater signal is used along with a larger energy step (1 eV) and short dwell time (i.e. integration time per energy step). To this end the survey scan serves it purpose revealing only oxygen, silicon from the bulk dielectric layer and surface carbon contamination. The scan was performed on a 5.5 nm SiO_2 film.

Despite the larger oxygen concentration relative to silicon (O:Si 2:1), the higher photoionisation cross-section of oxygen results in its substantially larger intensity. Silicon is represented by two transitions, namely the Si_{2s} and Si_{2p}. The smaller photoionisation cross-section of the Si_{2s} state and its relatively smaller bonding interaction makes the Si_{2p} state the preferred transition to investigate for bonding information. High-resolution scans were performed on the Si_{2p}, O_{1s}, and C_{1s} peaks. Here resolution is important in order to elucidate as best as possible chemical shifts on the primary peaks and so a pass energy of 20 eV, an energy step of 0.1 eV, and a dwell time of 0.25 sec are typical scan parameters. Figure 2.11 shows a high-resolution scan of the Si_{2p} peak shown in figure 2.10. The Si^{0+} substrate peak and chemically shifted (4 eV to lower kinetic energy) Si^{4+} oxide peak are clearly resolved. However, the spin orbit splitting (0.6 eV) on the substrate peak is not resolvable given that the experimental resolution achievable with the XPS instrument is approximately 1 eV.

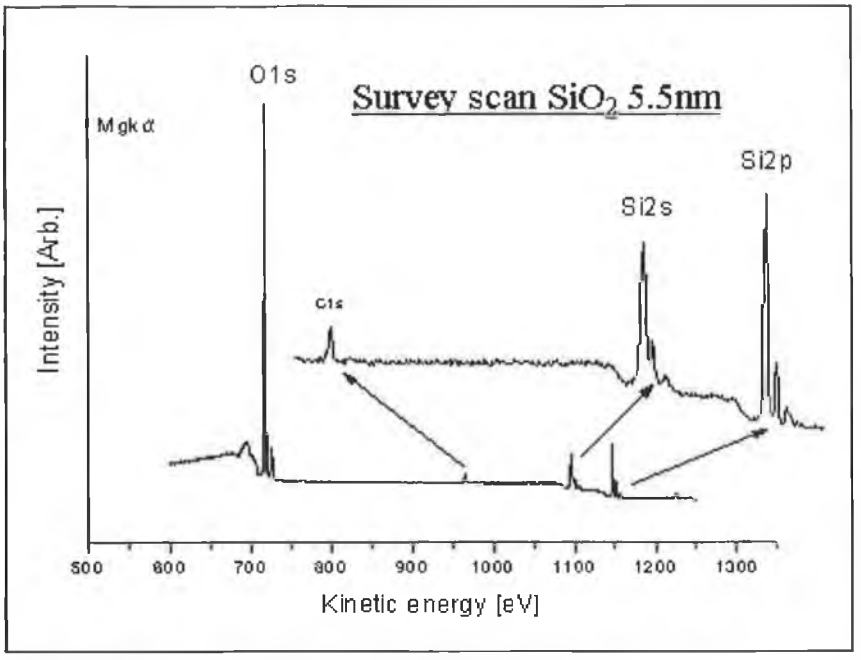

Figure 2.10: A wide energy "survey" scan reveals all elements present allowing a suitable energy window to be decided for subsequent higher resolution scans.

From the previous discussion of the operation of the analyser it is tempting to seek better resolution by decreasing the pass energy E_p of the analyser. However, as is often the case in optics there is a fundamental trade-off between resolution and intensity. When the slit width is very small, at small pass energies, the analysed photoelectron

flux is small and the signal to noise is dramatically affected. Some improvement can be found by dwelling for longer at each kinetic energy sampling step in the scan. Because the spectrum is a digital signal, which has been sampled with a finite resolution, it would be ambiguous to infer spectral structure beyond that resolution. Although it is acceptable to sample the signal with an energy step of say 0.1 eV, it is not acceptable to attempt to resolve with certainty spectral features beyond 1 eV. Despite this restriction spectra are typically de-convoluted beyond the available resolution based on a prior knowledge or expectation of the exact chemical state from say high-resolution synchrotron analysis.

2.3 Data Analysis

Under the control of a P.C. the analyser interrogates the kinetic energy of the incident photoelectron flux. The tiny photoelectron current (~nA) is then amplified by a channeltron and undergoes analogue to digital conversion were it is finally presented by the P.C. as a digital spectrum. Before peak de-convolution can be performed the background on which the spectrum sits needs to be identified and removed.

Background type / removal

Photoelectron peaks are found on a "stepped" background, which has contributions from:

- The Bremsstrahlung of the X-ray source and the tails of neighbouring peaks. This can be removed with a constant baseline fitted to the high kinetic energy side of the spectrum.

- Extrinsic losses from inelastic scattering events during electron transport through the solid. These losses have been study by Tougaard [15] and can removed by a Tougaard background.

- Intrinsic satellite losses inherent to the photoexcitation process in the atom and associated with it's nearest neighbours, and includes valence electron excitations

(shake–up) and excitation of vibrational motion, plasmon excitations, and interband transitions [16].

Background removal is complicated as both intrinsic and extrinsic contributions span similar energies and the peak intensity will depend on the method used to remove the background. For the samples studied in this thesis, intrinsic losses are of concern for the Si^{0+} when the substrate is highly doped and takes on metallic behaviour. The backgrounds obtained during synchrotron studies show a small stepped character and are best fitted with a Shirley [17] or Tougaard algorithm. For conventional XPS, a 4th order polynomial is used to fit the background. The polynomial is defined as:

$$P(X) = X_0 + X_1(X - X_p) + X_2(X - X_p)^2 + X_3(X - X_p)^3 + X_4(X - X_p)^4$$

Equation 2.10

X_p is an offset on the x-axis

X_i is the i^{th} coefficient of the polynomial

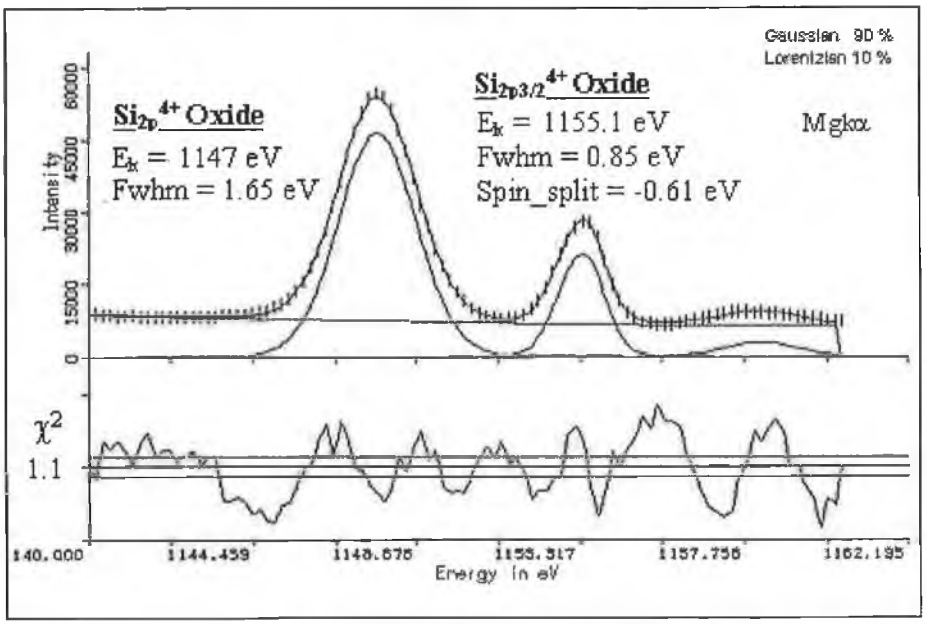

Figure 2.11: (Top panel) de-convolution of a 5.5 nm SiO_2 oxide spectrum into an overlying chemically shifted oxide and underlying substrate peak. (Bottom panel) Chi square value gives indication of the "goodness" of the fit or the extent of the agreement between the experimental data and the fit.

Figure 2.11 shows a fit to the Si_{2p} spectrum of a 5.5 nm oxide. The spectrum background was fitted using a 4th order polynomial. Here the polynomial background easily fits what is essentially a linear background, as checked by numerical differentiation of the fitted background. An initial guess for the background, peak intensity, kinetic energy, and FWHM were made.

Peak parameters

The spectrum was fitted with two Voigt peaks, as defined by equation 2.11, a linear combination of a Gaussian G(x), and a Lorentzian L(x) peak in order to express the influence, respectively, of the instrumental broadening of the energy distribution of the photoexcited orbital and the core-hole lifetime.

$$M(x) = aG(x) + (1-a)L(x) \qquad \textbf{Equation 2.11}$$

Where G(x) (the Gaussian) and L(x) (the Lorentzian) are curves with the same position and width. Because the peak is predominantly Gaussian the mixing parameter 'a' is 0.9, (i.e. 90% Gaussian and 10% Lorentzian).

The Gaussian is defined by:

$$G(x) = h\frac{1}{e^{4\ln 2\left[\frac{x-x_0}{w}\right]^2}} \qquad \textbf{Equation 2.12}$$

- h is the peak intensity
- x_0 is the position of the peak
- w FWHM

The Lorentzian is defined by:

$$L(x) = \frac{h}{1+4\left[\frac{x-x_0}{w}\right]^2} \qquad \textbf{Equation 2.13}$$

h is the peak intensity

x_0 is the position of the peak

w FWHM

Values for spin-orbit splitting of -0.6 eV and an intensity ratio of 0.5 are well established in the literature [7],[22],[49] and confirmed by our own synchrotron studies of clean silicon. They are held constant during fitting. Once started, the fitting program, through an iterative least squares fitting cycle seeks to reduce the chi–square χ^2 value [18] (sum of the squares of the deviations), which indicates the goodness of fit between the experimental and guessed peaks. In general, a smaller χ^2 value represents a better fit; with values less than 1 indicating that the fit and the data are indistinguishable within the experimental error. The bottom part of figure 2.11 shows the residues, the difference between the fitted and experimental data. The inability to detect interfacial suboxides is apparent by the goodness of fit across the energy window. The interfacial signal is small and attenuated by the overlying bulk. When a peak is required and has not been included in the fit the localized disagreement in the residue is a useful warning or indication of its absence.

2.4 Quantification [19]

In a simplistic view the intensity of a given elemental photoelectron peak can be interpreted in terms of the concentration of that element in the sample and the outgoing photoelectron signal suffering a simple Beer Lambert like attenuation with depth as shown in figure 2.12. It is only through careful spectral analysis involving background removal, peak de-convolution and taking instrumental factors into consideration that the percentage of each element detected can be calculated. Figure 2.12 [19] shows a simplified but useful representation of the attenuation of the photoelectron flux by the solid and overlayer when "deeply" (μm) penetrating X-rays are considered as stimulating photoemission throughout the bulk of the sample.

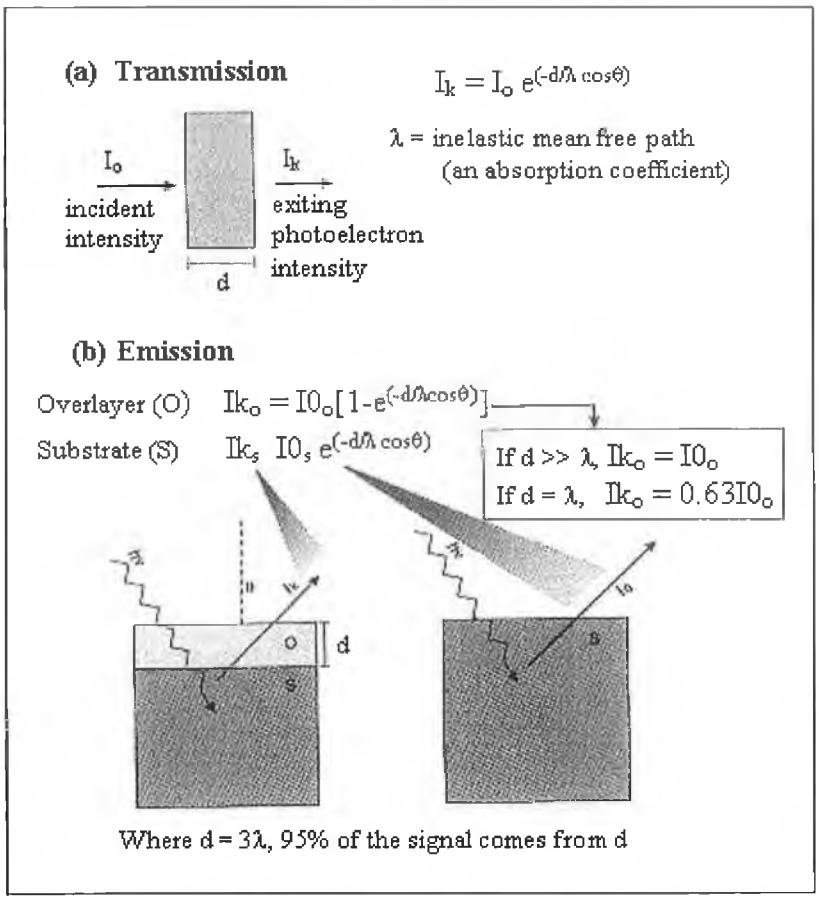

Figure 2.12: (a) for electrons transmitted through a sample, Beer's law of molecular absorption explains the total intensity loss for electrons that lose no energy in traversing the sample. (b) For electron emission from a thick sample, modifications of Beer's law can explain the photoemission intensity from an overlayer, or from the substrate covered by an overlayer. (Vickerman [19]).

With no overlayer the area of peak j from element i, is given by:

$$I_{ij} = KT(E_k)L_{ij}(\gamma)\sigma_{ij}\int n_i(z)\frac{1}{e^{\frac{z}{\lambda(E_k)\cos\theta}}}dz \qquad \textbf{Equation 2.14}$$

K	K is an instrumental constant
$T(E_k)$	is the transmission function of the analyser
$L_{ij}(\gamma)$	is the angular asymmetry factor for orbital j of element i
σ_{ij}	is the photoionisation cross-section of orbital j from element i
$n_i(z)$	is the concentration of element i at a distance z below the surface
$\lambda(E_k)$	is the inelastic mean free path
θ	is the take-off angle of the photoelectrons measure with respect to the surface normal

The instrumental constant K expresses the X-ray flux, area of sample irradiated, and solid angle of photoelectrons accepted by the analyser. The angular asymmetry accounts for the type of orbital the photoelectron is emitted from and the angle γ between the incident X-rays and emitted photoelectrons. The transmission function of the analyser includes the efficiency of the collection lens, the electron analyser and detector. The analyser was operated in fixed analyser transmission mode, by pre-retarding the incoming electrons to a constant pass energy in order to maintain constant energy resolution across the scan. The photoelectron ionisation cross-section σ_{ij} is the probability that the incident X-ray will create a photoelectron from the j^{th} orbital of element i. The values calculated by Scofield [20] were used and also values were calculated using quantification (Polymer) samples as discussed later.

2.4.1 SiO_2 Overlayer Model

A thin ($d<3\lambda$) SiO_2 film on an infinite Si substrate attenuates the photoelectron flux passing through it (see figure 2.12 (b)). Using equation 2.14 the intensities from the overlayer and substrate intensities are given by:

$$I_{SiO_2} = KT(E_k)L_{SiO_2}(\gamma)\sigma_{SiO_2}\int_0^d n_{SiO_2}\frac{1}{e^{\frac{d}{\lambda_{SiO_2}Cos\theta}}}dz \qquad \textbf{Equation 2.15}$$

$$I_{Si} = KT(E_k)L_{Si}(\gamma)\sigma_{Si}\lambda_{Si}\left(1-\frac{1}{e^{\frac{d}{\lambda_{Si}Cos\theta}}}\right) \qquad \textbf{Equation 2.16}$$

Emission from the substrate is attenuated by the overlayer and is thus multiplied by $\frac{1}{e^{\frac{d}{\lambda_{SiO_2}Cos\theta}}}$ to give:

$$I_{Si} = KT(E_k)L_{ij}(\gamma)\sigma_{ij}\lambda_{SiO_2}\left(\frac{1}{e^{\frac{d}{\lambda_{si}Cos\theta}}}\right) \qquad \textbf{Equation 2.17}$$

By consider the ratio of the intensities of the oxide to substrate peak the K and analyser transmission terms are common and cancel. The orbital angular asymmetry terms are neglected, as their correction is small. A number of assumptions which are reasonable for amorphous SiO_2 in the ultra-thin regime (<5 nm) are employed;

- Elastic scattering in the sample is neglected
- Electron diffraction effects are negligible
- The IMFP is independent of depth (the film is stoichiometric SiO_2)
- Reflection and refraction of X-rays is negligible
- The IMFP of SiO_2 and Si are approximately equal
- Angular asymmetry is neglected
- Surface roughness is negligible

This allows us to write:

$$\frac{I_{SiO_2}}{I_{Si}} = \frac{I_\infty}{I_0}\left[e^{\frac{d}{\lambda_{SiO_2}}} - 1\right] \quad \textbf{Equation 2.18}$$

where $I_\infty = n_{SiO_2}\sigma_{SiO_2}\lambda_{SiO_2}$ & $I_0 = n_{Si}\sigma_{Si}\lambda_{Si}$ are the intensities for an infinitely thick SiO_2 layer and bare Si substrate, respectively. Values for I_∞ / I_0 and λ_{sio2} are taken from Himpsel et al [7]. Rearranging equation 2.18 allows the thickness of the overlaying oxide to be calculated:

$$d = \mathrm{Ln}\left[\frac{I_{SiO_2}}{I_{Si}}\frac{I_0}{I_\infty} + 1\right]\lambda_{SiO_2} \quad \textbf{Equation 2.19}$$

2.4.2 Oxide Stoichiometry

The relative concentration of atom 'i' in an infinitely thick homogeneous sample can be calculated from the total intensity from:

$$N_i = \frac{I_i}{F_i} \qquad \textbf{Equation 2.20}$$

$$F_i = \sigma_i L(\varphi_i, \beta_i) \lambda_i T_i \qquad \textbf{Equation 2.21}$$

σ_i : atomic sensitivity factor based on Scofield's [20] photoionization cross sections.

$L(\varphi_i, \beta_i) = \frac{1}{4\pi}\left[1 - \frac{\beta}{2}\left(\frac{3}{2}\text{Cos}^2\left(\varphi - \frac{1}{2}\right)\right)\right]$: orbital angular asymmetry correction where β_i is the asymmetry term and φ is the angle between the excitation source and the analyser. The actual values for the IMFP of photoelectrons in matter are a function of the energy of the electrons and the nature of the sample through which they travel. For typical XPS energies the IMFP increases with electron kinetic energy. The E_k dependency of the inelastic mean free path can be accounted for through an exponential dependence $\lambda_i \propto E^a$ ($0.5<a<0.9$), 0.7 is typically used [21]. Equations that relate the IMFP to the electron energy and type of material (elements, organic materials or polymers) through which the electron travels have been developed by Seah and Dench [12].

T_i: as mentioned above is the transmission function of the analyser which includes the efficiency of the collection lens, the electron analyser, and detector. In this thesis work the analyser was operated in FAT mode, by pre-retarding the incoming electrons to a constant pass energy in order to maintain constant energy resolution across the scan. Thus the only variation in the transmission function with E_k of the photoelectrons was due to the retardation of the lens system.

Only the atomic sensitivity factor σ_i in equation 2.21 is considered in quantitative analysis. The orbital asymmetry term is small and the sample composition and analyser transmission function are common to each scan. The applied quantification of equation 2.20 gives relative concentrations thus the results should be normalised. It is usual to consider either the atomic percentage of element 'i' as in:

$$R_i = \frac{N_i}{\left(\sum_{i=0}^{i=n} N_i\right)} 100 \qquad \textbf{Equation 2.22}$$

N_i is the relative concentration of element 'i' from equation 2.20

R_i is the normalised relative concentration

Thus the atomic percentage of Si in the dielectric layer can be calculated using the Si_{2p}^{4+} oxide and O_{1s} peak intensities:

$$(\%Si) = \frac{\frac{I_{SiO_2}}{\sigma_{SiO_2}}}{\sum\left(\frac{I_{SiO_2}}{\sigma_{SiO_2}} + \frac{I_{O_{1s}}}{\sigma_{O_{1s}}}\right)} \qquad \textbf{Equation 2.23}$$

similarly for oxygen:

$$(\%O) = \frac{\frac{I_{O_{1s}}}{\sigma_{O_{1s}}}}{\sum\left(\frac{I_{SiO_2}}{\sigma_{SiO_2}} + \frac{I_{O_{1s}}}{\sigma_{O_{1s}}}\right)} \qquad \textbf{Equation 2.24}$$

I_{SiO_2} Si_{2p} Oxide photoelectron peak intensity

$I_{O_{1s}}$ O_{1s} Oxygen photoelectron peak intensity

σ atomic sensitivity factor based on Scofield's [20] photoionization cross sections

2.4.3 Quantification standard

In order to verify our values for O and Si sensitivity factors a standard polymer material was analysed. A thin film of polydimethysiloxane (PDMS) was allowed to flow over a thin silver foil. This polymer has a known elemental composition (except hydrogen) of 25% Si, 25% O and 50% C. Because of it's low surface energy the polymer can be prepared ex-situ with negligible adsorption of hydrocarbons, water and CO_2 that generally eliminate organic materials as standards [22].

Figure 2.13 shows a wide survey scan of the principal peaks; O_{1s}, C_{1s} and Si_{2p} of a thin PDMS film.

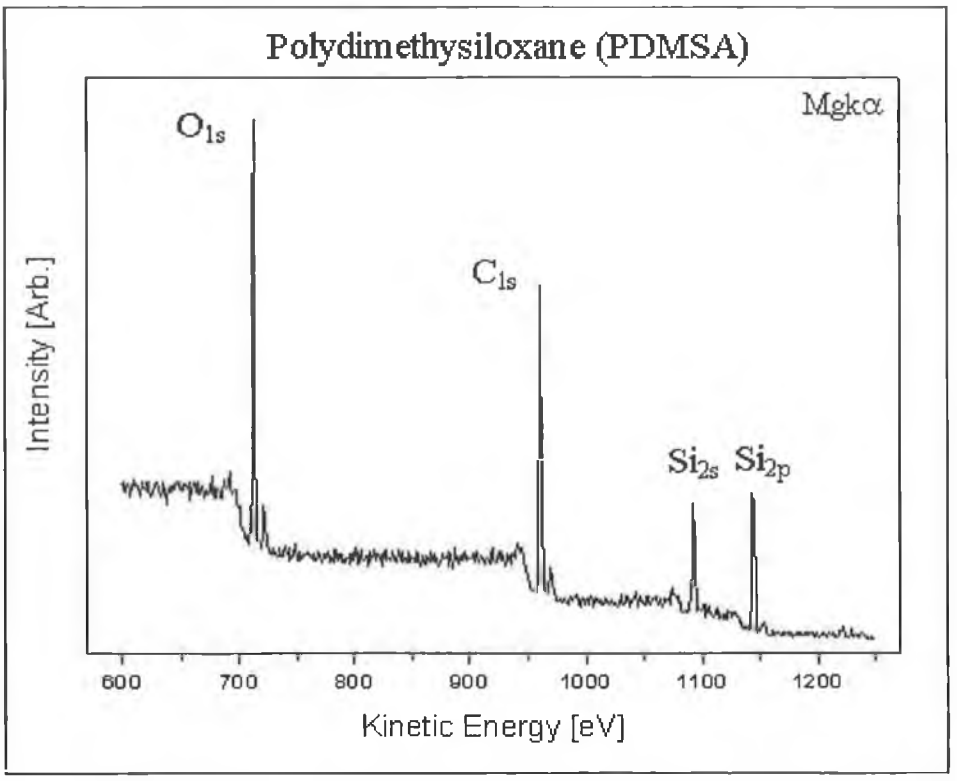

Figure 2.13: A wide survey scan of a thin PDMS film showing the principal peaks. The film has a known elemental composition of oxygen, carbon and silicon in percentages of 25%, 50% and 25% respectively.

In this scan all peaks are on the same absolute intensity scale and despite having twice the concentration of oxygen and being distributed uniformly through the film, it is apparent that the intensity of the carbon peak is not twice that of the oxygen peak, this is due to it's different photoionisation cross-section or sensitivity factor. From the known elemental composition of the PDMS film and using the intensities of the O_{1s}, C_s and Si_{2p} photoelectron peaks along with equation 2.22; values of sensitivity factors for O and Si can be calculated. Relative sensitivity factors for O and Si are obtained as there are three equations with three unknowns and so for a solution the sensitivity factor for carbon is set equal to 1.

Setting $\sigma_{C1s}=1.0$ and solving for σ_{Si2p} and σ_{O1s} gives:

$$(\%C) = \frac{\frac{I_{C_{1s}}}{\sigma_{C_{1s}}}}{\sum\left(\frac{I_{Si_{2p}}}{\sigma_{Si_{2p}}} + \frac{I_{O_{1s}}}{\sigma_{O_{1s}}} + \frac{I_{C_{1s}}}{\sigma_{C_{1s}}}\right)}$$

$$(\%Si) = \frac{\frac{I_{Si_{2p}}}{\sigma_{Si_{2p}}}}{\sum\left(\frac{I_{Si_{2p}}}{\sigma_{Si_{2p}}} + \frac{I_{O_{1s}}}{\sigma_{O_{1s}}} + \frac{I_{C_{1s}}}{\sigma_{C_{1s}}}\right)}$$

$$(\%O) = \frac{\frac{I_{O_{1s}}}{\sigma_{O_{1s}}}}{\sum\left(\frac{I_{Si_{2p}}}{\sigma_{Si_{2p}}} + \frac{I_{O_{1s}}}{\sigma_{O_{1s}}} + \frac{I_{C_{1s}}}{\sigma_{C_{1s}}}\right)}$$

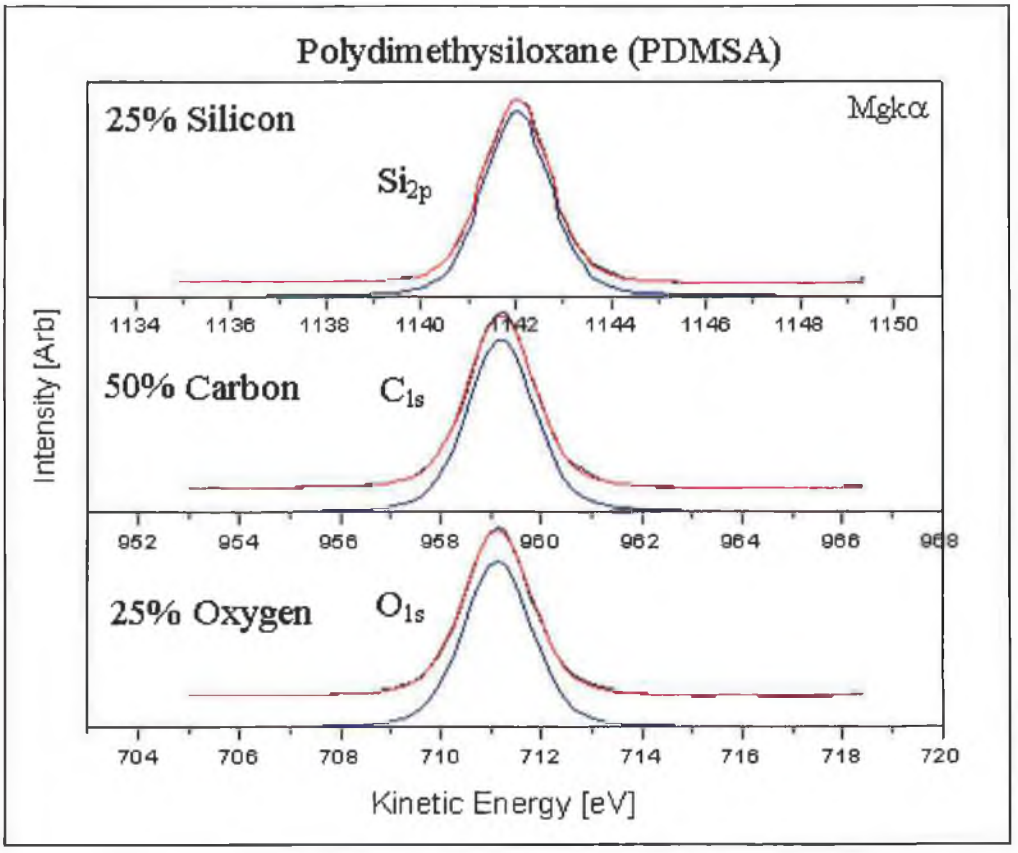

Figure 2.14: Silicon, carbon and oxygen photoelectron signals from a quantification standard (PMDS) for oxidised species.

Figure 2.14 shows high resolution scans of the oxygen carbon and silicon photoelectron peaks from the film.

2.4.4 Hydrocarbon Contamination

In the wide survey scan of an as-received SiO_2 film in figure 2.10 a small carbon peak is evident and is associated with hydrocarbon contamination. Hydrocarbon contamination is unavoidable when analysing a sample, which has been exposed to the laboratory atmosphere. The SiO_2 dielectric layer is water insoluble, chemically inert and so adsorption of hydrocarbons, water, CO_2 etc., exists in thickness in the order of a couple of monolayers. This hydrocarbon layer undermines quantitative analysis as it attenuates the photoelectron from the sample underneath it [23] (as discussed in chapter 3). The contamination layer is particular problematic in angular resolved experiments at high take-off angles where an outgoing photoelectron travels through an effectively thicker contamination layer because of the grazing emission angle. Hofmann et al [24] proposed a graphical method to remove the contamination effects from the value of stoichiometry. It assumes that the contamination layer thickness is one monolayer. Also in the model the contamination thickness can vary to less than an atomic diameter and the contamination layer is small relative to the escape depth for carbon in a carbon matrix. Hofmann checked his model with samples, which had undergone in-situ ozone cleaning, O_2 discharge cleaning and different degrees of ambient hydrocarbon contamination. The algorithm is computationally difficult to implement. Contamination could also be accounted for by including in equation 2.21 a surface contamination correction term $e^{-c/\lambda}$ as proposed by Evans et al [25] to give equation 2.25 below:

$$F_i = \sigma_i L(\varphi_i, \beta_i) \lambda_i \frac{1}{e^{\frac{c}{\lambda}}} \quad \textbf{Equation 2.25}$$

In this thesis work carbon contamination is a cause for concern primarily for the as-received samples where it is consistently small, given the precision which the environment in which the oxides were grown and stored. Assuming that surface contamination does not evolve with time or sampling processing; inter sample comparisons where peak intensity ratios (i.e. O_{1s}/Si_{2p}^{4+}) are considered will result in such effect being cancelled. This approach is motivated by the belief that an objective and non-ambiguous characterisation procedure for the oxide layer using XPS should

consider the evolution of as-received parameters (thickness, stoichiometry, chemical shift) in an inter as-received comparison as opposed to the calculation of absolute values of thickness, stoichiometry or chemical shift.

2.4.5 Oxide Charging

Charging effects arise from the inability of an insulator to respond to the depletion of photoelectrons due to X-ray illumination. In the SiO_2/Si system a core hole created in the silicon substrate can be quickly filled due to the moderate doping and good electrical contact with the spectrometer. In the oxide a core hole exists for a longer time due to the deficiency of mobile charge. The positive charging of the oxide layer causes the entire photoelectron spectrum to "charge" or shift to higher binding (lower kinetic) energy. Illuminating the sample with a flux of low energy electrons (< 5 eV) replaces the depleted photoelectrons. Because all peaks are shifted to the same extent, charge correction can be performed by referencing to the known substrate or surface contamination binding energy. The substrate is doped and is in electrical contact with the spectrometer, which is grounded and so cannot be depleted. For thick dielectric layers where the substrate peak signal cannot be "seen" through the oxide overlayer charge referencing was performed using the binding energy of adventitious hydrocarbon adsorption at 285.6 eV.

Charge referencing using the silicon substrate peak (Si^{0+}) [26,27] or Fermi edge is undermined by their variation with dopant type and concentration. The use of C-C peaks [28] is hindered by differential charging. In a round robin experiment by Hashimoto et al [29], charge correction in oxides using the hydrocarbon C_{1s} binding energy resulted in errors as large of 11 eV. The C_{1s} line for adventitious contamination is between 283.8 and 285.6 eV. The study concluded the best results would be obtained by referencing using the energy difference between the O_{1s} and Si_{2p}^{4+} oxide peak (i.e.: E_{BO1s}-E_{BSiO2}≡429.3 eV) having chosen a value of for the oxide binding energy ($E_{B\ SiO2}$≡103.0 eV). In this approach a chemical shift would result in a change in the oxygen to oxide energy difference but a charging shift would result in a constant separation. Because of the consistency and precision with which the dielectric layers studied in this thesis were

prepared (i.e. doping), charge correction was performed by referencing to the Si_{2p}^{0+} substrate peak binding energy at 99.3 eV and for infinitely thick oxides using the C_{1s} binding energy at 285.6 eV. As with stoichiometry it is potentially more useful to be concerned about the consistency in peak positions as opposed to elucidating absolute binding energies.

Image charge

In very thin (d<2 nm) dielectric layers a thickness dependent chemical shift is evident where electrons ejected from the Si atoms in the SiO_2 layer have a reduced binding energy due to the coulomb interaction with the core hole (positive ion) because they also feel the screening (repulsion) of its image charge in the substrate.

2.5 SiO_2 Chemical Depth profiling

XPS is effectively a chemical "flash torch" where high energy photons penetrate micrometers into the sample, however due to the strong interaction of electrons with matter, chemical state information is only "illuminated" within the sampling depth (3λ), giving rise to XPSs surface sensitivity. XPSs wide energy window (1486 eV) and large sampling depth ($3\lambda_{SiO2}\approx10$ nm) allows the quality of the overlying oxide in a SiO_2/Si layer to be ascertained from the consistency of the oxide elemental composition, bonding and thickness. Limited resolution, surface sensitivity and a desire to illuminate the Si/SiO_2 interface have motivated researchers to depth profile the film for better interfacial sensitivity. Profiling through the oxide layer has been performed using Ar^+ ion bombardment. It offers a reasonable removal rate across large areas, but is believed to preferentially remove oxygen in SiO_2 leaving a reduced and damaged outer surface, it also introduces lattice damage by re-ordering the inter-tetrahedral Si-O-Si bond angle resulting in an increase in Si_{2p}^{4+} oxide peak FWHM. The introduction of surface suboxides by ion bombardment, which cannot be distinguished from interfacial suboxides, would seriously undermine any attempt to probe the interface. Increased surface sensitivity has been achieved in angular resolved studies, where the chemical depth profile is reconstructed from the individual spectra considered at different take-off angles. The reconstruction is performed through an iterative optimisation algorithm

where the experimental results are compared with an expected chemical depth profile. The development and implementation of such a computer reconstruction algorithm is computationally difficult and suffers from mathematical problems (i.e. the problem is ill posed). Profiling of the oxide has also been performed ex-situ wet chemically. Here the oxide is immersed in a dilute (0.1% to 0.5%) concentration of HF acid. The acid preferentially etches the oxide and the etch terminates at the arrival of the silicon substrate where for full oxide removal it plays a role as surface passivator leaving the silicon surface hydrogen terminated. The etch process is uniform across the sample area and in time and can be tailored through the acid concentration. A brief treatment of each profiling technique is present below.

2.5.1 Inert ion bombardment

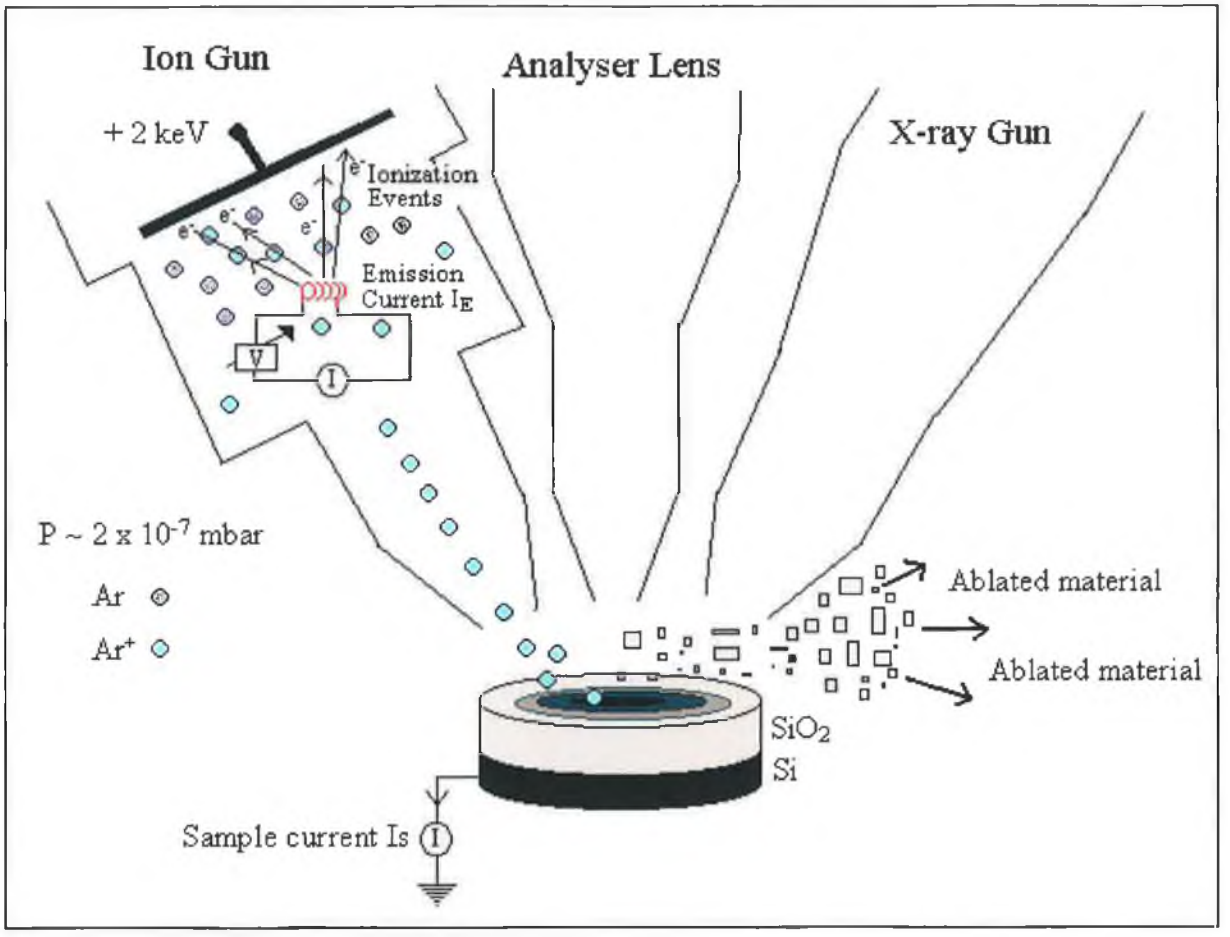

Figure 2.15: Emission current from a hot filament ionises Ar atoms. The ions are accelerated towards the sample through a potential difference of a few keV where they ablate the sample surface.

Figure 2.15 shows a typical XPS experimental set-up where due to the need to collect as much signal as possible the sample is usually in close proximity to the X-ray source, analyser lens and ion gun. In order to bombard the sample the chamber is back filled with argon to a pressure of approximately 2-5 x 10^{-7} mbar. The argon line is differentially pumped to maintain a constant flux of argon. A hot filament in the gun acts as a source of energetic thermionic electrons which discharges through a positive plate to give an emission current. This emission current can ionise the Ar atoms, which make up the background pressure. Once ionised, the Ar^+ ion can be accelerated towards the sample under the influence of the potential difference between the positive plate and the sample, which is grounded. The ions crash into the sample where their momentum and thermal energy is used to remove or ablate the outer surface of the sample. The rate of sample removal can be regulated through the accelerating potential difference, the background pressure of argon and the focusing of the ion beam. In profiling the oxide the gun was operated with the beam defocused in order to achieve uniform ablation. Ion bombardment is realised through a plasma discharge of ions which is inherently unstable and typically the removal rate is not uniform in time or spatially with a crater being formed in the centre of the sample which can lead to "shadowing" effects in off-angle analysis where the oxide signal is enhanced at the detriment of the substrate signal due to the crater realised during bombardment.

Figure 2.16 is a simplified illustration of the process. The ability to profile the sample in-situ thus avoiding re-exposure to the laboratory ambient using Ar ion bombardment is advantageous. Reproducibility and consistency in rate of oxide removal coupled with shadowing effects and ultimately the reduction of the outer surface region during bombardment (surface reduction is discussed at length in chapter 3, section 3.3) makes the technique unsuitable. When complete oxide removal was necessary and surface damage could be repaired through annealing as with germanium samples (chapter 6), where Ar ion bombardment proved very useful.

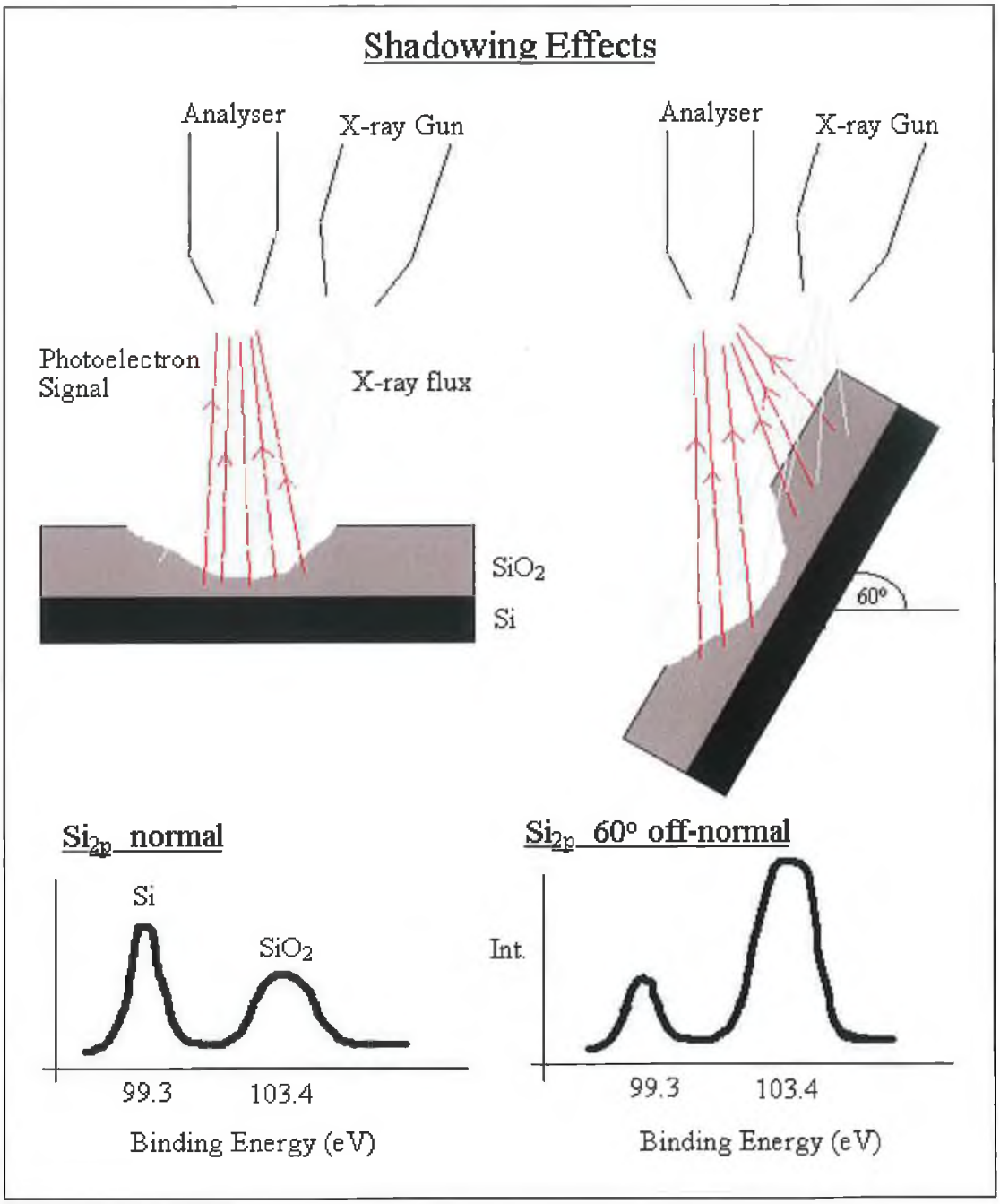

Figure 2.16: Due to instabilities in the bombardment process the removal of material can be non-uniform in time and across the sample as evidenced by the formation of a crater in the surface. This crater can lead to shadowing effects in off-angle analysis where the surface oxide is illuminated in a region out side of the target area undermining the true thickness value.

2.5.2 Wet chemical profiling

The thickness of a dielectric layer can be depth profiled wet chemically using dilute concentrations of hydrofluoric acid which were made by adding appropriate amounts of ultra-pure deionised water to concentrated (49%) HF acid. The as-received oxides were immersed in dilute HF acid in teflon beakers for given lengths of time after which the etch was terminated by the addition of a large amount of ultra pure deionised water. The oxides were then blown dry using nitrogen and immediately transferred into the vacuum system through a FEL. Introduction into UHV was achieved within 10 minutes. Unlike argon ion bombardment, HF etching was found to uniformly remove the oxide across the sample area thus avoiding shadowing effects and also was found to be both accurate and reproducible in realising different thickness. Etching was performed ex-situ and despite a fresh sample being used for each etch, surface carbon contamination was detected.

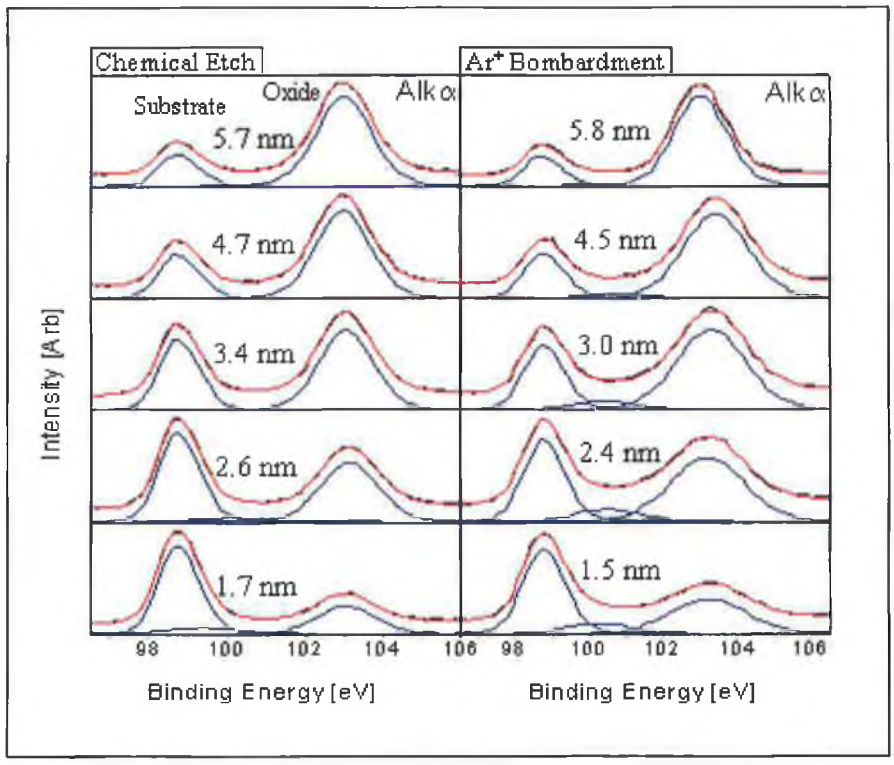

Figure 2.17: The damaging effect of Ar^+ bombardment is apparent by comparing the Si_{2p} spectra for various thicknesses realised by both bombardment and wet chemical HF etching. For the bombarded samples (right) a larger peak FWHM is evident and an increase of suboxide signal relative to the corresponding wet chemical thickness.

When profiling using ion bombardment such contamination was removed by the bombarding process. Figure 2.17 compares the Si_{2p} spectra of a 5.5 nm SiO_2 oxide etched to similar thickness using both Ar ion bombardment and dilute wet chemical etching. The damage induced in the oxide due to the collision cascade initiated by the incident ions is evidenced as a FWHM increase in the oxide peak. The reduction of the outer oxide region is evidenced by the earlier (relative to the wet chemical thickness) need to fit an intermediary oxidation peak in the fit. On the basis of initial measurements, Ar ion bombardment was found to be unsuitable as a means to depth profile the dielectric layers. Wet chemical etching using dilute HF acid was found to be suitable. In chapter 3 both techniques are discussed in more detail in terms of the implication of their processing effects on oxide characterisation using photoemission.

2.5.3 Angular Resolved XPS

By decreasing the acceptance angle θ of the analyser, figure 2.18, relative to the sample surface, the signal arising from deeper layers is attenuated more because the effective path of a grazing photoelectron at depth d is increased to d/Sin(θ), producing an enrichment of surface information in the spectrum.

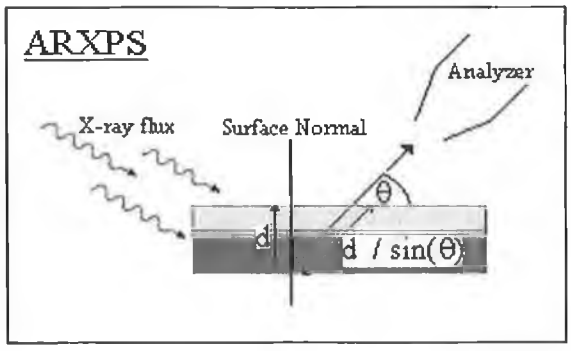

Figure 2.18: On increasing the take-off angle of the photoelectron analysed by the analyser either by rotating the analyser or sample, the photoelectron signal from the outer most surface can be probed.

For a layered structure like the SiO_2/Si system the overlying oxide signal can be enhanced at the detriment of the underlying substrate signal. Figure 2.19 illustrates the effect of such a rotation of the sample on the Si_{2p} spectrum.

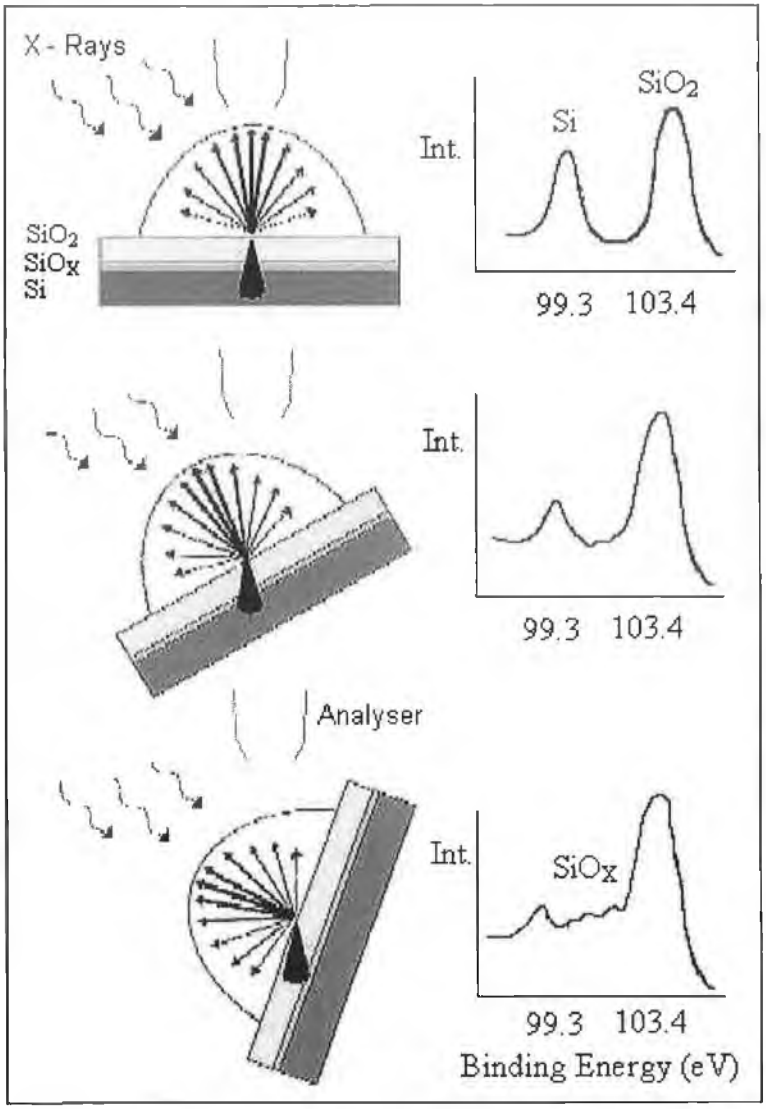

Figure 2.19: For increased take-off angle the photoelectron signal from the outer surface region is more exclusively imaged or collected through the acceptance angle of the analyser lens. For some value of take-off angle the interfacial (SiO_x) signal would be maximised.

The oxide signal grows at the cost of the substrate signal with increasing take-off angle. Due to the fixed geometry of the analyser the sample was rotated relative to the analyser, which is equivalent except for possible changes in illumination area by the incident X-ray flux. The objective of the angular resolved approach was to identify and maximise the interfacial suboxide signal at a given angle. Many ARXPS studies [30-34] have been undertaken on thin SiO_2 films to de-convolute the chemical depth profile (CDP) from the experimental data in order to calculate film thickness and identify inhomogenities in the chemical composition. A number of models have been used (maximum entropy [35], regularisation method [36], absolute[29]/relative ratio method [37]). The Laplace transform model [31] best conveys the inherent

mathematical difficulties associated with de-convoluting a CDP. Recalling the equation for peak intensity (equation 2.14) and considering for a dielectric layer the peak intensity ratios (Si_{2p}/O_{1s}) rather than considering absolute peak intensities, then the terms K, $T(E_k)$, $L_{ij}(\gamma)$, and σ_{ij} cancel.

$$I(\theta,z)_{ij} = KT(E_k)L_{ij}(\gamma)\sigma_{ij}\int n_j(z)\frac{1}{e^{\frac{z}{\lambda(E_k)Cos\theta}}}dz \quad \textbf{Equation 2.14}$$

This removes the complication arising out of angle dependent area of illumination and analyser response. Using the change of variables $p(\theta)=(\lambda\cos\theta)^{-1}$ gives, equation 2.26, where L denotes the Laplace transform.

$$I(p) = \int n(z)\frac{1}{e^{pz}}dz = L[n(z,p)] \quad \textbf{Equation 2.26}$$

Equation 2.26 is concerned with the intensities observed for a known CDP. Ours is the inverse problem of finding the CDP from measured peak intensities as given by:

$$c(z) = L^{-1}[I(p),z] \qquad \textbf{Equation 2.27}$$

The inversion of the Laplace transform is not straightforward. An analytical expression for I(p) is not available, instead there is a set of numerical measurements. The inversion problem is "ill posed" in that there isn't a single suitable CDP, but a set of equivalent profiles which satisfy the transformation. The inverse transform is very sensitive to noise in the input data and so there is a trade-off between uncertainty in composition with depth resolution. Cumpson et al [38] have reviewed ARXPS to date and highlighted the importance of the precision (which must be a few percent) of intensity measurements at the chosen emission angles rather than accuracy, if a successful de-convoluton is to be performed. ARXPS analysis was deemed to be prohibitively expensive in terms of complexity, time, cost of implementation of a working computer model.

Despite this, scans were performed at normal and 60° off-angle in order to obtain bulk and surface sensitivity information respectively.

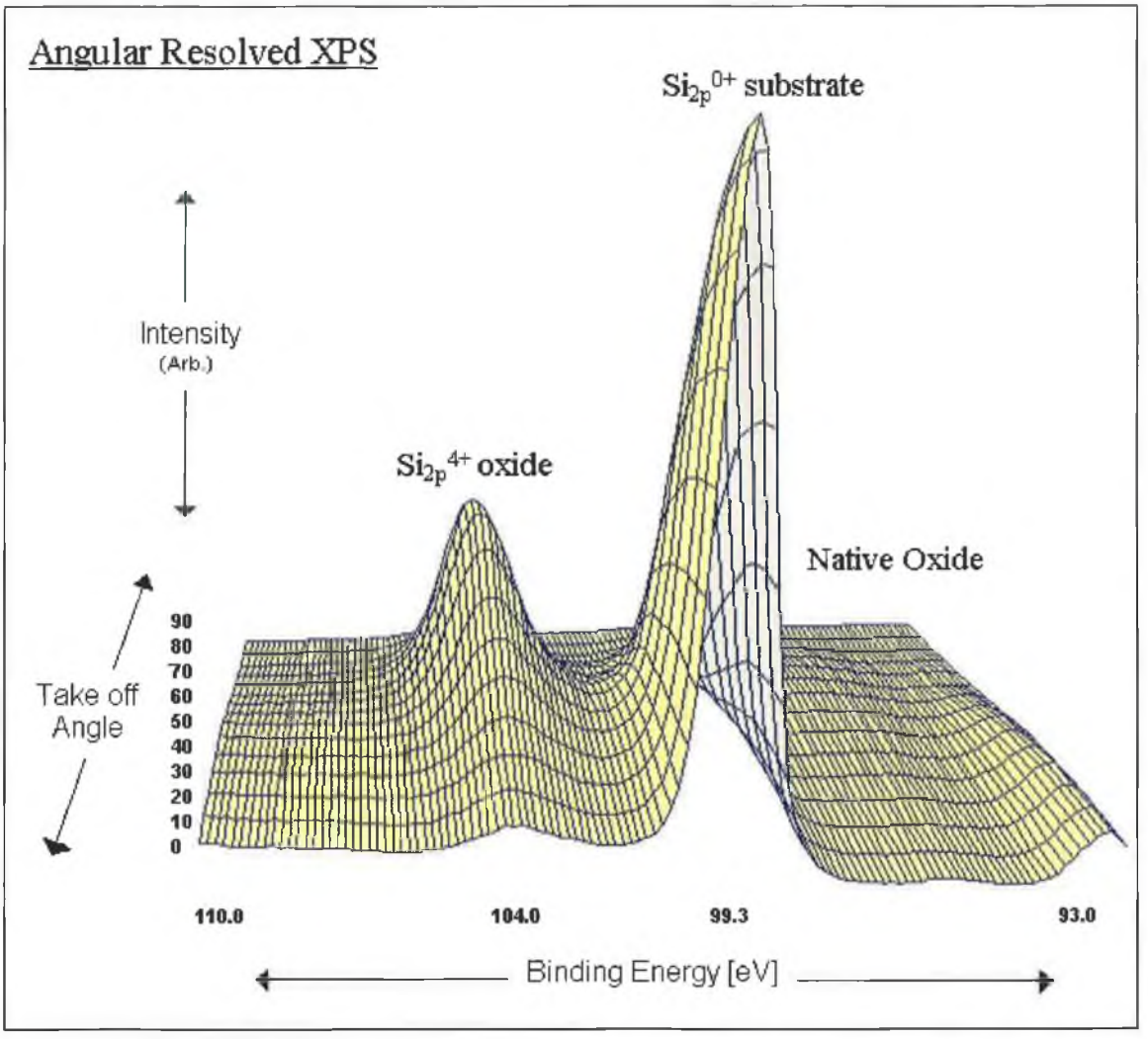

Figure 2.20: At high take-off angles the Si_{2p}^{4+} oxide signal of the native oxide is enhanced relative to the underlying Si_{2p}^{0+} substrate peak.

2.6 Atomic Force Microscopy (AFM)

Dilute HF acid etching was the preferred method of realising depth profiles in the oxide layers due to its uniform removal of the oxide across the sample and its non-invasiveness. AFM measurements were undertaken on the as-received and etched oxides in order to monitor the surface roughness through the surface root mean square (RMS) roughness value.

The instrument used was a multimode Digital Instruments nanoscope III which can operate in both contact and non-contact modes. In AFM a sharp tip is brought into contact or into close contact with a surface. As the tip approaches the sample it experiences an interaction with the surface, the extent of which in terms of magnitude and whether the interaction is attractive or repulsive is governed by the shape of the van der Waals force curve as shown in Figure 2.21 [39].

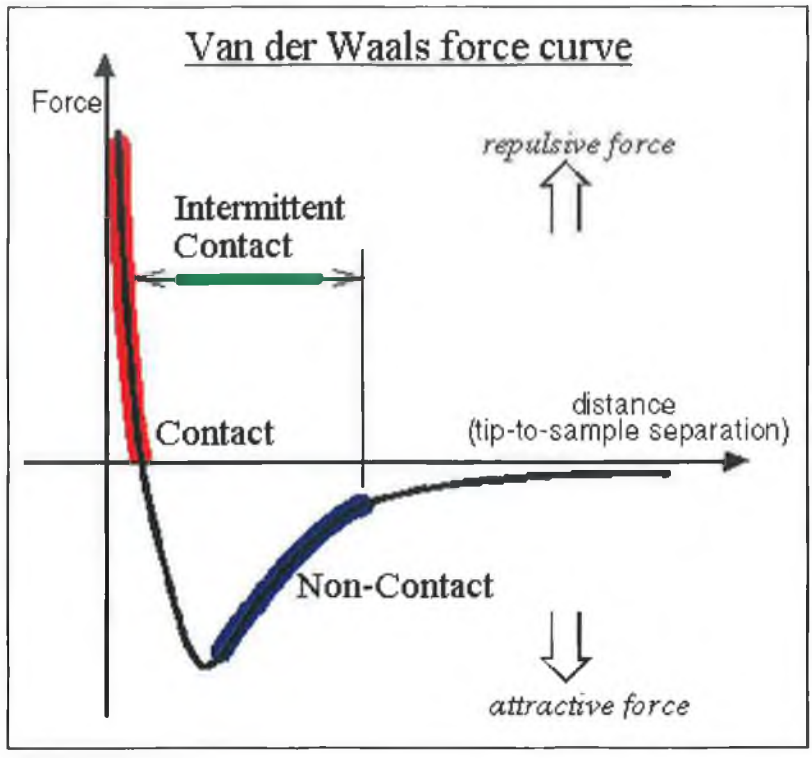

Figure 2.21: The sign and magnitude of the van der Waals force between tip an sample is dependent on the tip sample separation (Thermo micro [39]).

In contact mode the deformation of the cantilever to which the tip is attached is monitored via DC signal representing the voltage required to maintain a constant value of tip sample force. For vibrating modes of operation (i.e. non-contact and tapping) the resonant frequency of the oscillating cantilever varies as the square root of its spring constant. The spring constant of the cantilever varies with the force gradient experienced by the cantilever. The force gradient, which is the derivative of the curve shown in Figure 2.21 changes with tip-to-sample separation. In this way changes in the resonant frequency of the cantilever can be used as a measure of changes in the force gradient, which reflects changes in tip-to-sample spacing, or sample topography [39].

2.6.1 Contact Mode AFM

Figure 2.22 [40] illustrates the contact mode AFM process. A sharp tip with a radius of curvature of approximately 30 nm is attached to a relatively soft cantilever. The bending of the cantilever is actuated in a precise way by application of a suitable voltage to the piezo to which either the sample or cantilever is attached. In contact mode the tip sample distance is such that the tip sample interaction is predominately repulsive with a mean value of 10^{-9} N [42].

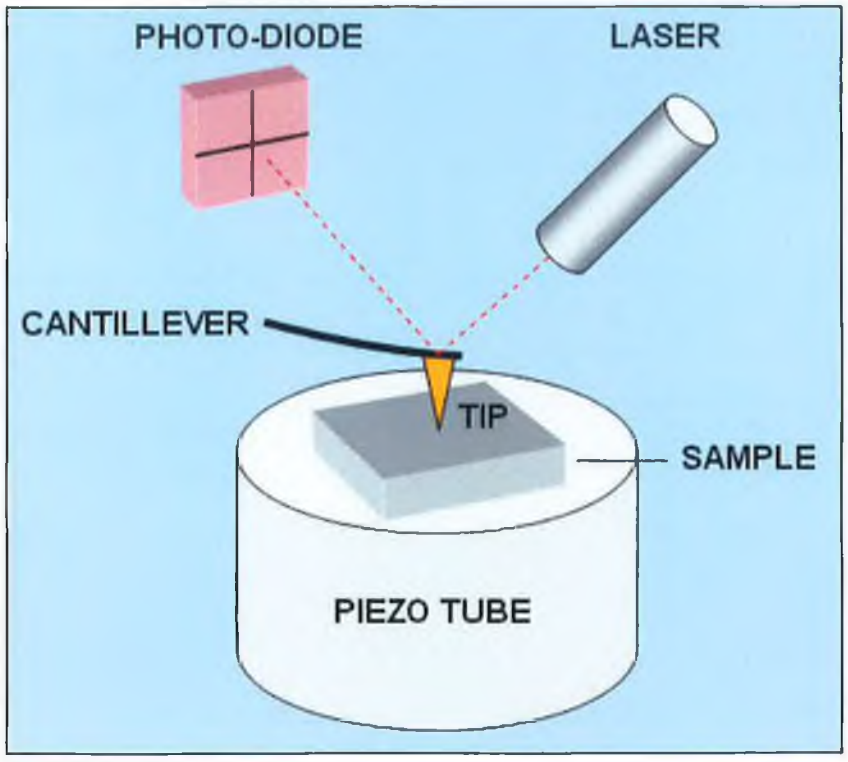

Figure 2.22: In contact mode AFM a sharp tip in contact with a surface is rastered across the sample. The initial contact is established by application of a suitable voltage to the piezo tube. The resultant bending of the cantilever is interpreted precisely by the photo diode through the extent of the deflection of the laser light reflected from the cantilever (Mauritz [40]).

This force is achieved by pushing the cantilever against the sample surface by application of a suitable voltage to the piezo tube. The deflection of the cantilever is sensed by the deflection of the reflected laser light on the quadrant diode detector and compared in a DC feedback amplifier to some desired value of deflection. If the measured deflection is different from the desired values the feedback amplifier applies a suitable voltage to the piezo to raise or lower the sample relative to the cantilever to

restore the desired value of deflection. The voltage that the feedback amplifier applies to the piezo is a measure of the height of the features on the sample surface. It is displayed as a function of lateral position on the sample as the sample is rastered relative to the tip.

Problems arise with contact mode because of excessive tracking forces applied by the probe to the sample. A contamination layer of water vapor and nitrogen exist in the outer most layer of the sample. When the probe touches this contamination layer, a meniscus forms and the cantilever is pulled by surface tension toward the sample surface. Also many samples, including semiconductors and insulators, can trap electrostatic charge and this charge can contribute to additional substantial attractive forces between the probe and sample. The problem is illustrated in Figure 2.23 [42].

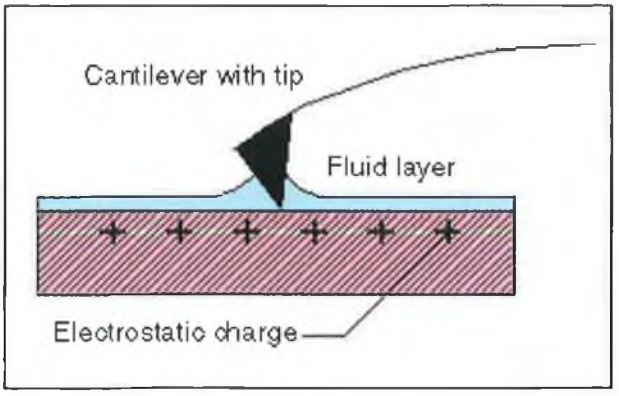

Figure 2.23: The formation of a meniscus between the tip and surface contamination coupled with sample charging in insulator and semiconductor samples combine to exert an attractive force on the tip toward the sample surface (Digital Instruments [42]).

The effects can be reduced by minimizing the tracking force of the probe on the sample, but there are practical limits to the magnitude of the force that can be controlled by the user during AFM operation.

2.6.2 Non-contact Mode AFM [41]

In non-contact mode AFM a stiff cantilever vibrates near its resonant frequency (100~400 kHz) with an amplitude of a few tens of an angstrom. The tip oscillates near the surface. As the tip is brought close to the sample the system monitors the change in resonant frequency or vibrational amplitude of the cantilever through the use of feedback signals, which move the scanner up or down. Changes in the resonant frequency of the cantilever can be used as a measure of changes in the force gradient, which reflect changes in the tip-sample-spacing or topography. In NC-AFM the cantilever is set into oscillation near the sample surface but does not touch it. The spacing between the tip and surface is on the order of 10 to 100 angstroms as shown in the van der Waals force curve [39] in figure 2.21. The total force between the tip and sample in NC-AFM is low (10^{-12} N) and allows the study of soft or elastic samples.

Problems arise with non-contact mode in trying to follow the sample topography when water exists on the surface. AFM operating in contact mode will penetrate the liquid layer to image the underlying surface whereas non-contact AFM will image the surface of the liquid layer. The problem is illustrated in Figure 2.24.

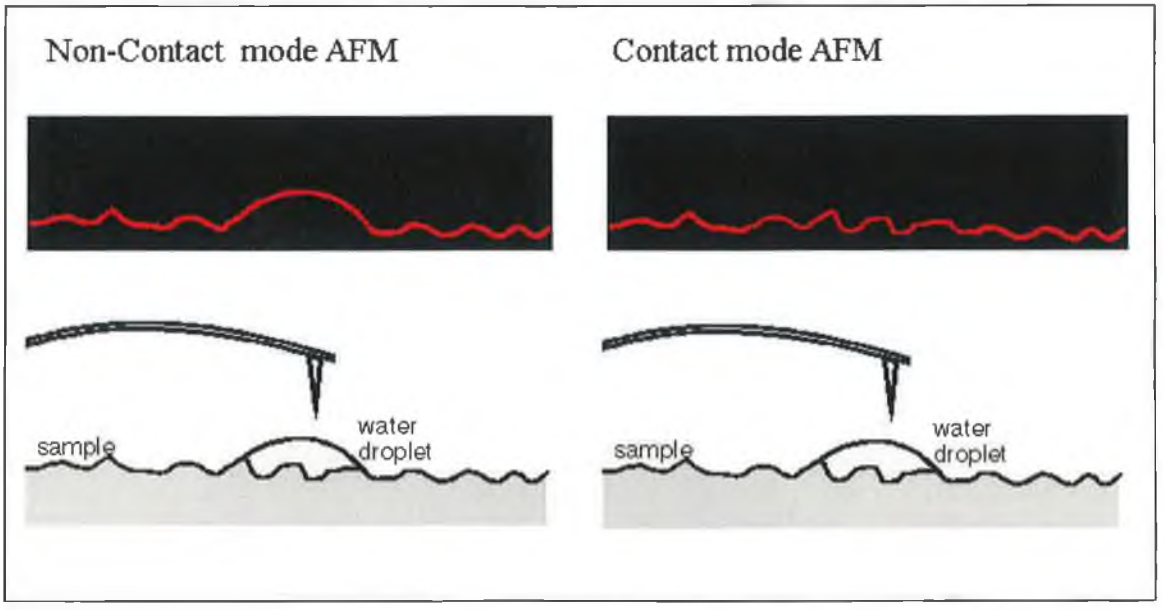

Figure 2.24: The relatively small tip-sample interaction of non-contact mode AFM allows soft samples to be imaged non-invasively but is not strong enough to image "through" adsorbed contamination or water droplets. In contact mode AFM the tip maintains contact with the surface and images the sample surface (Thermo micro[39]).

In order to achieve high resolution (vertical) in non-contact mode AFM, it is necessary to measure force gradients from van der Waals forces, which may extend only a nanometer from the sample surface. Generally the fluid contamination layer is substantially thicker than the range of the van der Waals force gradient and therefore, attempts to image the true surface fails as the oscillating probe becomes trapped in the fluid layer or hovers beyond the effective range of the forces it attempts to measure.

2.6.3 Tapping Mode AFM [40]

For the oxide layers considered in this thesis the AFM was operated in non-contact tapping mode. The operation process is illustrated in Figure 2.25 [40].

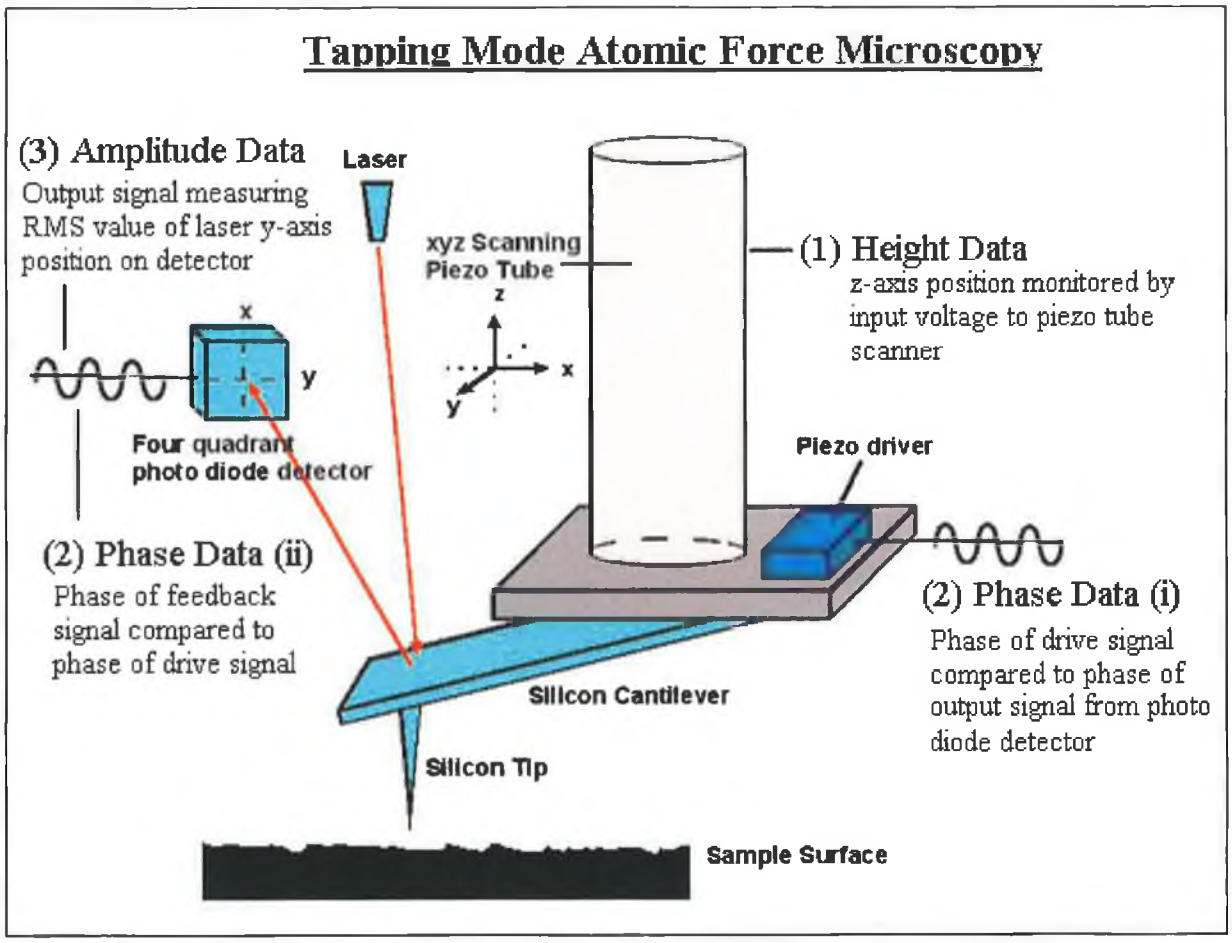

Figure 2.25: A sharp tip oscillates at the natural frequency of the cantilever to which it is attached. When the tip is brought close to the sample surface it's oscillation phase and amplitude are modified through Van der Walls interaction. The distance between the tip and sample is regulated through the voltage applied to the piezo, the extent of which is decided by the feedback signal from the detector to the piezo driver (Mauritz [40]).

In tapping mode, the silicon probe tip oscillates at the resonant frequency of the cantilever to which it is attached. The oscillating tip is rastered across the sample surface line by line. When it approaches the surface the tip interacts with the surface through Van der Walls forces which modify its amplitude and phase of oscillation. These modifications are measured at a four quadrant (allowing both vertical and lateral force microscopy) diode detector through the change in position and phase of laser light reflected from the oscillating tip.

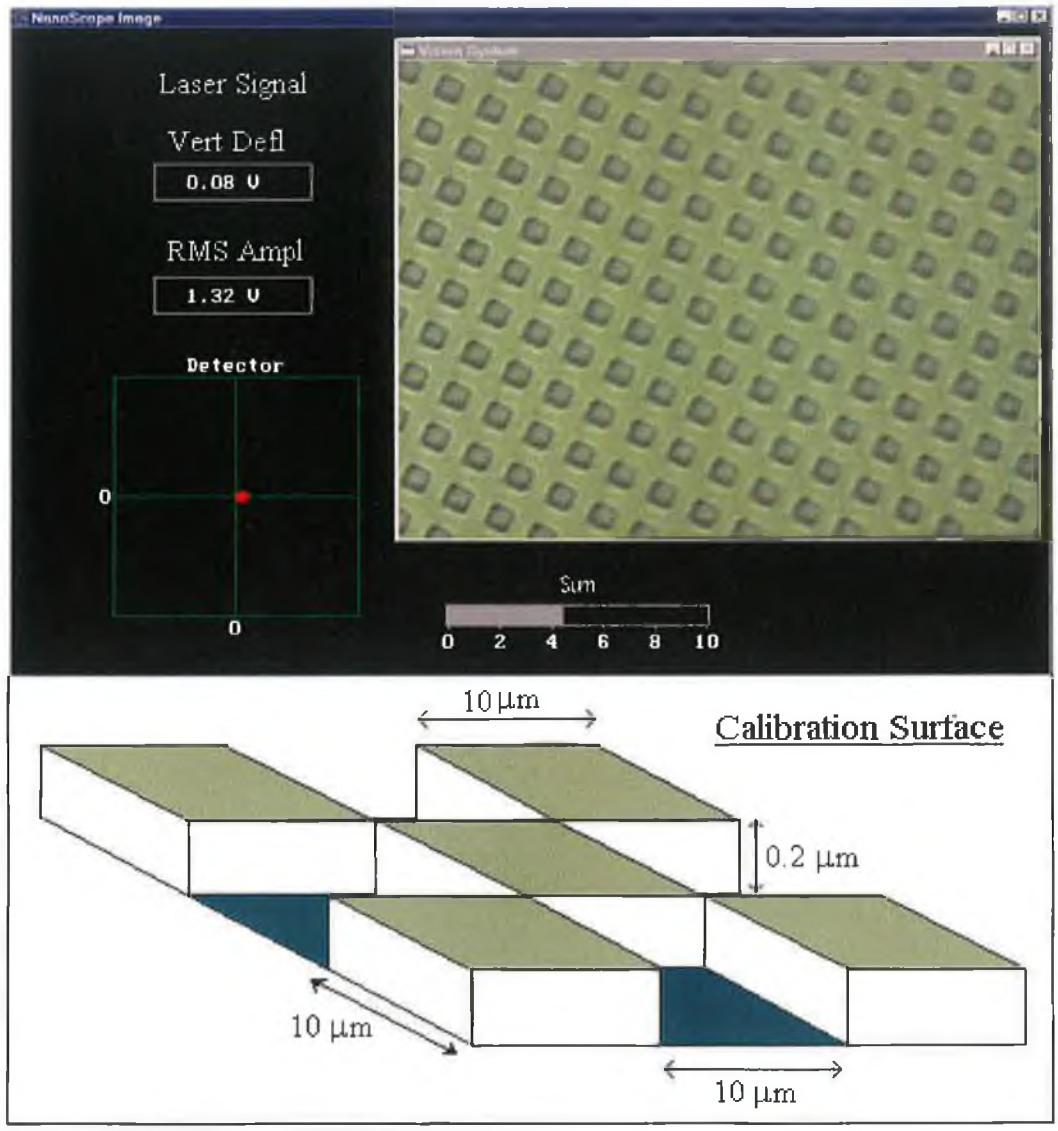

Figure 2.26: (Top) CCD image (~ 20 µm x 180 µm) from auxiliary magnification stage of calibration standard sample. Vert. Defl is almost zero as light reflected from tip on quadrant detector is almost in the centre. The RMS amplitude is that of free vibration. Sum is an indication of the extent of the reflection from tip. (Below) a simplified 3D schematic of the known surface topography.

The capabilities and limitation of tapping mode AFM are best expressed by considering its ability to map out a known topography. Figure 2.26 shows a calibration surface with known dimensions. The surface is made up of a periodic square array of wells of length 10 μm and depth 0.2 μm and separated by 10 μm. Figure 2.27 shows a high resolution tapping mode AFM image of a single well structure in the calibration standard. Height is interpreted in terms of colour. The full z height is 0.4 μm and so a feature this high or higher will be seen as white where as smaller features as seen as darker red.

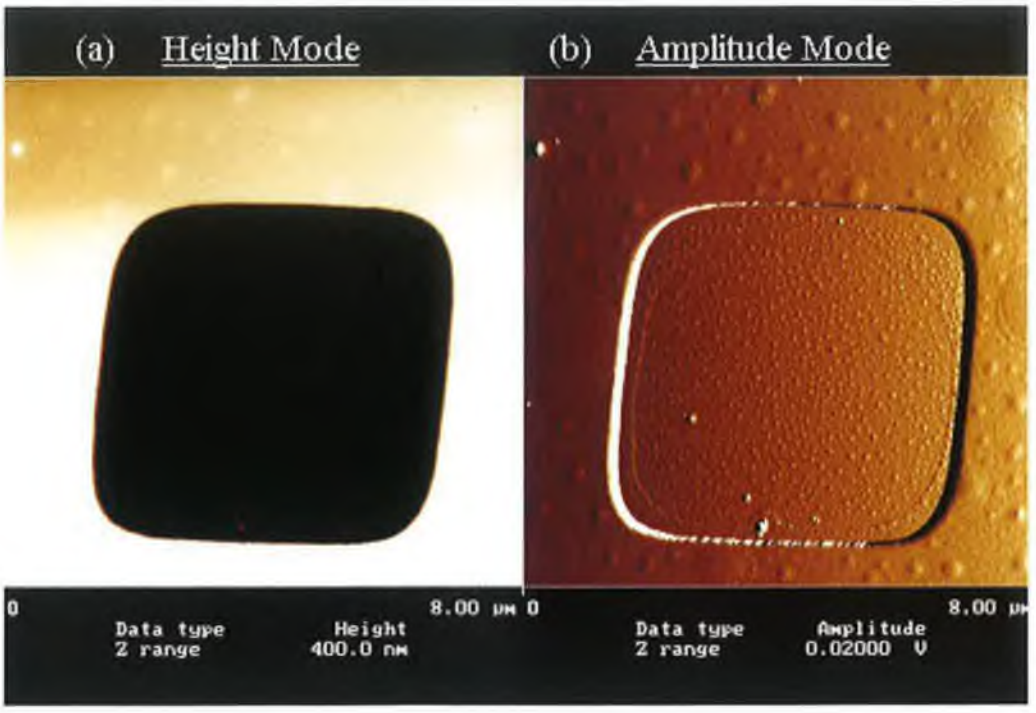

Figure 2.27: Tapping mode image of a single well structure from the calibration standard in (a) height mode and (b) amplitude mode.

The data is presented in two modes, height and amplitude. There are three formats in which data can be presented.

Height Data: The vertical position of the probe tip is monitored by noting changes in the length of the z-axis on the xyz scanning piezo tube. Input voltage to the scanning piezo tube is proportional to the length of the tube. The change in the z-axis is plotted as a topographical map of the sample surface. Height data is a good measure of the height of surface features but does not show distinct edges of these features.

Amplitude Data: The amplitude of the cantilever is monitored by the photo diode detector. The RMS value of the laser signal on the y-axis of the detector is recorded for each of the 512 segments on a given raster of the probe tip. These values are plotted as an amplitude map of the sample surface. Amplitude images tend to show edges of surface features well.

Phase Data: This type of imaging monitors the change in phase offset, or phase angle, of the input drive signal to the drive piezo with respect to the phase offset of the oscillating cantilever. The phase of the drive signal (i) is compared to the phase of the cantilever response signal (ii) on the photo diode detector. See (2) in the above figure 2.25. The phase offset between the two signals is defined as zero for the cantilever oscillating freely in air. As the probe tip engages the sample surface, the phase offset of the oscillating cantilever changes by some angle with respect to the phase offset of the input drive signal. As regions of differing elasticity are encountered on the sample surface, the phase angle between the two signals changes. These changes in phase offset are due to differing amounts of damping experienced by the probe tip as it rasters across the sample surface. These differences are plotted as the so-called "phase image".

In addition to the monochrome intensity interpretation of the surface topography, the current "line" being scanned or rastered can be viewed in scope mode where the trace and retrace of the line scan can be superimposed to gauge the stability of the scan and also to optimise the feedback controls of proportion and integral gain.

The sensitivity of amplitude mode to sharp features is evident in figure 2.28 from the relatively large signal associated with the local trace/re-trace disagreement at the "sharp" well edges in amplitude mode compared to height mode.

Unlike the above calibration standard the surface of an industrial oxide is not known exactly but is expected to be flat on a sub nanometer scale with a surface roughness characterised by it's RMS value of peak heights about the mean height on the surface. AFM is discussed in this context in chapter 4.

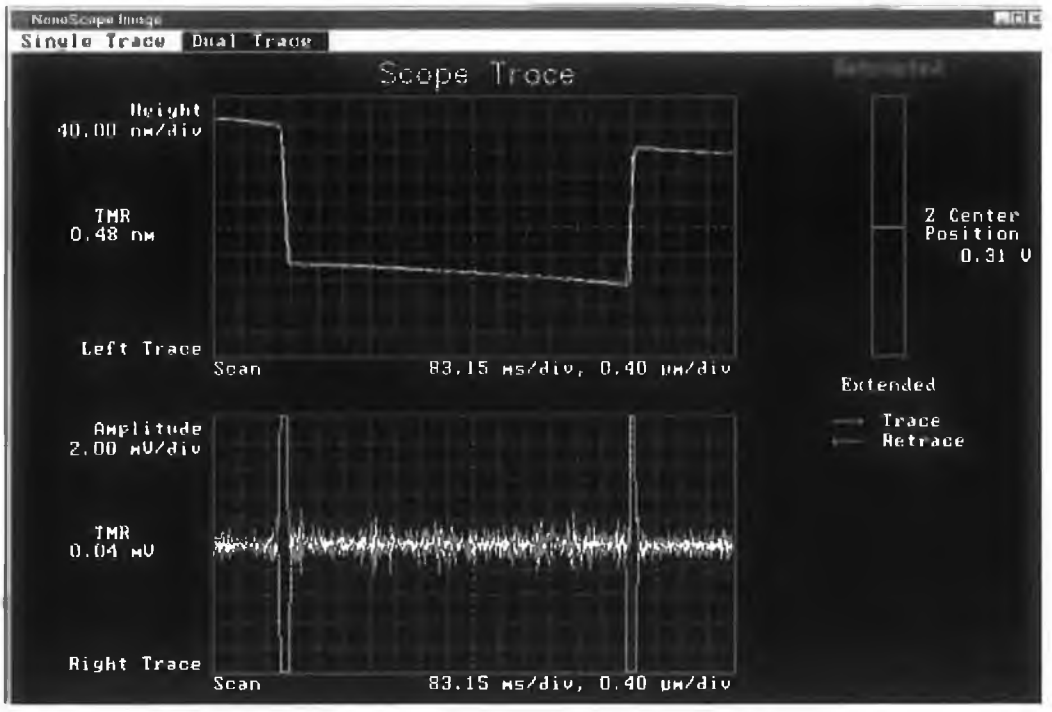

Figure 2.28: Line scan trace (yellow line) and re-trace (white line) for (top) height mode and (bottom) amplitude mode. The agreement between the trace and retrace allows the feed back corrections (integral and proportional) to be optimised for the sample terrain.

2.7 Low Energy Electron Diffraction

In bulk crystalline solids the basic repeating unit is contained within the unit cell, which is described with a set of basis vectors. The bulk periodicity can thus be mapped out by using suitable translation (lattice) vectors. The solid can be considered as being made up of planes of atoms with an inter-planar spacing d. Three coordinates can define any plane of atoms. Conventionally the planes are labelled using miller indices (h,k,l). The Miller indices of a plane bear a reciprocal relationship to the real intercepts of the plane with the axes; in the same way the wavelength of an X-ray beam (a real distance) bears a reciprocal relationship to the wavevector, k, of the beam whose magnitude is defined as:

$$k = \frac{2\pi}{\lambda} \qquad \textbf{Equation 2.28}$$

The wavevector is a measure of the momentum of the incident and diffracted beams. The change in wavevector of a beam on scattering from a plane of atoms will determine the direction of any emergent diffracted beams. In Figure 2.29 [43] the diffraction condition is readily evaluated using the principle of conservation of momentum.

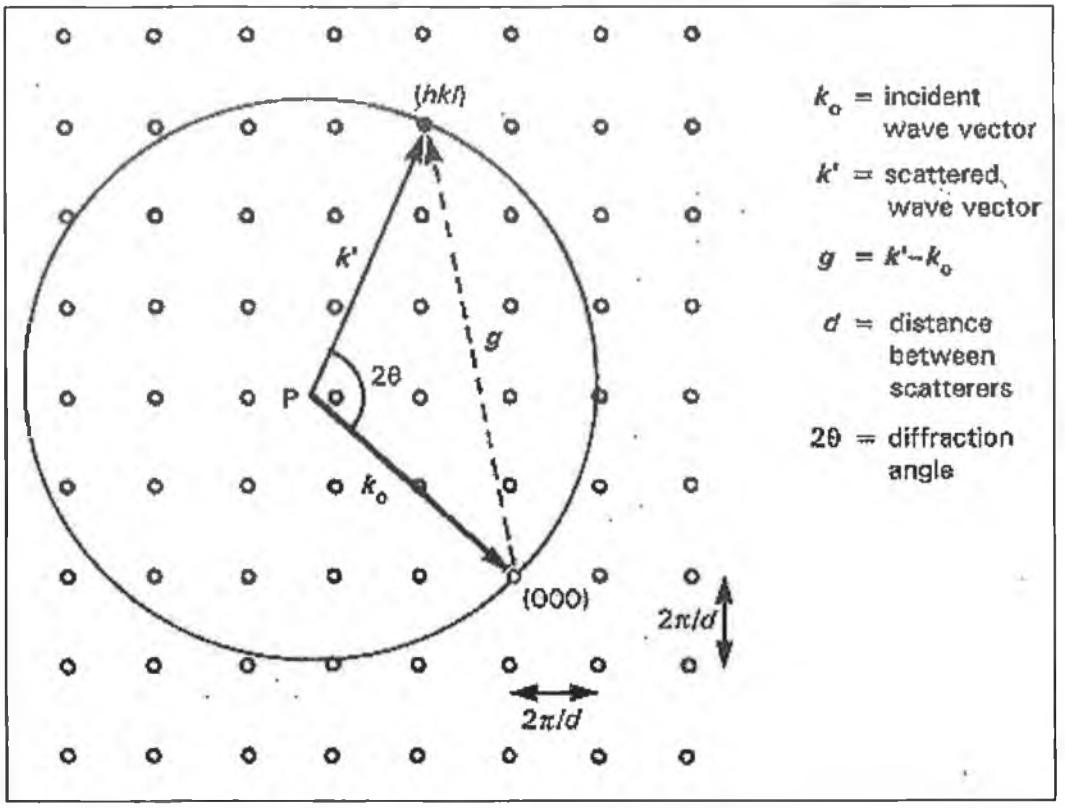

Figure 2.29: The Ewald sphere construction for a cubic lattice, (h,k,l) are the miller indices of the point on the Ewald sphere (Prutton [43]).

The wavevector of the incident X-ray is represented by k_0 and is elastically scattered (i.e. no change in energy) through an angle 2θ to k' resulting in a momentum change. The Bragg diffraction condition requires:

$$n\lambda = 2d\mathrm{Sin}(\theta) \qquad \textbf{Equation 2.29}$$

The condition is satisfied when the change in momentum ($\Delta k = k' - k_0$) is equal to a reciprocal lattice vector. The lattice shown is the reciprocal lattice, where the distance between adjacent points is $2\pi/d$, where d is the distance between points in real space.

A circle with radius k_0 is drawn and is the Ewald sphere. The position of the diffracted beams offers information about the crystal lattice size and symmetry. Analysis of the intensity gives information about the arrangement of atoms within the lattice (the crystal basis). The pattern produced by the crystal as a whole depends on the number of atoms in each unit cell and on their positions relative to one another.

A surface exists in two dimensions where the periodicity of the underlying crystal in the direction normal to the surface is lost. On a surface there is periodicity where the basic repeating unit is contained within a surface unit mesh, which can be mapped out with translation vectors. However, X-rays are limited in their use to probe the periodicity of the surface because of the small scattering interaction between X-rays and the charge distribution on atoms, which results predominately in bulk information, which would dominate the smaller surface signal. Low energy electrons, however, have a very strong interaction with matter and have a short mean free path (for E<150 eV). The wavelength of such electrons is slightly smaller (a few angstroms) than the typical inter-atomic spacing and therefore suitable for diffraction experiments. Figure 2.30 [44] shows an

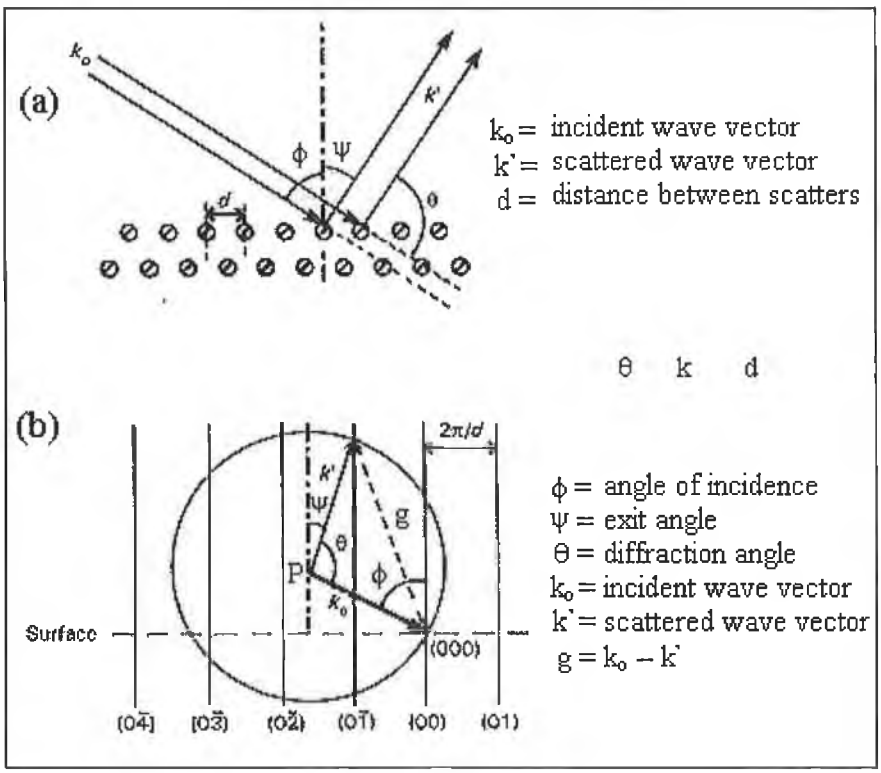

Figure 2.30: A schematic diagram of a diffraction process occurring at a surface in real space (a), with the corresponding Ewald sphere construction in reciprocal space (b) (Vickerman [44]).

electron characterised by a wavevector k_0 incident on a clean surface, the electron is scattered by the outer atoms whose separation is d. Because the surface is two dimensional the repeat distance normal to the surface is infinite and so the reciprocal lattice "points" along the surface normal are infinitely close forming rods. The diffraction condition is satisfied for every beam that emerges in a direction along which the sphere intersects a reciprocal rod. Like in X-ray diffraction, the position of the spots in a LEED pattern can be used to determine the size and symmetry of the surface unit mesh.

In three dimensions there are 14 different Bravis lattices. In two dimensions there are five different surface nets. In any net every lattice point can be reached from the origin by translation vectors

$$T = ma_s + nb_s \quad \textbf{Equation 2.30}$$

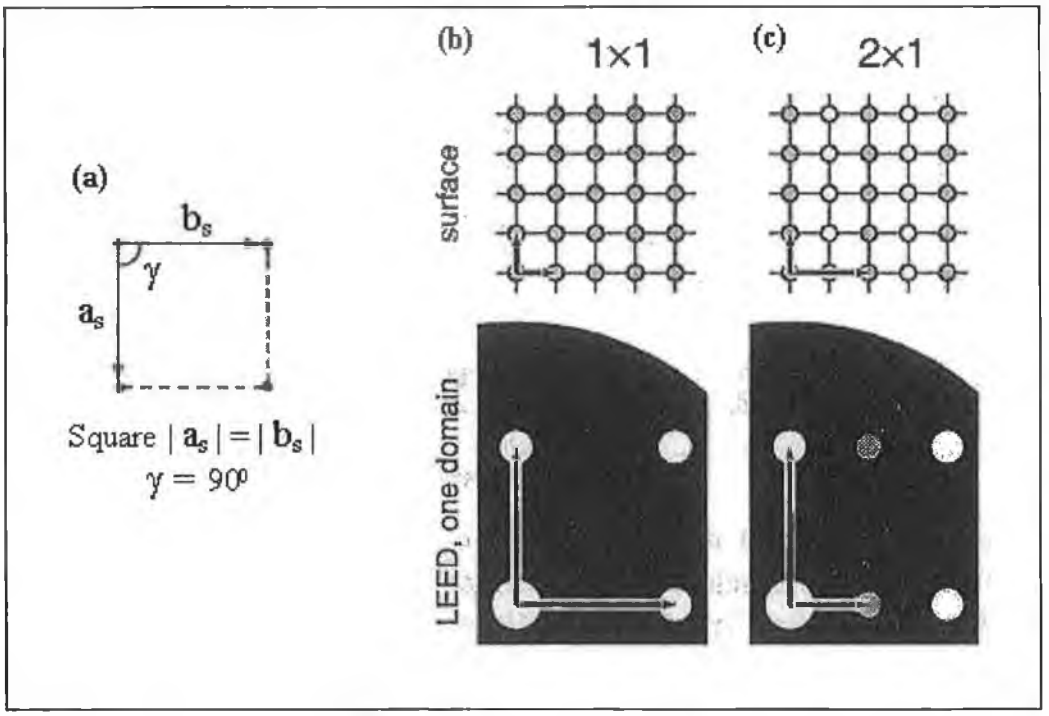

Figure 2.31: (a) square surface net, (b) (Top) real space (1x1) surface reconstruction, (Bottom) it's corresponding reciprocal space LEED pattern, (c) (Top) real space (2x1) surface reconstruction, (Bottom) its corresponding reciprocal space LEED pattern [45].

Where m and n are integers, and the vectors a_s and b_s define the unit mesh. Figure 2.31 [45] (a) shows the square system. Figure 2.31 (b) shows an unreconstructed surface and it's corresponding LEED pattern. When the surface reconstructs, the surface can be mapped using multiples of the translation vectors of the unreconstructed surface. In Figure 2.31 (c) (Top) the atomic spacing of the outermost atoms in the x direction is twice the value that would exist in an unreconstructed surface. The spacing in the y direction is the same and so the multiples on the x and y translation vectors are 2 and 1 denoting a 2x1 reconstruction. In reciprocal space (bottom) the scaling of the x and y lattice points has been inverted.

Figure 2.32 shows a LEED system, which allows the periodicity of a surface to be investigated. An electron beam of variable energy is produced by an electron gun and is incident on the sample.

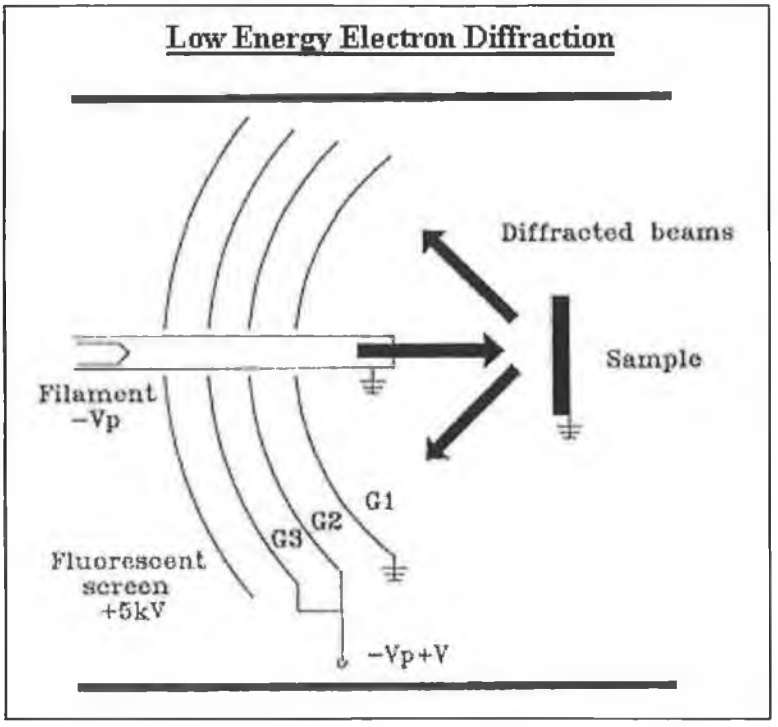

Figure 2.32: In a LEED experiment a beam of monochromatic low energy electrons is incident on the clean surface. The electrons are backscattered from the sample surface onto a system of grids. Only the elastically scattered electrons form the LEED pattern and are accelerated towards a fluorescent screen where a pattern of bright spots is seen. The inelastically scattered electrons are rejected by the negative potential of the other two grids.

Both elastic and inelastic electrons are backscattered onto a system of grids surrounding the gun. After reaching the first grid G_1 (which is earthed) elastically scattered electrons are accelerated towards a fluorescent screen where a pattern of bright LEED spots is seen. The grids G_2 and G_3 are held at an adjustable negative potential in order to reject most of the inelastically scattered electrons, which contribute to the diffuse background.

2.8 Synchrotron Radiation

When a charged particle (electron or positron) is made to traverse a curved (circular) path by say a magnetic field as shown in figure 2.33 [46] the charged particle emits electromagnetic radiation in a direction tangential to its centripetal acceleration.

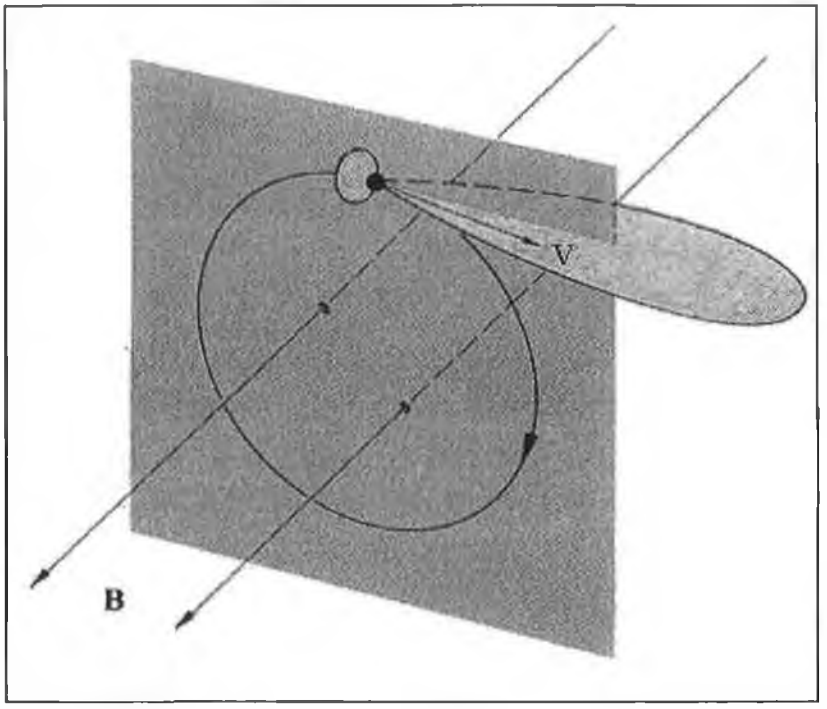

Figure 2.33: Radiation pattern for an orbiting charge in a magnetic field (Hecht [46]).

In a synchrotron radiation source a beam of electrons is injected into a storage ring, which is under UHV. The electrons are accelerated to energies of the order of GeV by a radio frequency (RF) accelerating cavity operated in phase with the arrival of the electron bunches. The electrons travel in bunches close to the speed of light and are

confined to a circular path by bending and focusing magnets. Because the electrons are travelling at relativistic speeds the SR is emitted in a narrow cone in a tangential direction from the bending curve at the time of emission. The emitted radiation is broadband (i.e. the high temporal localisation is realised through the addition of many frequencies), extremely intense, collimated and highly plane polarized (which facilitates wavelength selection). In a synchrotron facility the radiation is collected through beamlines, which are tangential to the ring. Figure 2.34 [48] shows a schematic of a typical synchrotron light source facility with experimental beamlines attached.

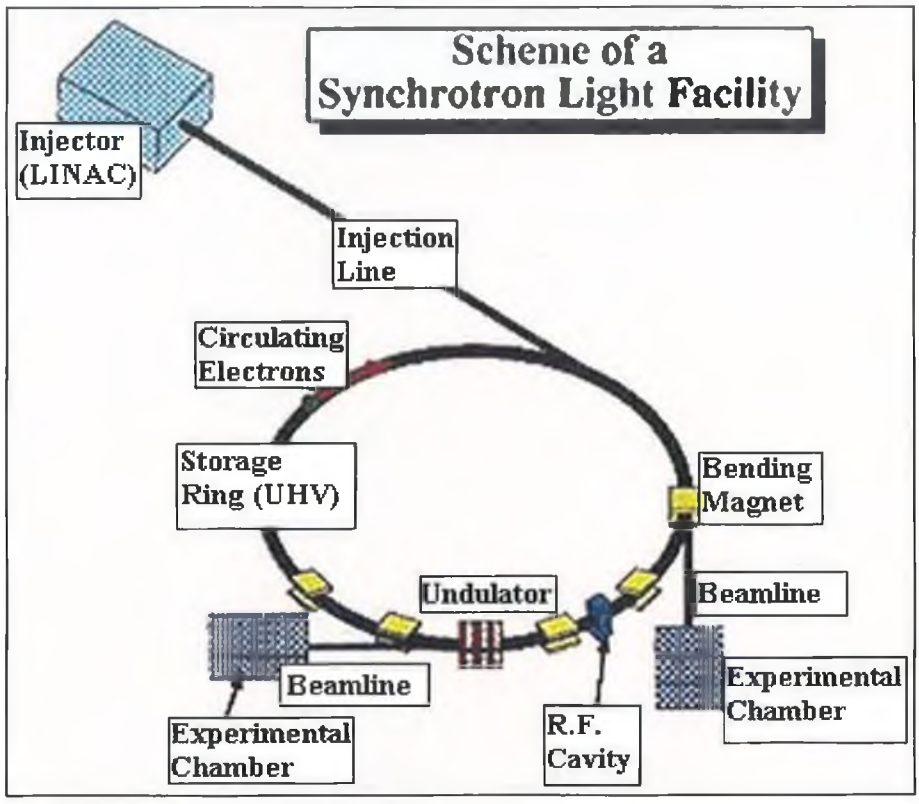

Figure 2.34: A schematic representation of a synchrotron radiation facility [48].

The advantages of synchrotron light for photoemission are in its intensity, its resolution, the ability to tune the energy (frequency) of the light. These properties allow the energy dependence of surface sensitivity to be exploited and thus depth profile a sample in the sub-nanometer regime or to resolve close lying chemical states. In angle resolved photoemission (UPS) the wave nature of synchrotron (polarisation of the E field) light is exploited in order to probe ("map") the electronic structure of materials [2].

Insertion devices [48]:

Electrons are injected into a storage ring in bunches, but on each pass each bunch illuminates any given beamline only once. By forcing electrons to follow a zigzag path a beamline located at the end of such a path can collect light several times per turn instead of once. The change in the electron trajectory is achieved using insertion devices such as a wiggler or undulator. In a wiggler or undulator electrons travel through a periodic magnetic structure.

Wiggler

A wiggler works as follows; it consists of a periodic series of magnets, placed in a ring section where the electron path would otherwise be straight; because of it's action, the electrons are forced to "wiggle" around the straight path resulting in a very high flux of X-rays along the wiggler beamline.

Undulator

An undulator is similar to a wiggler except it forces the electrons into a much weaker zigzag, so that during the entire zigzag motion synchrotron light continues to illuminate the undulator beamline. Without short pulses, there is no wide band of wavelengths, thus the undulator emission is not spread in a wide band but concentrated, producing high levels of flux and brightness.

2.8.1 NSLS U4A Beamline Characteristics

Soft X-ray photoemission experiments were performed on beamline U4A at the National Synchrotron Light Source (NSLS) at Brookhaven National Laboratory, New York. This facility is a second-generation light source with an X-ray and vacuum ultra violet (VUV) ring. The function of the beamline is to gather and monochromate the light emitted from the ring and finally focus the light into as a small spot onto the sample in the analysis chamber. Figure 2.35 shows the optical layout of the beamline.

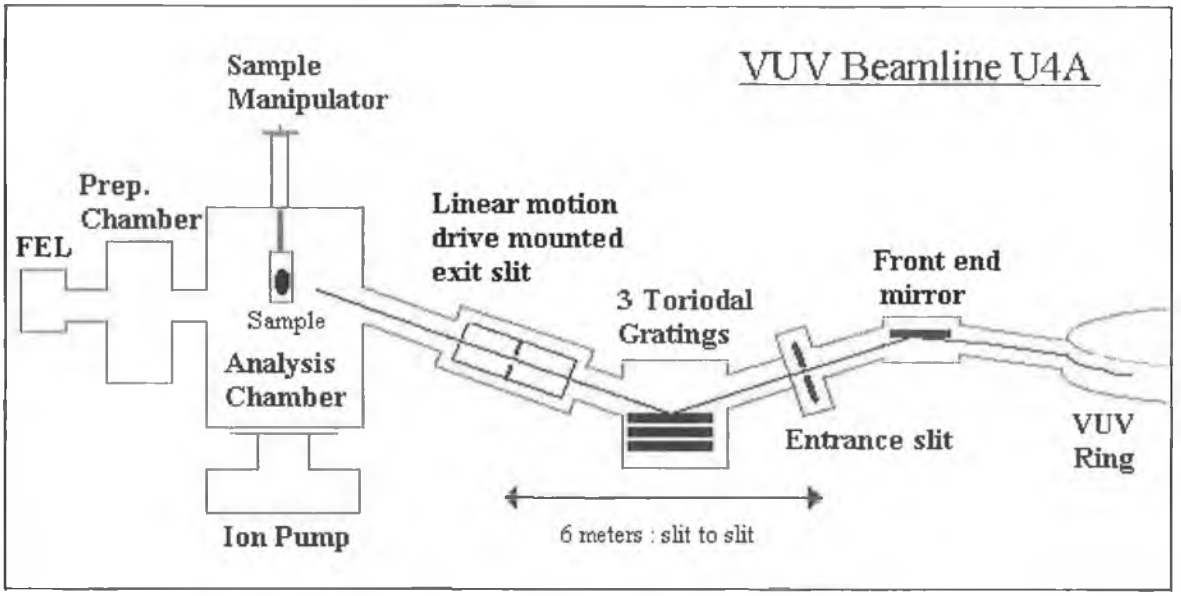

Figure 2.35: A schematic representation of the optical layout of beamline U4A. Light enters the line and is bent and focused onto the entrance slit to the monochromator by the front-end mirror. The monochromator selects the desired wavelength through dispersion. The exit slit focuses the light onto the sample in the analysis chamber.

The line is on bending magnets on the (0.8 GeV) UV ring, and can deliver light from 8 to 250 eV using three interchangeable gratings. The front-end mirror collects light directly from the bending magnet and focuses the light on to the monochromator gratings. The monochromator is a 6m/160° toroidal grating instrument, with three gratings with 288, 822, and 2400 lines per mm. The diffracted light passes through the exit slit which is mounted on a linear drive for beam optimisation. Finally the beam illuminates the sample in the analysis chamber.

The analysis chamber is equipped with a VSW analyser with collection lens. The sample manipulator allows xyz linear motion and rotation; also a sample can be heated by electron beam heating. The analysis chamber is equipped with a LEED system and an inert ion sputter gun for sample cleaning. UHV is achieved using suitably arranged rotary, turbo molecular and ion pumps. A FEL chamber is connected to a preparation chamber which is itself connected to the analysis chamber. This allowed the introduction of a sample from air into UHV within 10 minutes via a sample transfer mechanism. The analysis chamber is presented in more detail in chapter 6.

2.8.2 Synchrotron considerations

With excellent resolution and tuneable surface sensitivity synchrotron radiation allows the sampling depth to be varied and also close lying chemical states to be resolved. There may be some evolution in a spectrum with different photon energy due to a change in the shape of the background or the photoionisation cross-section or in resolution due to the response cure of the monochromator grating.

Background removal

The surface sensitivity of a photoelectron is maximized for a kinetic energy of ~40 eV, and so for Si_{2p} (E_B 99.3 eV), surface sensitivity is maximized using a photon energy of 130 eV. Figure 2.36 shows a Si_{2p} spectrum taken by Hollinger et al [49] at photon energy of 120 eV.

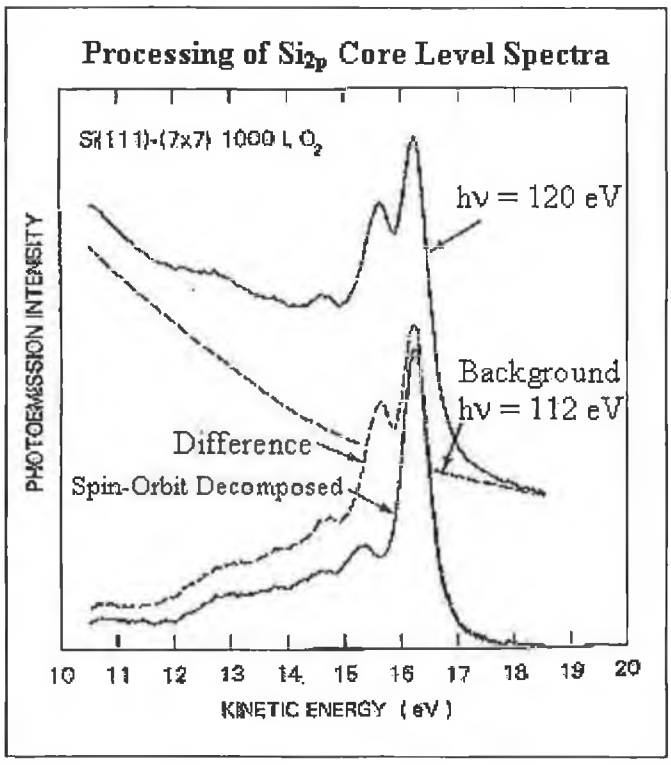

Figure 2.36: The background on which the Si_{2p} spectral envelope sits can be sampled in isolation of the Si_{2p} peak by considering the same energy window at a different photon energy. After subtracting the estimated background the redundant $Si_{p1/2}$ component of the spin orbit degeneracy is numerically removed in a spin stripping process (Hollinger [49]).

Difficulties arise when looking "deeper" into the surface with a more bulk sensitive photon energy of 120 eV. At 120 eV the peak sits quite high on the secondary electron background (see figure 4.25, chapter 4), which complicates background removal. By taking spectra in the same kinetic energy window but at different photon energies (112 and 120 eV) the background on which the peak sits can be seen in isolation of the peak thus allowing background subtraction. However as discussed earlier, there are extrinsic processes, and intrinsic processes inherent in the photoemission process which contribute to the peak intensity which could be unfairly subtracted in the approach above. Therefore when dealing with samples of a high doping or at bulk sensitive photon energies the background was sampled at a reduced photon energy and the remaining intrinsic loss process was approximated with a Shirley background.

Spin orbit stripping

While synchrotron light offers excellent resolution compared to conventional XPS sources, its resolution is finite and not always able to clearly resolve overlapping peaks. For Si_{2p} the constant branching ratio and spin-orbit splitting between the $Si_{2p3/2}$ and $Si_{2p1/2}$ component allows numerical subtraction of the smaller $2p_{1/2}$ component starting on the high kinetic energy side of the peak and implementing the following algorithm:

$$\text{Intensity}[E_k] = \text{Intensity}[E_k] + (0.5\text{Intensity}[E_k + \text{spin orbit split}]) \quad \textbf{Equation 2.31}$$

where Intensity[E_k] is the intensity at kinetic energy E_k.

Figure 2.37 shows a SiO_2 spectrum , after background removal. The red line shows the raw data and the black the spectrum after spin stripping. The background must first be removed before starting the spin-stripping algorithm.

Care must be taken not to introduce "artefacts" into the spectrum, as typically the spectrum is interpolated before stripping. The danger is that a "spike" or "artefact" made up of only two points in the raw data would span five points in the interpolated data and looks more like a legitimate peak. The point is illustrated in the inset in figure 2.30 where a local spike exists in the raw data.

However with careful examination of the raw data and removal of spikes, spin-orbit stripping is useful in elucidating the structure in the $Si_{2p3/2}$ spectral envelope.

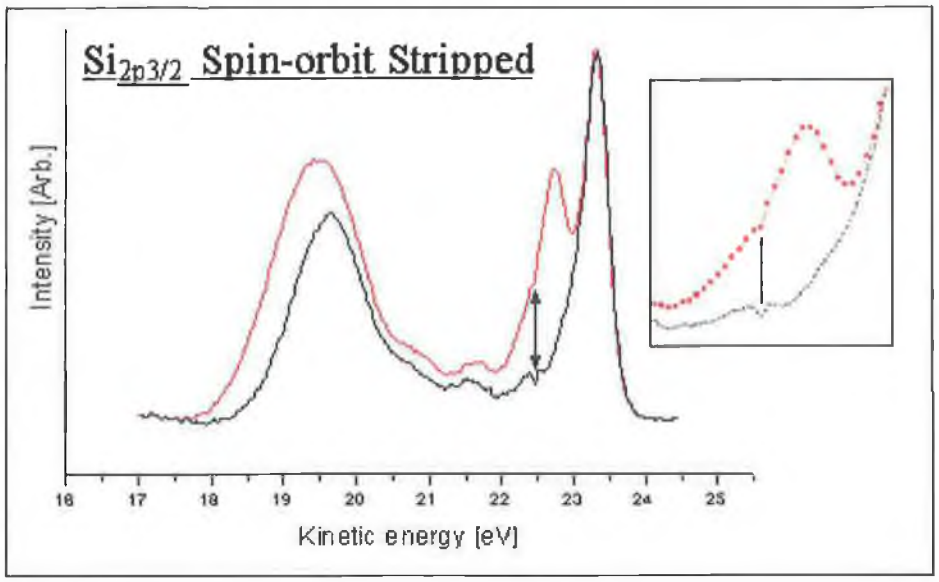

Figure 2.37: A high resolution Si_{2p} photoelectron spectrum (red) has the $Si_{2p1/2}$ component of the spin-orbit degeneracy removed numerically in order to better elucidate structure in the spectral envelope through the $Si_{2p3/2}$ component (black). The inset illustrates how a localised spike (single point) in the raw data can be propagated into a more legitimate peak (three points) through interpolation before stripping.

2.9 References for Chapter II

1 M. Cardona. L. Ley (Eds.). Photoemission in Solids. Parts 1 and 2. Springer. Berlin. 1978

2 K.E. Smith, Physics Dept. Boston University, Submitted for publication

3 S. Hufner, Photoelectron Spectroscopy. Solid State Sciences, ed. Springer. 1995

4 Private Communication, Prof. I. T. McGovern, Physics Dept. Trinity College Dublin

5 X-ray data booklet, Lawrence Berkeley National Laboratory

6 K. Siegbahn, C. Nordling, A. Fahlman, Nova Acta Societatis Scientiarum Upsaliensis, Ser. IV, **20** (1967) 5

7 F. Himpsel, F. McFeely, A. Taleb-Ibrahimi, J. Yarmoff, G. Hollinger, Phys. Rev. B **38** (1998) 6084

8 B. D. Ratner chpt 3, p52, Surface Analysis the Principle Techniques, J. Vickerman, Wiely & Sons (1997) p52

9 A. Pasquarello, M.S. Hybertsen, R. Car, Phys. Rev. Lett. **74** (1995) 1024

10 M. Banaszak Holl, S. Lee, F.R. McFeely, Appl. Phys. Lett **72** (1993) 2441 also M. Banaszak Holl, S. Lee, F.R. McFeely, Appl. Phys. Lett **65** (1994) 1097

11 B. Ratner, Surface analysis – the principal techniques, J. Vickerman, Wiely & Sons (1997) p.49

12 M.P. Seah and W.A. Dench, Surf. Interface Anal. **1** (1979) 2

13 Vacuum Scientific (VG) instrument manual for Clam analyser

14 Briggs and Seah, Practical Surface Science, 2nd Edt. Wiely & Sons(1994) p 76

15 S. Tougaard, Surf. Interface Anal., **11** (1988) 453

16 A.M. Salvia, J.E. Castle, J. Electron Spectrosc. Relat. Phenom. **95** (1998) 45

17 D.A. Shirley, Phys. Rev. B **5** (1972) 4709

18 P. Bevinton, Data Reduction and Error Analysis for the Physical Sciences; McGraw-Hill Book Company : New York 1992

19 B. Ratner, Surface Analysis – the Principal Techniques, J. Vickerman, Wiely & Sons (1997) p.60

[20] J.H. Scofield, H. Slater, J. Electron Spectrosc. Relat. Phenom., **8,** (1976) 129

[21] C. Powell, J. Electron Spectrosc. Relat. Phenom. **47** (1988) 197

[22] J. Shallenberger, J. Vac. Sci. Technol. A**14** (1996) 693

[23] J. Shallenberger, D. Cole, S. Novak, A**17** (1999) 1086

[24] J.H. Thomas III, S. Hofmann, J. Vac. Sci. Technol. A**3** (1985)1921

[25] S. Evans, R. G. Pritchard, J. M. Thomas J. Electron Spectrosc. Relat. Phenom.**14** (1978) 341.

[26] R.I.Hegde, Maiti, R.S.Rai, K. G. Reid, and P.J. Tobin, J. Electrochem. Soc. **145** (1998) L13

[27] H. C. Lu, E. P. Gusev, T. Gustafsson, E. Garfunkel, M. L. Green, D. Brasen, and L. Feldman, Appl. Phys. Lett. **69** (1996) 2713

[28] S. R. Kaluri, and D. W. Hess, Appl. Phys. Lett. **69** (1996) 1053

[29] S. Hashimoto, K. Hirokawa, Y. Fukuda, N. Usuki, N. Gennai, S. Yoshida, H. Horie, A. Tanaka, and T. Ohtsubo, Surf. Interface Anal. **18** (1992) 799

[30] J.E. Fulghum, Surf. Interface Anal., **20** (1993) 161

[31] T.D. Bussing and P.H. Holloway, J. Vac. Sci. Technol. A**3** (1985) 1973

[32] W. Aarnink, A. Weishaupt, A. Silfhout, Appl. Surf. Sci. **45** (1990) 37

[33] M. Ebel, Surf. Interf. Analy. **3** (1981) 149

[34] A. Ishizaka, S. Iwata, Appl. Phys. Lett. **36** (1980) 71

[35] G. Smith, A. Livesey, Surf. Interface Anal. **19** (1992) 175

[36] B. Tyler, D. Castner, B. Ratner, Surf. Interface Anal. **14** (1989) 443

[37] J. Hill, D. Royce, C. Fadley, F. Wagner, F. J. Grunthaner, Chem. Phys. Lett. **44** (1976) 225

[38] P.J. Cumpson J. Electron Spectrosc. Relat. Phenom., **73** (1995) 25

[39] Thermo Micro Web page http://thermomicro.com/spmguide/1-2-0.htm

[40] Prof. Kenneth A. Mauritz Department of Polymer Science University of Mississippi, http://www.psrc.usm.edu/mauritz/afm.html

[41] Department of Chemistry and Biochemistry, University of Guelph
http://www.chembio.uoguelph.ca/educmat/chm729/afm/details.htm

[42] Digital Instruments Web page
http://www.di.com/AppNotes/Semi/SemiMain.html#SRC1

[43] M. Prutton, Surface Physics, Clarendon Press, Oxford (1983)

[44] W. Flavell, Surface Analysis – The Principal Techniques, J. Vickerman, Wiely & Sons (1997) p.323

[45] Silicon Surfaces and Formation of Interfaces, Jarek Dabrowski, Hans Mussig, World Scientific, Page 89

[46] Hecht, Optics, Addison-Wesley publishing 2nd Edt. Page 50

[48] Trieste synchrotron Web page : www.elettra.trieste.it/visitors/

[49] G. Hollinger, F. Himpsel, Phys. Rev. B **28** (1993) 3651

Chapter 3

Chemical characterisation of thin SiON and SiO_2 films using X-ray photoelectron spectroscopy

3.0 Introduction

This chapter is concerned with the chemical characterisation of silicon dioxide and oxynitride dielectric layers using XPS. The primary objective was to determine whether XPS had the necessary resolution and surface sensitivity to analyse the changes in the dielectric stoichiometry in the near surface region. The as-received samples were evaluated using XPS in terms of chemical composition, thickness and oxidation states present in the layers. No interfacial silicon suboxides were detected in the as-received samples which consisted of a range of dielectric layers 20, 13.4, 7.2, 6.5 and 5.5 nm thick as was determined by ellipsometric measurements made following dielectric growth in commercial furnaces. The 20 nm film was effectively infinitely thick as the substrate silicon signal could not be detected and therefore yielded good fitting parameters for the oxidised silicon signal. Two different experimental approaches were used to thin the dielectric layer with the specific objective of analysing changes in chemical composition and oxidation states present in the near surface region. Argon bombardment was used to acquire a chemical depth profile of the dielectric layer, but as will be shown in the results section, the bombarding process itself affected the FWHM of the core level peaks and introduces suboxide core level features in to the spectrum. As one of the objectives of the study was to monitor the presence of suboxide states in the interfacial region, the generation of broadened peaks and suboxide species by the bombarding process ultimately made this approach untenable. The second approach involved the thinning of the dielectric layers using very dilute HF etching solutions. The experimental results for SiO_2 films thinned in this way illustrated that the peak FWHM was unaffected by thinning processes and suboxides were only detected in the immediate vicinity of the dielectric-silicon interface.

The nitrogen signal in the as-received dielectric layers (5.5 and 3.3 nm) consisted of a single N_{1s} chemical component. Studies of the evolution of this peak with dilute wet chemical etching revealed the presence of a chemically shifted interfacial nitrogen peak.

Analysis of the distribution of the nitrogen through the dielectric layers revealed a non-uniform distribution with there being nitrogen surface and interfacial regions, with relatively little in the bulk of the oxide layer. It was not possible to clearly resolve the overlapping oxide and interfacial components of the N_{1s} peaks. Ultimately an examination of the interface requires the resolution and surface sensitivity offered by a synchrotron, which is the basis of the following chapter. Despite this, the XPS studies have allowed the quality of device grade silicon dioxide layers and oxynitride layers to be affirmed.

3.1 SiO_2 As received

The as-received silicon dioxide 8" wafer sample set was made up of the following thickness; 20, 13.4, 7.2, 6.5, 5.5 nm, as determined by elliposimetry during production. Figure 3.0 displays the core level spectra of the as received samples using Mgk_α and Alk_α anodes respectively.

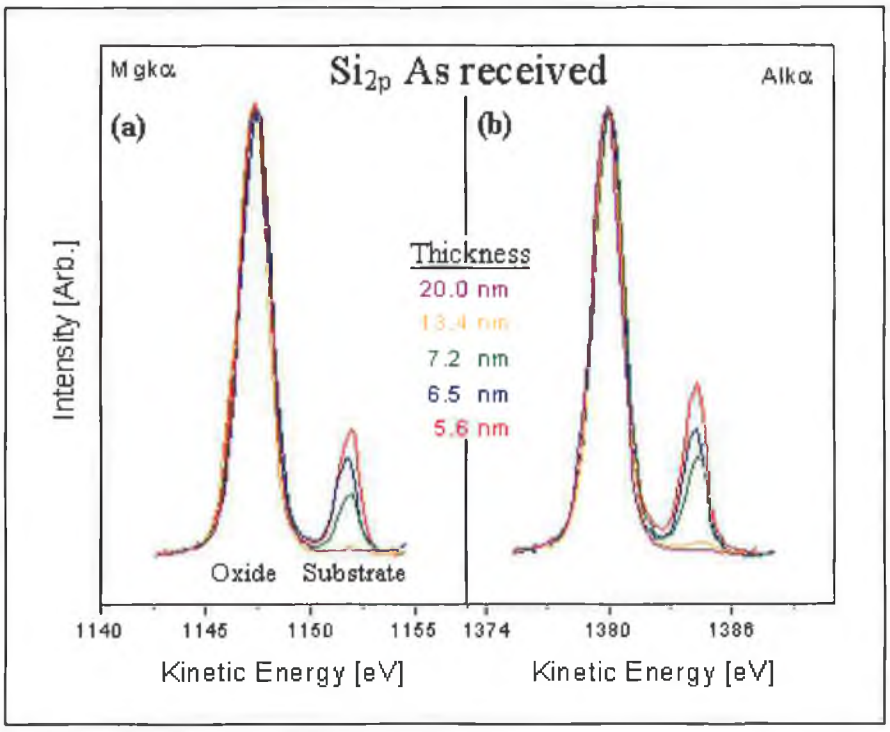

Figure 3.0: Normal emission XPS spectra of the Si_{2p} core level for the range of thicknesses investigated in this work using both Mgk_α and Alk_α

The larger IMFP, λ, of the higher energy Alk_α X-rays is visible in figure 3.0 from the larger substrate peak height relative to the overlaying oxide peak height than in the spectra acquired with the Mgk_α radiation source. Table 3.0 summarizes the peak parameters of the individual scans and displays the higher resolution available using the Mgk_α radiation source.

Mgk_α	FWHM					Alk_α	FWHM				
Thic. (nm)	Si_{2p} Oxide	$Si_{2p3/2}$ Subs.	O_{1s}	% O/Si	ΔE O-Si	Thic. (nm)	Si_{2p} Oxide	$Si_{2p3/2}$ Subs	O_{1s}	% O/Si	ΔE O-Si
20	1.60	---	1.49	2.08	430	20	1.72	---	1.64	2.08	430
13.4	1.60	---	1.50	2.11	429.6	13.4	1.71	---	1.65	2.11	429.6
7.2	1.61	0.92	1.48	2.05	429.8	7.2	1.74	0.97	1.65	2.05	429.8
6.5	1.62	0.87	1.52	2.05	429.5	6.5	1.75	0.85	1.67	2.05	429.5
5.6	1.64	0.84	1.52	2.07	429.6	5.6	1.75	0.83	1.68	2.07	429.6

Table 3.0: Summary of XPS peak parameters with thickness for Alk_α and Mgk_α.

There is a reproducible decrease in the FWHM of both the silicon substrate and the oxygen core levels with thickness, with smaller values evident for larger thickness. This trend is interpreted in terms of a reduced contribution of the interfacial intermediary oxidation state peaks to the substrate and oxygen core levels as the dielectric thickness increases. For both the 13.4 nm and 20.0 nm layers the substrate signal is too poorly defined to be fitted, even for illumination with the Alk_α anode.

All as-received films were found to be stoichiometric with only small variations around the expected value of 2.0. These variations are thought to relate to a combination of different degrees of hydrocarbon contamination for different samples and finite experimental accuracy. The stoichiometric values obtained are within experimental error and indicate that the correct relative sensitivity factor were used in the quantitative determinations. Charging was detected for all samples investigated and was corrected for using the silicon substrate binding energy value of 99.3 eV as a reference. Alternatively the kinetic energy separation between O_{1s} and Si_{2p} oxide peak can be used as a charge reference. A change in this energy separation would indicate a chemical rather than a charging shift. Its use, however, requires one to decide a value for the

oxide binding energy, which is equally as assumptive as fixing the substrate binding energy value at 99.3 eV. However, it is known that the Si_{2p}^{4+} oxide peak binding energy exhibits a thickness dependence when very thin and becomes poorly defined and hard to fit unlike the substrate. What is important in charge referencing is to be consistent, which is achieved in these studies by using the substrate peak as a reference at 99.3 eV.

3.2 Fitting parameters

When the oxide thickness is thin enough so that the underlying substrate can be detected (i.e. thickness$<3\lambda_{SiO2}$), so too can the thin interfacial region, where sub-oxidation states (Si^{1+} Si^{2+} Si^{3+}) between the substrate (Si^{0+}) and oxide (Si^{4+}) peaks exist. These suboxide states lie close in energy to both the Si^{4+} oxide and Si^{0+} substrate peaks and because of the limited resolution of conventional XPS; they effectively overlap with these peaks. If these suboxides could be unambiguously de-convoluted from the substrate and oxide related features, the interface could be evaluated quantitatively. For both an infinitely thick oxide and oxide free sample the oxide and substrate peaks can be investigated in isolation of the interfacial region and it is possible to determine the optimised curve fitting parameters for these peaks. In holding these parameters fixed for oxides of intermediary thickness it should in principle be possible to elucidate the interfacial suboxides in the spectra. To obtain good peak parameters for the Si^{4+} oxide peak, a 20 nm SiO_2 sample was analysed. For this thickness the substrate cannot be observed and because the interfacial region is approximately 1 nm thick, it cannot contribute appreciably to the oxide peak. Accurate peak parameters for the substrate are more difficult to obtain. The options are; (a) a surface covered with a native oxide, (b) an etched sample where the oxide has been removed or (c) an atomically clean sample. The native oxide offers a substantial substrate peak but still has some oxide. An atomically clean Si(100) surface was not a feasible option in the vacuum system available. Wet chemical etching provides a stable hydrogen terminated surface with no detectable silicon oxide but with some broadening due to Si-H (hydride) bonding. In this study, the wet chemically etched Si_{2p} core level spectrum was used.

For optimal resolution the analyser was operated at a pass energy of 20 eV and the number of scans was increased to compensate for the resulting loss of intensity, also

longer counting times per step of 0.3 sec were used in order to improve the signal to noise ratio. In order to consistently fit the experimental data sets, peak fitting parameters were held constant in fits of oxide thicknesses where the interface was significant in order to see whether interface specific features could be identified. Figure 3.1 shows a Si_{2p} spectrum of a 3.2 nm SiO_2 film which was realised by etching a 5.5 nm film in 0.5% HF for 1.2 mins. The oxide and substrate signals are comparable and therefore any interface related features should be detected if present. Using the reference parameters, (see Table 3.1) a satisfactory fit could not be achieved with just a Si^{4+} oxide and Si^{0+} substrate peak. The fit residue (bottom panel of figure 3.1) conveys the "goodness" of the fit across the energy window. As expected, the greatest disagreement occurs in the "trough" between the oxide and substrate where suboxides would be present. Initially an attempt was made to fit three suboxide peaks (Si^{1+}, Si^{2+}, Si^{3+}) chemically shifted by 0.9, 1.8 and 2.52 eV as done in high resolution studies [2,3]. This was unsuccessful, as neighbouring peaks simply collapsed into each other, indicating that so many peaks could not be maintained by the spectrum envelop.

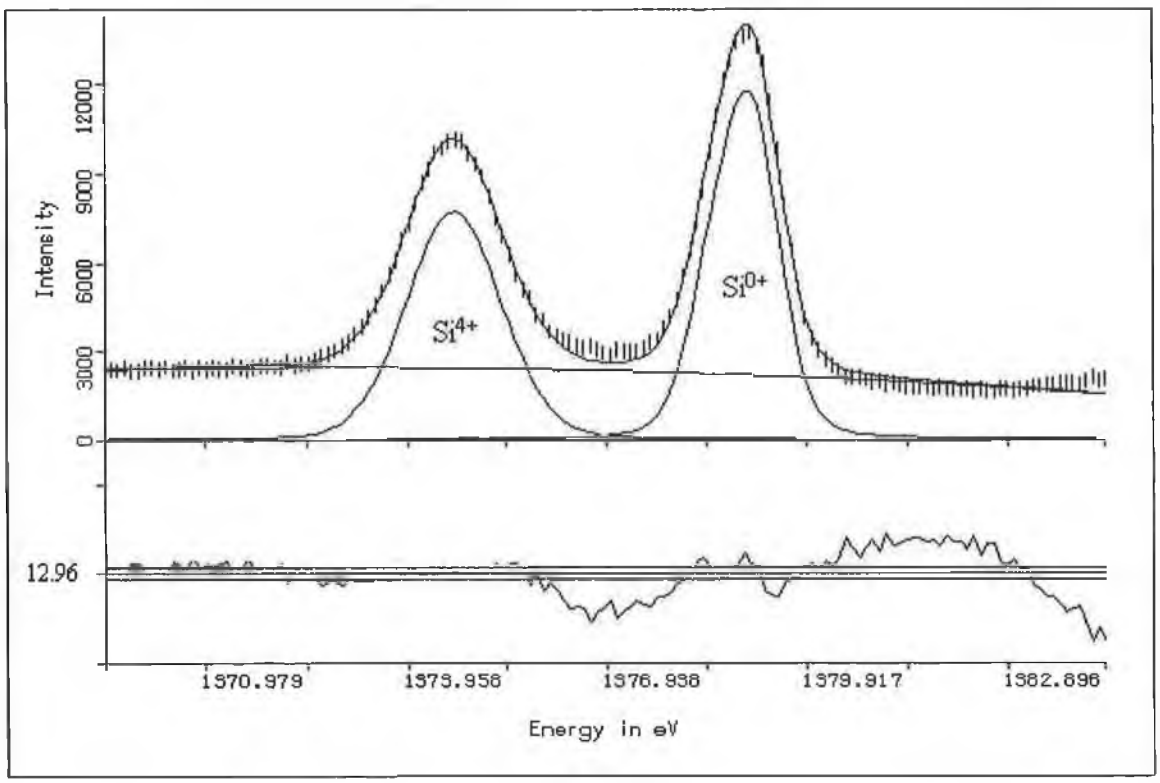

Figure 3.1: A fit to the Si_{2p} spectrum of a 3.2 nm SiO_2 oxide with just a substrate Si^{0+} and oxide Si^{4+} peak. The "goodness" of the fit is conveyed by the residue as shown in the lower panel. Intermediary oxidation states if present would exist in the trough between the Si^{0+} and Si^{4+}. The fit is poor in this region using just two peaks possibly due to the presence of intermediate oxidation states.

	Si^{4+}	Si^{x1+}	Si^{x2+}	Si^{0+}
$E_k - E_k[Si^{0+}]$eV	3.2	--	--	0
FWHM	1.5	--	--	0.89

Table 3.1: Si_{2p} fit parameters for figure 3.1

Next the spectrum was fitted using two suboxide peaks with one adjacent to the substrate and one to the oxide, the expectation being that these peaks could follow the emergence of the suboxide peaks adjacent to the main peaks, given that the main peak parameters were held to the reference values. When fitted with just two suboxide peaks as well as a Si^{4+} oxide and a Si^{0+} substrate peak an excellent fit was obtained as seen in figure 3.2. The fit parameters are summarized in table 3.2.

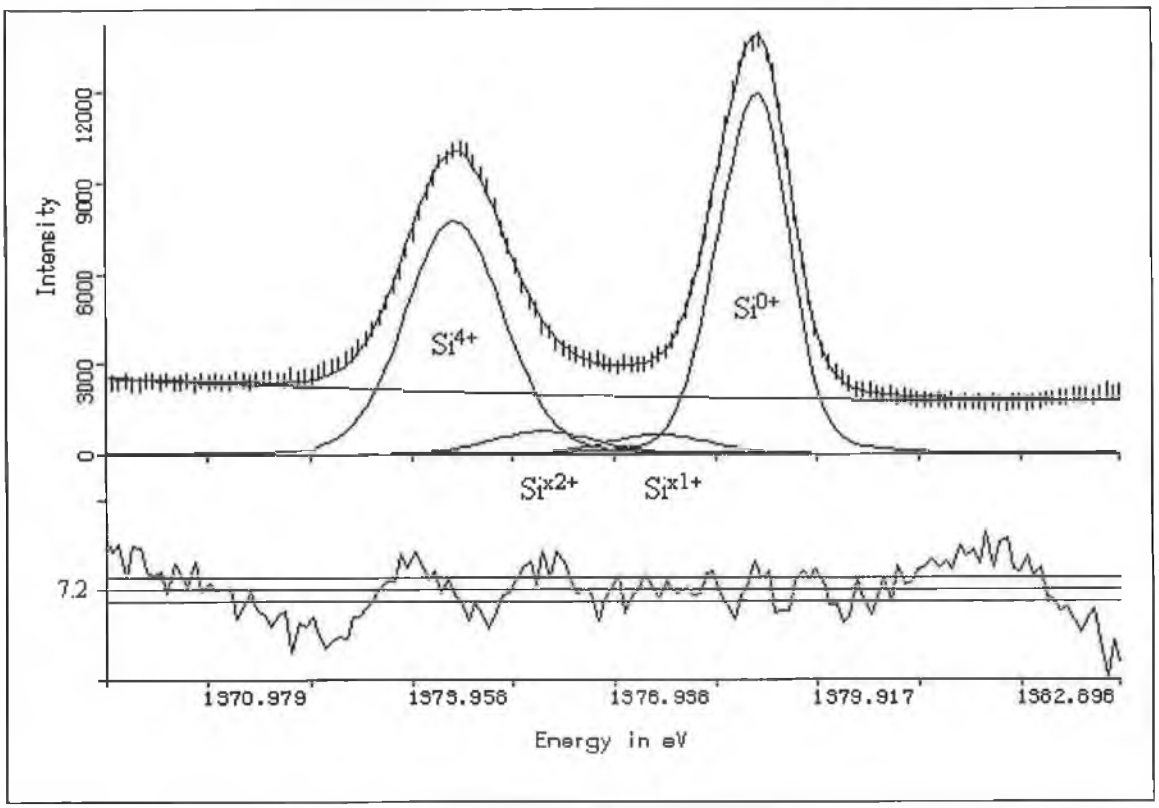

Figure 3.2: A fit to the Si_{2p} spectrum of a 3.2 nm SiO_2 oxide with two suboxide peaks. The agreement between data and fit is good across entire spectrum.

However, in the fit the kinetic energy position of the intermediary peaks was held constant. On allowing the energy positions of the peaks to vary, a different fit was obtained as seen in figure 3.3 whose fit parameters are summarised in table 3.3.

	Si^{4+}	Si^{x1+}	Si^{x2+}	Si^{0+}
E_k–$E_k[Si^{0+}]$eV	3.2	2.5	1.8	0
FWHM	1.5	1.2	1.2	0.89

Table 3.2: Si_{2p} fit parameters for figure 3.2

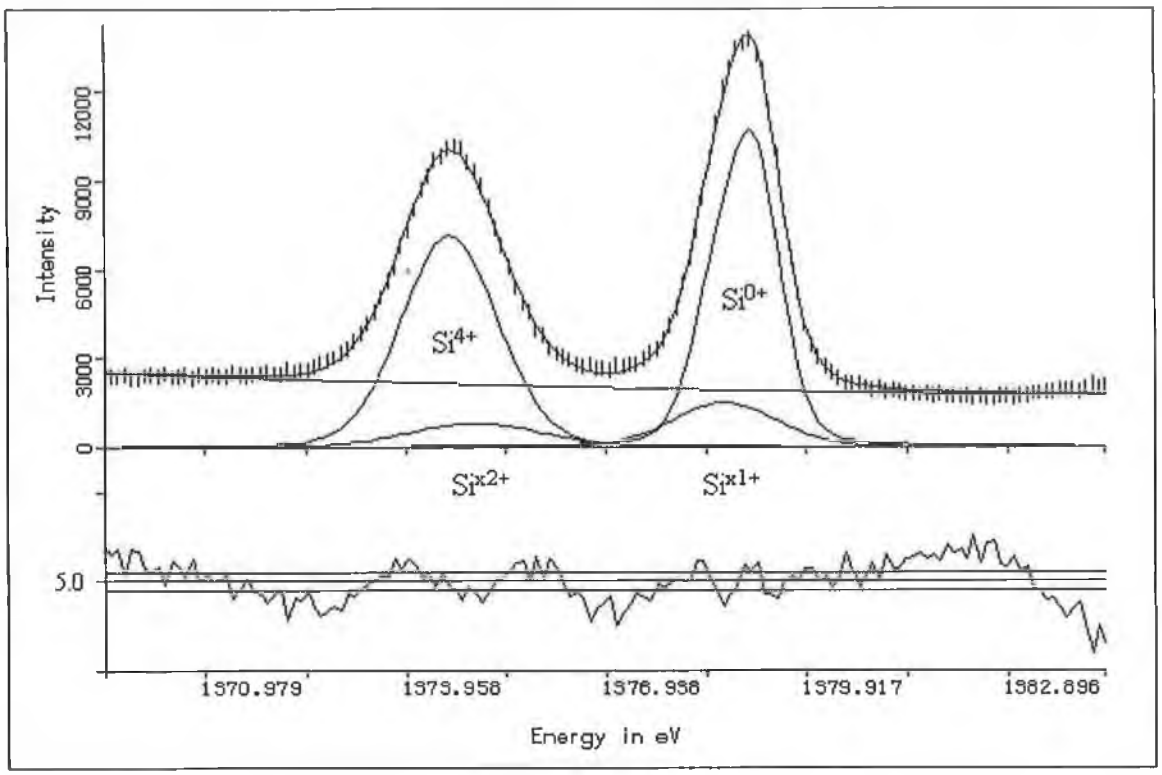

Figure 3.3: Due to the finite resolution of XPS on allowing the suboxide peak energy positions to vary, the suboxide peaks tend to "sit" underneath the larger adjacent peaks.

	Si^{4+}	Si^{xI+}	Si^{x2+}	Si^{0+}
E_k–$E_k[Si^{0+}]$eV	3.2	2.5	1.8	0
FWHM	1.5	1.2	1.2	0.89

Table 3.3: Si_{2p} fit parameters for figure 3.3.

The suboxide peaks are not well defined in the spectrum because they sit under the broad envelope of the larger oxide and substrate peaks, which is an unreasonable result.

The oxide layers are insulating and so the measured kinetic energy of the peaks shift as the samples charge positively at the surface. The chemical shift of the Si^{4+} oxide peak from the Si^{0+} substrate is known to be thickness dependent for ultra thin films (d<3 nm) [1]. Therefore, without being able to hold peak energy positions constant and because of the lack of structure in the Si_{2p} spectrum, the suboxide peaks tended to "sit underneath" the adjacent oxide and substrate peaks motivated by the fitting process to reduce the chi-squared value of the fit. From fitting the data it is apparent that the lack of structure in the Si_{2p} spectral envelope is due to the relatively poor resolution of a conventional XPS source (~1 eV) and will result in the larger Si^{4+} oxide and Si^{0+} substrate peaks "displacing" or overlapping their smaller neighbouring suboxide peaks.

Since the spectrum is a digital spectrum, which has been sampled with finite resolution, consideration has to be given to the extent of the spatial structure that can be inferred. In order to the resolve the Si^{3+} or Si^{1+} states which lie close to the oxide and substrate peaks respectively a monochromated XPS source or a synchrotron source would be required. Lu et al [2,3] have profiled thin SiO_2 films using dilute HF acid and using monochromated Alk_α X-rays (see figure 3.4(a)) and soft synchrotron radiation, see

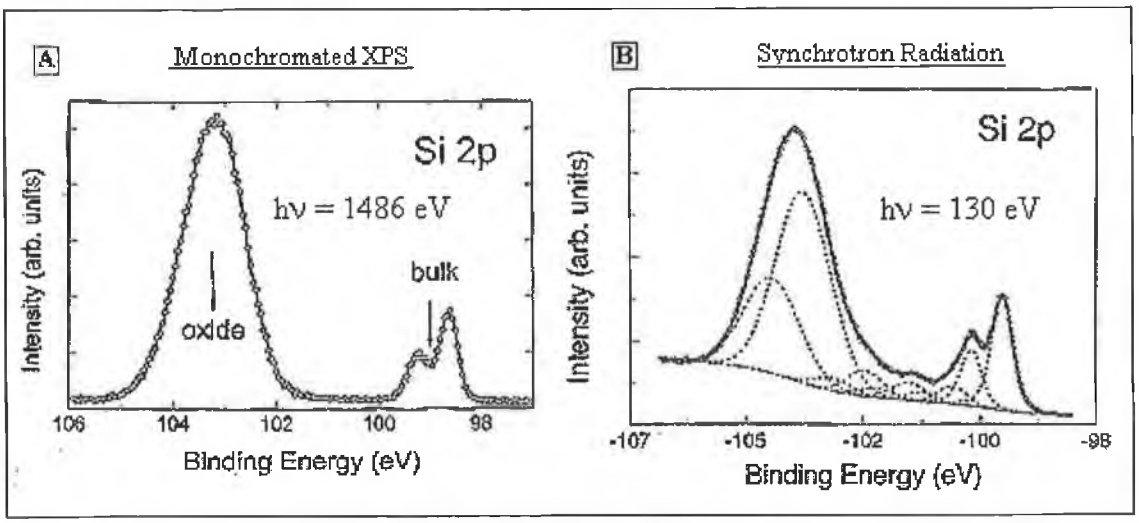

Figure 3.4: The superior resolution of a (b) (Lu [2]) synchrotron radiation source even compared to a (a) (Lu [3]) monochromated XPS system is evident from the resolution of the intermediate oxidation states.

figure 3.4(b) and have succeeded in de-convolving the Si_{2p} spectra into the constituent oxidation states. In figure 3.4(a), the oxide thickness is 6.4 nm thick. The oxide thickness is not reported for the spectrum in figure 3.4(b) but considering the photon energy is 130 eV the thickness is estimated to be between 0.9 and 0.14 nm. The difficulties of de-convoluting the interfacial signal from the oxide has meant that in most XPS studies no attempt has been made to de-convolute the interfacial signal from the oxide. Rather, the emphasis has been on film thickness [2],[4], stoichiometry [5,6] and elemental composition.

The ultimate goal of quantitatively assessing the interface it seems is a " bridge too far " which cannot be spanned with the degree of surface sensitivity and resolution capabilities of a conventional XPS source. However, motivated by the high quality of the dielectric, a qualitative interpretation of the interface was pursued in this thesis by allowing the FWHM of the oxide and substrate to vary freely and fitting a single suboxide peak with a fixed FWHM of 1.7 eV, which was allowed to vary in position. The objective of the study was to give indication of the emergence of the interface states by conveying approximately the energy position of the suboxides and any changes in the FWHM of the silicon in the substrate or in the bulk oxide layer.

No suboxide peak could be fitted in the as-received spectra. Even for the thinnest oxide (5.5 nm), no interfacial suboxide peak could be detected which was attributed to the fact that the small interfacial signal was being attenuated by the overlying oxide. It was necessary therefore to thin the oxide in order to determine whether interfacial sub oxides could be detected. As mentioned previously, two approaches were used to remove the bulk of the overlying oxide layer, argon bombardment and weak HF acid etching.

3.3 Ar ion Bombardment

Due to their full outer shells and large atomic number argon atoms are inert and relatively heavy (Z=18). When ionised in an electron discharge they can be accelerated under the influence of an applied electric field and crashed into a sample surface thus removing some of the outer surface atoms. For sample cleaning purposes this is useful

because all the samples have been exposed to the laboratory atmosphere and suffer from hydrocarbon contamination, which attenuates the signal from the oxide, this is especially problematic in off angle studies. When depth profiling there is a need to consider the effects of the removal process on the underlying region revealed. In SiO_2 the incident argon ions become embedded in the oxide matrix. In fact for long bombard times an Ar peak could be detected in the survey scans. While SiO_2 is amorphous and posses no long range order the short range tetrahedral bonding is well defined with a Si-O-Si bond angle of 109°. The effects of bombardment are of concern because of possible damage to the outer surface due to the collision cascade through the SiO_2 matrix, which is initiated by the delivery of the ion's momentum to the sample. Much work has been carried out to investigate the post bombardment effects of ion type and energy on thin silicon oxides. Hoffman and Thomass [7] found that bombardment with He^+ to be the most damaging due to the large ion penetration depth. Bombardment with Ne^+ and Ar^+ were the most efficient due to their high sputter yield. They reported that low energy bombardment was damaging with the SiO_2 surface reduced to elemental Si from direct ion knock-on processes and preferentially sputtering of oxygen [8] for ion voltages below and equal to 2 keV. Also, an increase of oxide FWHM was evident and attributed to a random distortion of the Si-O-Si bond angle in the bulk oxide. Hoffman's

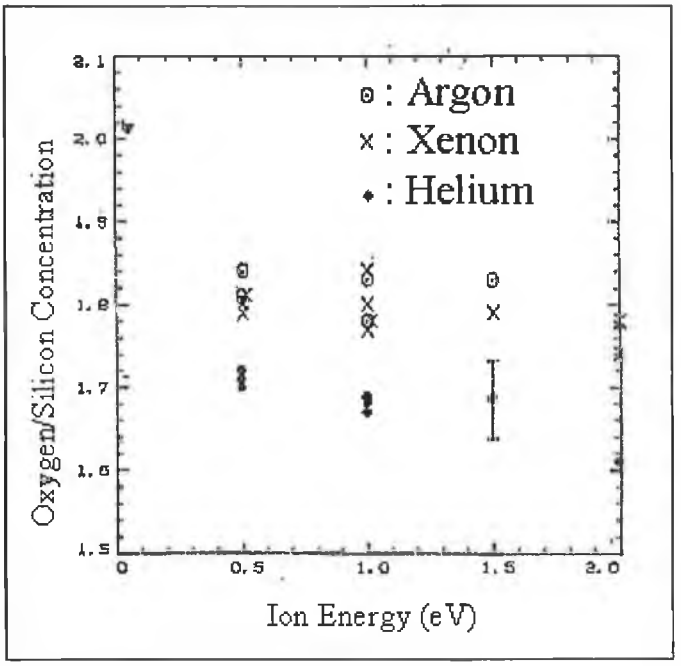

Figure 3.5: Dependence of film stoichiometry on bombardment ion energy for He^+, Ar^+, and Xe^+ (Hoffman [7]).

thickness estimate of the reduced silicon region was 0.4 nm and so he reasoned that he couldn't detect elemental Si associated with it given the large sampling depth of XPS. Instead, he carefully monitored the film stoichiometry (see figure 3.5) having corrected for carbon contamination and attributed the sub-stoichiometric values to an outer layer where oxygen had been preferentially sputtered leaving a silicon rich elemental region.

Other workers have also reported that the surface of a bombarded SiO_2 film contained reduced silicon oxides [9],[11]. However, there is disagreement about the effects of bombardment, with a recent study by Benkherourou and Deville [11] using both He and Ar ions showing no indication of surface reduction as evidenced by a constant Si:O stoichiometry and O_{1s} to Si_{2p} energy difference. Surprisingly they found that the O_{1s} and Si_{2p} peak FWHMs were also unchanged, indicating that no damage to the Si-O-Si bond angle was introduced. Paparazzo [12-13] et al have undertaken extensive studies of the effects of ion bombardment on SiO_2. However, before considering their findings it is useful to consider the results of a round robin study lead by Hashimoto et al [14] who classified oxides by the change in chemical state caused by sputtering using two parameters: the change in free formation enthalpy (arising from thermal reduction of oxides) and the ionicity.

Enthalpy:

Is a state function in thermodynamics and is defined as the heat absorbed by a system at constant pressure. The oxidation of silicon, which is performed at constant pressure and temperature, is exothermic (the system surrenders heat to it's surroundings) and thus results in a negative enthalpy change. The enthalpy change of formation is a measure of the stability of a compound formed from its reactants. For example a piece of wood when burned gives off heat, the final state, carbon is much more stable than the original wood state, the enthalpy change is negative.

If the oxidation process is viewed as one where the SiO_2 system is highly perturbed and the enthalpy of reactants (Si and O) is compared to that of the product (SiO_2). Which is more stable? What will the system do? From a physics perceptive one expects the system to tend to a minimum energy, but from a thermodynamics perspective consideration must be given to entropy (a measure of the disorder of the system).

Energy:

A ball rolls down a hill until it's potential energy reaches a minimum at the bottom. For reactions at constant pressure (i.e. where the system does no work) the change in energy (internal energy) equals the change in enthalpy. So just like the ball, in exothermic reactions the system losses heat until the total enthalpy reaches a minimum.

Entropy:

The spontaneous mixing of two different separated gases at the same pressure can occur without a change in energy but results in a more random dispersal of the total energy, or an increase the disorder. In an endothermic reaction the system can gain energy and still proceed spontaneously, here the entropy dominates.

Both enthalpy and entropy terms are balanced in the Gibbs equation:

$$\Delta G = \Delta H - T\Delta S \qquad \textbf{Equation 3.0}$$

ΔG Is the free energy change of a reaction system

ΔH Is the enthalpy change

ΔS Is the change in entropy

T Is temperature

Hashimoto's perceptive is unconventional, as ordinarily the stability of formation of a compound from it constituents is considered. Water formation for example results in a negative enthalpy as the final state is more stable than the initial.

$$2H_2(\text{gas}) + O_2(\text{gas}) \rightarrow 2H_2O(\text{liquid})$$

If considered in reverse then the enthalpy change would be positive in order to convey the same result. Hashimoto is not considering oxidation but rather reduction. Also, the use of thermal reduction is misleading as he is referring to the "thermal vibration " or perturbation arising from the bombardment process. This explains the signs of the enthalpy changes suggested by him below in classifying oxides in terms of whether or not they will be reduced when bombarded in terms of their ionicity and enthalpy change.

Ionicity>0.5 and ΔH_a>0	The oxide doesn't change.
Ionicity<0.5 and ΔH_a>0	The oxide is damaged but not reduced.
ΔH_a<0	The oxide was reduced and new components appear.

Since temperature is always positive on the absolute scale, when a reaction occurs at constant temperature and pressure the free energy of the system decreases. Hashimoto is effectively saying that SiO_2 is unlikely to disassociate into suboxides when highly excited as that would correspond to an increase in Gibbs energy (equation 3.0). Other oxides like TaO_5 or TiO_2 for example whose free formation enthalpy change is negative are reduced during bombardment as the constituent parts state is more stable than the final oxide.

The role of ionicity is seen given that the effects of bombardment for low energy (E<3 keV) ions is to disrupt the solid to a depth of around 10 nm below the surface [15]. The local vibration of atoms can displace them from their mean positions. For oxides with a large ionicity the disturbed atoms can recover their original positions due to the long-range coulomb interaction of the recoiled atoms, where as for oxides with low ionicity the atoms may stabilize at positions different from their original ones and such oxides are damaged.

SiO_2 has a positive enthalpy change and an ionicity below 0.5 and so from Hashimoto's perspective a reduction of the surface is not expected, but lattice damage via Si-O-Si bond angle randomisations resulting in a peak FWHM increase is reasonable.

Hashimoto's approach is simple and useful but fails to anticipate an outer reduced oxide region in SiO_2. Speculatively, the reason may exist in the deliverance of the ion energy to the outer surface. In laser ablations experiments where intense energy is delivered in short pulses to the outer region where the energy absorbed cannot be conducted away quickly enough and so the outer surface exists in a highly excited state and is ablated. Analogously it is possible that the outer region of the oxide absorbs the impact of the incident ions, the impulse imparted is felt locally to the extent that a surface localised "damage region" exist where oxygen is preferentially sputtered. The "shock" of the incident ion flux is transmitted below this region and it is here that Hashimoto's

formalism is valid with a displaced oxygen being recovered and the collision cascade initiated at the surface effecting only the peak FWHM. It is interesting to consider, how thick the damage zone is. Is it on the order of the ion penetration depth? Does it depend on the ion energy? Can it be detect with XPS?

At high accelerating voltages (~5 keV) Paparazzo et al [12] have considered the evolution of the silicon and oxygen Auger parameters α^* which are defined as:

$$\alpha^*\mathrm{Si} = \mathrm{E_k}(\mathrm{SiKLL}) + \mathrm{E_b}(\mathrm{Si2p})$$

$$\alpha^*\mathrm{O} = \mathrm{E_k}(\mathrm{OKVV}) + \mathrm{E_b}(\mathrm{O1s})$$

where E_k(Si KLL) and E_k(O KVV) are the kinetic energies of the silicon and oxygen induced Auger transitions respectively, E_b(Si 2p) and E_b(O 1s) are the silicon 2p and oxygen 1s binding energies respectively. (Note: Conventionally the difference between Ek and Eb is considered but here the sum is used in order to always obtain positive values [16]). Investigating the effect of ion energy on the chemical state of the SiO_2 films Paparazzo et al [12] found that for energies above 5 keV the surface is reduced with the introduction new surface SiO_x components in the Auger parameters. These were due to the loss of surface oxygen and the subsequent Si-Si recombination of truncated Si-O bonds. The merits of the SiLVV spectra in detecting these new artefacts arises from it's ability to follow differences between Si-Si and Si-O bonding states as this auger peak involves transitions (to both continuum and discrete states) of valence electrons.

For ion energies in the range 1 to 2.5 keV Paparazzo found virtually no evidence of damage using the XPS Si_{2p} and SiKLL peaks. But for the same bombardment conditions, damage was detected in surface sensitive synchrotron radiation studies [16], leading Paparazzo to the conclude that SiO_x damage is detectable only when the attenuation length of the probing photoelectron is comparable to the damage depth which in turn is related to the ion energy and mass. This is a reasonable result when one considers that a 0.4 to 0.8 nm damage region (for 2 keV ions) is negligible in thickness compared to the 7-10 nm sampling depth typically found in XPS (E_k>1380 eV), but comparable to the 1 nm sampling depth of 130 eV synchrotron radiation (E_k~30 eV).

Paparazzo further concluded that the FWHM increase arises from a random re-ordering of the Si-O-Si bond angle and bombardment induced surface roughening.

The effect of bombardment time (for 2 keV ions) on peak FWHM observed by Paparazzo is shown in figure 3.6. He reported that both O1s and O KVV peak FWHM behaved in the same way as the Si^{4+} oxide and $SiKL_{23}L_{23}$.

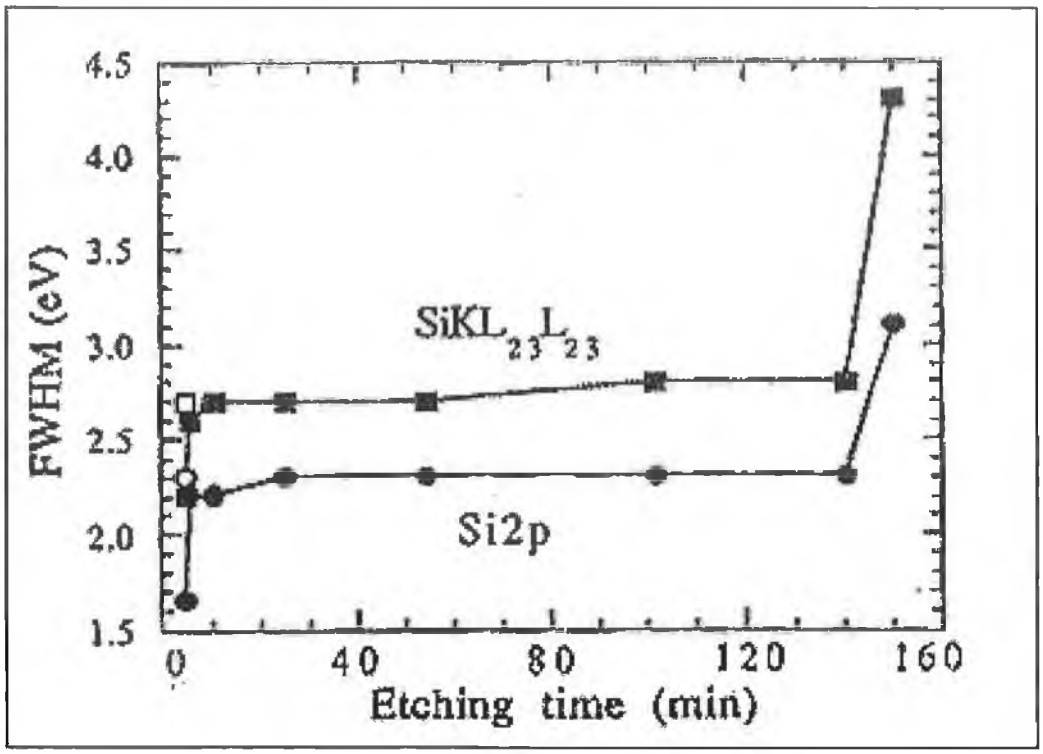

Figure 3.6: FWHM values of Si_{2p} and X-ray induced Si $KL_{23}L_{23}$ signals of the oxidised components of silicon in the SiO_2/Si system as a function of the 2 keV Ar^+ etch time. (Paparazzo [12])

Figure 3.7 shows the evolution of both the Si_{2p} and O_{1s} spectra of a 13.4 nm SiO_2 oxide after successive bombardments at 2 keV. Shown are the fitted peaks without the raw data or experimental fit, with background removed and charge referenced to the $Si_{2p}{}^{0+}$ substrate peak at 99.3 eV.

Note: The omission of raw and fitted data in figure 3.7 is unconventional. The presence of both ordinarily allows one to assess the "goodness" of the fit. However, the aim was to show the evolution of peak position and FWHM with thickness, which is best done with all spectra plotted in the same window. With the kinetic energy of the suboxide

peak free to vary the agreement between raw and fitted data was good and so the approach was thought to be justified.

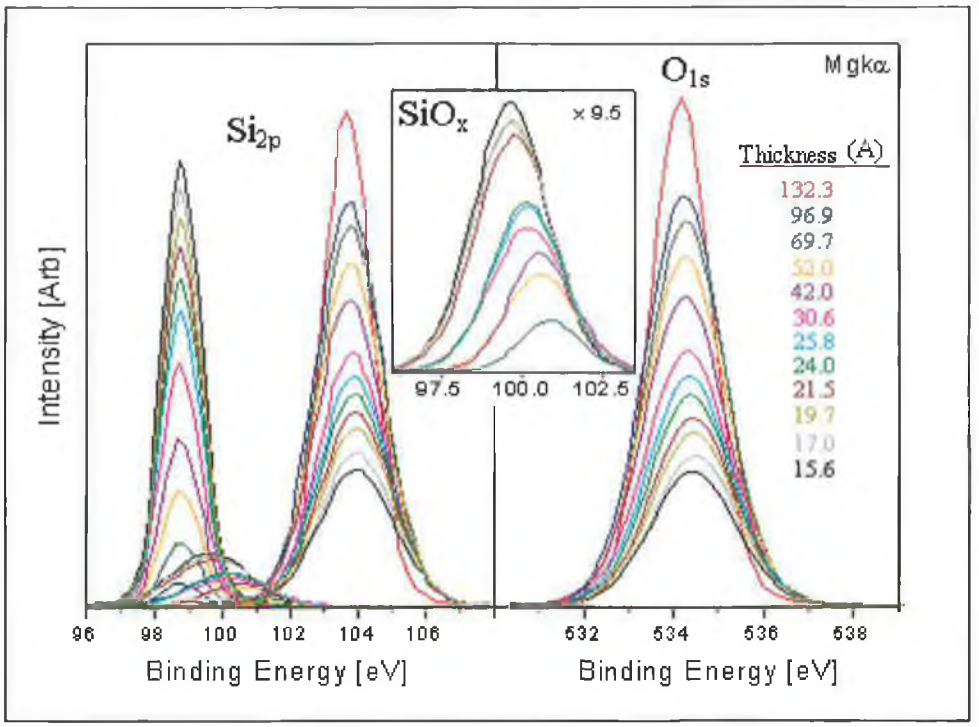

Figure 3.7: (left) Si^{0+},SiO_x, Si^{4+} peaks fitted to Si_{2p} spectra (not shown) for 2keV Ar^+ bombard times leading to the thicknesses shown in (A). (right) the corresponding O_{1s} peaks. Inset shows a magnified view of the SiO_x peak.

Figure 3.8 shows the plot of peak FWHM with bombard time. The plot shows that both the Si^{4+} oxide and the oxygen peak FWHM broaden and show the same behaviour of, initial rise followed by plateau region as reported by Paparazzo et al. However, it is also apparent from figure 3.8 that the substrate peak FWHM is also increasing. The significance of the substrate broadened FWHM value is that this broadening becomes apparent at thickness, which are far larger than the ion penetration depth and the values are larger than the substrate FWHM values of as-received oxides of similar thickness. These results can only be reconciled by the existence of a reduced outer region. In his study Paparazzo did not report the behaviour of the substrate peak, as his sample was 150 nm thick and so it's unlikely he ever profiled thin enough to illuminate the substrate. In the 20 nm oxide an elemental silicon signal associated with surface reduction was not detected after initial bombardments.

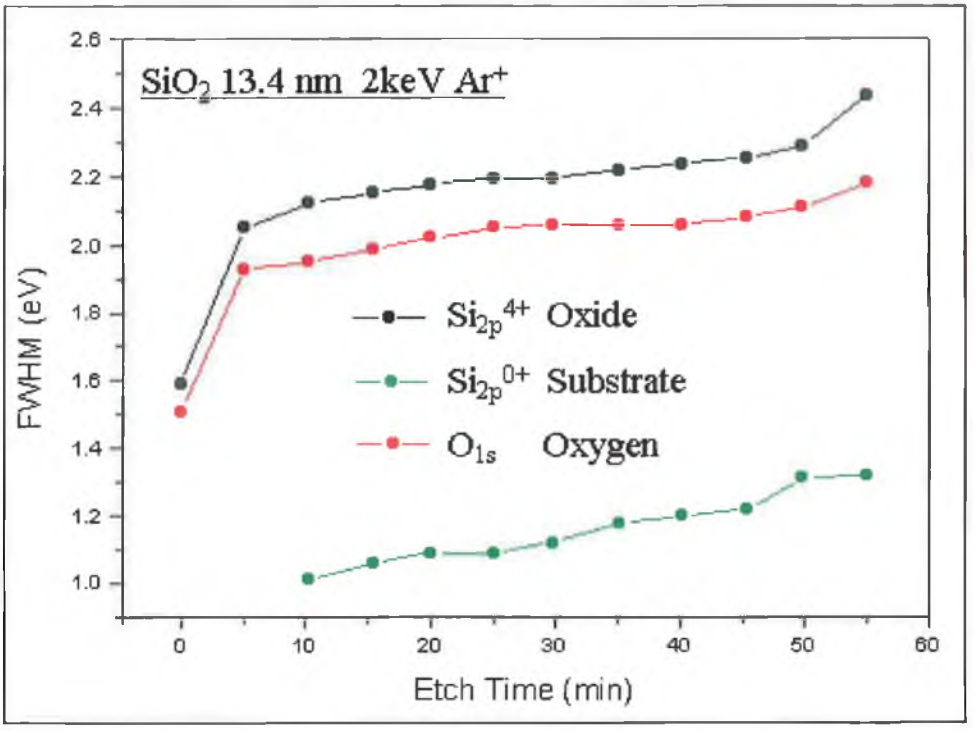

Figure 3.8: Plot of Si_{2p}^{0+},Si_{2p}^{4+} and O_{1s} peak FWHM with bombard time. The FWHM behaviour is similar to that of figure 3.6. The increase in the Si^{0+} FWHM is unexpected however, and may arise for surface species.

If Paparazzo's argument in relation to the extent of the damage region being much smaller than the sampling depth is accepted then this finding is not unreasonable. Its interesting to consider if the substrate FWHM when detected after the overlying oxide has been bombarded to a thickness comparable to the sampling depth, can reveal the presence of the thin reduced damage region through the increased contribution to the substrate peak FWHM from the reduced region. Table 3.4 summarizes the peak parameters obtained in bombarding the 13.4 nm oxide.

Ar bombardment of 13.4 nm SiO_2 film											
Etch	Thick	FWHM (eV)			Quantification				Peak E_k separation		
(min)	(nm)	Si^{4+}	Si^{0+}	O	Stio	%Si	$\%Si_{ox}$	%O	$4^+ - 0^+$	$_{ox}{}^+ - {}_0{}^+$	$O-0^+$
0	132.3	1.59	--	1.51	2.02	9.97	0	90.02	--	--	430.7
5	96.9	2.05	--	1.93	1.94	10.31	0	89.68	4.94	--	430.7
10	69.7	2.12	1.01	1.95	1.94	10.31	0.24	89.44	4.97	2.08	430.7
15	52.0	2.15	1.06	1.99	1.96	10.19	0.49	89.31	4.96	1.82	430.7
20	42.0	2.17	1.09	2.02	1.95	10.18	0.70	89.10	4.95	1.83	430.7
25	30.6	2.19	1.09	2.05	1.98	10.04	0.80	89.14	5.01	1.74	430.7
30	25.8	2.19	1.12	2.06	1.94	10.23	0.90	88.86	5.06	1.63	430.7
35	24.0	2.21	1.18	2.06	1.89	10.46	1.07	88.45	5.08	1.62	430.7
40	21.5	2.23	1.2	2.06	1.83	10.72	1.50	87.77	5.13	1.53	430.7
45	19.7	2.25	1.22	2.08	1.83	10.70	1.76	87.53	5.15	1.5	430.7
50	17.0	2.28	1.31	2.11	1.80	10.83	1.91	87.25	5.15	1.55	430.7
55	15.6	2.44	1.32	2.18	1.76	11.00	2.29	86.69	5.15	1.44	430.7

Table 3.4: Evolution of FWHM, stoichiometry and peak positions for Ar^+ of 13.4 nm SiO_2

3.3.4 Discussion of results

Argon bombardment has allowed a depth profile of the oxide layer to be realised. The bombarding process itself is damaging to the oxide as evidenced by the FWHM increase in the Si_{2p} and O1s peaks and a reduced surface region. The detection of a FWHM increase of the Si^{0+} substrate peak for thickness far larger than the substrate signal depth suggests the increase is associated with a reduced outer surface region. Thick (20 and 13.4 nm) films bombarded to thickness greater than the thinnest (5.5 nm) oxide (in which no suboxide was detected and was stoichiometric) were found to be non-stoichiometric and incorporated suboxides. The need to fit an intermediary suboxide peak was more pronounced when bombarded samples were analysed at high take off angles suggesting the damage region was surface localised. Interestingly the O_{1s} to Si_{2p} oxide kinetic energy separation (429.6 eV) who's constant value is used for charge correction and which deviation from is interpreted as a chemical shift was invariant to bombardment induced chemical state changes.

We obtained a larger value of (430.7 eV), and the oxide Si^{4+} peak to substrate Si^{0+} peak energy separation increased with bombardment time. In attempting to limit the peak parameters it was acknowledged that the peak parameters were evolving legitimately. In other words after each bombardment a different film was being "illuminated", in the sense that it has been damaged to a different extent and to a new depth. There was no prior knowledge of how it should behave "exactly" and so it was allowed to "speak freely" by leaving it's parameters unconstrained.

The suboxide peak chemical shift (relative to the silicon substrate Si^{0+}) and intensity behaviour was the same for samples where the substrate could and could not be detected. It displayed an initial shift of approximately 2.1 eV from the Si^{0+} peak and moved progressively closer to the substrate as the oxide was thinned.

As a means to better illuminate the interface by removing the bulk of the overlying oxide, argon ion bombardment appears to have too many drawbacks. Having to "look through" a damaged oxide and surface suboxides, it is very difficult to distinguish between interfacial and surface suboxides in an unambiguous way. In this thesis, the detection and inferrel of a reduced surface region is uncertain, and questioned by the more extensive work of Paparazzo et al. Nonetheless ours was not the pursuit of ion bombardment induced effects on SiO_2 but rather the suitability of bombardment as a profile mechanism, to this end it's unfeasibility has been ascertained because the introduction of suboxides by the bombardment process makes it impossible to determine which signal originates from suboxide species present prior to bombardment.

3.4 SiO_2 Chemical depth profile using weak HF etching

Depth profiles of the 5.5 nm SiO_2 oxide were realised by immersion for successively longer times in dilute (0.5%) HF acid. At this HF concentration an average etch rate of 1.9 nm per minute was obtained. No surface pre-treatment was performed; the samples were immersed as-received. The etch was terminated by the addition of a large quantity of deionised water to the etching solution. Prior to the sample introduction into the XPS instrument, the sample was blown dry with nitrogen and inserted into the vacuum system load lock as quickly as possible.

In this way the etched surface was exposed to the laboratory atmosphere only for the time taken to dry and insert it, which is less than 10 min. Every effort was made to achieve reproducibility and consistency in the etching procedure so as to minimise sample differences arising from differences in etch time, rinse time or involuntary contamination. Figure 3.9 shows the Si_{2p} spectrum of 5.5 nm SiO_2 films etched for 2.0 mins in 0.5% HF solution.

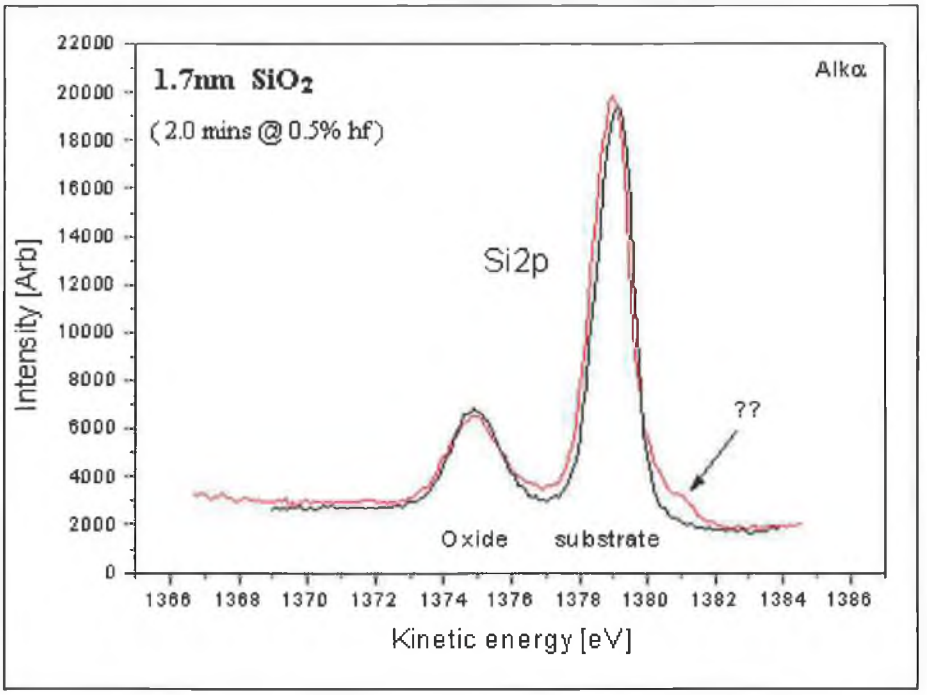

Figure 3.9: An unknown contribution to the Si_{2p} spectrum of an etched oxide due to surface contamination, shown in red. An identical sample without contamination is shown in black.

One sample was contaminated by falling onto its face and is represented by the red spectrum. Shown in black is the spectrum of an un-contaminated oxide etched for the same time. In figure 3.9 the reproducibility of the oxide and substrate peak intensities is extremely good. However, an additional feature is evident on the high kinetic energy side of the substrate peak, which cannot be identified and indicates the precautions, which must be followed in sample handling.

3.4.1 Quantification concerns

A key parameter in a SiO_2 film depth profile is the ratio of the Si^{4+} oxide to oxygen peak intensity as it reflects the stoichiometric composition of the layer. While this ratio doesn't show the oxide stoichiometry directly, because there is the need to correct for sensitivity factors. But these factors are constant values. The point is that the absolute stoichiometry value is not important but rather its evolution with depth; this evolution is enshrined in the oxygen to oxide ratio. For sample thickness less than 5.5 nm, the film stoichiometry was consistently seen to increase above a value of 2.0 as the layer was thinned. The extent of the increase was less pronounced for the Ar bombarded samples. It is most likely that the films are in fact stoichiometric (O/Si=2.0) and tend to a sub-stoichiometric (O/Si<2.0) value as expected at low oxide thickness but the combined effects of; "freedom" of peak FWHM, increased influence of surface contamination and interfacial suboxide regions "conspire" to undermine the reliability of the quantification analysis at small oxide thickness.

Quantitative analysis is concerned with the concentration of different elements in the sample. The sample is assumed to be homogeneous with each element uniformly distributed with depth. Shallenberger et al [20] as discussed below addresses the special quantification difficulties in oxides arising from a non-uniform nitrogen distribution with its surface signal exaggerated and interfacial signal underestimated. He points out the role of surface hydrocarbon in attenuating the underlying oxide and substrate signal. For both silicon dioxide and oxynitride films, surface contamination, although thin, forms a larger fraction of the overall film thickness as the film is thinned. So does the interfacial suboxide region who's signal is more pronounced as the attenuating overlying oxide is thinned. Also in the context of Grunthaner's [21] work we are mindful of the possibility of a strained stoichiometric SiO_2 region sandwiched between the suboxide region and the bulk oxide, its presence would become more significant with thinning.

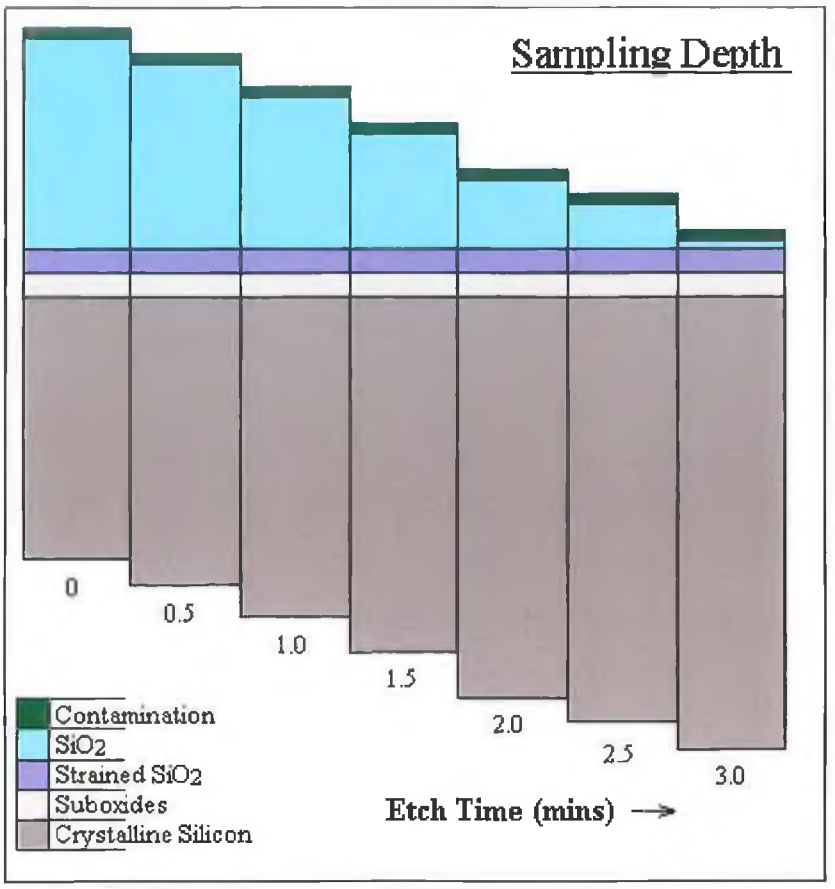

Figure 3.10: A simplified representation of the regions illuminated by the sampling depth (3λ), as the oxide is wet chemically profiled.

Figure 3.10 is a pictorial representation of the regions illuminated by the sampling depth (~10 nm) as the 5.5 nm SiO_2 oxide is thinned in successively longer dilute HF wet chemical etches. In order to investigate the above quantification issues the 5.5 nm SiO_2 sample was etched for the same etch times as the SiON samples and examined at 0^o and 60^o degree take-off angles as shown in figure 3.11.

The upper panel shows the Si_{2p} spectra, the inset shows a magnified view of the suboxide peak. Normal emission data is shown on left and 60^o off angle data on the right. The lower panel shows the oxygen 1s spectra, the inset shows the carbon 1s peaks. Peak colours correspond to different etch times. The data has been charge corrected relative to the $Si_{2p3/2}$ substrate at 99.3 eV.

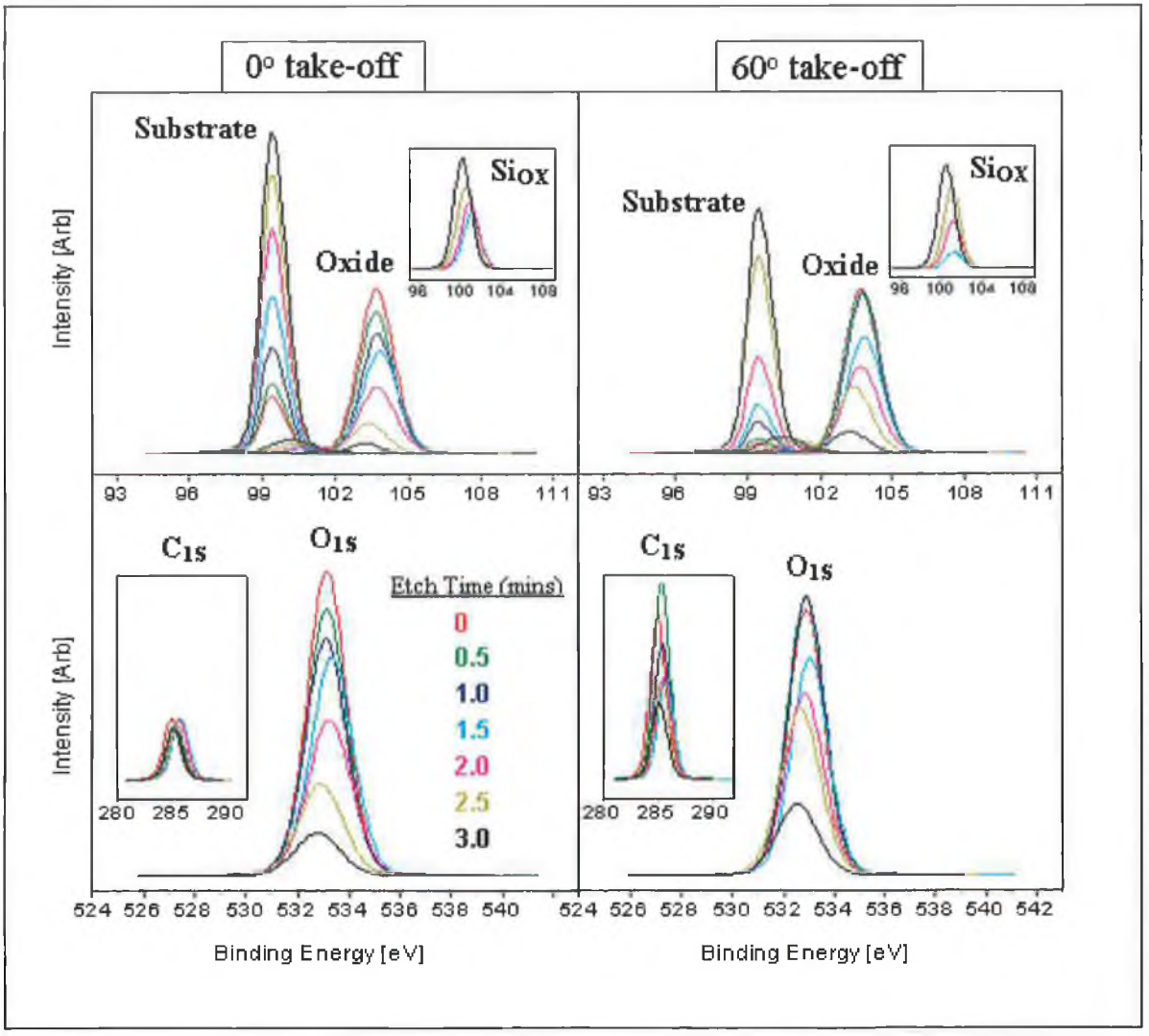

Figure 3.11: Evolution of Si_p, O_{1s} and C_{1s} peaks of a 5.5nm SiO_2 film with dilute wet chemical HF etch time at 0° and 60° take-off angle. The fitted peaks only are shown for clarity.

The 0° and 60° degree take off data are plotted on the same intensity scales and obtained from the same sample for each etch. Table 3.5 summarizes the peak parameters for the data at 0° take off angle. There are a number of key observations from figure 3.11 and table 3.5. A reduced absolute intensity is evident at a higher take-off angle in all spectra except for the carbon peak, which is enhanced. This is reasonable as the carbon signal originates from the outermost region (the contamination layer) whereas the other signals originate from underneath the contamination and so at grazing incidence the O_{1s} and Si_{2p} signals travel through a thicker effective contamination layer and are thus attenuated more while C_{1s} signal is enhanced.

Thick.	FWHM								
(A)	Oxide	Subs	Sox	O	Stio	%Si	%O	ΔE	O-Si
56.9	1.426	0.823	---	1.671	2.03	33	67	4.2	429.6
47.3	1.379	0.824	---	1.67	2.12	31.89	68.11	4.2	429.6
33.8	1.371	0.826	---	1.759	2.33	29.47	70.53	4.3	429.6
26.1	1.495	0.862	1.7	1.804	2.42	28.59	71.41	4.3	429.7
17.3	1.504	0.886	1.7	1.883	2.75	25.63	74.37	4.2	429.7
9.2	1.384	0.851	1.7	1.899	3.8	19.32	80.68	3.9	429.7
6.1	1.159	0.843	1.7	1.965	5.93	12.87	87.13	3.7	429.7

Table 3.5: Evolution of O_{1s} and Si_{2p} peak parameters of a 5.5 nm SiO_2 etched for 0 to 3.0 mins in 0.5% HF acid as shown in figure 3.11.

The Si^{4+} FWHM reduces initially and increases again when the suboxide peak is detected and finally falls again as the oxide coverage becomes so small that the peak becomes poorly defined. This initial fall in Si^{4+} FWHM was not observed in thicker oxide samples (20 nm and 13.4 nm SiO_2) when they were etched for the same lengths of time as the 5.5 nm oxide. Also, the suboxide peak does not overlap the oxide peak, and it is shown later that their intensities are unrelated. The fall in oxide FWHM could arise from the removal of the amorphous oxide and the uncovering of a more ordered (compressed) underlying oxide layer (which would still be stoichiometric) as envisioned by Grunthaner et al [21]. However, the same trend is present in the silicon substrate peak FWHM and here a relationship is apparent, as discussed later, between the substrate and suboxide signal where the final reduction in substrate FWHM is related to the overlap of the substrate peak with the suboxide peak.

A small increase in the Si^{4+} oxide peak chemical shift from the substrate peak is evident after etch times of 1.0 and 1.5 mins. The oxygen to oxide kinetic energy difference remained relatively constant removing the possibility of a chemical state change. Also in figure 3.11 the peak binding energy position of oxide and oxygen seem to be "locked together" with an initial rise and fall evident in both. Interestingly Grunthaner [21] resolved the Si_{2p}^{4+} and O1s peaks into two different structural states with one component associated with an inter-tetrahedral bond angle $\theta_{Si\text{-}O\text{-}Si}$ of 144^0 (bulk value) and the other with a reduced inter-tetrahedral bond angle $\theta_{Si\text{-}O\text{-}Si}$ of 120^0 (due to a region

of compressed SiO_2 above the SiO_x region). An assumption in this de-convolution is that the energy positions of these peaks in the Si^{4+} oxide and O_{1s} peak be mirror images of each other as the chemical shift is due to structural changes SICT not chemical.

The silicon-oxygen stoichiometry increases as the film is thinned; this is unexpected as the film is expected to be stoichiometric (Si:O 1:2) until the suboxide (SiO_x) region. The film stoichiometry is calculated using the oxide and oxygen peak areas. After all the Si^{4+} oxide peak is exclusively associated with silicon bonded to four oxygens, however, the oxygen peak has contributions from the contamination and suboxide layers which both constitute a larger fraction of the oxygen intensity with reduced oxide thickness. The problem is compounded as the oxide peak shifts closer to the substrate due to image charge effects from the substrate and becomes poorly defined as the oxide is thinned.

An increase in carbon and oxygen peak intensity is evident in figure 3.11 after the sample has been etched for 0.5 min (green peak) in the 60^o take-off angle spectra, yet the corresponding oxide and oxygen spectra in the normal angle spectra show the expected decrease with thickness. It is reasonable that many of the carbon bonds in the contamination layer are oxygen related and so a related oxygen peak intensity increase (which could not be de-convoluted during analysis) would adversely affect stoichiometry calculations. However, the corresponding 60^o off angle oxide intensity is also enhanced which makes the possible effect hard to calculate and shows ultimately that absolute peak intensities are not comparable.

For each sample every effort was made to reproduce the same sample size and position for each etch. Differences in position and size can shadow the incident X-ray flux resulting in a different area being illuminated. However, if the ratio of each peak intensity to that of the oxide is considered, the analysis is immune to these effects, and such ratios are comparable. The interpretation of such a ratio with etch time is straightforward; (especially when both peaks in the ratio reduce with thickness) if the oxide peak reduces by the same amount as the oxygen after each etch the ratio remains constant, an increase in ratio suggests an oxygen rich region, a decrease an oxygen depleted region. But as outlined earlier the stoichiometry value, which is based on such a ratio, becomes less reliable as the oxide is thinned because of the large fixed sampling depth and increased influence of the suboxide and contamination regions on the peaks.

Profiling the SiO_2 oxide has difficulties due to the above. It is worthwhile to obtain a better understanding of the origin and implications of these effects in SiO_2 because silicon oxynitride films present additional difficulties during profiling due to the presence of nitrogen (as is discussed later). Therefore, by comparison it maybe possible to isolate these additional effects by using the SiO_2 profile as a control.

It is likely that the poor behaviour of the data at reduced thicknesses comes in part, from the peak FWHM being allowed to vary freely. However, while such freedom is certainly worthwhile in order to let the data "speak freely", its interpretation has to be reconciled with our prior knowledge of the sample structure. To this end the data was interrogated by re-fitting the data and then considering the evolution of both individual peak intensity and peak intensity ratios, having held certain peak parameters fixed.

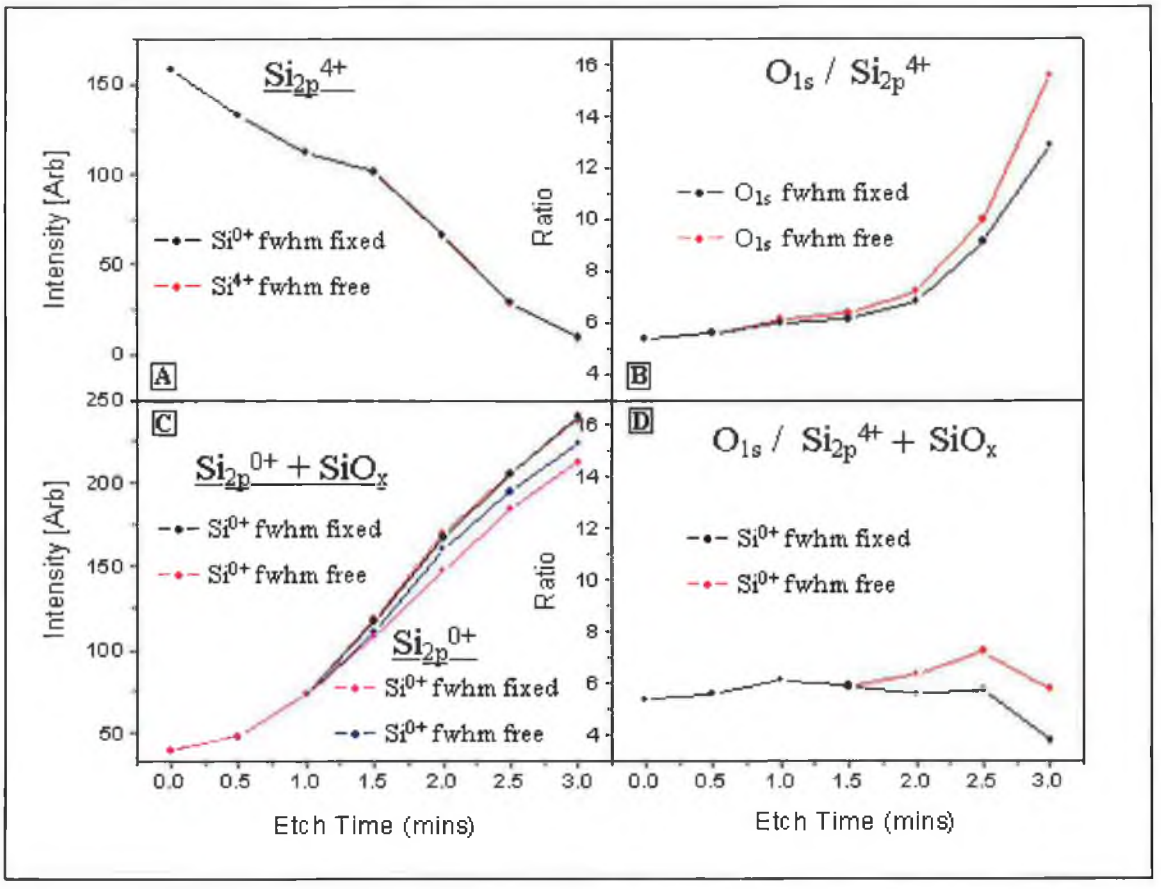

Figure 3.12: The effects of certain peak's FWHM being free and fixed on the intensity of other peaks was investigated for a) the effect of freedom Si^{0+} FWHM on Si^{4+} intensity. (b) The effect of freedom Si^{0+} FWHM on Si^{0+} intensity and close proximity of SiO_x peak. (c) The effect of freedom of O_{1s} FWHM on the O_{1s}/Si^{4+} intensity ratio. (d) The effect of SiO_x intensity on the O_{1s}/Si^{4+} intensity ratio.

In order to investigate the effect of the substrate peak FWHM being free on the oxide peak intensity during wet chemical profiling, the Si_{2p} spectra of figure 3.11 (for normal incidence) were refitted with the substrate peak FWHM free and fixed. Figure 3.12 (A) shows the Si^{4+} oxide intensity versus etch time with the silicon Si^{0+} substrate peak FWHM fixed (shown in black) and free (shown in red); both data sets lie on the same curve. The two data sets are very similar, suggesting the Si^{4+} oxide peak FWHM is not affected by the substrate, which is reasonable given the distance between the oxide and substrate peaks.

In order to investigate the change (if any) of the substrate Si^{0+} peak FWHM and the effect of the adjacent SiO_x suboxide peak on the substrate intensity figure 3.12 (C) shows the silicon Si^{0+} substrate intensity versus etch time with its FWHM free to vary (shown in Blue) and fixed (shown in pink). Initially both intensities are similar, but, for longer etch times the substrate intensity of the free FWHM data (Blue) grows relative to the intensity of the fixed FWHM data (shown in Pink). The tendency of the substrate peak FWHM to grow for long etch times may be arise from broadening of the substrate peak due to interfacial hydride bonds. To see how the substrate intensity is affected by the close proximity of the suboxide SiO_x peak intensity, the substrate intensity plus the suboxide intensity when the substrate FWHM is free (red) and fixed (black) respectively are also shown in figure 3.12(c). The divergence between the blue and pink for long etches and the relatively constant agreement between the red and black suggests that the SiO_x suboxide peak intensity grows when the substrate FWHM is fixed, only at the loss of the neighbouring Si^{0+} substrate intensity.

In order to investigate the impact of possible hydrocarbon contamination and suboxide signal contribution to the oxygen peak intensity figure 3.12 (B) shows the ratio of the O_{1s} oxygen peak intensity to Si^{4+} oxide peak intensity with the oxygen FWHM free (red) and fixed (black) respectively. In the black graph the oxygen FWHM to was held to its as-received value to try to limit the possible effect of any hydrocarbon contamination contribution to the peak at small oxide thickness. After all, the oxygen peak intensity has contributions from the contamination and suboxide layers which cannot be de-convolute from it. These contributions sustain the oxygen intensity while the oxide intensity dies. If the oxygen FWHM value is held to its as-received values

then it may be possible to "clip" their contribution from the peak. However, only a marginal decrease results.

In order to investigate the impact of the SiO_x suboxide peak intensity on the oxygen to oxide ratio figure 3.12(D) shows the ratio of the O_{1s} oxygen peak intensity to the sum of Si^{4+} oxide peak and the SiO_x suboxide peak intensity with the substrate FWHM free (red) and fixed (black) respectively. Note: both graphs on the right hand side are plotted using the same intensity scale. Comparison of the graphs shows the addition of the suboxide peak intensity to the oxide intensity has a dramatic effect on the ratio. Table 3.6 shows the atomic percentages of silicon and oxygen in the oxide calculated with both the substrate and oxygen FWHM fixed and with suboxide peak intensity added to the oxide.

Etch time (mins)			
	Stoichiometry	%Si	%O
0.0	2.10	32.22	67.77
0.5	2.19	31.31	68.68
1.0	2.36	29.74	70.25
1.5	2.22	30.98	69.01
2.0	2.06	32.61	67.38
2.5	2.09	32.34	67.65
3.0	1.32	42.98	57.01

Table 3.6: Evolution of Si and O atomic percentages with HF etch time.

3.4.2 Discussion of results

The data is now certainly much better behaved and in agreement with what would be expected. Whether the approach in terms of FWHM constraint and consideration of the suboxide intensity is reasonable is however, uncertain. It is clear that a fixed well-defined set of peak parameters cannot follow the evolution of the oxide as it is thinned as evidenced by the behaviour of peak FWHM, chemical shift and intensity. As for the

intimate relationship between suboxide and substrate intensity, it is reasonable to hold the FWHM of the substrate constant. The tendency of the substrate peak to displace the suboxide peak at the detriment of it's intensity is driven by the fitting program's desire for a good fit. We proceed on the bases that we are consistent in our quantification method for each sample and so the data constraints for the SiO_2 system are applied identically to the SiON system. Incidentally such restraints could not be applied to the bombarded SiO_2 system because here the silicon network is progressively damaged more and more for each bombard cycle and the FWHM is legitimately larger (and incalculably so) reflecting this damage as the Si-O-Si bond angle has been randomised resulting in peak broadening.

3.5 HF / Ar^+ bombard comparison

The above approach to quantification, formulated after analysis and re-analysis of experimental data is now more consistent and allows for more reasonable inter sample comparisons. In performing wet chemical depth profiles of the oxide layers it was possible to make direct comparison with the results from the argon bombarded samples in order to highlight differences in suboxide signal and to lend weight to our interpretation of the bombarded induced suboxide signal as been surface localised. These differences were further investigated by successively argon bombarding a 5.5 nm SiO_2 oxide to realise the same thickness as obtained by wet chemical etching. Figure 3.13 shows the wet chemical HF and argon bombardment profiles of a SiO_2 film. An ion current of 0.7 μA and an ion voltage of 2 keV realised an etch rate of 0.7 nm per minute. The average etch rate for 0.5% HF was 1.9 nm per minute. In each case a fresh sample was used. Tables 3.7 and 3.8 summarise the peak parameters.

Argon ion Bombardment											
Alkα	Relative Intensity					Alkα	FWHM				
Thic. (nm)	$Si_{2p3/2}$ I^{4+}	$Si_{2p3/2}$ I^{ox+}	$Si_{2p3/2}$ I^{0+}	% O/Si	ΔE^{ox+}_{0+}	Etch (min)	Si_{2p} Oxide	Si_{2p} Subx	$Si_{2p3/2}$ Subs	O_{1s}	ΔE O-Si
5.8	75	---	25	2.10	---	0	1.44	---	0.83	1.60	430
4.5	64	3	33	2.0	2.1	0.5	1.97	1.7	0.95	1.72	429.6
3.0	52	6	42	1.97	1.9	1.2	2.12	1.7	0.93	1.75	429.8
2.4	40	8	52	1.9	1.8	1.6	2.25	1.7	0.96	1.78	429.5
1.5	26	8	65	1.91	1.7	2.1	2.31	1.7	1.1	1.8	429.6

Table 3.7: Evolution of O and Si XPS peak parameters for different thickness realised by Ar^+ ion bombardment.

Dilute Hf etch [0.5%]											
Alkα	Relative intensity					Alkα	FWHM				
Thic. (nm)	$Si_{2p3/2}$ I^{4+}	$Si_{2p3/2}$ I^{ox+}	$Si_{2p3/2}$ I^{0+}	% O/Si	$\Delta E_{ox+\ 0+}$	Etch (min)	Si_{2p} Oxide	Si_{2p} Subx	$Si_{2p3/2}$ Subs	O_{1s}	ΔE O-Si
5.7	74	---	26	2.08	---	0	1.41	---	0.82	1.63	429.6
4.7	67	---	33	2.11	---	2.0	1.40	---	0.82	1.67	429.5
3.4	53	---	47	2.0	---	4.0	1.50	---	0.85	1.75	429.7
2.6	39	3	57	2.0	1.5	4.8	1.37	1.7	0.83	1.80	429.5
1.7	22	5	72	1.97	0.6	6.1	1.35	1.7	0.89	1.88	429.6

Table 3.8: Evolution of O and Si XPS peak parameters for different thickness realised by dilute HF acid etching.

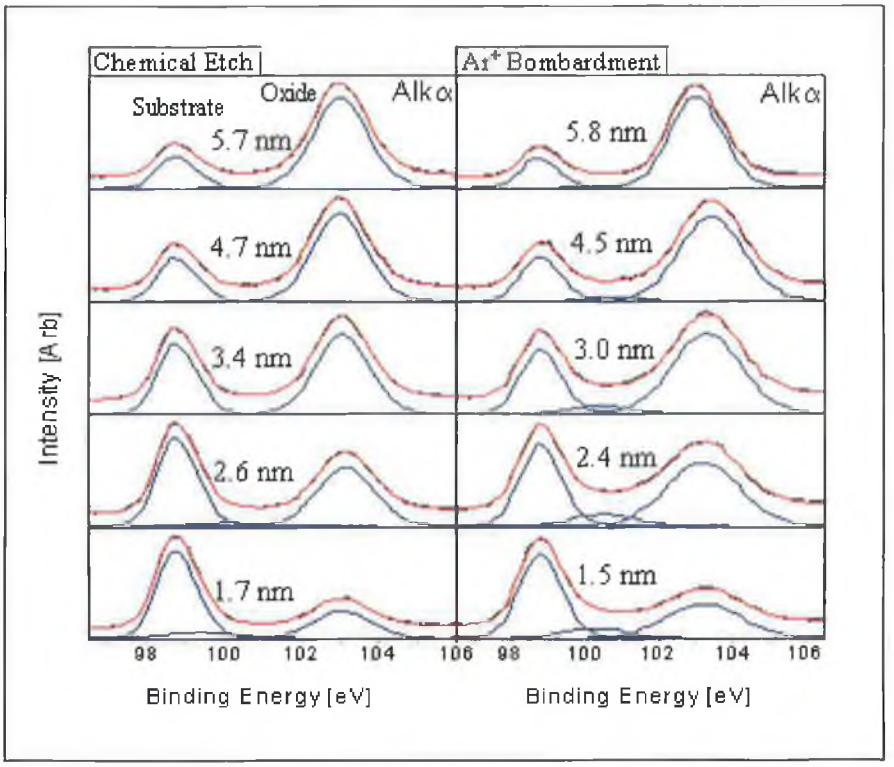

Figure 3.13: The damaging effects of Ar^+ bombardment are apparent by comparing the Si_{2p} spectra for various thicknesses realised by both bombardment and wet chemical HF etching. For the bombarded samples (right) a larger peak FWHM is evident and an increase of suboxide signal relative to the wet chemical thickness.

The key result in figure 3.13 is the need for a suboxide peak immediately after bombardment where as in the wet chemically etched spectra a suboxide peak does not emerge until a thickness of approximately 2.6 nm has been realised.

The SiO_x peak, reflecting the qualitatively presence of suboxides, lies closer to the substrate peak than to the Si^{4+} peak. The substrate FWHM shows a gradual but small increase as the substrate is approached. The expectation of the intermediary peak is that it is "following" this evolution of the substrate. However, when almost all oxide is removed, the peak tends to sit directly underneath the substrate peak and thus becomes impossible to fit with a high degree of confidence. Also, in the thickness range where the intermediary peak establishes itself, the oxide peak has becomes broad, small, poorly defined and also difficult to fit consistently.

The detection of suboxides during wet chemical treatment as primarily interfacial in origin is based on the following observations:

When 20 nm and 13.4 nm thick oxides were bombarded to a thickness where the substrate could be detected and fitted, the substrate FWHM value was larger than in the as received samples (5.5, 6.5, 7.2 nm) and continued to increase with bombardment. The substrate FWHM increase was associated with the reduced outer damage region.

There wasn't any need to fit an intermediary peak in the as received thickness (5.5, 6.5 or 7.2 nm where the substrate could be fitted). Therefore, the detected suboxides signal cannot originate from the interface.

A suboxide peak is necessary in bombarded samples in the ultra-thin regime while unnecessary in wet chemically etched oxides of the same thickness. Suboxides can be detected in wet chemically thinned oxides only at certain thickness near the interface.

While the literature could attribute the oxide FWHM increase to random bond angle rearrangement, an increase in substrate FWHM, which lies well below the expected damage zone for 2 keV ions is more likely to arise from surface localised low oxidation states (i.e. Si^{1+} or Si^{2+}) who's line shapes would overlap with the substrate.

The above observations supported the conclusion that suboxide species detected after bombardment were surface localized. The absence of any suboxide for oxides of the same thickness prepared wet chemically along with off-angle behaviour supports the damage as being surface localised.

3.5.1 Discussion of results

Wet chemical etching appears to be non invasive structurally, in that surface roughing induced by the etching is small (as shown by AFM analysis in chapter 4) compared to the overall film thickness. However, the chemical effect of hydrogen in the acid and its possible incorporation into the oxide or bonding at the interface in the form of hydrides is unknown. The films under investigation are device grade dielectric layers which have

undergone a final high temperature anneal in hydrogen atmosphere to reduce the interfacial defect density. It is possible that hydrogen incorporation in the interfacial region is responsible for the increase in substrate FWHM as the interface is approached. However, the use of dilute HF for gradual thinning of oxide is common and hydrogen induced changes have not been reported by other workers [22].

3.6 Oxynitride Analysis Overview

Incorporation of nitrogen into ultra-thin SiO_2 films has advantages in reducing boron migration from the (MOSFET) transistor gate, in increasing the oxide dielectric constant and in reducing interfacial suboxide density. Higher dielectric constant material allows a thicker oxide to be used to alleviate the transistor gate-tunnelling problem. As nitrogen is bonded to three silicon atoms at the interface compared to doubly coordinated oxygen. This N bonding is effectively more "compact" than oxygen and is more "resistant" to forming positive defects than oxygen.

A number of different procedures have been developed to incorporate nitrogen into SiO_2 films either during oxidation or by post oxidation, by rapid thermal annealing RTA, the oxide in a nitrogen ambient. The choice of precursor (N_2O, NO and NH_3) and process used, affects the nitrogen spatial distribution and it's bonding environment. For example, RTA [23] results in a narrow spatial concentration of nitrogen at the interface while nitrogen incorporation during furnace oxidation shows a more uniform distribution of nitrogen through out the oxide. Nitrogen incorporation using NO results in interfacial nitrogen existing mostly on the substrate side of the SiO_2/Si interface and a small amount incorporated into the bulk oxide [24]. Incorporation using N_2O results in interfacial nitrogen existing mostly on the oxide side of the SiO_2/Si interface and a larger amount incorporated uniformly in the oxide. Nitridation using NH_3 results in nitrogen rich regions at both the interface and surface with a small amount incorporated into the oxide [25].

All incorporation methods result in a nitrogen "pile up" at the interface. Excess N at the interface has the detrimental effect in MOSFETs of reduced carrier mobility in the channel and enhanced electron trapping' [26-27]. Lucovsky et al [28] have sought to

engineer the ideal nitrogen distribution through a two step plasma process giving a nitrogen rich surface and giving a small nitrogen concentration in the oxide and interface.

While the selective incorporation of nitrogen into stacked ON dielectrics using PECVD may realise the optimal nitrogen distribution. Such processes have not yet been optimised for current sub micron CMOS production technologies.

Figure 3.19 shows the nitrogen SIMS profiles associated with the traditional nitridation processes discussed above. Novak [29] et al in a recent extensive review concluded that using grazing incidence and low energy beams, SIMS can give both the distribution and concentration of nitrogen in ultra-thin silicon oxynitrides with acceptable accuracy. This information is complementary to XPS studies where the chemical bonding of the incorporated nitrogen can be profiled using either ARXPS or wet chemical treatment.

Shallenberger et al [20] have outlined how XPS also offers quantitative information, from homogenous samples using integrated peak areas and applying relative sensitivity factors. However, nitrided samples are problematic because the samples have an inhomogeneous distribution of nitrogen within the sampling depth. The signal is detected from the SiON layer (which may have a non-uniform N distribution) as well as from the substrate and an adsorbed surface organic layer. Given these difficulties much of the quantification has been undertaken in SIMMS [29-30], MIES [31] and NRA [32] studies while XPS has concentrated on the nitrogen chemical state.

In order to depth profile the nitrogen distribution, the oxide layers were wet chemically etched using dilute HF acid solutions as for SiO_2. The fact that the nitrogen concentration in the samples under investigation is low (≈0.7–3%) and the photoionisation cross-section of the N_{1s} is small means that the detected signal is small.

Nitrogen's bonding environment is related to it's spatial location in the film [20]. It is believed that nitrogen at the interface which bonds to the silicon substrate exists in a chemical state similar to bulk Si_3N_4 with an interfacial silicon bonded to three nitrogen atoms, and has an associated binding energy of 397.8 eV.

Nitrogen in the bulk oxide is shifted to a higher binding energy due to it's more electronegative bonding oxygen neighbours [38]. Lu et al [2-4],[33] have undertaken extensive photoemission (both monochromated XPS and synchrotron) studies of ultra-thin SiO_2 and SiON films using wet chemical treatment to profile their oxides.

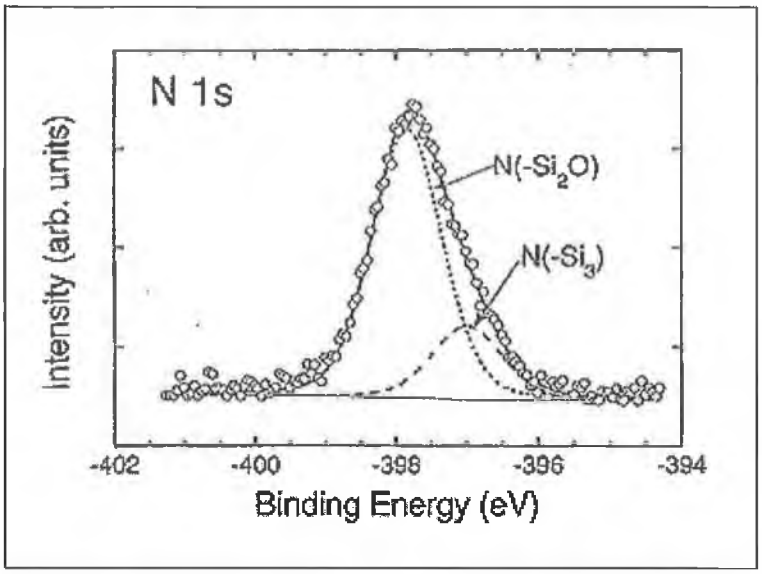

Figure 3.14: N_{1s} XPS spectrum from a rapid thermal nitridation sample etched back wet chemically. The lower binding energy peak at 396.97 eV is similar to that in Si_3N_4 and is referred to as N(-Si_3). The higher binding peak is assigned to a N bonded to two Si and one O and is referred to as N(-Si_2O) (Lu [33]).

They have detected both interfacial (N(-Si_3)) and oxide (N(-Si_2O)) N phases (see figure 3.14) and have shown the interfacial nitrogen to have helped reduce interfacial suboxide intensity (see figure 3.15).

Note: figure 3.14 was acquired with a monochromated XPS system while figures 3.15 (a) and (b) were acquired using synchrotron radiation. Figure. 3.16 shows the nitrogen concentration of the different detected nitrogen chemical states with depth. The upper panel represents a RTN film while the bottom is RTO followed by RTN.

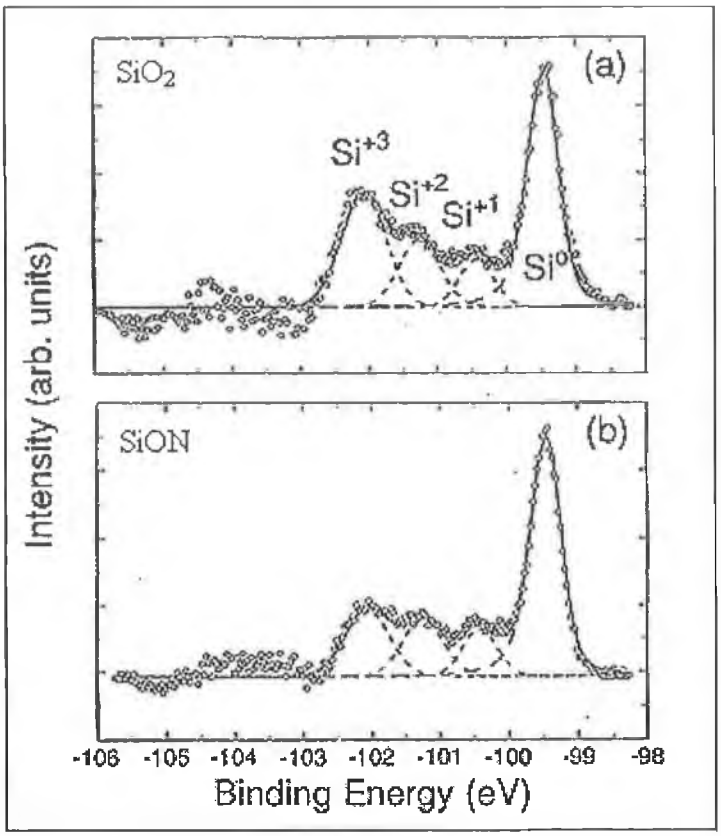

Figure 3.15: Synchrotron photoemission Si_{2p} spectra taken from (a) a RTO sample and (b) a RTN sample. The $Si_{2p1/2}$, the background and Si^{4+} peak have been subtracted in order to show the reduction in suboxide state (Si^{1+},Si^{2+},Si^{3+}) intensity due to nitrogen incorporation. (Lu[33])

Lu's binding energy of 396.97 eV for interfacial nitrogen N(-Si_3) was in excellent agreement with that obtained for a bulk Si_3N_4 film of 397.0 eV. He de-convoluted the N spectrum into an interfacial peak N(-Si_3) and an oxide peak chemically shifted by +0.85 eV which was attributed to N bonded to two silicons N(-Si_2O) and an oxygen. He explains the localisation of the nitrogen region near the interface as arising from the fact that it's Si atom density value (g Si_3N_4 : $4x10^{22}$ atoms/cm^{-3}) is intermediary between that in SiO_2 (g SiO_2 : $2.2x10^{22}$ atoms/cm^{-3}) and that in the silicon substrate (g Si : $5x10^{22}$ atoms/cm^{-3}). Therefore, the inclusion of Si_3N_4 near the oxide/Si interface creates a buffer layer which reduces the Si atomic density mismatch induced strain at the oxide/Si(100) interface. This is reasonable and is supported by the reduction of interfacial suboxide signal in the nitrided samples as illustrated in figure 3.15.

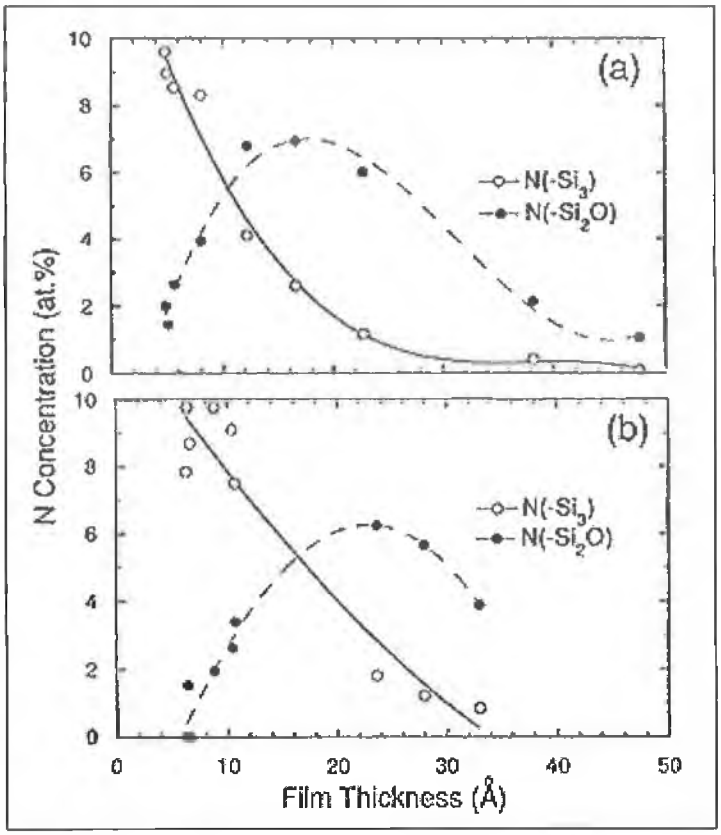

Figure 3.16: N concentration profiles as a function of oxynitride film thickness for (a) a RTN sample and b) a RTO/RTN sample. The data show that the N(-Si_3) is distributed mainly within the first 1 nm region of the interface while the N(-Si_2O) is distributed mainly about 2 nm away from the interface (Lu [33]).

What appears unreasonable about Lu's findings in this work is his assignment of the oxide nitrogen phase to N bonded to two silicon atoms and an oxygen. Also, no evolution of the N peak parameters with thickness is mentioned suggesting the two N chemical states identified remain unchanged with thickness.

It is arguable that there may be another interpretation of Lu's results in which there is no nitrogen/oxygen bonding at any depth and where N exists only in a Si_3N_4 like phase. This interpretation is based on the broader findings reported in the literature which provide an alternative for the second observed N phase and it's behaviour with thickness. Lu has not considered his findings in the context of the disagreement about N peak assignment / de-convolution in oxynitrides which exists in the literature. While NO, N_2O and NH_3 nitridation processes result in N incorporation in both the oxide and interface, yet there is considerable evidence to suggest that the nitrogen bonds directly with silicon atoms only. Oxygen-nitrogen related bonds have been reported using other nitridation process.

The chemical shifts are in the range 1.6-3.0 eV [17],[34] and attributed to N-SiO_2O bonding. Chang et al [35] found peaks shifted by 3.8 and 6.1 eV, which they assigned to N-SiO_2O and N-O_3 configurations respectively. These chemical shifts relating to N-O bond formation are significantly larger than those reported by Lu et al. As will be outlined below no evidence of direct nitrogen oxygen bonding was evident in the studies present in this thesis, although a variation in the N peak binding energy, intensity and FWHM with thickness was found. In order to interpret our own results in the context of this disagreement a brief outline it's origins and implications is given.

For interfacial nitrogen, there is general agreement about it's bonding environment being that of N(-Si_3) but a spread in it's binding energy of 0.9 eV has been found with conflicting interpretations [23],[33],[38].

For oxynitrides prepared using N_2O (E_{N1s} 398.4 eV), NO (E_{N1s} 398.2 eV) and NH_3 (E_{N1s} 397.9 eV) a single asymmetric N(-Si_3) peak has been detected [20]. The binding energy of this interfacial peak was found to show a thickness dependence, tending to lower binding energies (ΔE = 0.4 eV) for thinner oxides [36]. For ultra-thin oxides consistent peak shifts for all oxide elements can be attributed to charging of the oxide or to image charge effects arising from the close proximity of the conducting substrate. However, Carr and Buhrman [23] considered the energy separation of the N_{1s} and O_{1s} peaks from the Si^{4+} oxide peak with thickness and they found a constant value for O_{1s}-Si^{4+} separation but a decreasing value for the N_{1s}-Si^{4+} separation. They dismissed the possibility of structural changes associated with interfacial strain (as proposed by Grunthaner [21]) as an explanation for these differences. Direct N-O bonding would result in a chemical shift of 2.0-2.5 eV per N-O bond (far larger than Lu's 0.85 eV shift). Hedge et al [24] also found a single asymmetric interfacial N peak showing the same thickness behaviour as Carr and Buhrmans [23]. Their SIMS profiles showed nitrogen to be both in the oxide and at the interface. So how can it only exist in one phase? Miura et al [37] considered the effect of re-oxidation on interfacial nitrogen, expecting oxygen atoms to contribute to the nitrogen bonding configurations as the interfacial region is "displaced" out into the oxide (during re-oxidation) by the new interface below. The interfacial nitrogen was incorporated into the oxide but the binding energy shift was the same as found above (ΔE=0.4 eV) ruling out the possibility of N-O bonding.

The nitrogen dilemma has been addressed in an extensive study by Shallenberger [20] and Novak and independently by Novak [29]. They prepared five oxynitride samples through different recipes which where examined under identical conditions, eliminating differences in analysis conditions as a cause of uncertainty. The nitridation processes consisted of; (a) N_2O, (b) NO,(c) NH_3, (d) RTP treatment (I) and (e) HRP treatment (II). Figure 3.17 shows the N_{1s} peaks obtained with peak binding energies and a real N concentration. The only N-O related peak detected was the peak at 402.8 eV produced by the (HRP) treatment and assigned $(O\text{-})_2N\text{-Si}$. As for the interfacial peak, Car and Burhman [23] had attributed the increased N_{1s} binding energy with thickness to N

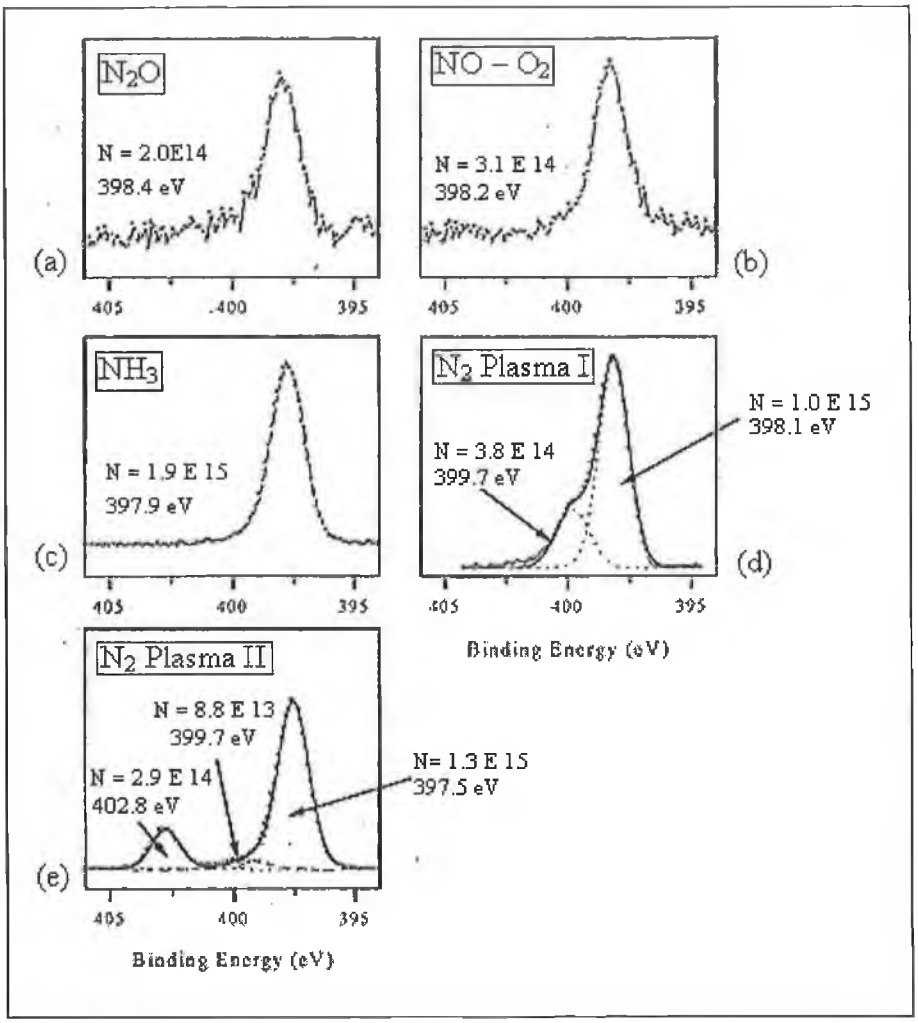

Figure 3.17: High-resolution N_{1s} spectra from oxynitrides grown in a) N_2O, b) NO/O_2 mixture, c) NH_3 d) N_2RTP plasma treatment type I and e) N_2 remote plasma treatment type II. The peaks at 397.5-398.4 eV in a) to e) are due to $N(\text{-}Si_3)$. The peak at 399.7 eV d) and e) are due to $O\text{-}N(Si)_2$ The peak at 402.8 eV e) is due to $(O\text{-})_2N\text{-Si}$. The areal density of the different nitrogen species is listed for the individual nitrogen coordinations (Shallenberger [20]).

bonded to two silicons and a dangling bond $N(-Si)_2$ or a hydrogen related bond $N\text{-}Si_2H$. However, the absence of a corresponding number of associated defects in capacitance-voltage (CV) analysis seriously questions Car's theory. Bouvet et al [38] proposed that the increase in chemical shift of the nitrogen component in the oxide with thickness was due to the increased effects of second nearest neighbour oxygens in the oxide. Shallenberger [20] tested Bouvet's [38] second nearest neighbouring oxygen theory by calculating the areal density of N in the five samples. He found a correlation (shown figure 3.18) between nitrogen concentration and binding energy, where there was a shift to higher binding energy at lower nitrogen concentration (i.e. higher oxygen concentration). This trend in binding energy was attributed to the increasing concentration of oxygen as the next nearest neighbour to the SiN_3 bonding environment.

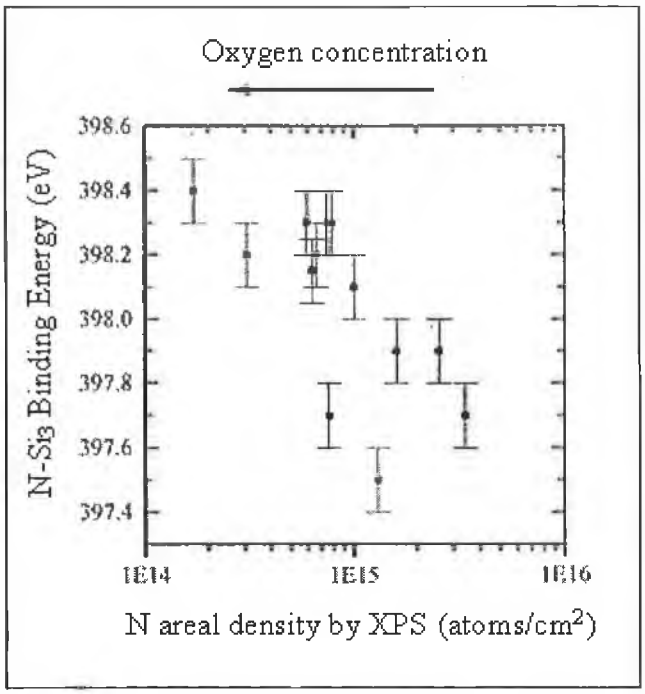

Figure 3.18: Plot of the $N(-Si)_3$ nitrogen 1_s binding energy as a function of N areal density measured by XPS. The shift to higher binding energy at lower N concentration (i.e. higher O concentration) is due to the presence of the more electronegative next nearest neighbour oxygen atoms (Shallenberger [20]).

However, when Shallenberger [20] compared the XPS N areal concentrations with those calculated using NRA he found poor agreement for some samples and good agreement for others. The reason for the departure of XPS from the NRA results for some samples was found in their SIMS profiles as shown in figure 3.19. Nearly all the N is piled up in the interface region 3.5nm below the surface in the N_2O #2 sample. Since on average

the nitrogen photoelectrons are originating from deeper in the oxide than the Si^{4+} photoelectrons, the nitrogen signal is disproportionately attenuated resulting in an underestimate of the true nitrogen concentration by XPS.

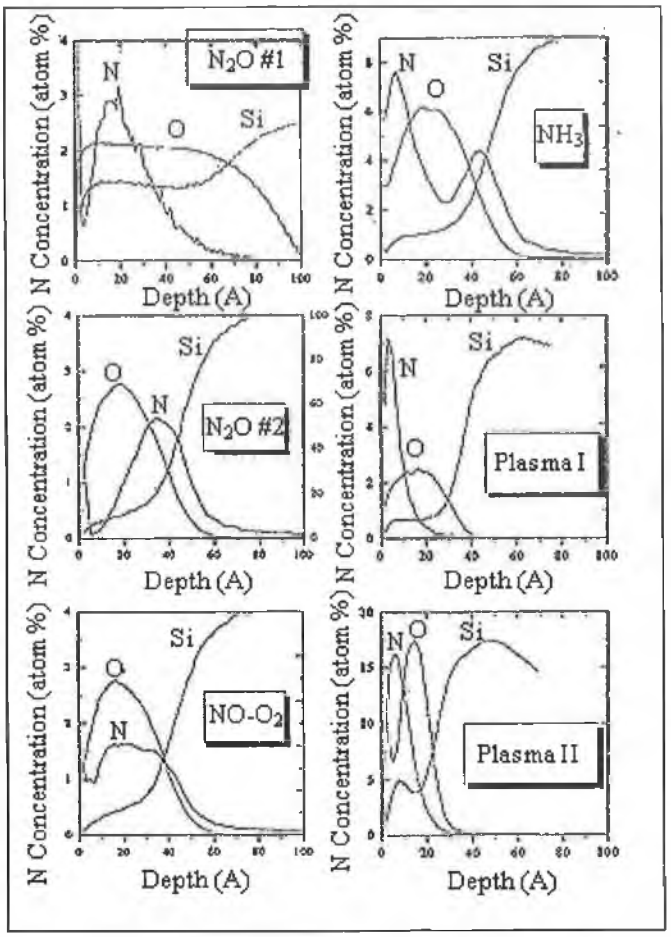

Figure 3.19: SIMS depth profiles showing nitrogen in-depth distribution for different nitridation process (Shallenberger [20]).

The NO/O_2 sample exhibited a more uniform nitrogen distribution within the oxide layer yielding a better agreement with the NRA result.

The N_2O #1 oxynitride had nitrogen located near the outer surface of the layer, which resulted in an overestimate of the nitrogen concentration, by XPS because of the disproportionate attenuation of the Si^{4+} photoelectrons relative to the nitrogen photoelectrons.

Rignanese and Pasquarello [39] having calculated core level shifts for N in various environments support the view that the variation in the N binding energy with thickness is related to the increased influence of next nearest neighbour oxygens. This analysis would suggest that nitrogen exist only in a Si_3N_4 environment, throughout the oxide layer.

However, in the oxide the increased influence of oxygen atoms in the second coordination sphere results in a nitrogen chemically shifted peak at a different binding energy to the nitrogen in the interfacial region which is less oxygen rich. The extent of the shift is related to the extent of the nitrogen concentration. The overlap of these two peaks results in a an asymmetric N_{1s} envelope whose intensity and position are decided by how much of each phase that can be "seen" which is complicated by the presence of a nitrogen rich region both at the surface and at the interface, as the surface phase is exaggerated and the interface phase underestimated.

3.7 SiON As received

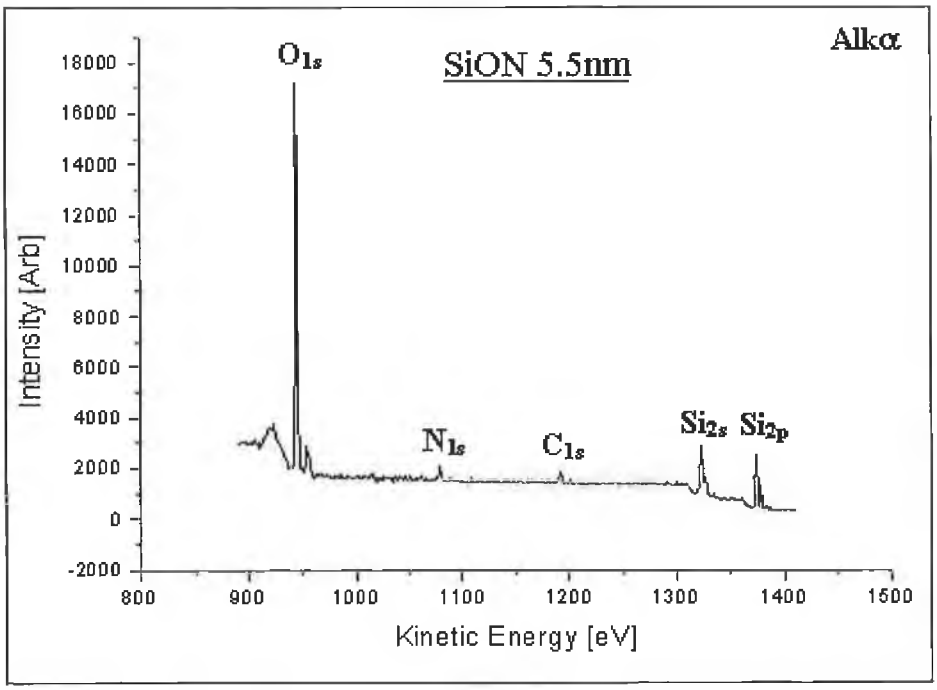

Figure 3.20: The elemental composition of a 5.5 nm SiON film is revealed in a survey scan. The low nitrogen concentration is apparent from its relative intensity. The C_{1s} signal arises from surface hydrocarbon contamination.

The oxynitride sample set investigated consisted of two thickness 5.5 nm and 3.3 nm as determined by elliposimetry. The samples were realised by RTA of 5.5 and 3.3 nm SiO_2 wafers in a NH_3 ambient in an industrial processing environment. Figure 3.11 shows an XPS survey scan of the 5.5 nm SiON film. As with the SiO_2 samples investigated in this study the oxide integrity was evident from the presence of only silicon, oxygen, nitrogen and surface carbon. Each peak was scanned using a pass energy of 20 eV, a step size of 0.15 eV and an integration time of 0.3 sec. Lu et al [33] using a monochromated source reported scan times of several hours just to acquire the N peak because of its small concentration and photoionisation cross section.

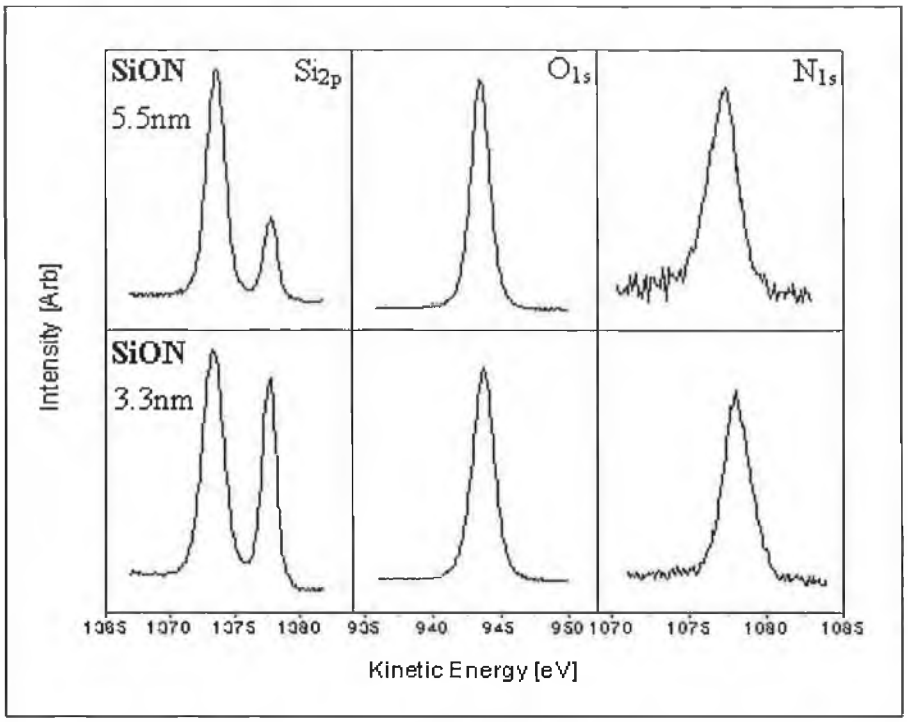

Figure 3.21: Comparison of principal photoelectron peaks (Si_{2p}, O_{1s} and N_{1s}) from (Top) 5.5 nm SiON and (Bottom) 3.3 nm SiON.

In order to attain reasonable intensities in this study the N window was scanned 60 times, the silicon 20 and oxygen 10 times. Figure 3.21 shows the spectra of Si_{2p}, O_{1s} and N_{1s} in the 5.5 nm (upper panel) and 3.3 nm (lower panel) SiON samples respectively. As shown in his SIMS profiles in figure 3.19 and explained by Shallenberger [20], NH_3 annealed SiO_2 layers are particular problematic given the presence of both a surface and interfacial nitrogen region in the oxide.

It is therefore interesting to speculate as to how a quantitative interpretation of the film composition is affected as the oxide is thinned. Also, as was apparent from the behaviour of the stoichiometry results from etched SiO_2 films already investigated; it was necessary to establish a consistent methodology to curve fit the data sets.

Thickness

In order to accurately calculate the thickness of the SiON films using equation 2.19, there is a need to know the value of IMFP λ_{SiON} for the oxynitrides.

$$d = Ln\left[\frac{I_{SiO_2}}{I_{Si}}\frac{I_0}{I_\infty} + 1\right]\lambda_{SiO_2}$$

However, as the nitrogen concentration through the film is non-uniform, the IMFP would vary through the film. In order to proceed many researchers have simply ignored the nitrogen concentration and calculated the thickness using the IMFP for SiO_2. After all, the nitrogen concentrations involved are extremely small (<1 at.%) and an absolute value of thickness is not ultimately of concern. Using equation 2.19 and the SiO_2 parameters, the calculated thickness values of 5.7 nm and 2.8 nm were obtained for the 5.5 nm and 3.3 nm samples respectively.

3.71 Wet Chemical Depth Profile for 5.5 nm oxynitride

Figure 3.22 shows the evolution of the Si_{2p} spectrum following successively longer (0.5 min per etch) wet chemical etches for the 5.5 nm thick SiON layer in dilute (0.5%) HF acid. A fresh sample was used in each etch cycle which consisted of etching, rinsing in ultra pure deionised water followed by blow drying in N and insertion into UHV within 10mins. For 0.5% HF a reduced etch rate of was observed in the SiON samples compared to the SiO_2 layers. Other workers have also observed a reduced etch rate for their SiON samples [42,43]. The SiON samples were etched for up to 3.5 mins in steps of 0.5 mins. The spectra on the left in figure 3.22 were acquired at 0^o degree take-off angle and those on the right at 60^o degrees off angle. The Si^{4+} oxide and substrate peak FWHM were both larger than in SiO_2. Also, there was a need to fit an additional

suboxide related peak even before etching and, from the angular behaviour of this peak, it appears to be interface localised.

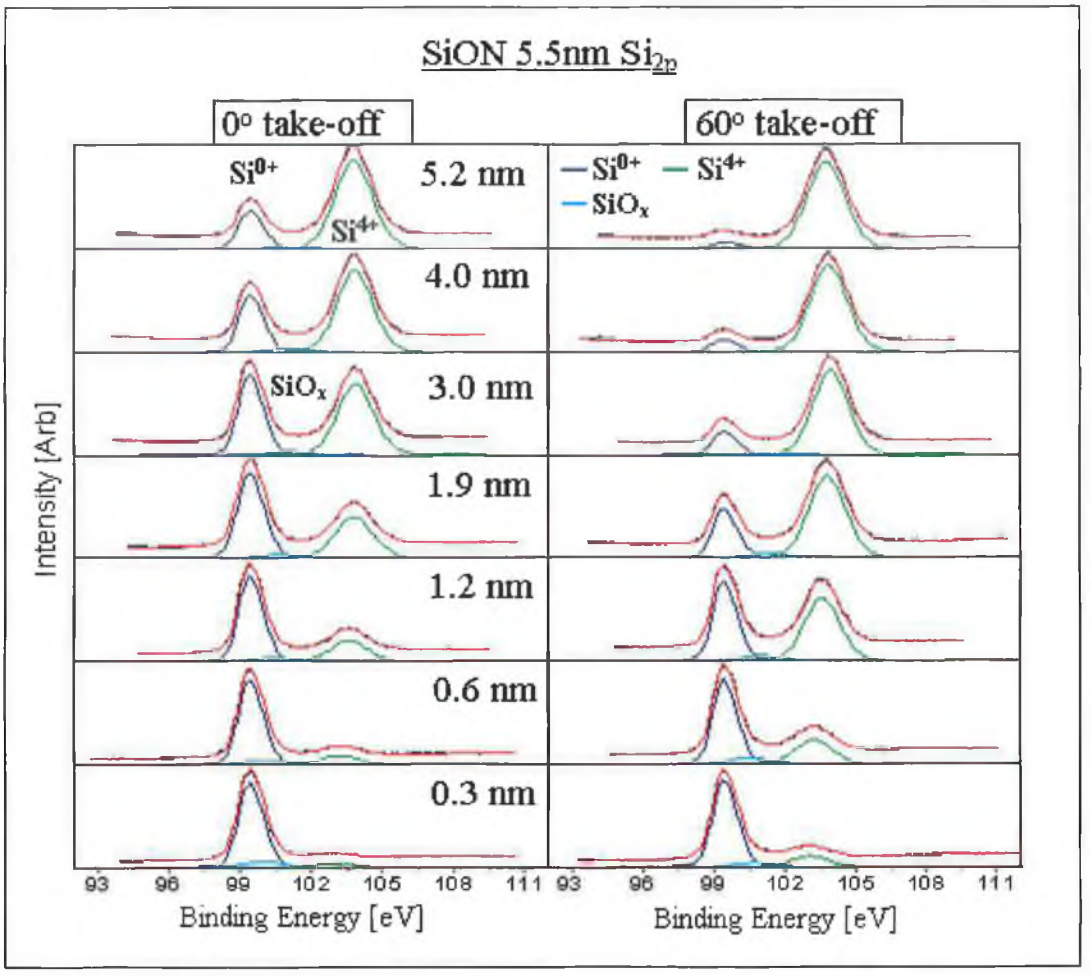

Figure 3.22: Evolution of Si_{2p} spectrum of 5.5 nm SiON oxide layer with wet chemical etch for (left) normal emission and (right) 60° take-off angle.

This was deduced from the fact that the suboxide peak was significantly less pronounced in the 60° off spectra, which are more surface sensitive than the normal emission spectra. Table 3.9 compares the spectral parameters for a 5.5 nm SiO_2, SiON and 3.3 nm SiON sample. The larger FWHM of the SiON samples can be attributed to the presence of both oxides and nitrides in the film. Also, the post oxidation NH_3 anneal has most likely led to the formation of a more distributed interface resulting in the earlier detection of suboxides. As with the SiO_2 samples, the oxide tends to a lower binding energy and becomes poorly defined below a thickness of 2 nm.

Alkα	FWHM SiON 5.5 nm					**FWHM SiON 3.3 nm**				
Etch (min)	Si_{2p} Oxide	$Si_{2p3/2}$ Subs	$Si_{2p3/2}$ Subx	O_{1s}	ΔE O-Si	Si_{2p} Oxide	$Si_{2p3/2}$ Subs	$Si_{2p3/2}$ Subx	O_{1s}	ΔE O-Si
0	1.62	0.87	1.7	1.72	429.6	1.73	0.92	1.7	1.81	429.7
0.5	1.54	0.85	1.7	1.67	429.8	1.65	0.94	1.7	1.79	429.5
1.0	1.56	0.86	1.7	1.71	429.7	1.61	0.93	1.7	1.81	428.6
1.5	1.63	0.87	1.7	1.75	429.7	1.56	0.94	1.7	1.87	430.0
2.0	1.58	0.88	1.7	1.73	429.7	1.47	0.94	1.7	1.91	430.0
2.5	1.60	0.90	1.7	1.82	430.0	1.32	0.96	1.7	1.95	429.9
3.0	1.63	0.95	1.7	1.85	430.0	---	1.02	---	2.05	---
3.5	---	0.97	---	1.82	429.9	---	1.11	---	---	---

Alkα	**FWHM SiO_2 5.5 nm**				
Etch (min)	Si_{2p} Oxide	$Si_{2p3/2}$ Subs	ΔE O-Si	O_{1s}	ΔE O-Si
0	1.42	0.82	429.6	1.67	429.6
0.5	1.38	0.82	429.6	1.67	429.6
1.0	1.37	0.82	429.6	1.76	429.6
1.5	1.49	0.86	429.7	1.8	429.7
2.0	1.51	0.87	429.7	1.88	429.7
2.5	1.35	0.86	429.7	1.89	429.7
3.0	1.23	0.88	429.6	1.96	429.6
3.5	---	0.92	---	---	---

Table 3.9: Summary of XPS peak parameters for oxide and oxynitride samples after dilute 0.5% HF acid etching.

Figure 3.23 (a) and (b) shows the corresponding N1s spectra also obtained at 0^0 take-off and 60^0 degree take-off respectively. The spectra were charge corrected using the Si_{2p} substrate at 99.3 eV as a reference. The as-received (0 min etch) N_{1s} peak was slightly asymmetric and could be fitted well with a FWHM of 1.8 eV at a binding energy of 398.8 eV. However, as the film was thinned, this peak broadened to 2.0 eV and shifted to 398.3 eV and finally as the interface was approached, it's FWHM was 1.3 eV and binding energy 397.9 eV. Given the change of the N peak envelope with thickness and take-off angle the spectrum was fitted with two peaks instead of just one. The first peak was an interfacial peak corresponding to Si_3N_4 with a fixed binding energy of 397.9 and

a FWHM of 1.3 eV and a second peak with a FWHM of 1.6 eV who's binding energy was allowed to freely vary in energy position.

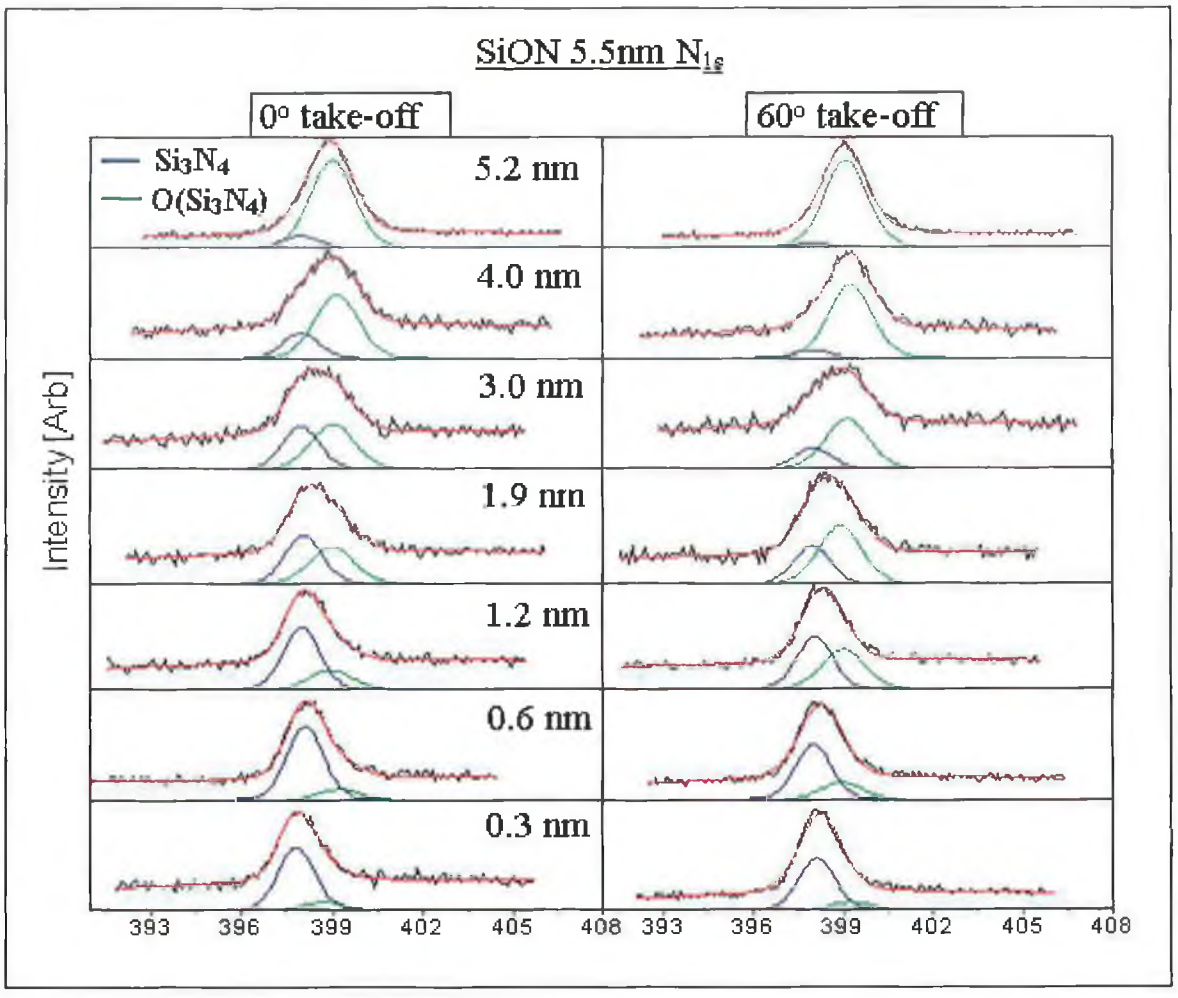

Figure 3.23: Evolution of N_{1s} spectrum with wet chemical etch for (left) normal emission and (right) 60° take-off angle. The peak is de-convoluted into two components an interfacial Si_3N_4 like peak and an oxide related phase which is tentatively assigned $O(Si_3N_4)$.

When the charge corrected N spectra were fitted with two peaks, with only the FWHM fixed, the binding energies of the peaks agreed with the literature values for interfacial and surface localised nitrogen [20],[33],[36]. Figure 3.24 shows the envelope of the fit to the N spectra, the intensities are uncorrected. Normally to cater for changes in the intensity due to difference in sample sizes, positions or off-angle shadowing effects all peak intensities are normalised to that of the Si oxide peak. Thus, the raw intensities cannot be compared here but the graph does convey the consistency of the peak positions after charge correction in both the normal and off angle spectra. The vertical hatched lines give a visual indication of the nitrogen peak positions.

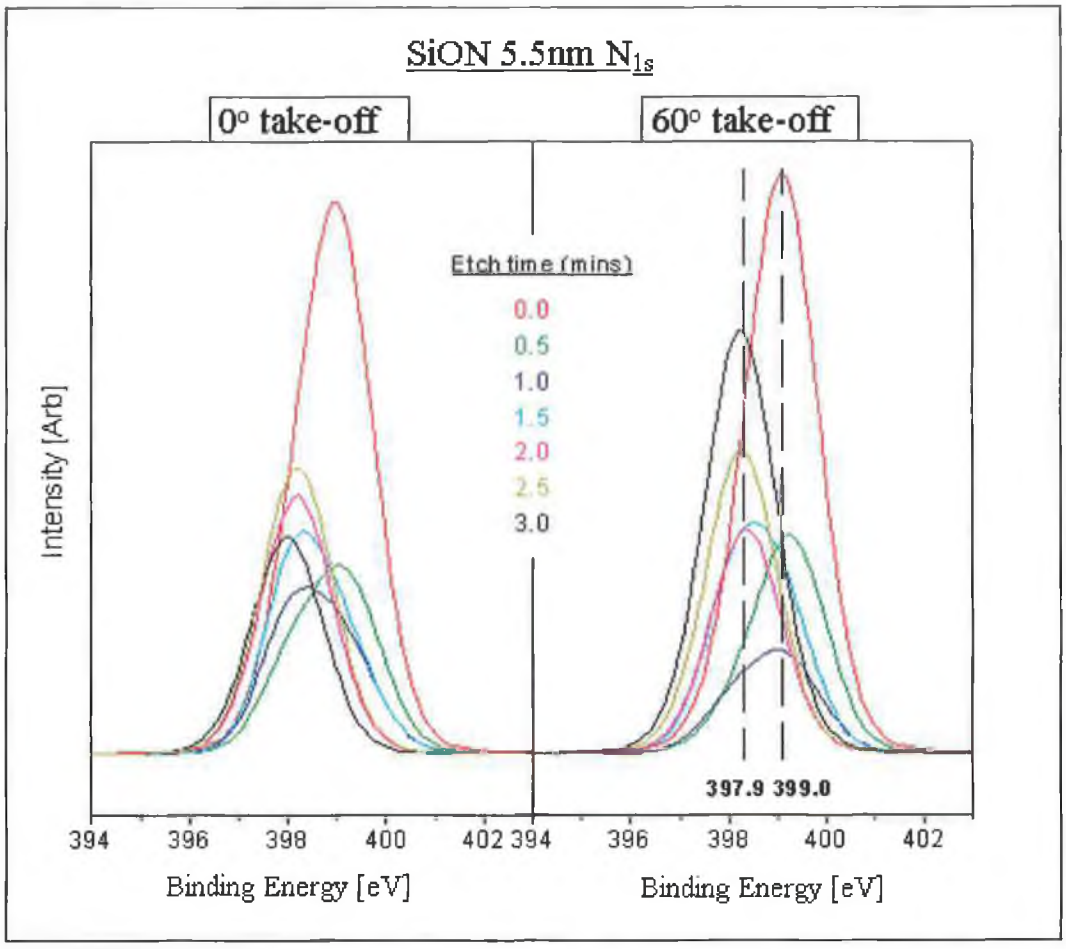

Figure 3.24: The binding energy shift of the centre of the N_{1s} peak with etch time and with take-off angle gives an indication of the evolution of the interface and oxide nitrogen components which make up the peak. The hatched vertical lines guide the eye to the expected binding energy positions for the interface and bulk components.

Etch Time	Thickness (A)	% Oxygen	% Nitrogen	% Silicon	(O/Si)
0	52.4	63.44	0.35	36.20	1.75
0.5	40.1	66.76	0.14	33.09	2.01
1.0	30.1	64.89	0.14	34.96	1.85
1.5	19.3	66.42	0.21	33.36	1.99
2.0	11.7	69.50	0.32	30.17	2.30
2.5	6.03	63.85	0.55	35.58	1.79
3.0	3.04	61.94	0.65	37.40	1.65

Table 3.10: Variation of oxygen, silicon and nitrogen elemental concentrations with dilute 0.5% HF acid etching for 5.5 nm oxynitride.

Table 3.10 shows the atomic percentages of each element calculated from the peak intensities after correction for the atomic sensitivity factor. A more commonly used measure of the nitrogen concentration in wet chemical profiles is the ratio of nitrogen intensity to nitrogen plus oxygen [23],[40-42]. This ratio identifies the difference in normalised nitrogen signal between samples, which have been etched to different thickness in order to determine the amount of nitrogen contained in the etched thickness. Thus, the ratio allows a quasi depth profile of the nitrogen distribution throughout the film to be determined, rather than the exponentially weighted average over the complete sampling depth.

Bersani et al [43] (figure 3.25) found a higher nitrogen concentration at the interface using NO during oxidation compared to N_2O.

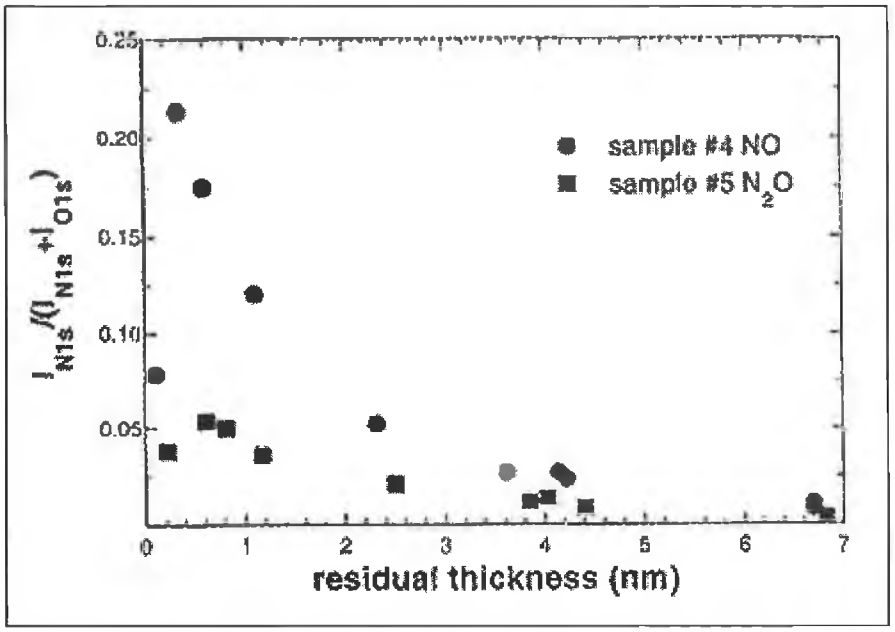

Figure 3.25: Nitrogen concentration depth profiles for NO and N_2O processes. NO results in an increased N incorporation at the interface (Bersani [43]).

Car and Buhrman [23] (figure 3.26) found a uniform N distribution using N_2O in furnace oxidation compared to a high interface N concentration with little oxide incorporation using N_2O in a RTA process.

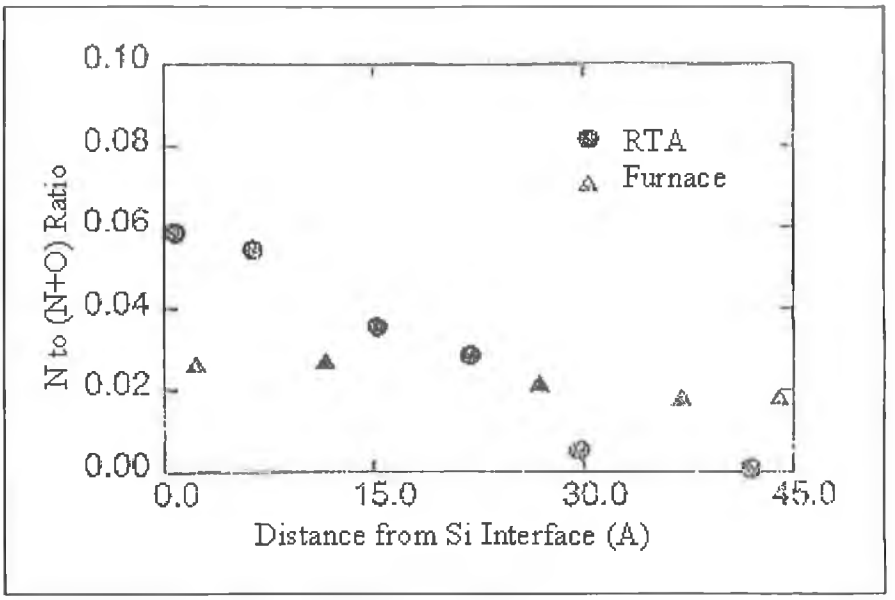

Figure 3.26: XPS intensity ratio as a function of distance from the Si-SiO_2 interface. The RTA and furnace oxides were initially 9.3 and 10nm (Car and Buhrman [23]).

Vasquez and Grunthaner et al [44-47] have under taken extensive investigations of the nitridation process of SiO_2 films using NH_3. From modelling of the nitridation kinetics and XPS measurements they have concluded the following:

- A surface and interface rich nitrogen region exists in the oxide.

- For a nitridation temperature of 800 °C the peak of the interfacial nitrogen distribution remains at the interface. For temperatures above 1000 °C it moves away from the interface due to a reduction in the diffusion of nitrogen species and local oxidation at the substrate.

Figure 3.27 shows the XPS results of a N chemical depth profile performed by Grunthaner et al [44]. Grunthaner's interfacial N distribution is displaced approximately 2 nm from the interface due to the nitridation temperature (>800 °C). He found a correlation between the nitrogen and oxygen concentrations and Si_{2p} chemical shift (E_b:Si_{2p}^{4+}-E_b: Si_{2p}^{0+}), where the shift was reduced in the interfacial nitrogen region and then increased again as the substrate was approached.

To explain this he proposed the existence of a non-homogeneous SiO_2 region in the oxide in which the inter-tetrahedral Si-O-Si bond angle is reduced due to compressive interfacial stress arising from the lattice mismatch between the silicon substrate and it's oxide. This strained SiO_2 region is more reactive to NH_3 than the bulk oxide and it is here, within 3 nm of the interface that the nitrogen rich region is formed. He also observed an oxygen rich region within 1.5 nm of the interface.

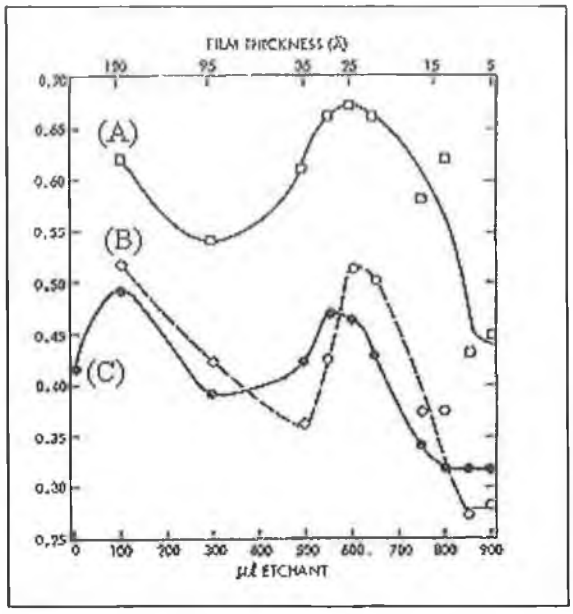

Figure 3.27: (a) I_{N1s}/I_{Si2p} ,where I_{Si2p} is the corrected intensity of the chemically shifted Si^{4+} oxide peak. b) $I_{N1s}/(I_{N1s} + I_{O1s})$, where I_{N1s} and I_{O1s} are the N_{1s} and O_{1s} peak intensities corrected for photoionisation cross sections. (c) D^O_{ox} / $(D^N_{ox} + D^O_{ox})$, where D^N_{ox} and D^O_{ox} are the atomic densities of nitrogen and oxygen in the oxynitride, respectively (Vasquez [44]).

He attributed this region to the formation of a nitride barrier negating further nitride diffusion in the anneal process and leaving an oxygen rich region. Alternatively, he suggested that the oxygen rich region arises from the reaction of by products from the SiO_2 NH_3 reaction (such as hydroxyl species) with the substrate. Figure 3.28 shows the nitrogen profiles determined in this study by the ratio method for the 5.5 nm SiON oxide. The results suggest that a narrow nitrogen region exists at the outer surface and a larger broader nitrogen distribution at the interface.

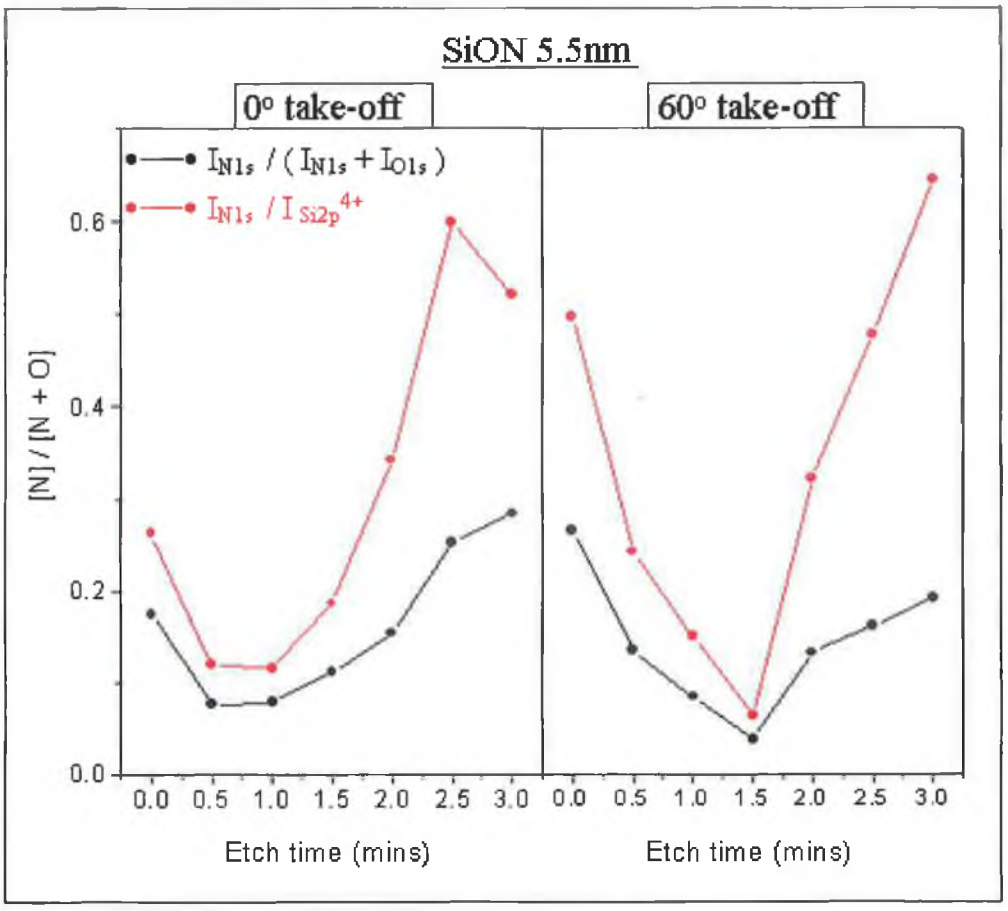

Figure 3.28: N concentration depth profile (I_N/I_N+I_O) and evolution of I_N/I_{Si2p}^{4+} for normal emission (left) and 60° take-off (right).

3.72 Wet chemical depth profile for 3.3 nm oxynitride

Figure 3.29 shows the 0° and 60° off angle evolution of the Si_{2p} spectrum of the 3.3 nm oxynitride subjected to the same etching sequence as the 5.5 nm oxynitride. Table 3.11 shows the atomic percentages of each element. As with the 5.5 nm oxynitride there was an initial high concentration with which decreased as a function of etch time and subsequently increased to a maximum value in the interfacial region.

Etch Time	Thickness (A)	% Oxygen	% Nitrogen	% Silicon	(O/Si)
0	35.3	60.86	0.46	38.66	1.57
0.5	25.1	62.68	0.26	37.04	1.69
1.0	15.5	63.94	0.32	35.72	1.78
1.5	7.5	60.47	0.56	38.96	1.55
2.0	4	62.73	0.83	36.42	1.72
2.5	1.7	58.60	0.79	40.59	1.44
3.0	0	99.03	0.96	0	--

Table 3.11: Variation of Oxygen, Silicon and Nitrogen elemental concentrations with dilute 0.5% HF acid etching for 3.3 nm oxynitride.

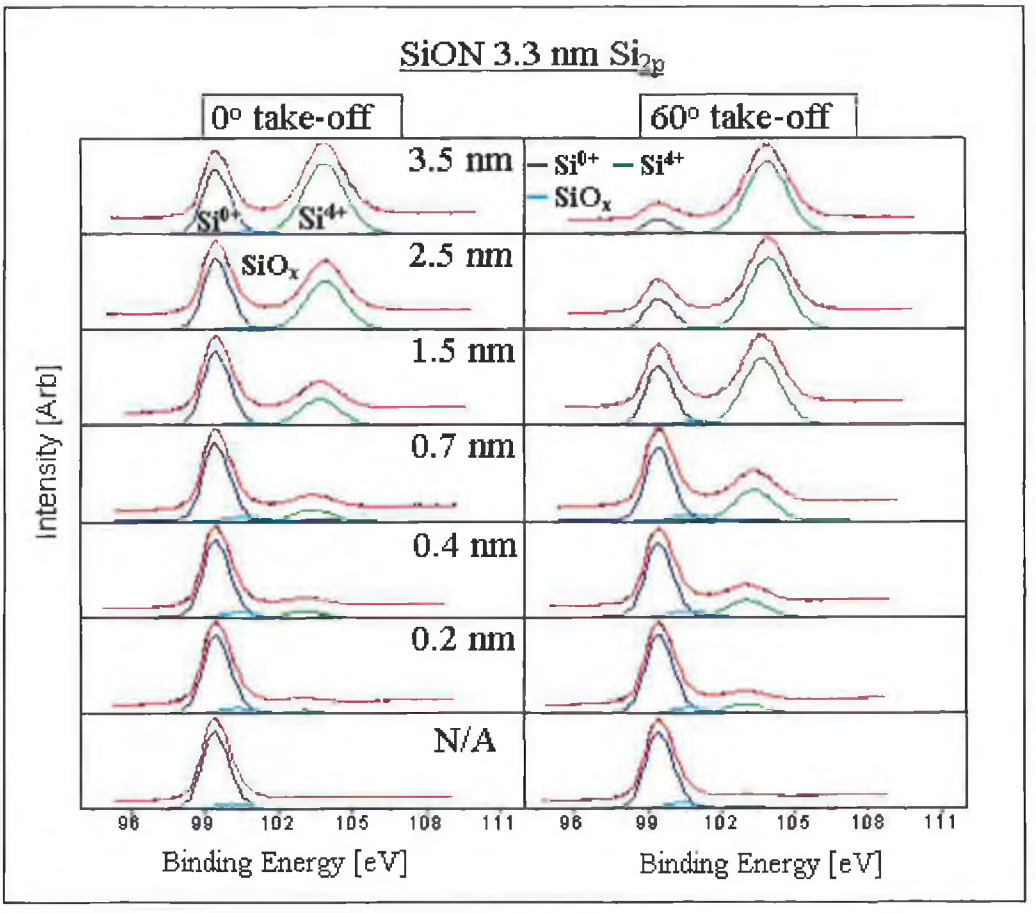

Figure 3.29: Evolution of Si_{2p} spectrum of 3.3 nm SiON oxide layer with wet chemical etch for (left) normal emission and (right) 60° take-off angle.

For the 3.3 nm oxynitride a 2.5 min etch almost results in complete removal of the oxide compared to the 5.5 nm layer. After 3 mins etching, the 3.3 nm SiON oxide peak at normal emission was too poorly defined to fit, but in the corresponding 60° take-off

scan an appreciable intensity could be detected. Figure 3.30 shows the normal and 60° off-angle behaviour of the N_{1s} peak with thickness for the 3.3 nm oxide.

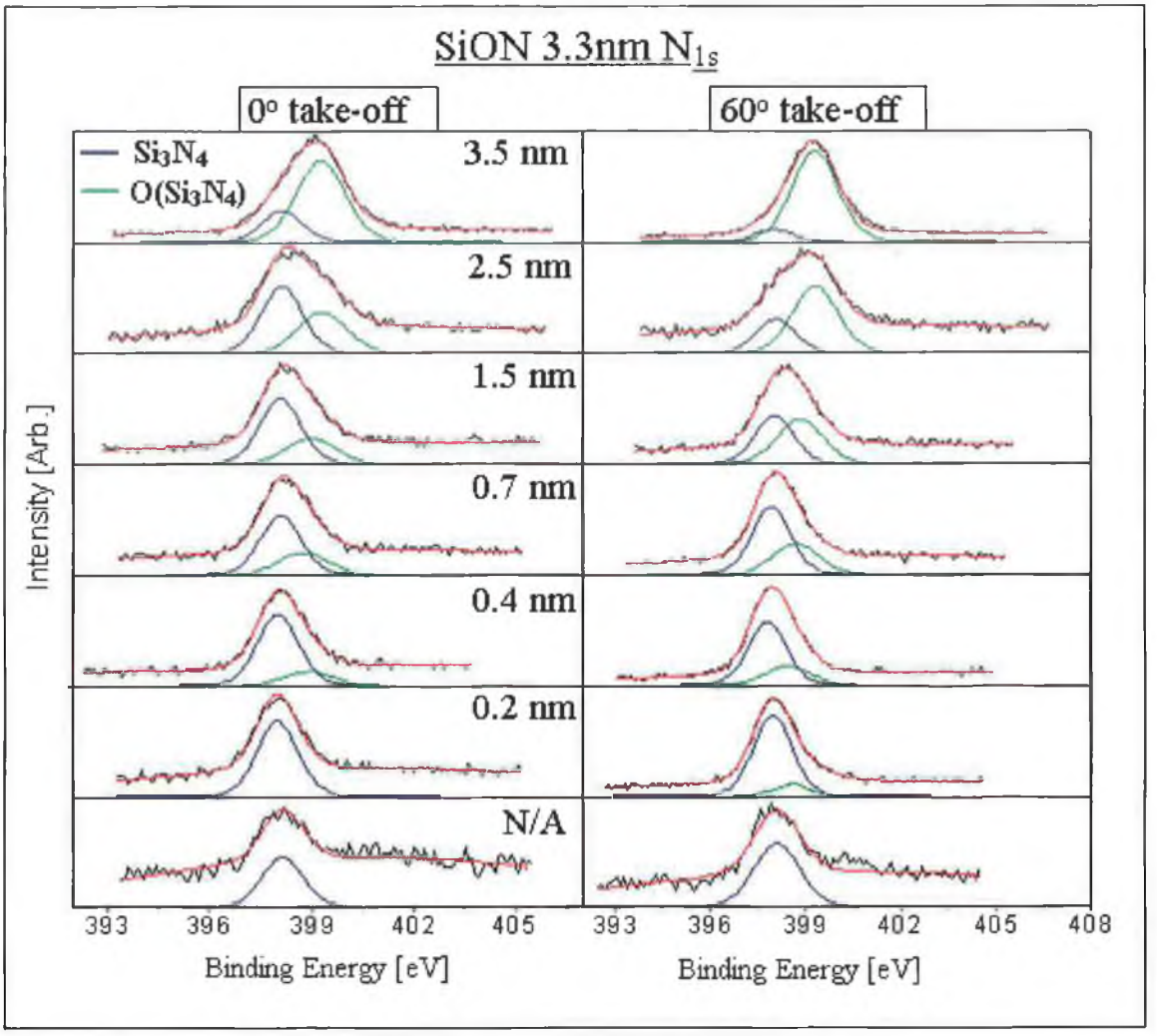

Figure 3.30: Evolution of N_{1s} spectrum with wet chemical etch for (left) normal emission and (right) 60° take-off angle. The peak is de-convoluted into two components an interfacial Si_3N_4 like peak and an oxide related phase which is tentatively assigned $O(Si_3N_4)$.

Similar to the 5.5 nm SiON N_{1s} spectra, the 3.3 nm N_{1s} spectra were initially fitted with a single peak to see how it's as received value of FWHM and kinetic energy evolved. An initial FWHM of 1.8 eV grew during the fit and finally reduced to a value of 1.3 eV. This final value was used for the FWHM of the interfacial Si_3N_4 like phase and the FWHM for the oxide phase (1.6 eV) was retained from the 5.5 nm fit.

Similar to the 5.5 nm SiON film the binding energy of the peak reduces with thickness. Also, like the 5.5 nm oxynitride the binding energy shift of the oxide related nitrogen component decreased from an as-received value of 398.8 eV to a final value of 399.7 eV. Given the behaviour of the 3.3 nm SiON nitrogen peak envelope with thickness and take-off angle the spectra were fitted with two peaks instead of one. The interfacial Si_3N_4 like peak was with a fixed binding energy of 397.9 eV and a FWHM of 1.3 eV and the oxide peak with a FWHM of 1.6 eV who's binding energy was allowed to freely vary in energy position. The spectra were charge corrected using the Si_{2p} substrate at 99.3 eV as a reference.

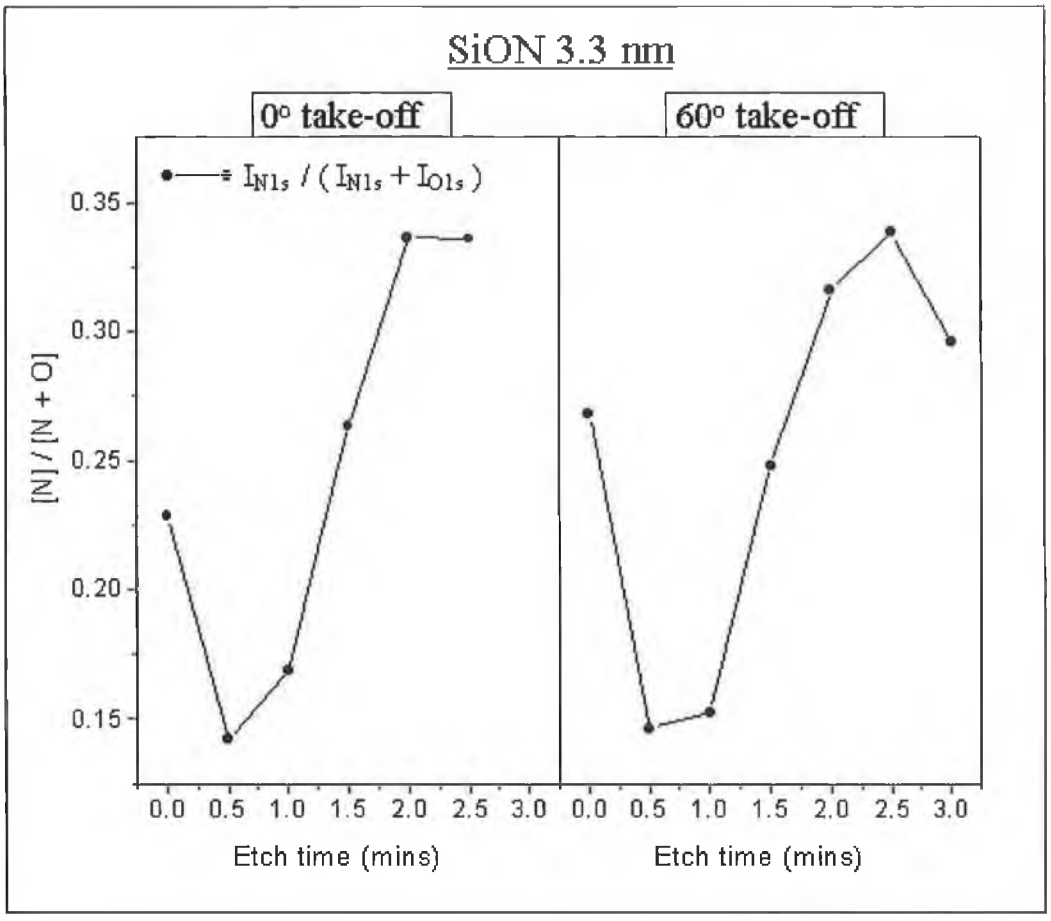

Figure 3.31: N concentration depth profile (I_N/I_N+I_O) for normal emission (left) and 60° take off (right).

Figure 3.31 shows the N concentration depth profile realised from etching the 3.3 nm oxynitride. The same trends are evident as was found for the 5.5 nm oxynitride sample with a surface and interface rich nitrogen region.

3.73 Discussion of Results

Nitrogen spatial distribution

Figure 3.32 is a simplified representation of the spatial distribution of the various oxidation sates in the oxides considered in this thesis. Apart from a region of suboxide sates the SiO_2 sample is expected to be stoichiometric over the extent of the oxide

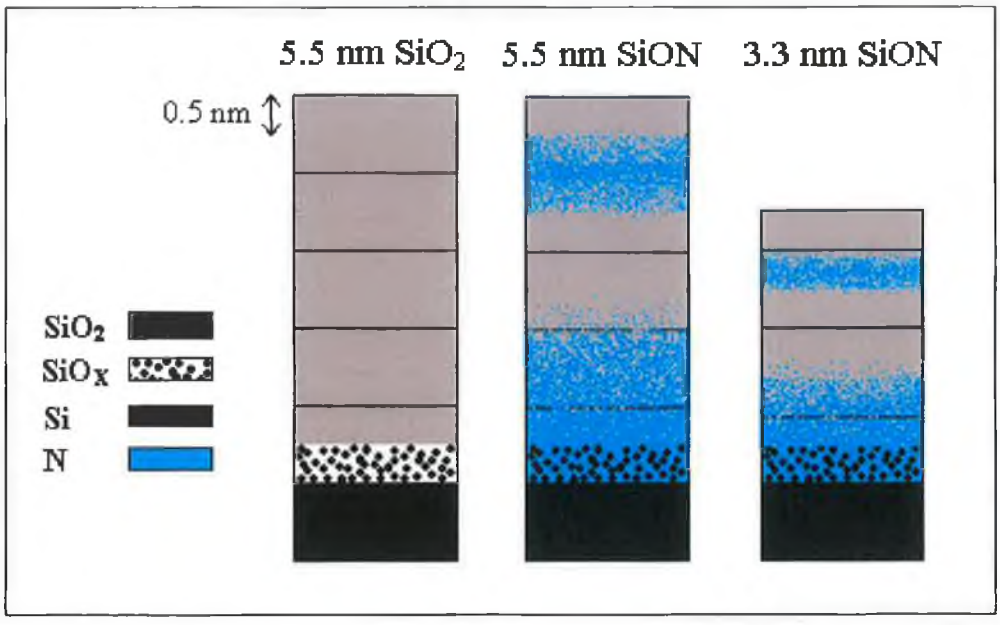

Figure 3.32 Simplified representation of the spatial distribution of the oxidation states in both the nitrided and non-nitrided samples. The nitrided regions are progressively more percolated with SiO_2 as one moves away from the nitrogen rich region to show that in such a region the nitrogen concentration is more dilute.

From consideration of the results of Grunthaner [44] and Shallenberger [20] who's samples under went a similar nitridation process (i.e. NH_3) as ours, a surface and interface rich nitrogen region is expected. This expectation was verified by the quasi depth profiles of figures 3.28 and 3.31 for the 5.5nm and 3.3nm SiON layers respectively. Figure 3.32 is unable to convey the source of the thickness dependent chemical shift seen in the N_{1s} spectral envelope. Instead it seeks to show that there is a single nitrogen chemical state, which is affected by the nitrogen concentration becoming more dilute with distance from the nitrogen rich regions. Finally, although the N concentration is largest at the interface, it is likely that both sub nitrides and sub oxides co-exist in the interfacial region. This possibility is considered further in chapter 4.

Thickness dependent chemical shift

From the behaviour of the shape and binding energy position of the N_{1s} peak with thickness and with take-off angle it was de-convoluted into two peaks. An interfacial component who's FHWM and binding energy value was chosen from the spectrum after the longest etch (thinnest sample) where it is best seen in isolation of the oxide phase. By holding the binding energy and FWHM of the interfacial N phase fixed the intensity and energy position of the N oxide phase of figure 3.23 (5.5 nm SiON) and figure 3.30 (3.3 nm SiON) resulted.

The binding energy shift of the N oxide phase was found to decrease with thickness for both samples from an initial shift of approximately 0.81 eV to a final value of approximately 0.38 eV. These values are approximate and the change in the shift with thickness only qualitative for the following reasons:

- For both samples a dramatic evolution of N_{1s} peak shape is evident for etch times of 0, 0.5, 1.0 mins and with take-off angle. These etch times represent the removal of the N rich surface region in both samples. For longer etches the contribution of the oxide related phase is diminished as the oxide is progressively removed. The implications of this for peak fitting are that after the initial evolution in the N_{1s} spectral envelope it tends towards a single phase with a resulting lack of peak structure in it's spectral envelope making it difficult to sustain the N oxide phase in the fitting software unassisted. In other words, it collapses into the adjacent interfacial peak. This is essentially the same limitation, which existed in relation to fitting interfacial sub-oxidation states in the Si_{2p} spectra unassisted due to the finite resolution of an XPS source.

- Also as proposed by Shallenberger [20] and discussed earlier the implications of a surface and interface rich N region are an initial under estimation of the interfacial phase and over estimation of the oxide related phase and due to the attenuation and lack of attenuation of the outgoing N_{1s} signals from these respective regions. This effect can be seen in figure 3.24 where the increase in N_{1s} intensity above a previous lower value from a thicker oxide thickness is evident, over the extent of the etch profile.

Also the effects of shadowing, size and position for the same sample can be seen by comparing the 0 and 60 degree of scans of the N_{1s} intensities whereas the increase in N_{1s} intensity above a previous lower value which was associated with a thicker oxide thickness is evident over the extent of the etch profile.

Stoichiometry

The interpretation of the shifted oxide related N phase has been mixed [23,24],[33]. Lu et al [33] de-convoluted the N_{1s} peak into an interfacial component (Si_3N_4 like) and attributed a second component shifted by 0.8 eV to N-O related bonds. However, this shift is smaller than that expected for a N-O related bond and there aren't any results from Lu about the thickness dependence of the value of the shifted component. Others [23],[48] interpreted the large N_{1s} line width as evidence for the presence of a twofold coordinated N atom carrying a dangling bond as in -N-Si_2 or a N-Si_2H configuration. Our results agree best with those of Bouvet et al [38] where the dispersions in the N_{1s} chemical shift results from N atoms in a N-Si_3 configuration but with a differing number of oxygen atoms in their next-nearest-neighbour shell. Replacing the second nearest neighbour silicon atoms by oxygen affects the charge transfer between Si and N [39]. In addition, there can be a variation in E_b due to core hole screening, which depends linearly on the thickness of the dielectric layer [39],[49].

It is reasonable to expect that the variations in oxygen concentrations, which affect the Si-N related chemical shift, should be detectable or be mirrored in a corresponding variation in stoichiometry.

In Figure 3.12 the effects for quantification of the freedom of peak parameters (FWHM and E_k) and the increased contributions of SiO_x and hydrocarbon contamination signals were investigated to try to recover a value of stoichiometry from the above mentioned effects. For the same recovery prescription, the stoichiometries of the 5.5 nm and 3.3 nm SiON layers shown in Tables 3.10 and 3.11 respectively were not recovered. Unlike the SiO_2 sample, a quantification standard for the oxynitride samples was not available. Also, a thick oxynitride film with a surface rich nitrogen region and a thin oxynitride film with an interfacial nitrogen rich region would allow peak parameters (IMFP, E_b and FWHM) for both regions to be established in isolation of each other.

The same behaviour as found for SiO_2 might be expected with local deviations initially and finally arising from the surface and interface N rich regions. Finally the poor behaviour of the oxynitride stoichiometry was attributed to a convolution of the thickness dependent effects outlined by Shallenberger et al [20] and the increased influence of contamination and suboxide signal with reduced thickness.

3.8 Conclusion

In investigating device grade ultra-thin oxide layers using XPS, the high quality of the oxides was affirmed by the consistency of the values of thickness, elemental composition and stoichiometry in the as-received films. The inability to detect and resolve the interfacial suboxide signal results from the large value of IMFP and finite resolution of the XPS source resulting in a lack of sensitivity. In undertaking a depth profile of the oxide, argon ion bombardment was found to be unsuitable due to the progressive modification of the photoelectron peak FWHM and the possible introduction of surface suboxide species making the detection of interfacial suboxide species more difficult. The possibility of bombardment-induced suboxides would be better-tested using synchrotron radiation and XPS measurement together. Dilute HF acid etching was found to be uniform and consistent in removing the oxide and realising a non-invasive depth profile. However, there are experimental quantification limitations arising from the increased contributions of surface contamination and interfacial suboxide species for small values of oxide thickness.

Quantification is further hindered by the inability to fit a consistent set of peak parameters over the extent of the depth profile and the tendency of the Si_{2p}^{0+} substrate FWHM to grow and the Si_{2p}^{4+} oxide peak to become poorly defined. Nitrogen was detected in dilute concentrations in the oxynitride films. Dilute HF etching revealed a surface and interface rich nitrogen region in the oxynitride films. The N_{1s} signal was de-composed into an interfacial Si_3N_4 like signal and a chemically shifted oxide phase, which was consistent with findings in the literature. Having applied the same peak constrictions as were applied to SiO_2, a reasonable behaviour in the oxynitride stoichiometry was not obtained. Potentially, SIMS or NRA analysis could help here in yielding a spatial distribution of N in the oxide. Ideally measurements at a synchrotron

radiation source where the N, Si and O windows could be seen at a reasonable resolution and in which the surface sensitivity could be tuned in order to see the as-received surface and interfacial N regions more exclusively.

3.9 References for Chapter III

1 F. J. Grunthaner, P.J. Grunthaner, Mater. Sci. Rep. **1** (1986) 65

2 Z. Lu, M. Graham, J. McCaffrey, B. Brar, L. Feldman, S. Tay, Appl. Phys. Lett. **71** (1997) 2764

3 Z. Lu, M. Graham, S. Tay, D. Jiang, J. Vac. Sci. Technol. B**13** (1995) 1626

4 D. Mitchell, K. Clark, J. Bardwell, W. Lennard, G. Massoumi, Surf. Interface Anal. **21** (1994) 44

5 J. Shallenberger, J. Vac. Sci. Technol. A**14** (1996) 693

6 R. Alfonsetti, G. Simone, L. Lozzi, S. Santucci, Surf. Interface. Anal. 22 (1994) 89

7 S. Hofmann, J. Thomass III, J. Vac. Sci. Technol. **A3** (1985) 1921

8 J. W. Coburn, Thin solid films, **64** (1979) 371

9 R. Holm, S. Storp, Phys. Scr. **16** (1977) 442

10 G. McGuire, Surf. Sci. **76** (1978) 130

11 O Benkherourou, J P Deville, Vacuum **49** (1998) 121

12 E. Paparazzo, M. Fanfoni, and E. Severini, Appl. Surf. Sci. **56-58** (1992) 866

13 E. Paparazzo, M. Fanfoni, and C. Quaresima, J. Vac. Sci. Technol. A**8** (1990) 2231

14 S. Hashimoto et al, Surf. Interface Anal., **18** (1992) 799

15 R. Behrisch, Sputtering by Particle Bombardment I. Springer Verlag, Berlin (1981)

16 R. Alfonsetti, L. Lozzi, M. Passacantando, P. Picozzi, App. Surf. Sci. **70-71** (1993) 222

17 M. Ebel, H. Ebel, A. Hofmann, R. Svagera, Surf. Intface Anal., **22** (1994) 51

18 R. Flitsch, S. Raider, J. Vac. Sci. Technol., **12** (1975) 305

19 M. Hecht, F. Grunthaner, P. Pianetta, L. Johansson, I. Lindau, J. Vac. Sci. Technol., A**2** (1984) 584

20 J. Shallenberger, S. Novak, D. Cole, J. Vac. Sci. Technol. A**17** (1999) 1086

21 F. J. Grunthaner, P.J. Grunthaner, R. Vasquez, B. Lewis , J. Maserjian, A

Madhukar, Phy. Rev. Lett. **43** (1979) 1683

[22] Z. Lu, S. Tay, T. Miller, T. Chiang, J. Appl. Phys. **77** (1995) 4110

[23] E.C. Carr, and R.A. Buhrman Appl. Phys. Lett. 63 (1993) 54

[24] R. I. Hegde , P. J. Tobin, K. G. Reid, Appl. Phys. Lett. **66** (1995) 2882

[25] Y. Yoriume, J. Vac. Sci. Technol. B**1** (1983) 67

[26] G. Lucovsky, Y. Wu, Microelectronics Reliability **39** (1999) 365

[27] C Mian, I Flora, Solid-State Electronics **43** (1999) 1997

[28] G. Lucovsky, J. Non Cryst Solids **254** (1999) 26

[29] S. Novak, Appl. Surf. Sci **175** (2001) 678

[30] H. Hwang, W. Ting, B. Maiti, D. Kwong, J. Lee, Appl. Phys. Lett. **57** (1990) 1010

[31] H. Lu, E. Gusev, T. Gustafsson, E. Garfunkel, M. Green, d. Brasen, L. Feldman, Appl. Phys. Lett **69** (1996) 2713

[32] H. Tang, W. Lennard, M. Zinke, I. Mitchell, L. Frldman, M. Green, D. Brasen, Appl. Phys. Lett. **64** (1994) 3473

[33] Z. Lu, S. Tay, R. Cao, P. Pianetta, Appl. Phys. Lett, **67** (1995) 2836

[34] M. Bhat et al, Appl. Phys. Lett. **64** (1994) 1168

[35] J. Chang et al, J. Appl. Phys. Letts. **87**, (2000) 4449

[36] R. Browning, M Sobolewski, C. Helms, Phys. Rev. B **38** (1998) 13407

[37] Y. Miura, H, Ono, K Ando, Appl. Phys. Lett. **77** (2000) 220

[38] D. Bouvet et al, J. Appl Phys. **79** 7114 (1996) 7114

[39] G. Rignanese, A. Pasquarello, Phys. Rev. B**63** (2001) 075307

[40] G. Tallarida, F. Cazzaniga, B. Crivelli, R. Zonca, M. Alessandri, J. Non Cryst Solids **245** (1999) 210

[41] S. Miyazaki, T. Tamura, m. Ogasawara, H. Itokawa, H. Murakami, M. Hirose, Appl. Surf. Sci. **159** (2000) 75

[42] A. Kamath, D. Kwong, Y. Sun, P. Blass, S. Whaley, J. White, Appl. Phys. Lett. **70** (1997) 63

[43] M. Bersani, L. Vanzetti, M. Sbetti, M. Anderle, Appl. Surf. Sci. **144** (1999) 301

[44] R. Vasquez, M. Hecht, F. Grunthaner, Appl. Phys. Lett. **44** (1984) 969

[45] R. Vasquez, A. Madhukar, F. Grunthaner, M. Naiman, Appl. Phys. Lett. **46** (1985) 361

[46] R. Vasquez, A. Madhukar, J Appl. Phys. **60** (1986) 234

[47] R. Vasquez, A. Madhukar, F. Grunthaner, M. Naiman, J. Appl. Phys. **60** (1986) 226

[48] S. Kaluri, D. Hess, Appl. Phys. Lett. **69** (1996) 1053

[49] G. Cerofolini, A. Caricato, L. Meda, N. Re, A. Sgamellotti, Phys. Rev. B**61** (2000) 14157

Chapter 4

A chemical state investigation of the SiON and SiO_2 interface using synchrotron soft X-ray photoelectron spectroscopy

4.0 Introduction

The final oxide realised from thermal oxidation of silicon is dependent in a complex manner on the initial surface chemical and physical state (morphology and cleanliness), the growth conditions (substrate temperature / pressure of oxidising species) and post oxidation treatment (high temperature anneal). Oxidation is an interfacial phenomenon, the interface formed is distributed spatially and is comprised of structural transition regions on both sides of the interface, which sandwich a chemical transition region. Initially the theoretical models of the SiO_2/Si interface in the literature are considered in the context of their predictions and limitations and in order to form an expectation of the interfaces examined in this thesis. The mechanism of uniform oxide removal is outlined and surface passivation using HF acid and it's role in the preparation of a suitable surface for oxidation. The evolution of the interface during oxidation at various stages of oxidation is considered in terms of initial surface morphology and the role of high temperature post oxidation treatment. The roughness of the oxide surface during wet chemical treatment is measured using AFM.

The results of soft X-ray (synchrotron) photoemission analysis of the SiO_2 interface are presented and discussed. In order to realise suitable thickness ($d<0.17$ nm) dilute (0.5% HF) acid etching was used to gradually profile the oxide. With the tuneable surface sensitivity and high resolution of synchrotron radiation, the distribution and relative intensity of sub-oxidation states in the interfacial region were resolved and measured. From comparison with the established SiO_2 results, an attempt was made to elucidate the interfacial Si-N bonding relationship in the Si_{2p} spectra of the nitrated samples.

4.1 Theoretical interpretation of interface

The investigation of the Si/SiO_2 interface experimentally is difficult because the interface is buried beneath an amorphous overlayer; also its spatial extent is small and is comprised of both chemical and structural transition regions. This is primarily because of the inability of the oxide and substrate to form an epitaxial relationship. Most theoretical models work by "fusing" into a slab, crystalline silicon (diamond structure) and a crystalline form of SiO_2 (e.g. tridymite or cristobalite). In order to emulate the amorphous nature of the oxide a randomising process of bond switching (where one of the second neighbours of a randomly chosen atom is switched to become it's first neighbour, and that of the first neighbour becomes the second) and bond conversion (where a randomly chosen Si-Si or Si-O-Si bond is swapped with a neighbour bond of opposite type) is applied to the crystalline SiO_2 [1]. After each move, the structure is then relaxed and the difference between initial and final energies is used to decide whether the move is acceptable.

Theoretical models have sought to model the interface between silicon and SiO_2 in order to examine the abruptness of the interface (i.e. is it abrupt or is it graded?) and the distribution of the bonding states random bonding model (RBM) or random mixture model (RMM). It is useful before considering ours and other's experimental results to summarises the findings of theoretical models.

Vanderbilt et al [1] in a Monte Carlo approach generated an interface, which was contained within 2 nm of the substrate with the Si^{1+}, Si^{2+} states lying closest to the substrate and the Si^{3+} lying further out. This is a relatively wide interface and as discussed later in the chapter, the experimental observation of Si protrusions as far as 3 nm into the oxide can explain the distribution of the Si^{3+} state and the results are in qualitative agreement with XPS and PES studies. The model suggests a very large density of sub-oxide states, 4.7 monolayers compared to the 1 and 2 monolayer values found experimentally. The model doesn't give an indication of a structural transition in the near interfacial region as the distribution of Si-O-Si bond angles is centred at 140^o, which is the bulk oxide value. The convergence of the values on 140^o is testament to the usefulness of the approach in modelling the oxide. In other theoretical studies, Pasquarello et al [2,3] attached tridymite (a crystalline form of SiO_2) to Si(100) and

observed a range of suboxide states for the interface formed. The model was believed to be artificial and introduced significant stress across the interface. Subsequently using a molecular dynamics approach they observed an abrupt interface (0.5 nm) with a relatively small concentration of suboxides (1.5 monolayers).

Demkov et al [4] has recently pointed out the limitations of the traditional theoretical approaches of interfacial structure modelling considered above, suggesting that some of the results are inherent or "built into" in the construction process. For example, the generation of a continuous random network of structures free of dangling bonds is an inherent consequence of the Monte Carlo process used by Vanderbilt [1]. Also, the abruptness of the interface observed by Pasquarello in his approach.

Hirose et al [5] calculated the electronic structure of the O_{2s} and valence band using a first principle molecular orbit calculation for a silicon/oxygen cluster ($Si_2O_7H_6$). In experimental valence band studies using monochromated XPS he subtracted the SiO_x and substrate valence band signal from a 0.8 nm oxide. In the resulting spectrum the energy separation between the O_{2s} and the top of the valence band was consistently found to be 0.2 eV less than the separation in the bulk oxide. He attributed this reduction to the extent of a shift associated with a inter tetrahedron Si-O-Si bridging bond angle change of 140^o to 130^o in SiO_2. This result is an experimental verification of Grunthaner's [6] structural transition region above the suboxide region, where compressive stress results in the formation of smaller tetrahedral rings and the resulting reduction in bridging bond angle gives rise to a second component in the Si^{4+} and O_{1s} peaks as described by the structure induced charge transfer model (SICT). This was a remarkable result because of the agreement of the theoretical and experimental values and because it affirms the existence of a structural transition region in the near interfacial region.

There is a diversity in the results of theoretical models of the interface which likely arises from the difficulty in modelling such a complex interface which in reality is realised at high temperature underneath a growing oxide. However, the models demonstrate the non-existence of an epitaxial relationship between silicon and it's oxide and the resulting suboxide and structural transition regions.

As a final theoretical consideration we outline the two major perspectives on suboxide distribution at the interface, namely the RBM and the RMM. It is useful to consider these models as they describe the distribution of bonding tetrahedra in amorphous alloys based on their stoichiometry.

The distribution of bonding states in an oxide alloy (SiO_x) indicates whether silicon has segregated from an oxide resulting in Si clusters in a SiO_2 matrix or whether it remains sub-stoichiometric in the basic tetrahedral bonding geometry. In the interfacial chemical transition region of the oxides studied in this thesis an alloy exists where the number and type (i.e. Si, O, or N) of silicon's first co-ordination neighbour changes giving rise to a distribution of sub-oxidation states which we attempt to measure using photoemission.

In the RBM there is a statistical distribution of the five bonding states SiO_x (i.e. Si^{0+}, Si^{1+}, Si^{2+}, Si^{3+},Si^{4+}). Hubner [7] and Martinez et al [8] revealed the relationship between x and the concentration of the individual bonding units. The relationship is obtained from considerations based on the statistical replacement of Si-Si bonds in amorphous Si by Si-O-Si bonds while maintaining the fourfold co-ordination of silicon and the two co-ordination of oxygen (similar to the bond switching and conversion considered earlier). The intensities of the individual states is given by equation 4.0.

$$I_n(x) = \frac{4!}{(4-n)!}\left(\frac{x}{2}\right)^2\left(1-\frac{x}{2}\right)^{4-n} \qquad \textbf{Equation 4.0}$$

The second model is the RMM. Here the alloy segregates into two phases; crystalline silicon and amorphous SiO_2, and so there are only two Si_{2p} (Si^{0+} and Si^{4+}, 2 eV wide and 4 eV apart) peaks in the photoemission spectra instead of the five associated with the RBM. The intensities of the two states from the RMM is given by equation 4.1.

$$I_0 = 1-\frac{x}{2} \; and \; I_4 = \frac{x}{2} \qquad \textbf{Equation 4.1}$$

Figure 4.0 (a) shows a plot of the relative concentration of the intensities for the RMM

(dashed lines) and the RBM (solid line). Figure 4.0 (b) shows the relative concentration of intensities from experimental fits of SiO_x layers prepared in-situ by Bell and Ley [9] and examined by photoemission. The inability to fit core level spectra with just the two peaks of the RMM and the good agreement between theoretical and experimental distribution of suboxide intensities confirms the RBM distribution of oxidation states.

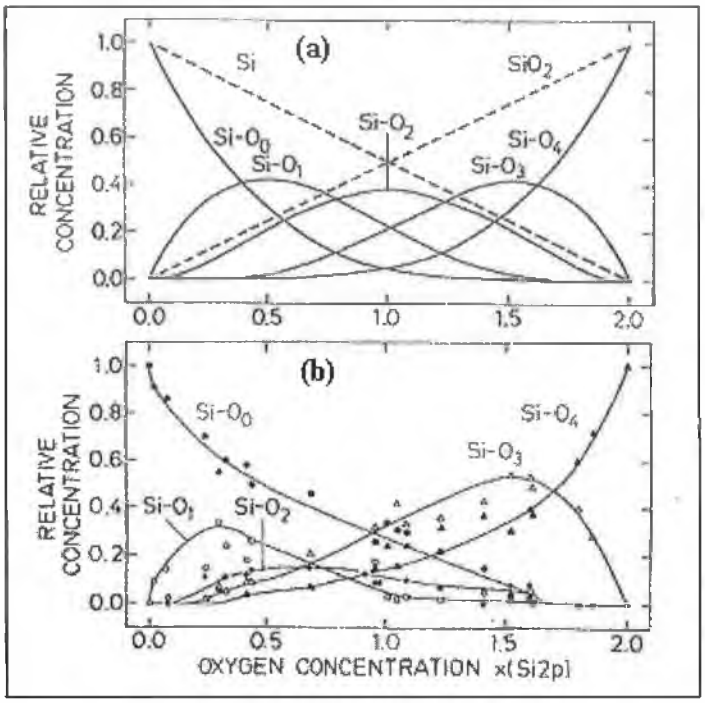

Figure 4.0: (a) Relative concentration of the basic bonding units (tetrahedra) shown by solid lines for the random-bonding model (RBM) and by dashed lines for the random mixture model (RMM). b) Experimental relative concentrations of the basic bonding units vs oxygen concentration (Bell [9]).

4.2 Re-examination of Si_{2p} chemical shift interpretation

From the above theoretical considerations the expectation of the distribution of the oxidation states in the interfacial region is that of the RBM where there is a statistical distribution of the five stoichiometries $SiO_{x\ (x=0,1,2,3,4)}$. The experimental measurement of the relative intensities of the interfacial oxidation states is an optimal process in that there is the need to be able to resolve the overlapping states and to exclusively illuminate the interfacial region. In the XPS analysis presented in chapter 3, it was not possible to resolve the individual oxidation states and after wet chemical profiling to the

interfacial region, the oxide peaks were poorly defined due to the large IMFP. Researchers with access to a synchrotron source optimise surface sensitivity by tuning the photon energy window in the range hν=120 to 140 eV because of the short IMFP for 2p electrons with kinetic energies between 20 and 40 eV [10]. The resolution typically achievable in soft X-ray synchrotron studies at these photon energies are normally less than 150 meV. Before considering the mechanism by which oxide thicknesses comparable to such an optimal sampling depth is achieved, the interpretation of soft X-ray Si_{2p} spectra in terms of its limitations and recent revision is considered.

In chapter 1, the ball and stick model (see figure 1.1) of the $Si(100)/SiO_2$ interface was ideal, in the sense that it was atomically abrupt and all the dangling bonds were hydrogen terminated. In their pioneering synchrotron work on ultra-thin Si(100) and Si(111) interfaces, Himpsel et al [10] detected all three possible suboxide states

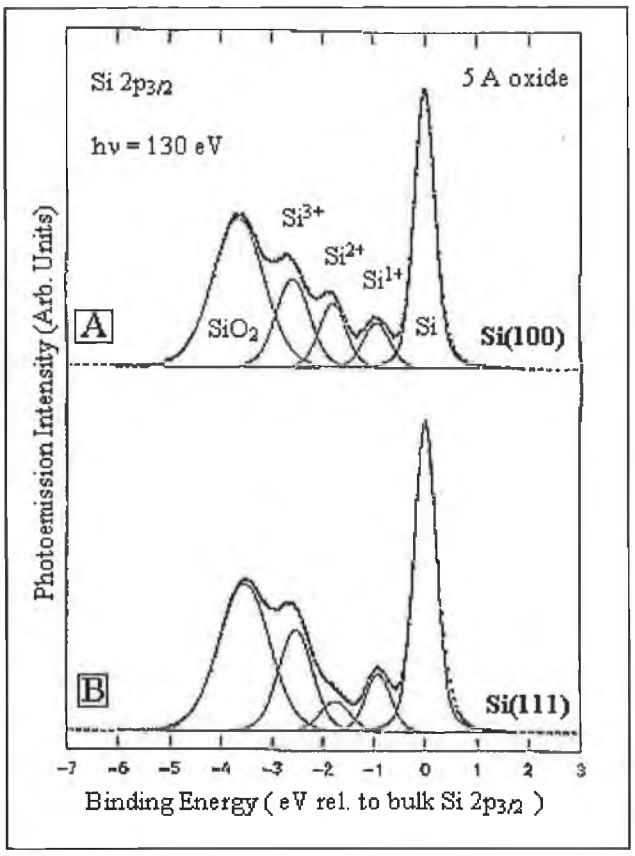

Figure 4.1: The distribution of silicon oxidation states for 0.5 nm dielectric layers grown in UHV on atomically clean Si(100) and Si(111) (Himpsel [10])

(Si^{1+}, Si^{2+}, Si^{3+}) in the Si_{2p} spectrum as shown in figure 4.1(a) and (b) for and Si(100) and Si(111) respectively, where each state Si^{n+} corresponds to a silicon co-ordinated to n oxygens and (4-n) silicons. The presence of the Si^{1+} and Si^{3+} states coupled with their being distributed within 2 nm of the interface showed the interface to be non-ideal and non-abrupt. Himpsel proposed that the chemical shift experienced by a silicon atom directly bonded to a more electronegative oxygen should scale linearly with the number of first-nearest-neighbouring oxygens, with a shift per oxygen of ~ 1 eV.

The experimental chemical shifts of the Si^{1+}, Si^{2+}, Si^{3+} and Si^{4+} oxidation states relative to the substrate Si^{0+} were 0.95, 1.75, 2.48 and 3.9 eV respectively which shows the linear relationship to be only approximate. This model has enjoyed widespread acceptance and is universally utilised in the assignment of Si_{2p} core level oxidation shifts. Note the model perceives the contribution of second-nearest oxygen bonds to be negligible. Holl and McFeely [11-13] using a cluster model system, sought to investigate the influence of the second-nearest-neighbour oxygens on the Si_{2p} core level shifts. The model consisted of a cubic spherosiloxane molecule whose sides are spanned by Si-O-Si linkages and whose vertices consisted of H-Si-O_3 units as shown in figure 4.2 [13].

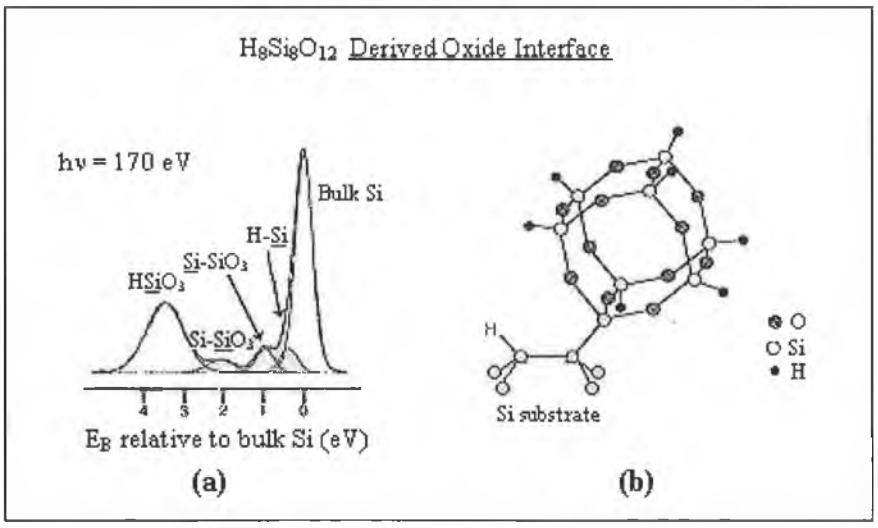

Figure 4.2: (a) $H_8Si_8O_{12}$ cluster derived silicon/silicon oxide interface. (b) schematic of cluster attached to Si(100) (Mc Feely [13])

They argued that exposure of the molecule to a clean Si(100) surface would result in attachment of the intact cube (single vertex attachment) (see figure 4.2 (b)) to one side of a Si dimer on the (2x1) reconstructed surface along with the formation of a Si-H bond on the other end of the dimer.

For such a structural model, the linear oxidation model predicts a single significant Si_{2p}^{+3} oxidation state shifted by 3.5 eV, given that the eight silicons in the cube are all directly co-ordinated to three oxygens. Also present in the spectrum were two additional features shifted by 1.0 and 2.2 eV. The latter was attributed to the silicon of the cube attached to the surface. The former was attributed to the surface silicon under the influence of the second-nearest-neighbour oxygen atom of the cube. These findings called into question the Si_{2p} peak assignments of previous high-resolution oxidation studies in the literature.

However, Raghavachari et al [14] through surface infrared measurements and quantum cluster calculations revealed that although the single vertex attachment is thermodynamically favoured, cube decomposition resulting in surface species via Si-O bond scission is motivated by kinetic factors. They found excellent agreement between XPS data and core level calculations of the chemical shifts associated with these surface species. Pasquarello et al [15] contributed to the defence of the linear oxidation model by showing through ab-into slab calculations that second-nearest-neighbour effects on the core level spectrum of silicon are negligible. From the above discussion of peak assignment the interpretation of Si_{2p} core level shifts adopted in this thesis are based on the linear oxidation model with a shift of 0.9 eV per oxidation state.

4.3 Wet chemical processing

Here briefly, the mechanism by which hydrofluoric acid removes the oxide to uncover the underlying substrate and the role it plays as a surface passivator is considered. Himpsel's [10] oxides were grown on atomically clean, reconstructed silicon surfaces in UHV. At atmospheric pressure a clean Si surface quickly forms a native oxide due to the chemically reactive un-terminated dangling bonds. The high quality oxides of modern sub micron fabrication processes (which operate in clean environments at

atmospheric pressure) are dependent on the integrity of the underlying substrate because it is at the substrate where oxidation starts.

The ex-situ engineering of flat and stable substrates was achieved after much research based on the ability of hydrofluoric acid to remove silicon's oxide and keep the underlying silicon surface chemically inert (passivated). The passivation of silicon surfaces by HF acid and the realisation of a stable surface was initially attributed to fluorine termination (teflon like) of the surface [16]. After all, the Si-F bond (6 eV) is more stable than the Si-H bond (3.5 eV). Ubara et al. [17] recognised that the Si-F bond is highly polar and causes polarisation of the Si-Si back bonds exposing them to further nucleophilic attack by the acid. The reaction is given below.

$$Si_{bulk} - Si - Si^{\delta+} - Si^{\delta-} + HF \rightarrow Si_{bulk} - Si - H + F - Si - F$$

This reaction is repeated for each of the three backbonds of the Si atom, giving SiF_4 as a final product and a hydrogenated surface. The process is illustrated in figure 4.3 below. Dilute HF has been shown to roughen the Si(100) surface on an atomic scale [18-20]. Immersion of silicon samples in concentrated HF (49%) etches the silicon dioxide without attacking the Si surface and in this way uncovers the buried Si/SiO_2 interface [21,22]. A key finding in the investigation of wet chemical preparation effects on Si

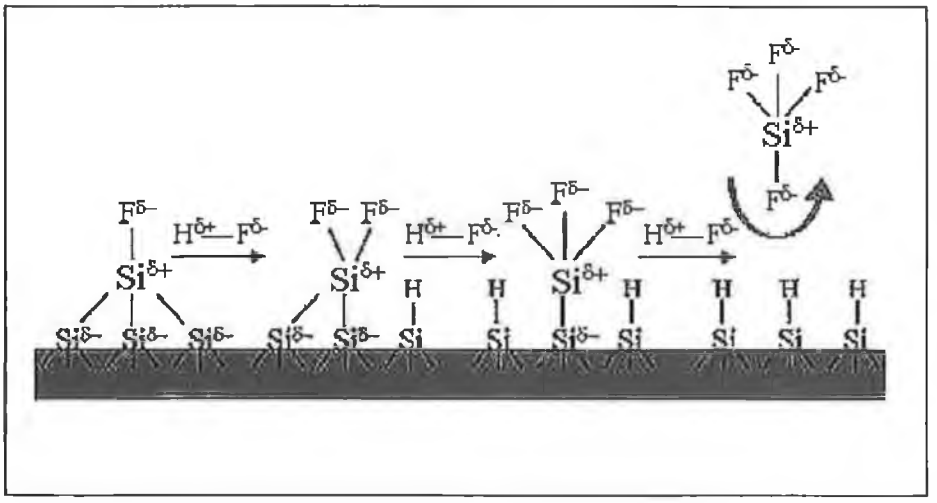

Figure 4.3: Schematic illustration of process of oxide removal and surface passivation resulting from polarisation of the Si-Si back bonds and subsequent nucleophilic attack by the acid (Ubra [17]).

surface morphology prior to oxidation, was based on the modification of the etch pH and the addition of impurities [23,24]. Much smoother surfaces could be realised through such modifications. For example an atomically flat hydrogen terminated silicon H-Si(111) surface could be realised after immersion in a buffered ammonium fluoride HF solution with a pH of 7.8. Hagishi and Chabel [23] in an STM and infrared absorption study obtained large (100 nm wide) unreconstructed Si(111) terraces with ideal monohydride termination and separated by atomically sharp steps as shown in figure 4.4. Hattori [24] exploited the polarisation dependent interaction of the electric field wave vector of infrared light in selectively exciting H bond vibrational modes in the surface region.

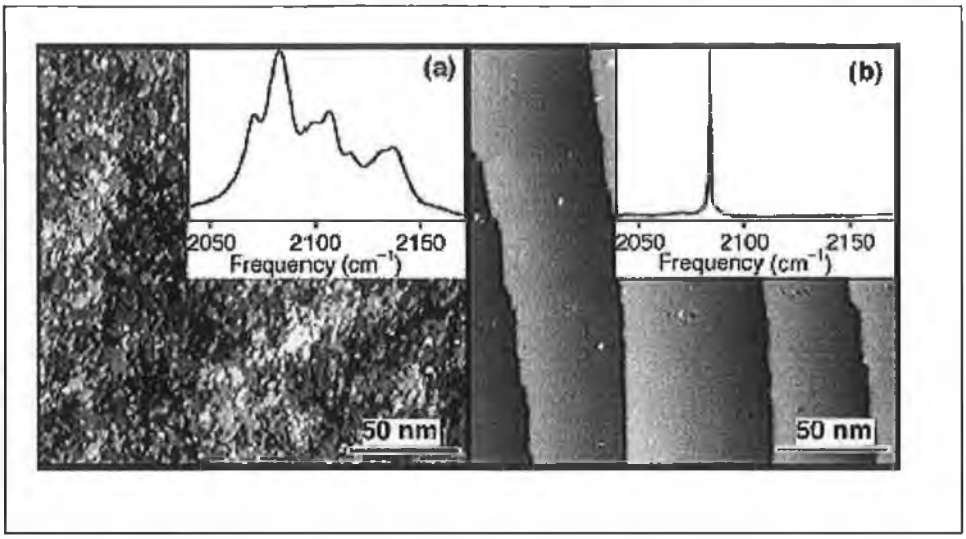

Figure 4.4: STM images of Si(100) after an etch in (a) concentrated HF, (inset) FTIR spectrum showing the presence of mono,di and tri hydrides. (b) Buffered ammonium fluoride HF solution, (inset) FTIR spectrum showing the presence of monohydrides only which is characteristic of a smooth surface (Chabel [23]).

Basically the absorption of p-polarised (E vector parallel to the plane of incidence) infrared light and lack of absorption of s-polarisation (E vector normal to the plane of incidence) infrared light indicates that the electric dipole of the Si-H bond has only a component normal to the Si(111) surface characteristic of monohydride coverage, see figure 4.5 (a). Where as on the surface etched in concentrated HF, mono, di and tri hydrides were detected (as found by Chabel et al [23], see figure 4.4 (a) inset). Wet chemical optimisation of the Si(100) surface cannot achieve an atomically flat surface as indicated by the presence of mono, di and tri hydrides in both polarisations in figure 4.5 (b).

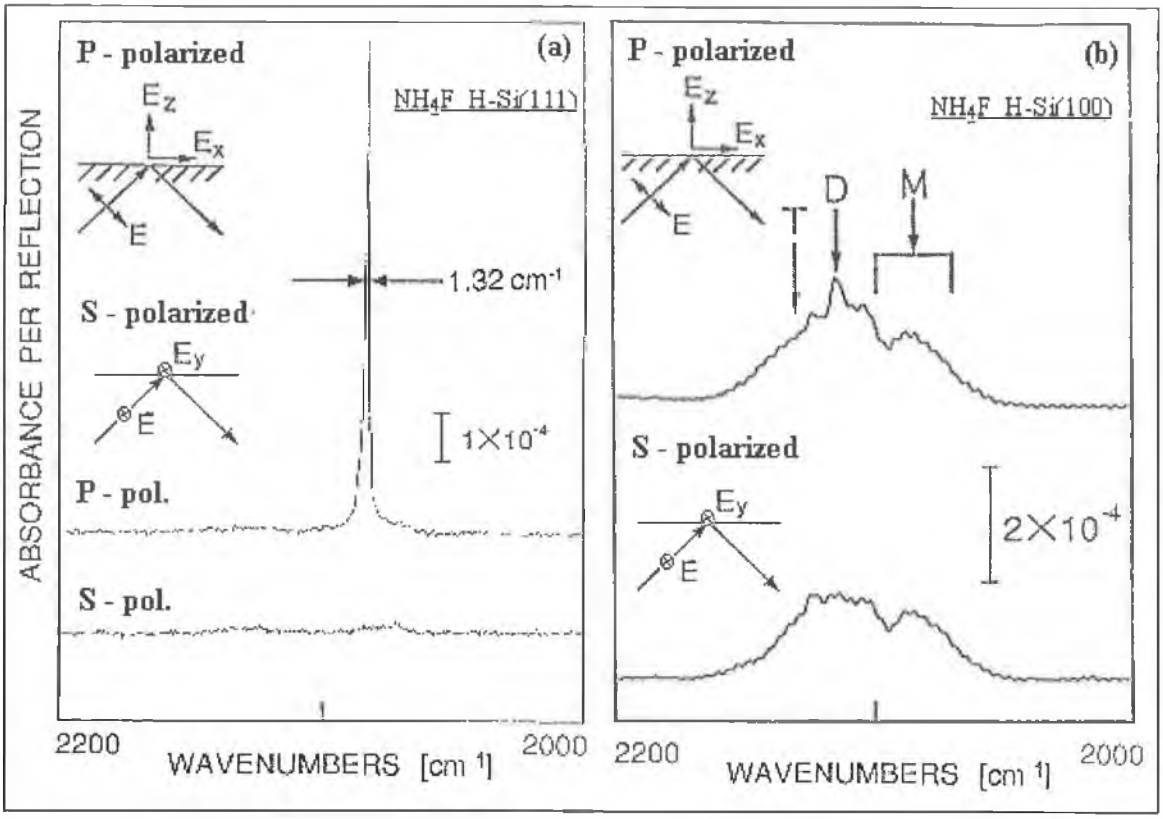

Figure 4.5: Polarisation dependent interaction of E field with H related surface bonds after oxide removal and passivation using an ammonium fluoride HF solution. (a) for Si(111) a smooth surface can be achieved. (b) For Si(100) surface microughness as evidenced by mono,di and tri hydrides is inevitable from the etch (Hattori [24]).

4.4 Surface morphology / Oxidation induced roughness

Extensive investigation of initial surface condition (roughness) and crystal orientation (<111> or <100>) has revealed how the interface and oxide surface evolve during oxidation and that they are dependent on initial conditions. Hatorri et al [25-28], have undertaken substantial studies of the oxidation of Si(111) and Si(100) in terms of growth mode and the effect of surface roughness. By measuring the distribution of oxidation states at different thickness (0.5, 1.0, 1.7 and 2.0 nm) during oxidation on Si(111), Hatorri, figure 4.6 (b), observed that the normalised spectral intensity of the suboxides saturated at 0.5 nm consistent with his expectation of an abrupt interface. Although the total amount of suboxide saturates at 0.5 nm, the areal density of Si^{1+} and Si^{3+} repeatedly increased and decreased with oxide thickness and with a period of 0.7 nm for thickness less than 1.7 nm. Also the Si^{1+} and Si^{3+} areal intensities oscillated in

antiphase, see figure 4.6 (c). If the interface was atomically flat, the minimum amounts of Si^{1+} and Si^{3+} would be zero and the amount of Si^{2+} would be close to zero at every stage of oxidation. In order to explain the coexistence of Si^{1+} and Si^{3+}, Hattori considered the existence of monatomic steps at the interface at every stage of oxidation.

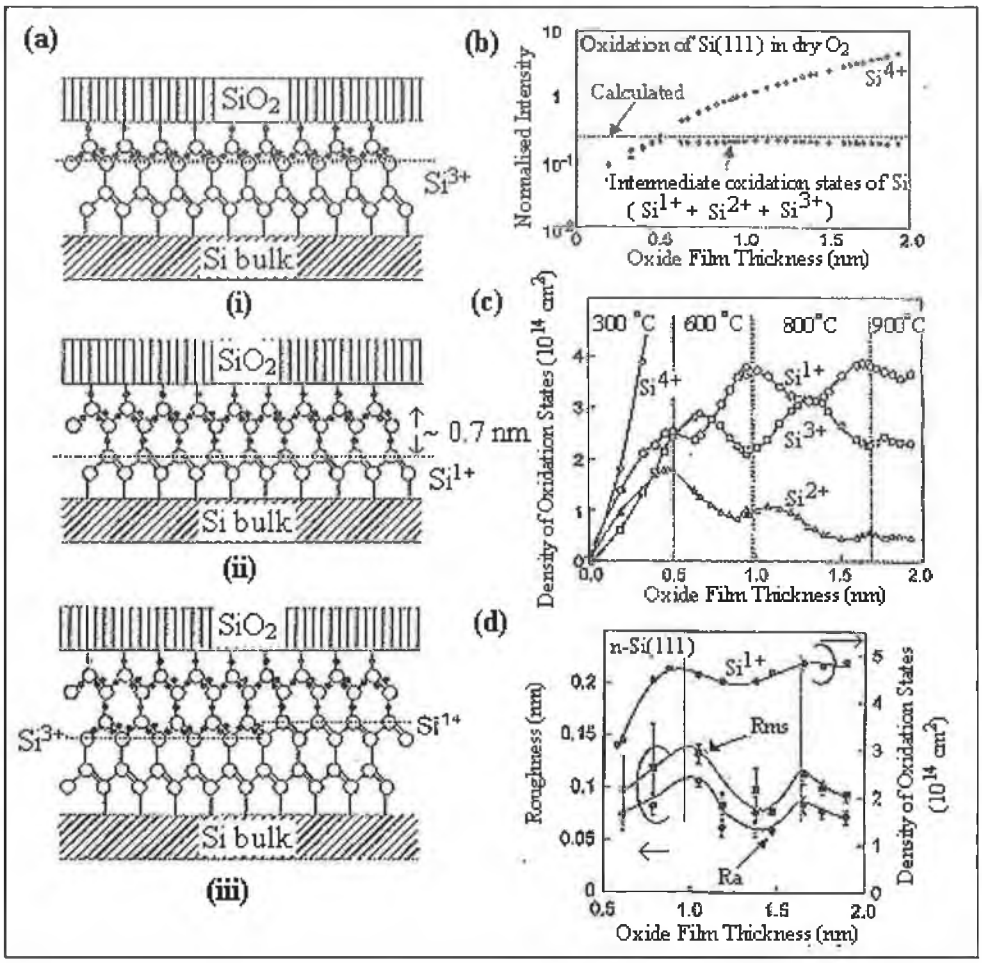

Figure 4.6: (a) Atomically flat SiO_2/Si(111) interface structure: (i) consisting only of Si^{3+}; (ii) consisting only of Si^{1+}; (iii) with a monatomic step. (b) Normalised spectral intensity of the Si^{4+} and summation of intensities for all suboxides as a function of oxide film thickness. The dashed lines show the normalised spectral intensity calculated for abrupt interface. (c) Dependence of areal densities of Si^{1+},Si^{2+},Si^{3+} and Si^{4+} on thickness. (d) Two kinds of surface microughness of oxide formed on Si(111) and the density of Si^{1+} shown as a function of oxide film thickness (Hattori [26,25]).

Oxidation occurs locally on the surface "layer by layer" with the monatomic step density decreasing with increased thickness. Hattori using non-contact AFM found that the surface micro-roughness changed periodically with the progress of oxidation and could be correlated, figure 4.6 (d), with the periodic changes in the amount of Si^{1+}.

He explained this result in terms of the oxidation mechanism. In forming the Si^{1+} state (by the insertion of an oxygen atom between two Si atoms consisting of a Si-Si bond orientated along the <111> direction) the interface expands the oxide network only along the <111> direction, while in the case of Si^{3+} formation the insertion of an oxygen atom between two Si atoms consisting of a Si-Si bond at the interface expands the oxide network mostly along the direction perpendicular to <111>. The formation of Si^{1+} at the interface results in an increase in surface micro-roughness caused by the formation of protrusions on the oxide surface.

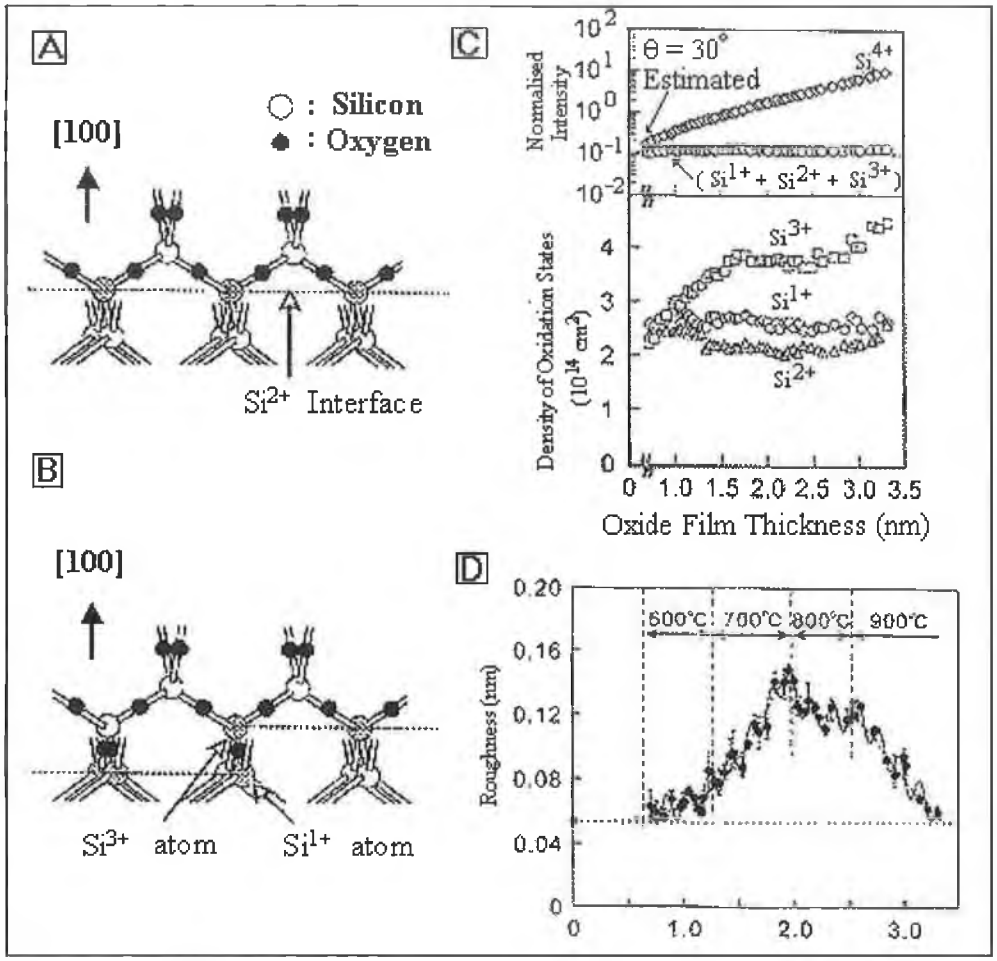

Figure 4.7: Atomically flat SiO_2/Si(100) interface structure consisting of (a) Si^{2+} only and (b) with a monatomic step. (c) (Top) Thickness dependence of normalised spectral intensity of Si^{4+} and suboxides normalised by the Si^{0+} intensity. The dashed line is calculated for an abrupt compositional transition. (Bottom) thickness dependence of areal densities of Si^{1+}, Si^{2+} and Si^{3+}. (d) changes in rms surface roughness with respect progression of oxidation (Hattori [28]).

For Si(100), periodic changes in interface composition with the progress of oxidation are not expected if the interface consists only of Si^{2+}, as in figure 4.7 (A) " the ideal case", and so no oscillation in surface roughness is expected. An oscillation in surface microroughness, figure 4.7 (d), with a period of 0.19 nm up to a thickness of 1.2 nm was observed by Hattori for Si(100). He suggested that a layer by layer reaction occurs uniformly at the Si(100)/SiO_2 interface on an atomic scale with monatomic steps, figure 4.7 (b). When one Si layer is completely oxidised the surface roughness must be the smallest. When another half Si layer is oxidised the surface roughness must be largest. Figure 4.7 (c) shows the areal densities of sub-oxidation states. Like the Si(111) interface they saturate at a thickness of 0.5 nm consistent with an abrupt interface. Hattori has investigated the evolution of roughness with oxidation. However, not all thicknesses were realised at the same temperature. Figure 4.8 shows the distributions of heights on the sample surface as measured by AFM at thicknesses of 0.83, 1.53, 1.92, 2.28, 3.15 nm which where grown in the temperature regions of 300°C-600°C, 600°C-700°C, 700°C-800°C, 800°C-900°C, 900°C-1000°C respectively.

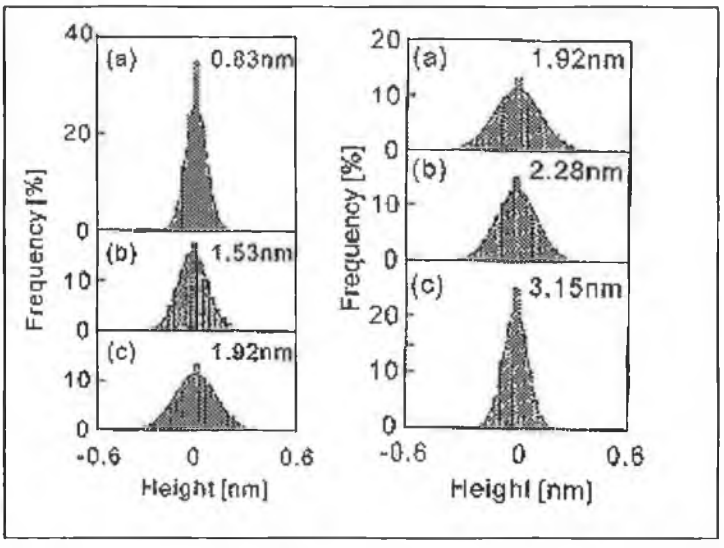

Figure 4.8: Experimental AFM height distributions for different oxide thicknesses (Hattori [28]).

The RMS roughness is plotted for these temperatures and thickness regimes in figure 4.7 (D). Above 1 nm (the thickness of the transition layer) the oxide "relaxes" the oxidation volume induced stress (due to Si/SiO_2 lattice mismatch) with an increase in the broadness of the surface height distribution with increasing thickness at 700 °C.

The FWHM of the height distribution decreases and saturates at 800° C. After subsequent oxidation at 900 °C the FWHM further decreases until the roughness is on the order of the single atomic-step height on the Si(100).

The surface roughness was found to oscillate with constant amplitude and with a period of 0.19 nm up to a thickness of 3.15 nm, which is produced by the layer-by-layer oxidation reaction at the interface (which occurs on an area of 5 nm^2) at 700 °C and increases with temperature.

An attempt to wet chemically profile through an oxide gives rise to a number of questions based on the above considerations, which are. Will the etching process roughen the surface? Using concentrated HF can the original oxide morphology be uncovered? Will the original surface morphology be that of the final surface? The possibility of etch induced roughness is of concern because in soft X-ray photoemission analysis the outer atomic layers are probed due to the short IMFP of low kinetic energy electrons. Surface roughness will lead to an increase in peak FWHM and severe roughening would undermined thickness calculations due to local variations in oxide thickness. Whether or not the growing oxide conserves the original interface morphology or as predicted by the Sune et al [29] model it finishes with a flat surface irrespective of the initial surface roughness resulting in local oxide thickness variations, see figure 4.9(c), has huge implications for final device operation given the (exponential dependence) sensitivity of tunnelling current to thickness variations. This issue has been resolved to some extent by the results of Hattori above. Also, the observation of modulations in the Fowler Nordheim tunnelling current through oxides which were grown on purposefully roughened Si surfaces prior to oxidation by Irene et al [30] showed no dependence of oscillation amplitude on roughness. According to the Sune model the distribution of oxide thickness would "de-phase" tunnelling electrons and thus rougher samples should exhibit a larger dampening in the tunnelling current oscillation amplitude.

Before considering our oxide roughness results in the context of the above, it is useful to examine the effect of temperature on roughness given that the oxides studied in this thesis were grown at high temperature and have undergone a high temperature post oxidation anneal. Hattori [28] above, figure 4.7(d), observed a decrease in surface

microroughness for oxidation at high temperatures. Carim and Sinclair [31] proposed an explanation from their observation of roughness behaviour with oxidation temperature using transmission electron microscopy (TEM). Figure 4.9(a) shows a high-resolution micrograph of the interface in which the silicon protrusions from the substrate are clearly visible. Carim suggests the degree of interface roughness is decided by two competing processes. Those which contribute to interfacial aspirates (initial surface irregularities, local fluctuation in interface reaction rate) and those which alleviate roughness (the transition to diffusion limited growth during oxidation, stress relaxation at high temperatures or long times by viscous flow and de-localisation of strain during growth). During oxidation, expansion occurs and creates stress, see figure 4.9(b) in the oxide with lateral compressive strain in the oxide and tensile strain in the near interface silicon. From consideration of the increase in free volume associated with protrusions, Carim suggested that the interface oxidation reaction rate was accelerated in flat regions between protrusions making the protrusions more pronounced as oxidation progressed.

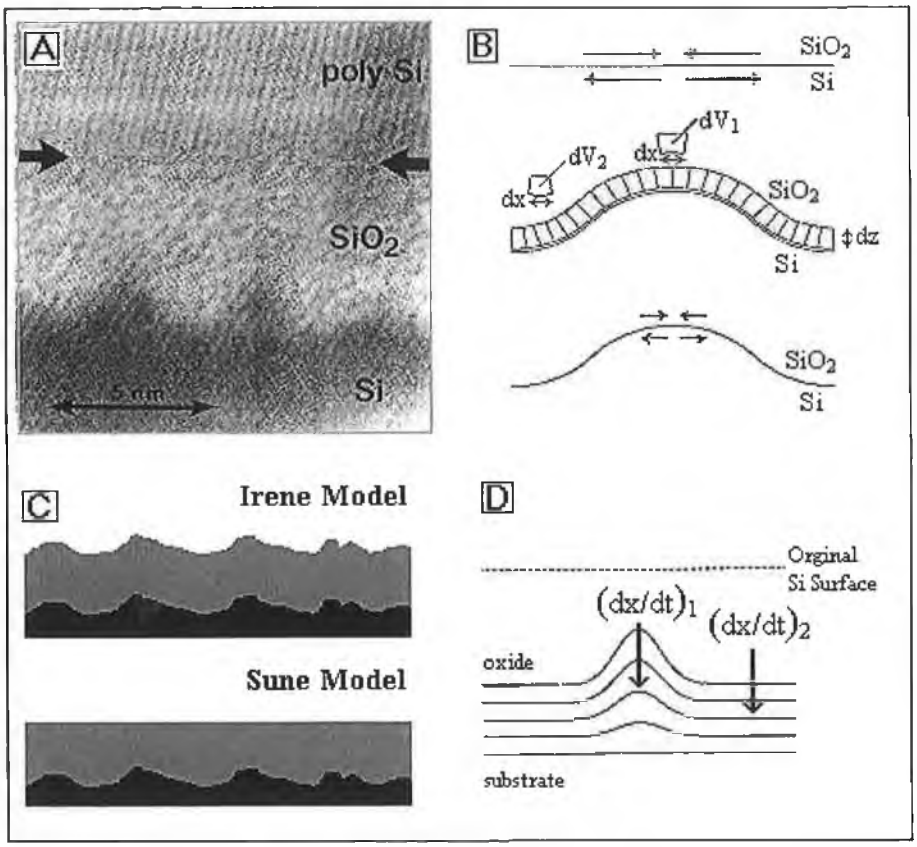

Figure 4.9: (a) High-resolution transmission electron micrograph indicating non-uniform oxidation resulting in roughness of the substrate/oxide interface. (b) Changes in the substrate and oxide strains resulting from differences in accessible volume at protrusions. (c) Growth models for the oxide. (d) Reduction of interfacial protrusions during continued oxidation requires accelerated oxidation at the asperities with respect to the flat surface (Carim [31]).

The interface reaction rate variations lose their significance as the supply of oxygen to the interface becomes rate diffusion limited leading to a greater oxidation rate under the thinner oxide at protrusions, figure 4.9(d). The final consideration in the interplay between roughening and smoothing is the relaxation of stress at high temperatures with the onset of the viscose flow region in the oxide where the reduction of planar interface stress and localised stress concentrations assist in the redistribution of silicon atoms away from protrusions by interfacial diffusion. Thus, ultimately the effect of a long anneal at high temperature is to reduce interface roughness.

4.5 Atomic Force Microscopy Analysis

The following is an account of our AFM analysis of oxide morphology and it's evolution during wet chemical etching. An AFM image is rendered through the electro-mechanical interaction of a sharp (radius of curvature of tip ~ 30 nm) vibrating (at a resonance frequency) SiN tip with the topography of the underlying surface. By optimising the feedback loop gains (which seek to maintain a constant tip sample interaction) and imparting a relatively small amount of energy into the surface (i.e. by "lightly" tapping) we can gauge the surface roughness through the root mean square (RMS) roughness value. The surface roughness of the SiO_2 and SiON samples were measured both as received and after each etch. All measurements were performed in tapping mode as opposed to contact mode to avail of better sensitivity and reduced interaction with surface contamination. Figure 4.10 shows a screen shot of the software window as seen on the machine during analysis. Here a 1μm x 1μm area of an as received 5.5 nm SiO_2 sample was examined in both height (LHS) and amplitude (RHS) mode. The "granular nature" nature of the oxide is visible in the images.

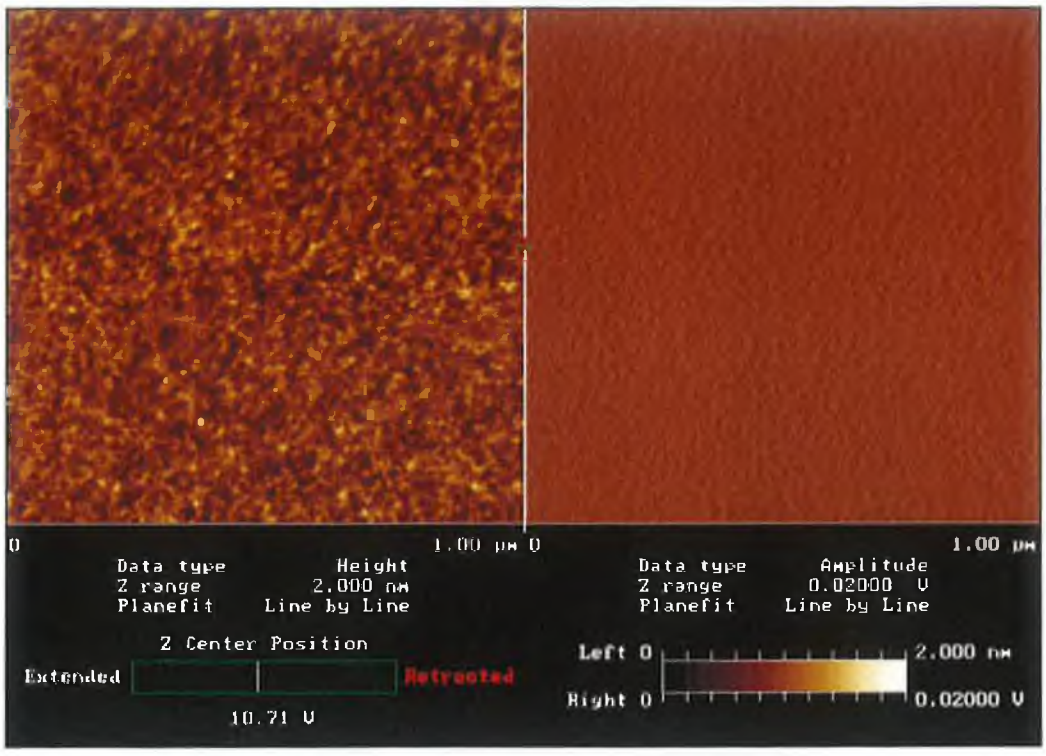

Figure 4.10: Large area scan of as-received SiO_2 oxide in (left) height mode and (right) amplitude. The colour gives indication of the height, with saturation in white at 2 nm.

Typically images contained artefacts due to interaction of the tip with water adsorbed on the surface or from ambient perturbations. It became apparent in optimising scan parameters such as the gains, amplitude set point and scan rate (in order to "exactly" follow the topography), that the scan image was more susceptible to scan instabilities such as tip lift off, tip jumps, drift and high frequency noise. While it is important to follow the surface topography as closely as possible it is also necessary to be able to compare images from different samples and so it was also important to be reproducible in our scan parameters and procedure. Roughness values are influenced by the tip, scan size, scan conditions and image processing [32]. Therefore a trade off between fidelity and reproducibility was made. Figure 4.11 shows a 3 dimensional plot of the images of figure 4.10.

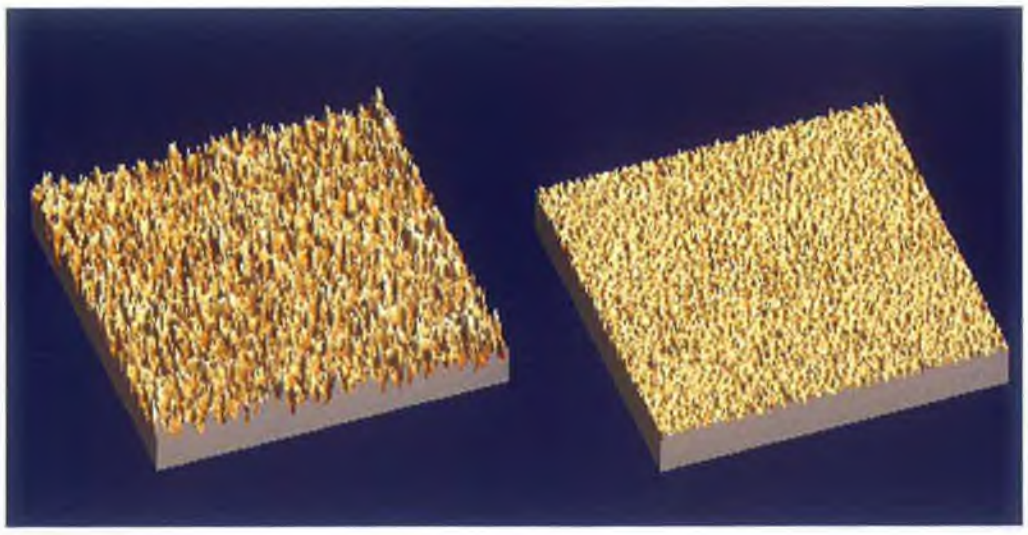

Figure 4.11: 3 dimensional plot of the surface topography in (left) height and (right) amplitude mode.

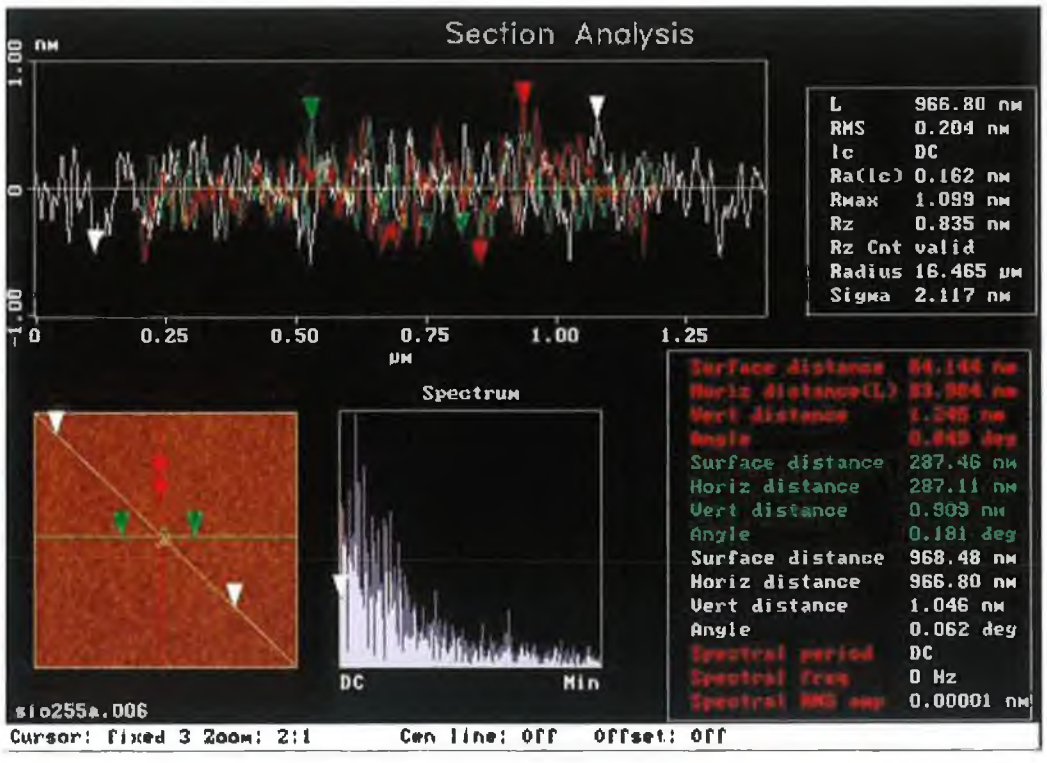

Figure 4.12: The uniformity of surface topography across the sample is considered by considering the agreement between roughness sampled along the coloured lines shown. The spectrum gives information of possible periodicity in surface features.

In figure 4.12, cross-sections of the image show the topography in the directions of the red, green and white lines. The uniformity of the sample topography across the extent of the sample is affirmed by the agreement in each section. The frequency spectrum of the

line sections were mostly DC with a continuous tail (characteristic of a random distribution of roughness [33]). Any periodicity in the surface would be evident in the frequency spectrum as peaks at well-defined coherence lengths. Samples were fitted to a first order plane in order to correct for tilt, and where sample "bowing" resulted from tall features in the scan, the image was flattened.

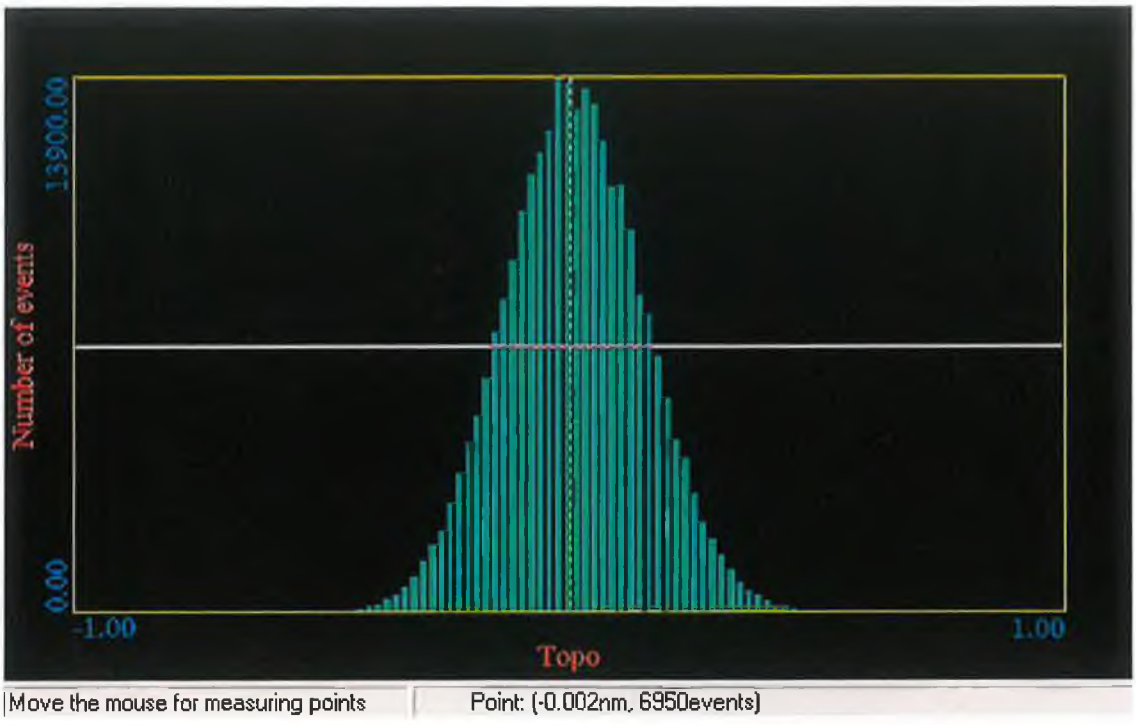

Figure 4.13: Distribution of surface feature heights is Gaussian like and offers information about the surface from it's skew value and FWHM. The fwhm is proportional to the RMS roughness.

Figure 4.13 shows the distribution of peak heights about the mean for the as-received 5.5 nm SiO_2 oxide. The distribution is Gaussian like and symmetric, suggesting there are an equally distribution of "crests" as "troughs". A value of FWHM was obtained from the software from measuring the width in (nm) at half the frequency (height) at the centre (dashed yellow line). Figure 4.14 shows the height distributions of the surfaces exposed to the same etch conditions (0.5% HF) that were used prior to photoemission. The etch time in minutes is shown beside the resulting distribution. For comparison of the widths each distribution window is 1 nm wide. The distribution remains symmetric and becomes broader with increased etch time.

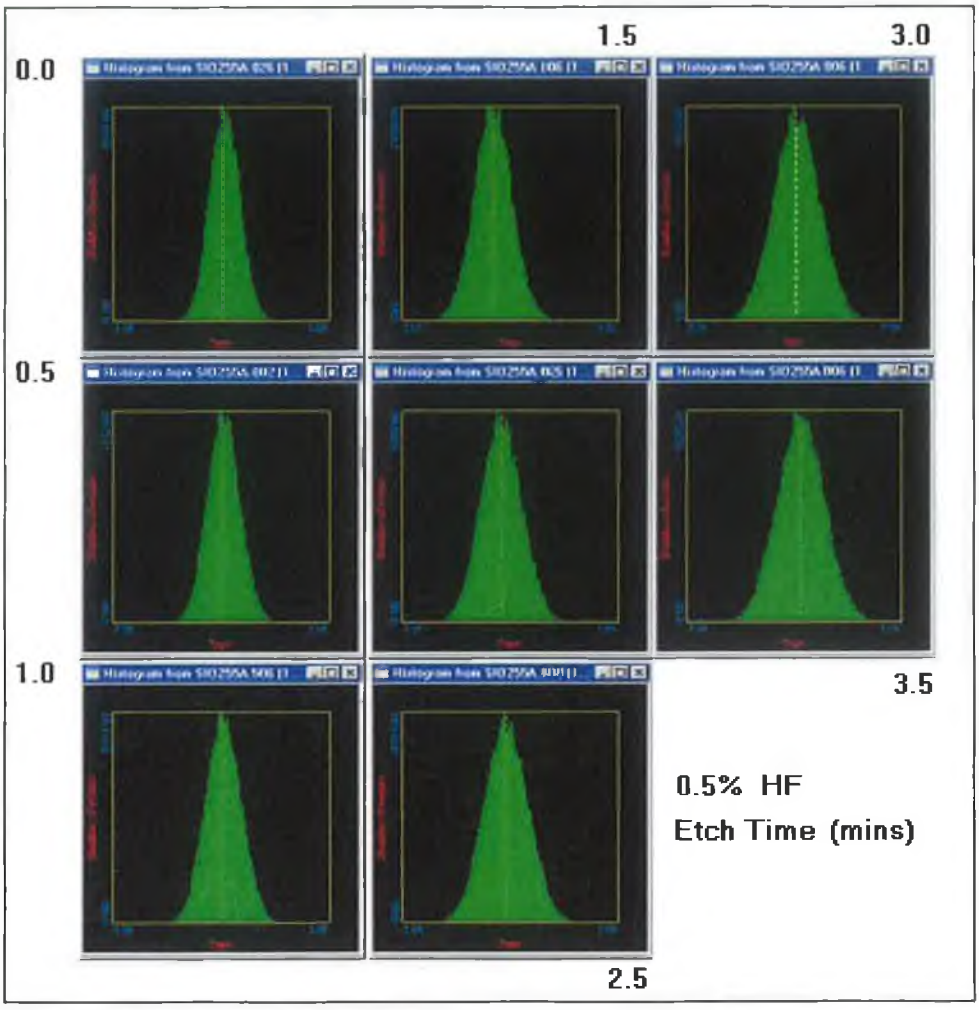

Figure 4.14: Evolution of height distribution with (0.5% HF) etch time. The distribution remains relatively symmetric but shows some broadening in it's FWHM.

Conventionally the surface is evaluated in terms of its RMS roughness. Figure 4.15 shows the roughness parameters for a 0.5 μm x 0.5 μm scan on an as-received 5.5 nm SiO_2 sample. "Image statistics" pertain to the whole image; "box statistics" pertain to the region contained in the white box. Below is a brief definition of the values in the roughness analysis.

Z range	the distance from the highest peak to the lowest valley
Mean	mean value of data contained within the image
Raw mean	mean value of data without application of plane fitting
RMS (R_q)	Root mean square of the roughness relative to a plane drawn through a surface at the mean surface height.
R_a	Arithmetic average of the absolute values of surface height

deviations measured from the surface plane.

Img. Srf. Area — The three dimensional area of the analysed region. This value is the sum of all the area of all the triangles formed by three adjacent data points.

Img. Srf. Area Diff — The percentage difference of the integrated area of the image compared to the areas of the square, which would be represented by a flat surface (i.e. difference between the images three dimensional surface area and it's two dimensional footprint area).

Skewness — A dimensionless quantity (like standard deviation) which gives an indication of the distribution of the data around the mean. A negative value suggests the surface is predominantly pitted. A positive value suggests it is "mountainous". Zero suggests an even distribution of both.

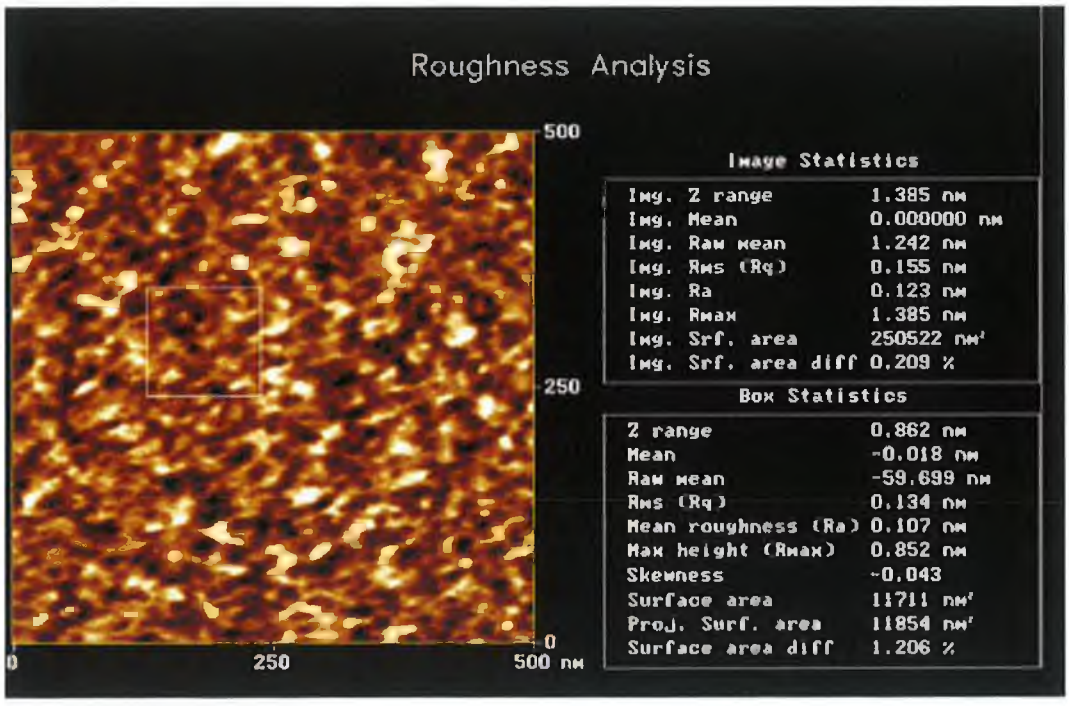

Figure 4.15: Roughness analysis of an as received SiO_2 sample. The surface topography is characterised by it's RMS roughness value, also the skew value gives indication of whether the surface is predominately pitted or peaked.

Figure 4.16 shows a graph of RMS roughness versus etch time. The height distribution values closely follows the RMS roughness value with etch time as shown in table 4.0. This relationship arises from the distribution of heights being Gaussian like, the RMS

value is the standard deviation about the mean and from statistics, a Gaussian curve's FWHM is 2.35 times the standard deviation. Table 4.0 summarises the results of the roughness analysis of the SiO_2 sample.

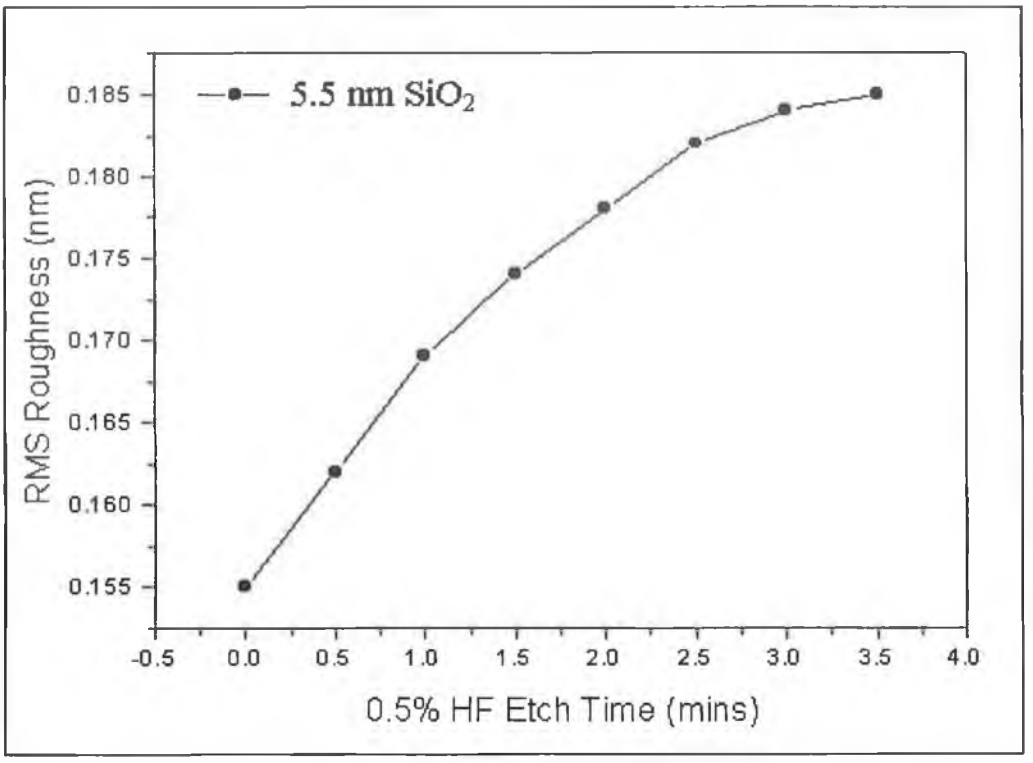

Figure 4.16: The increase in surface RMS roughness with acid etch time suggests that the surface is being roughened.

SiO_2 5.5 nm 0.5 % HF					
Etch time (mins)	RMS (nm)	skew	FWHM (nm)	Thick (A)	EtchRate A/min
0.0	0.155	-0.043	0.356	56.9	---
0.5	0.162	0.021	0.373	47.3	19.1
1.0	0.169	0.130	0.401	33.8	23.1
1.5	0.174	-0.035	0.407	26.1	20.5
2.0	0.178	-0.029	0.411	17.3	19.8
2.5	0.182	-0.017	0.417	9.2	19.1
3.0	0.184	0.011	0.423	6.1	16.9
3.5	0.185	-0.031	0.427	N/A	N/A

Table 4.0: Evolution of AFM scan parameters with dilute HF etching.

In table 4.0 the third significant figure in the data is included to show the trend in values rather than an indication of accuracy. An assessment of our roughness values in absolute terms is not straightforward. It is useful to consider the values found by others but in doing so we should consider these RMS values in the context of the sample's processing history.

Hattori [25,26],[28] in monitoring roughness during the initial stages of oxidation measured RMS roughness values, which were on the order of a single atomic step height (0.135 nm). Irene et al [33] considering the effect of water concentration in post oxidation anneal found that the surface became smoother with increased water incorporation.

ppm V	Z range (nm)	RMS rough (nm)
30	0.81	0.11
50	0.77	0.10
315	0.58	0.07

Table 4.1: Effect on RMS roughness value of extent of water incorporation during post oxidation anneal (Irene [33])

Table 4.1 summarises their roughness values. Hirose et al [34] considering the effect of purity of cleaning chemicals on morphology observed a change in R_{rms} value of 0.41 to 0.32 nm with the use of ultra-pure water (Fe, Cu contamination <0.05 ppb). The diversity of roughness values arises from the diversity in the processing each sample has undergone and so it is not possible to compare results in absolute terms with others, especially given the considerations mentioned earlier of the effect of high temperature post-oxidation anneal on roughness. From the evolution of RMS roughness values with etch time it is apparent that the surface is roughened but not enough to significantly degrade the photoemission analysis as evidenced by the stability of the Si^{4+} oxidation state FWHM with thickness as seen in our synchrotron photoemission results (presented below). On approaching the interface the etch rate etch rate slowed and an increase of the RMS value after an etch time of approximately 1.0 min was observed The XPS analysis of residual oxide thickness for this etch time yields a thickness of approximately 3.4 nm. Consideration was given to the possible existence of a region of

compressed stoichiometric SiO_2 (a structural transition region as proposed by Grunthaner [6]). Miyazaki et al [35] while depth profiling oxides using dilute HF acid, have observed changes in oxide etch rate which they attributed to such a structural transition region. Given the reduced reliability of our XPS thickness measurements for small thickness (given the large IMFP) our values of etch rate are not reliable in this thickness regime and so it's difficult to find a correlation between etch rate and thickness. Interestingly though, it is in this thickness region that a change in oxide FWHM in the XPS analysis is observed, although the result is counter intuitive as the FWHM increases, and one would normally associate a more ordered compressed region with a reduced FWHM.

Figure 4.17 shows the evolution of RMS roughness with etch time of the two nitrided oxide samples, 5.5 and 3.3 nm. Again, the samples were exposed to the same etch conditions which were used before XPS analysis with each etch being performed on a fresh sample.

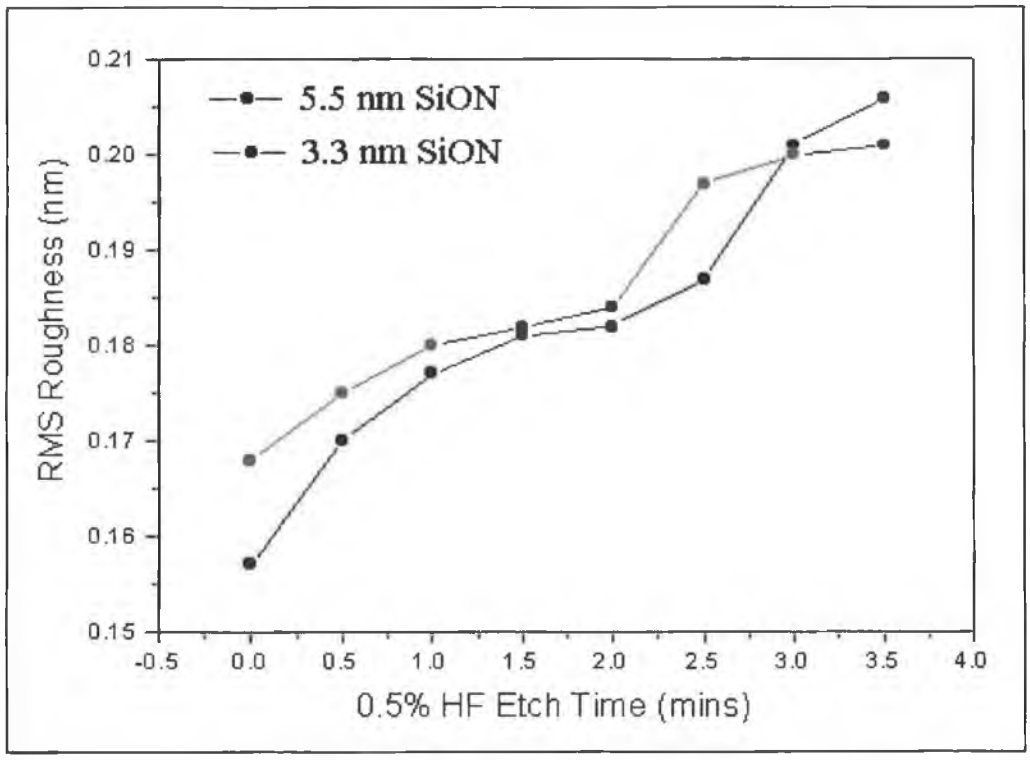

Figure 4.17: Surface rms roughness versus etch time for the oxynitride sample is similar but a reduction in etch rate is evident which is not seen in the SiO_2 sample.

Table 4.2 summarises the roughness parameters.

	SiON 5.5 nm 0.5 % HF					SiON 3.3 nm 0.5 % HF				
Etch time (mins)	Rms (nm)	skew	FWHM (nm)	Thick (A)	EtchRate A/min	Rms (nm)	skew	FWHM (nm)	Thick (A)	Etch Rate A/min
0.0	0.157	0.018	0.357	52.4	---	0.168	0.046	0.388	35.3	---
0.5	0.170	-0.023	0.382	40.1	24.6	0.175	-0.023	0.404	25.1	20.4
1.0	0.177	-0.056	0.399	30.1	22.3	0.180	0.056	0.416	15.5	19.8
1.5	0.181	-0.027	0.416	19.3	22.1	0.182	0.011	0.418	7.5	18.5
2.0	0.182	0.065	0.414	11.7	20.0	0.184	0.032	0.426	4.0	10.4
2.5	0.187	-0.043	0.423	6.0	18.5	0.197	-0.053	0.457	1.7	13.4
3.0	0.201	0.025	0.437	3.0	16.4	0.200	-0.038	0.471	N/A	---
3.5	0.206	0.047	0.451	N/A	---	0.201	-0.031	0.475	N/A	---

Table 4.2: Comparison of evolution of AFM scan parameters with HF etching between nitrided and non-nitrided samples.

For both nitrided samples the initial RMS values are larger than the SiO_2 value. The 3.3 nm SiON sample is initially rougher than the 5.5 nm SiON sample. The SiON samples show an initial rise in roughness followed by a plateau region which is followed by a final rise which is different from the SiO_2 roughness behaviour. Tallarida et al [36] investigated the effect on morphology of nitrogen incorporation. He used NO and N_2O during post oxidation anneal. He profiled wet chemically through the oxide using dilute HF and considered the roughness at three stages; no etch (E1), a short etch (E2) (which brought the thickness to within 4 nm of the substrate), and a long etch (E3). Table 4.3 summarises his results. He proposed that in the long etch, the etch process is terminated when the nitrogen rich interfacial region is reached. He suggested that the change in etch rate after this time indicated the arrival of the nitrogen rich region in the oxide.

N conc. (atoms/cm^2)	[E1] Surface rms (nm)	[E2] Oxide rms (nm)	[E3] N region rms (nm)	Skew
1.8×10^{13}	0.15	0.15	0.13	0.55
6.4×10^{14}	0.14	0.16	0.12	-0.19
1.1×10^{15}	0.16	0.17	0.12	-0.06
1.6×10^{15}	0.15	0.15	0.16	0.88
2.0×10^{15}	0.15	0.15	0.30	0.79
9.0×10^{14}	0.17	0.17	0.15	-0.63

Table 4.3: AFM rms roughness values evaluated at three different depths in a nitrided oxide (Tallarida [36])

He proposed that in the long etch, the etch process is terminated when the nitrogen rich interfacial region is reached. He suggested that the change in etch rate after this time indicated the arrival of the nitrogen rich region in the oxide. The initial etch process (E2) showed no signs of roughening as evidenced by the closeness to the as received values in table 4.3 above. At the nitrogen rich region, the surface appears to become smoother. Tallarida concluded that the nitride layer realised using N_2O was compact and smooth unlike NO nitridation, which results in a non-uniform interfacial nitrogen region. From the skew value, he further concluded that the RMS roughness value was not enough to characterise the surface morphology as NO samples were found to be predominately pitted (skew<0) and N_2O samples peaked (skew>0). In our XPS analysis of the 5.5 nm SiON sample the largest nitrogen concentrations at the surface and interface were encountered after etch times of 0.5 mins and 2.5 mins and for the 3.3 nm SiON sample after etch times of 0.5 and 1.5 mins respectively. It is tempting to associate the stepped behaviour of the RMS value, see figure 4.17, in the nitrides samples to surface and interface nitrogen regions. Unlike Tallarida though, a peaked or pitted surfaces was not observed as evidenced by the skew values and their closeness to zero, see table 4.2. The final value of roughness after the 3.5 mins etch is larger in the nitrated samples than for the SiO_2 sample. A rough substrate could arise from non-uniform etching as the oxide is completely removed due to the reduced susceptibility of interfacial nitride bonds to etching. Equally, the roughening could be attributed to the etch induced roughness as found by Chabel [23], see figure 4.4(a).

Our analysis so far has been obtained from samples etched in dilute HF in order to gradually and uniformly profile the oxide. In an attempted to gauge the initial surface morphology, an etch in concentrated HF 49% was performed.

Figure 4.18 (a) and (c) show the height distributions realised by etching a 5.5 nm SiO_2 sample for 15 mins and 0.5 mins in 0.5% HF and 49% HF respectively. Table 4.4 summarises the results. It was found that for a prolonged exposure to dilute acid the surface became roughened and from the asymmetry in the height distribution was pitted, as seen in figure 4.18 (A) and the skew value in table 4.2.

Etch Time (mins)	RMS (nm)	Skew
0.0 [As received]	0.155	0.012
3.3 [0.5%]	0.18	0.160
15.0 [0.5%]	0.22	-0.183
0.5 [49%]	0.16	0.016

Table 4.4: Effect of etch concentration on AFM rms and skew values.

In the XPS analysis an oxide peak could not be detected after a 0.5% HF etch of ~ 3.5 mins and so it was concluded that the acid on removing the oxide begins to roughen the underlying substrate. After 0.5 min etch in concentrated HF a smooth surface was uncovered which incidently was rougher than the as-received oxide surface. The RMS roughness results from the nitrided samples were not consistent. Working with concentrated HF is difficult because of the handling precautions required.

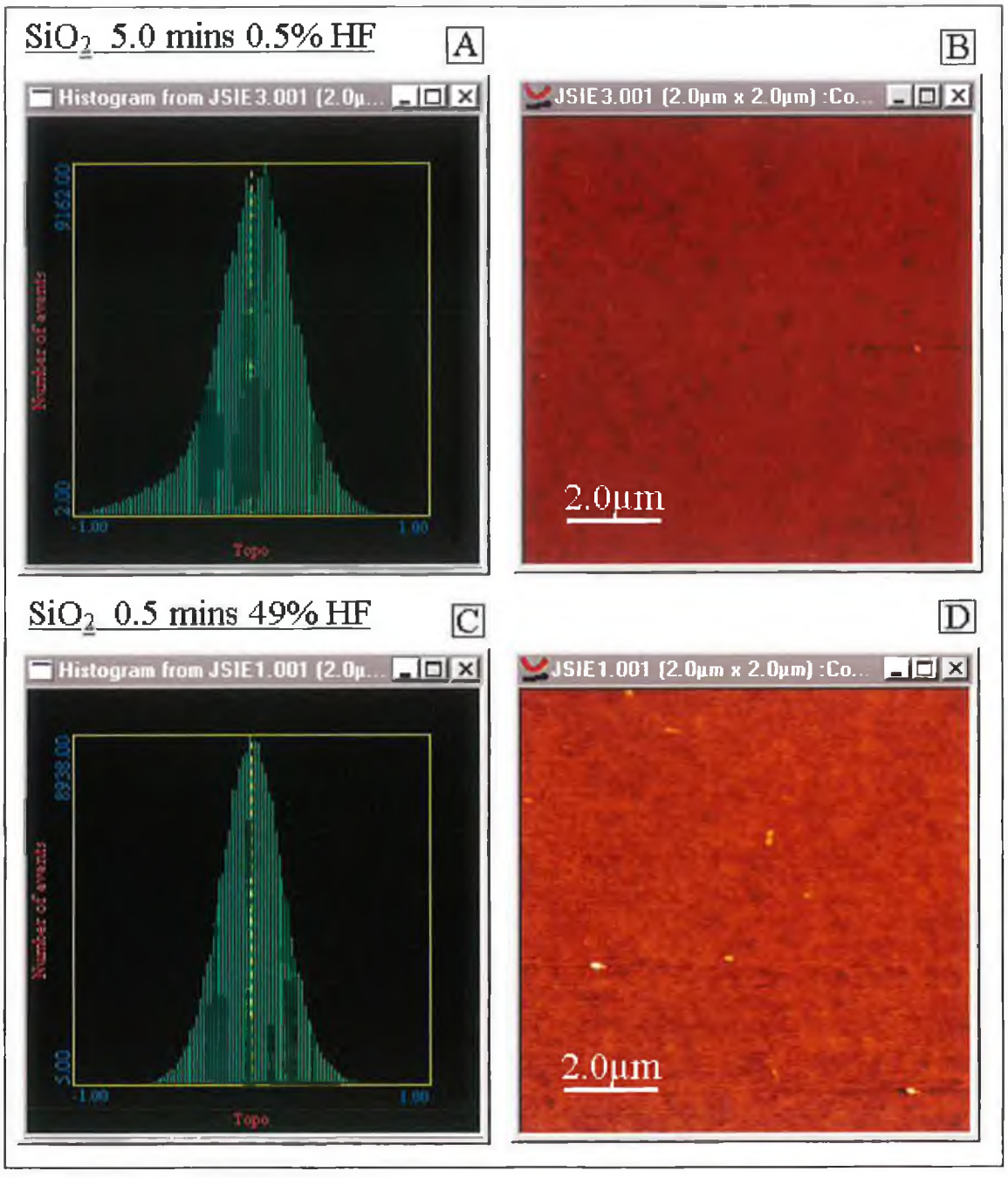

Figure 4.18: (a) Height distribution of surface features for dilute 0.5% HF etch for SiO_2 film, (b) Corresponding height mode AFM scan. (c) Height distribution of surface features for concentrated 49%HF etch for SiO_2 film, (d) Corresponding height mode AFM scan.

The data set was not as large for concentrated etches as for dilute etching and because the attainment of good quality images typically requires several etching attempts the results were not conclusive. It is interesting to consider to what extent the interface morphology had evolved from that of the surface in the samples given that they underwent high temperature anneals and that for the oxynitride samples nitrogen was incorporated near the interface.

4.5.1 Discussion of results

There have been many studies probing the extent of surface and interface roughness and its relationship to initial surface morphology, chemical treatment, surface orientation, oxidation temperature and post-oxidation anneal. Given the diversity of the experimental procedures employed and the fact that some surfaces have been purposely roughened and some samples partially processed in these studies it is difficult to compare our results with them. The oxides studied in this thesis have been realised through a highly optimised industrial process dedicated to oxide uniformity both in thickness and composition. The quality of the interface is evidenced by the size of the RMS roughness value of the interface uncovered in the concentrated etch. The agreement between the interface and surface roughness is encouraging. At 0.5 % concentration the acid progressively roughens the surface but the extent of the roughening is not significant enough to undermine our photoemission analysis. When profiling using ion bombardment we were interested in it only to know if it could realise controllable depth profiles uniformly. It was found to damage the oxide progressively but the damage was non-uniform (spatially) and was significant. Analogously, here we have found wet chemical etching to be progressively damaging but the damage is uniform spatially (from the skew value) and is not significant enough to undermine the XPS analysis.

4.6 SiO_2 Synchrotron Analysis Overview

When the thickness of an oxide is comparable to the sampling depth it is possible to see the underlying substrate through the oxide and interface. With tuneable photon energy and high-resolution monochromators, researchers can resolve the overlapping oxidation states, which greatly aids in the elucidation of interface chemistry. As mentioned previously, there has been disagreement about the interfacial width and sub-oxide density with some finding an atomically abrupt chemical transition region consisting of 1.4 ML of suboxides. Others have found a graded interface consisting of 2 ML of suboxides. In measuring the distribution of oxidation states at the interface there are two conventional approaches:

Firstly for a fixed photon energy, changing the take off angle of the outgoing photoelectron changes the "effective thickness" being probed as described by equation 4.3.

$$d_{eff} = \frac{d_{ox}}{Sin(\alpha)}$$ **Equation 4.3**

d_{eff} is the reduced oxide thickness being probed

d_{ox} is the actually oxide thickness

α is the angle between the analyser and the surface plane (i.e. $\alpha = 90'$ is normal; small angles are glancing)

The extent of surface sensitivity can be regulated for the same photon energy and the spatial distribution of the individual oxidation states can be inferred.

In the second approach, for a fixed take off angle the photon energy and hence the kinetic energy and surface sensitivity of the resulting photoelectrons can be regulated. The IMFP has a minimum at the photon energy 130 eV [11] for silicon.

Both approaches have limitations. In changing the photoelectron take off angle consideration needs to be given to photoelectron diffraction effects. In ordered materials photoemission is anisotropic with large modulations in intensity for photoemission along crystal axes that correspond to nearest neighbour directions (Bardwell [37]). Figure 4.19 [37] shows the crystal structure of silicon. At a take-off polar angle of 35°, the photoelectron trajectory is exactly in line for maximum interaction with a nearest neighbour, in the [111] direction, a similar maximum interaction at 45° take-off is expected for the [101] direction.

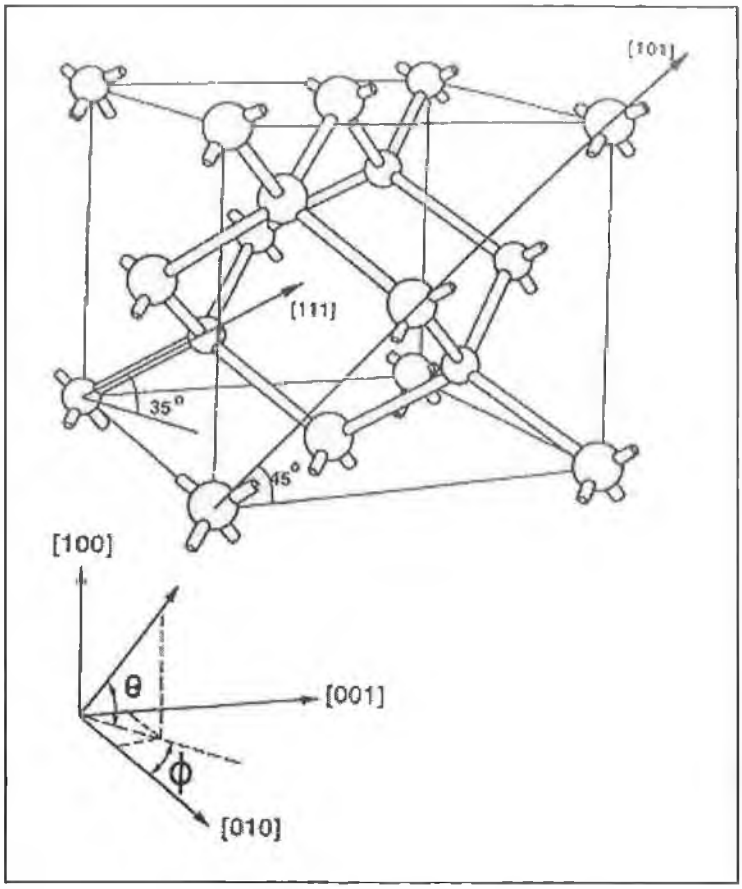

Figure 4.19: The crystal structure for Si, showing the explanation for the relationship between the effects of photoelectron diffraction at 35° and 45° take-off angles. (Bardwell [37])

Due to the amorphous nature of the SiO_2 oxide, diffraction effects are expected to average out, and are usually not considered significant. Given the presence of structural transition regions, the possibility of local crystalline order and the convention of normalising the oxidation state intensities using the substrate intensity, angular resolved result should be considered with care. Hattori et al [38] studying photoelectron diffraction effects in the Si_{2p} photoelectron spectra found that diffraction effects were not fully smeared out at low oxide thickness. Figure 4.20 (a) shows the azimuthal angle dependence of the Si_{2p} photoelectrons emitted from a H-Si(111) at two take off angles. The diffraction effect is dependent on both the azimuthal angle and photoelectron take-off angle. Figure 4.20 (b) show the experimental and simulated curves for non-scattered and elastically scattered Si_{2p} photoelectron signal arising from the substrate.

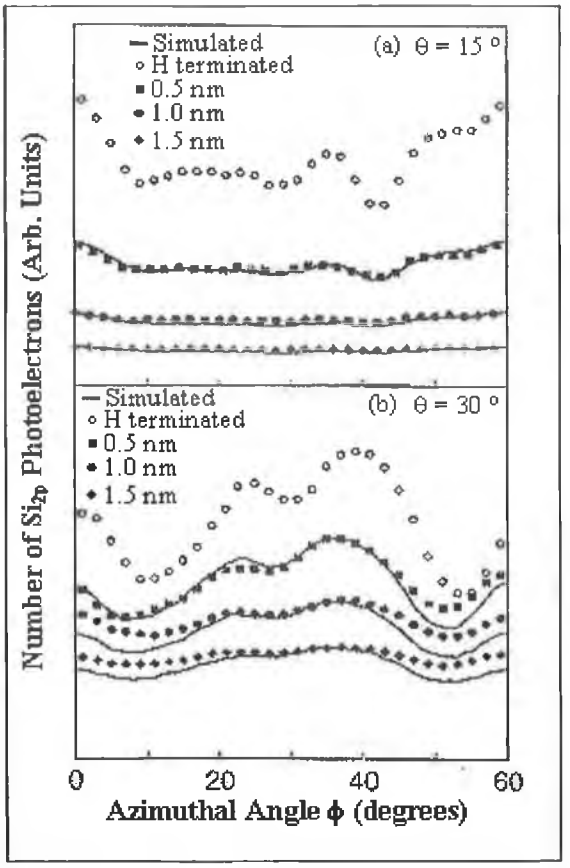

Figure 4.20: Azimuthal angle dependence of non-scattered and elastically scattered Si_{2p} photoelectron spectral intensity measured at two photoelectron take-off angles a) 15° and b) 30° degrees with oxide thickness as a parameter and azimuthal angle dependence of elastically scattered Si_{2p} photoelectron spectral intensity measured for H-terminated Si(111)-1x1 surface and simulated curves (Hattori [38]) .

Oh et al [39] recently undertook an angular soft X-ray photoemission analysis of the Si/Si(100) interface. Figure 4.21 (a) and (b) show the Si_{2p} spectrum at 0 and 60 degrees take off angle respectively, the enhancement of the more surface localised Si^{4+} state relative to the underlying bulk Si^{0+} state is visible in the spectra. Figure 4.21 (c) shows the normalised (relative to the Si^{0+}) intensity ratios of the oxidation states versus take-off angle. The Si^{1+} and Si^{2+} states have the same depth distribution but different populations, in that the Si^{1+} to Si^{2+} ratio is constant. The ratio value of 1.8 suggests the Si^{2+} species are twice as "popular" as the Si^{1+}. The Si^{3+} is distributed farther from the interface. Luh et al [40] found a similar distribution of oxidation states for the Si/Si(111) interface which they explained using an abrupt interface model based on statistical bond connection with Si^{1+} and Si^{2+} confined to an atomic layer just below the interface boundary.

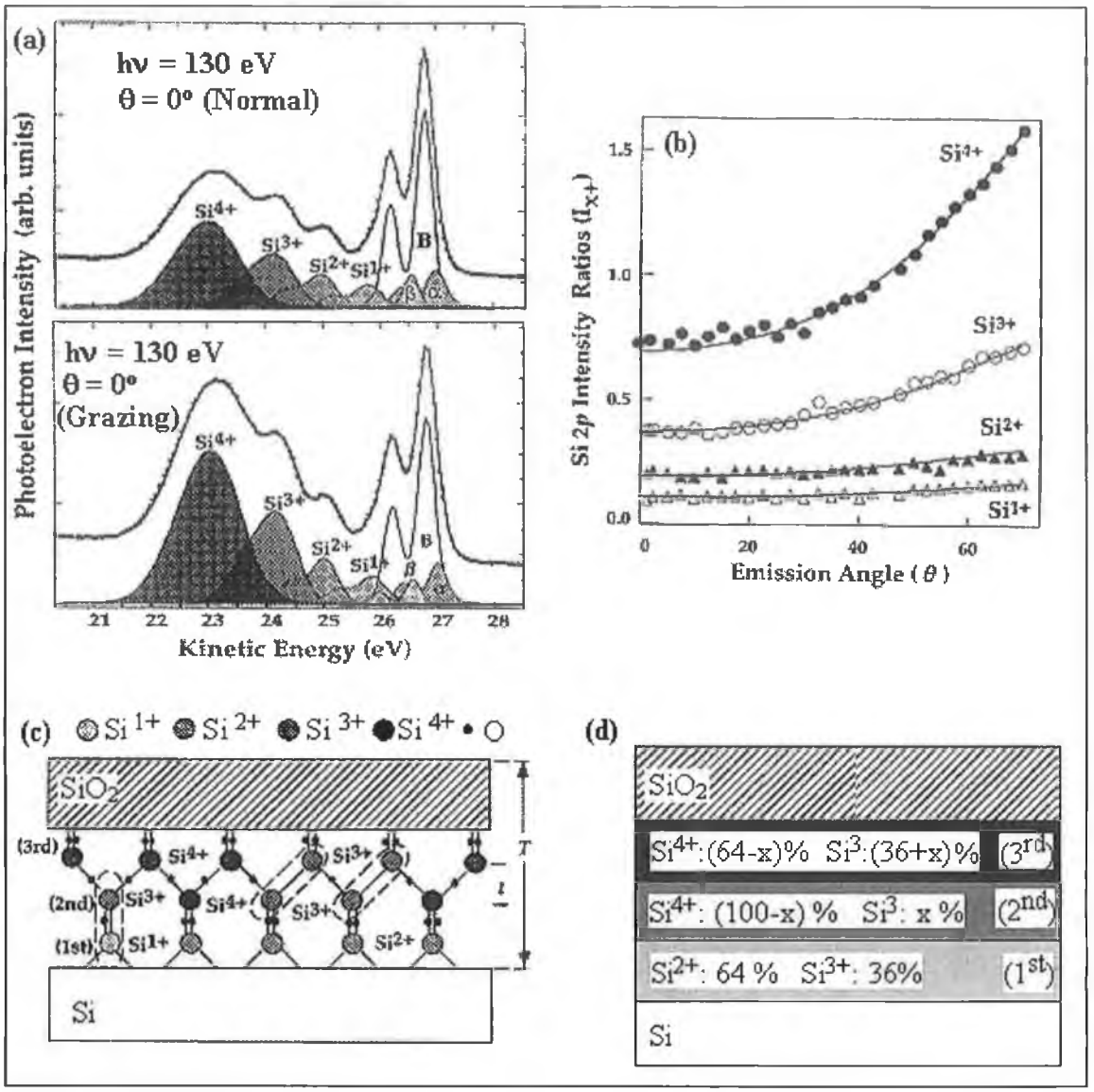

Figure 4.21: (a) (top) normal emission and (bottom) 60^0 off angle Si_{2p} core-level spectra taken from ultra-thin SiO_2/Si(100) interface oxide. (b) Intensity ratios of the Si_{2p} oxidation states to the total intensity of the Si substrate-related components as a function of the polar emission angle (θ) (Oh [39]).

Oh [39] however could not explain the existence of the Si^{3+} state nor the strong take-off angle dependence of the Si^{3+} state. Instead he proposed a non-abrupt graded interface model. At least three transition layers are required to explain Oh's results, see figure 4.21 (c). Si^{1+} and Si^{2+} exist only in the first and second layers with a population of (36% and 64% respectively). Si^{3+} exists in the second and third layers. Using a simple electron damping model scheme which relates the intensity of each oxidation state to it's population in each transition region the solid lines of figure 4.21 (b) were obtained which agree well with the experimental data (dots) in figure 4.21 (b). Figure 4.21 (d)

shows the optimised statistical distribution of each oxidation state in each of the three transition regions. Other graded interface models have been put forward by Ohdmoari et [41] al who sought to resolve the density mismatch between Si and SiO_2 through two transition layers. The difference between Oh's and Ohdmoari's results is the distribution of the Si^{3+} state. Oh's results are in disagreement with recent theoretical papers [42,43] which suggest an abrupt interface model. Unlike Hattori earlier, Oh does not give consideration to the effects of protrusions or photoelectron diffraction on the interpretation of his results.

An interesting result in Oh's Si_{2p} analysis is his inability to obtain a good fit without the introduction of high and low binding energy peaks (labelled α and β respectively see figure 4.21(a)) at energies of -0.25 and 0.28 eV relative to the bulk Si^{0+} peak. He associated these states with strained Si bonds (not bonded to oxygen) at the termination of the crystalline substrate. In chapter 3 in the context of Grunthaner's structural transition region above the SiO_x region, it was mentioned that a structural transition region is also thought to exist below the interface. Haight and Feldman [44] in a non-destructive study of the interface structure and stoichiometry using ion backscattering channelling methods (NRA, RBS) found that in the near interfacial region there is a zone with excess Si, corresponding to non-epitaxial layers within the single crystalline substrate. They associated the result with a vertical displacement of two atomic layers of silicon next to the interface.

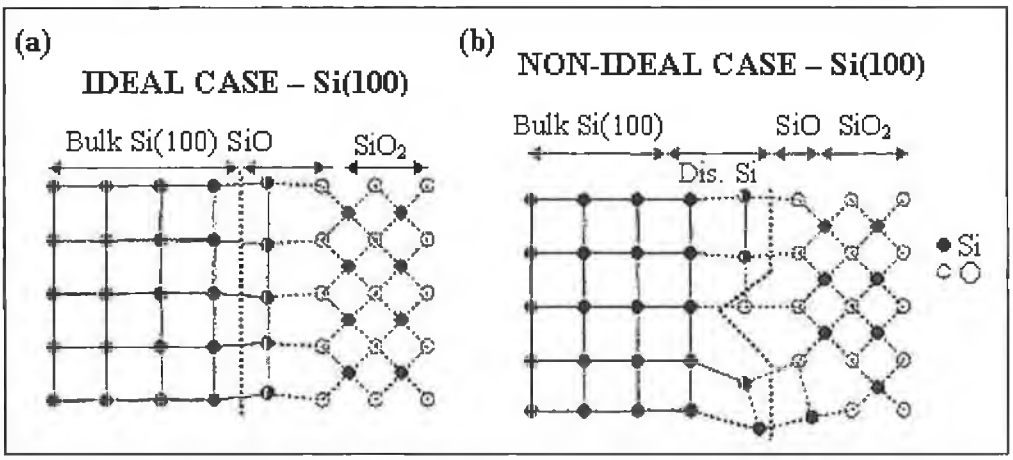

Figure 4.22: Illustration of the theoretical model of the Si/SiO_2 interface for an (a) ideal case and (b) realistic case (Atluri [45]).

Figure 4.22 shows the Si/Si(100) interface for the "ideal" and the actual case as found by Atluri et al [45] who examined the disorder of silicon surfaces for various cleaning conditions (i.e. optimised RAC chemistry) using NRA, ion channelling and AFM. Their results suggested the existence of unregistered Si atoms below the interface in a disordered layer, which helps to relieve interfacial strain. These findings are interesting because many researchers (including ourselves) report FWHM of bulk silicon peaks, which are larger than Himpsel's values of 0.28 eV or values typically found for clean Si surfaces. Next, an account of our soft X-ray photoemission results is given. Suitably thin oxide thickness were realised from the as-received samples by dilute wet chemical etching. Angular resolved photoemission measurements were not performed, but instead have used variable photon energy and etch time to investigate the spatial distribution of oxidation states at the interface.

4.6.1 SiO_2 Experimental

Soft X-ray photoemission analysis was performed on beamline U4A at the NSLS. The beamline includes a 6 m toroidal grating monochromator (TGM), which produces a photon beam width ≤0.1 eV resolution at a photon energies of 100–200 eV. The photoelectron kinetic energy was measured with a VSW 100 mm hemispherical analyser fixed at 45° to the photon axis. Other details about the beamline are given in chapter 2. The oxide sample set (as used in XPS analysis chapter 3) consisted of a 5.5 nm SiO_2, a 5.5 nm and a 3.3 nm SiON oxide. Monochromator number 1 offered the best resolution for photons in the surface sensitive 120 to 140 eV photon range, which is ideal for probing the Si_{2p} peak, however the monochromator's capability spans an energy window of 10 to 170 eV. It was not possible to access the C_{1s}, O_{1s} or N_{1s} in order to monitor contamination or examine stoichiometry or chemical shifts. Using a combined resolution of 150 meV, scans of the Si_{2p} were performed at a pass energy of 10 eV, a step size of 0.05 eV and an integration time of 0.3 sec. These parameters afforded good signal to noise within a reasonable acquisition time.

All Si_{2p} states were fitted with Voigt functions with 0.1 eV Lorentzian FWHM and different Gaussian FWHM (taken from Himpsel et al [10]) for each Si_{2p} state, which were kept fixed during fitting. In all spectra the total width of the Voigt profiles used

was dominated by the Gaussian component (typically 90% Gaussian, 10% Lorentzian), which represent a quadrature sum of the instrumental width (≤0.15 eV), the phonon broadening, and any inhomogeneous disorder broadening. The Lorentzian component represents the lifetime broadening of the core hole. Fitting was performed using a non-linear least square fit procedure after fitting a fourth order polynomial background. A branching ratio of 0.5 and spin-orbit splitting of 0.602 eV were used. Samples were thinned by dilute HF (0.5%) etching followed by rinsing in ultra pure de-ionised water, and immediate transfer via FEL to UHV (i.e. P< $9x10^{-10}$ mbar) within 10 minutes, minimising exposure to surface contamination. Figure 4.23 shows the Si_{2p} spectrum of a 0.14 nm oxide grown on Si(100) by Himpsel et al [10]. The lower spectrum is the $Si_{2p3/2}$ component after the subtraction of the smaller $Si_{2p1/2}$ component from the original through a numerical spin stripping process after background removal.

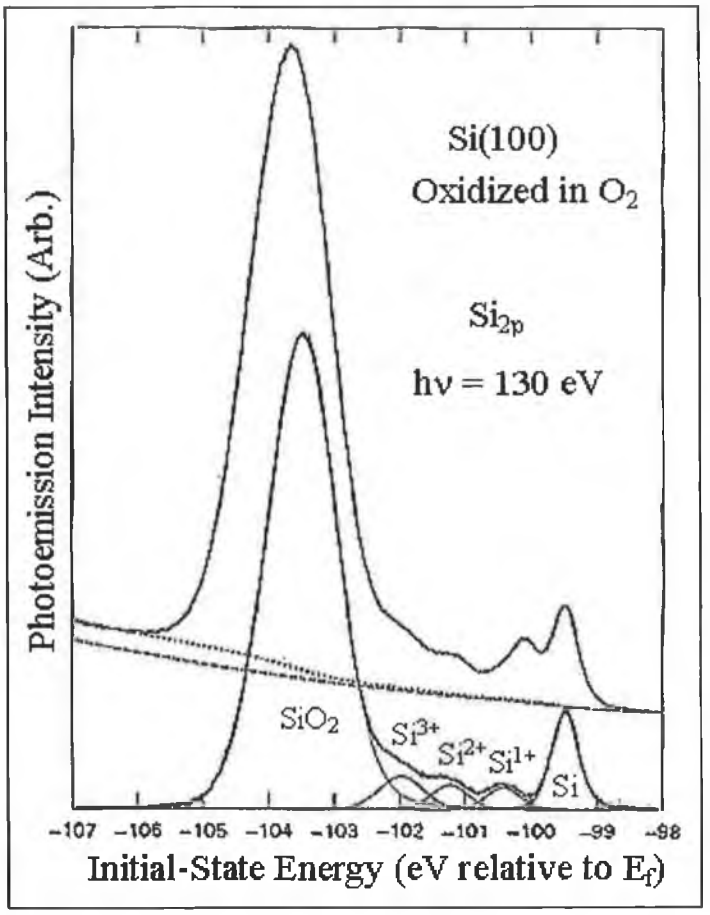

Figure 4.23: Intermediate-oxidation states at the SiO_2/Si(100) interface, identified by their Si_{2p} core-level shifts. Top curve is Si_{2p} raw spectra. Bottom curve shows $Si_{2p3/2}$ component after subtraction of background. All three intermediate oxidation states are seen. For an ideal truncated bulk structure only Si^{2+} would be present since the Si(100) surface has two broken bonds per atom (Himpsel [10]).

Figure 4.24 shows the spectrum of our 5.5 nm SiO_2 sample thinned to 0.13 nm after etching for 2.5 mins in 0.5% HF. The black line is the experimental data, the red line is the experimental fit, the background is represented by the dashed line. The individual $Si_{2p3/2}$ states were fitted to the spin stripped spectrum and are shown in blue.

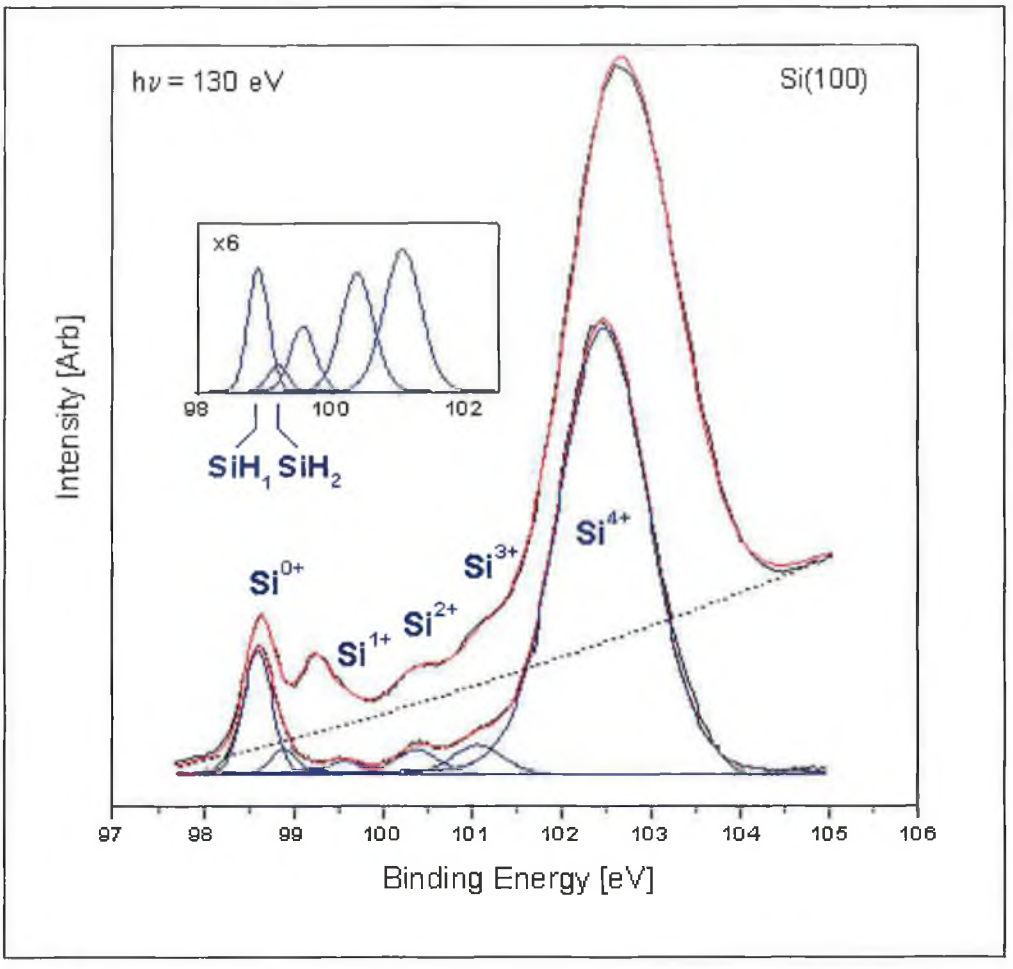

Figure 4.24: De-convolution of Si_{2p} spectrum of a 1.3 nm SiO_2 film after background removal and numerically removing the $Si_{2p1/2}$ component. The spectrum was fitted with four oxidation states as well as two interfacial hydrides. Inset shows a magnified view of intermediate oxidation states.

The peaks SiH_1 and SiH_2 represent interfacial monohydrides and dihydrides respectively arising from post oxidation treatment in a H ambient. The inset shows a magnified (x6) view of the hydrides and suboxides with Si^{0+} and Si^{4+} states omitted for clarity. In order to measure the change in surface sensitivity with photon energy, a 5.5 nm SiO_2 oxide was etched to a thickness 0.5 nm, where both the Si^{0+} and Si^{4+} intensities were appreciable.

Then the intensity of the Si^{0+} relative to the Si^{4+} was monitored at different photon energies. For high photon energies the energy window is limited by the range of the monochromator. For photon energies below 120 eV the spectral information sits on a secondary electron tail (see figure 2.1, chapter 2) who's severe gradient makes background subtraction difficult. Himpsel et al (see figure 2.35, chapter 2) have sampled the background in the appropriate kinetic energy window in the absence of the peak (by using a lower photon energy) and used this signal for background subtraction. Figure 4.25 shows the raw Si_{2p} spectra obtained over the photon energy range 120 to 145 eV. The steeper background encountered at lower photon energies as well as the shift from surface to bulk sensitivity is visible from the diminished oxide intensity relative to the substrate.

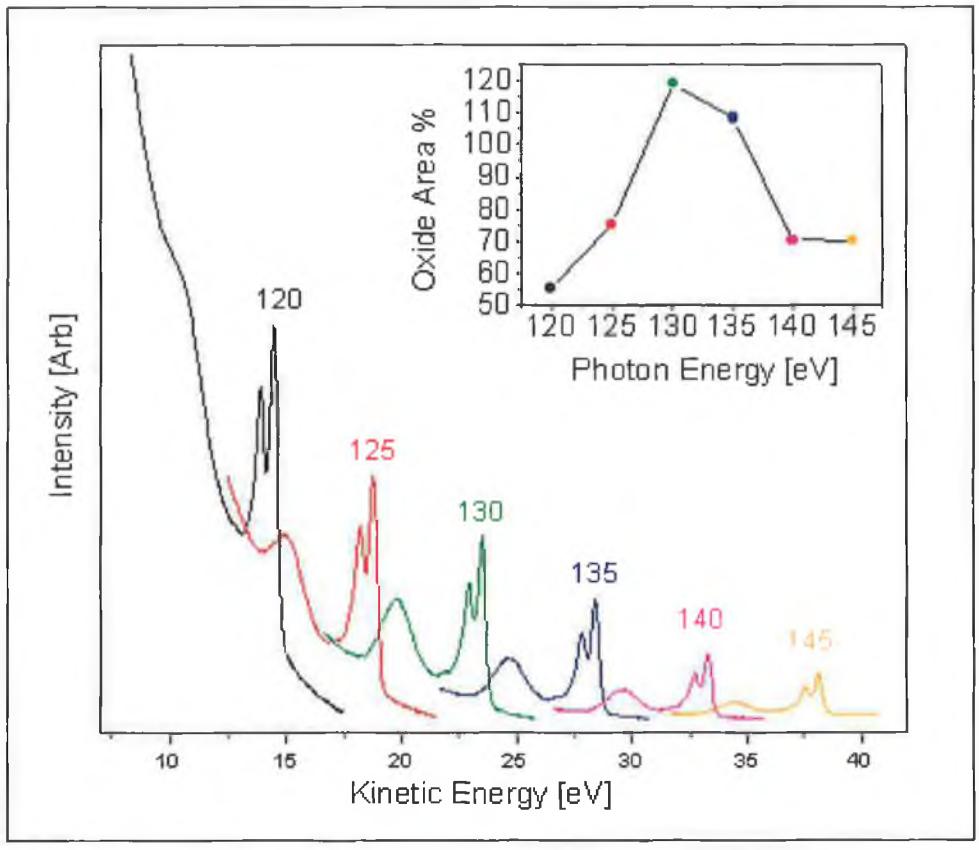

Figure 4.25: Shows the increased severity of the background on which the Si_{2p} spectrum sits with reduced photon energy. Inset plots Si^{4+} oxide peak area as a function of the substrate Si^{0+} intensity, a maximum surface sensitivity is evident at a photon energy of 130 eV.

The inset plots the intensity of the oxide (Si^{4+}) as a percentage of the substrate intensity (Si^{0+}) with photon energy. A maximum surface sensitivity is evident at 130 eV with a more serve drop on the low kinetic energy side. Oxide thickness were calculated as they were in the XPS analysis using equation 2.19, chapter 2 and using Himpsel's [10] values for the IMFP in silicon dioxide for the various photon energies. In order to find these values Himpsel rearranged equation 2.19 for an oxide of known thickness (in the range 1.0 to 3.0 nm) and solved for λ_{SiO2}. Accurate measurement for the oxide thickness was determined by ellipsometry and transmission electron microscopy.

Table 4.5 summarises Himpsel's and our $Si_{2p3/2}$ fitting parameters. As mentioned earlier we detected interfacial hydride states (SiH: monohydride SiH_2: dihydrides), which were attributed to a post oxidation H anneal.

Himpsel's				Ours		
State	ΔE	FWHM		State	ΔE	FWHM
Si^{0+}	0	0.28		Si^{0+}	0	0.37
Si^{1+}	0.95	0.44		Si^{1+}	0.95	0.45
Si^{2+}	1.75	0.58		Si^{2+}	1.75	0.58
Si^{3+}	2.48	0.66		Si^{3+}	2.48	0.66
Si^{4+}	3.9	1.15		Si^{4+}	3.9	1.17
				SiH	0.3	0.37
				SiH_2	0.57	0.37

Table 4.5: Comparison of peak fitting parameters for Si_{2p} spectrum between (left) Himpels [10] and (right) ours.

These are similar to the bonding units detected by Chabel et al [20] investigating H passivation using FTIR (see figure 4.4). Himpsel didn't detect hydrides, as his oxides were grown in-situ on atomically clean Si(100) surfaces in UHV using ultra pure oxygen. The oxides in this thesis were grown ex-situ at atmospheric pressure on a hydrogen passivated surface and underwent a final anneal in a hydrogen containing environment. Of the two hydride intensities the mono-hydride was found to be the dominant hydride in the spectra.

Yamamoto et al [46] studied H-adsorption on clean Si(100) [2x1] surfaces (see figure 4.26). Moving anti-clockwise in figure 4.26, the clean surface reconstruction, peak A is the bulk, peaks B and C are surface core level shifts who's assignment is controversial and is discussed in chapter 5. For low hydrogen doses a dihydride dominated distribution was observed, which changed at higher doses to a monohydride dominated distribution. The mono and dihydrides were chemically shifted by 0.3 and 0.5 eV from the substrate respectively and were fitted with the same FWHM as the substrate.

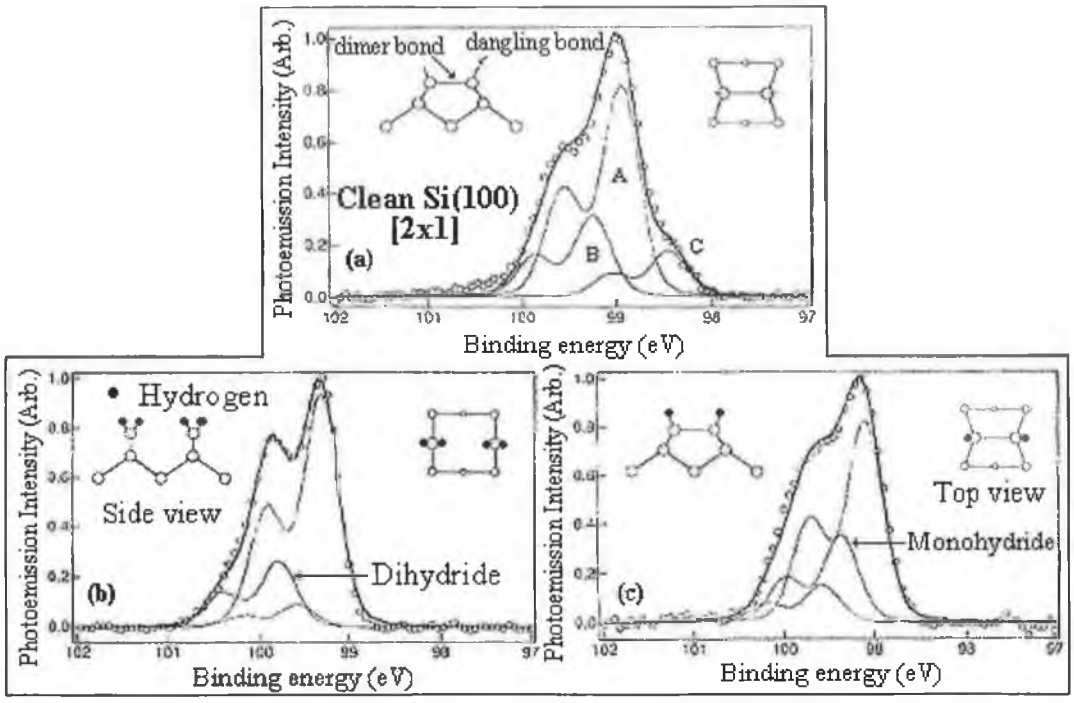

Figure 4.26: Si_{2p} photoelectron spectra of (a) clean Si(100) surface fitted with a bulk and two surface core level peaks, also model for clean surface structure. (b) Dihydride pahse (1x1-2H) and model of H-adsorption. (c) monohydride pahse (1x1-1H) and model of H-adsorption (Yamamoto [46])

Hydrides have been found in other photoemission studies. Uhrberg and Landemark [47] in a similar study found a hydrogen related peak at 0.26 eV from the bulk Si peak. Niwano et al [48] studying ultra-thin oxides on Si(100) detected a hydride shifted 0.35 eV from the substrate peak and associated it with unavoidable water content in their oxidation furnace.

Initially we were concerned by the possibility that the films realised by etching were in fact the result of re-growth (in the H_2O rinse) after complete oxide removal by the acid, and that the detected hydrides were introduced from hydrogen in the acid. However,

Yamamoto's [46] studies of oxide re-growth on hydrogen passivated Si(100) show films whose structure is poor and are so thin that peak assignment is unrealistic. The oxides studied in this thesis however, are well defined and are of a comparable quality to those grown to similar thickness in UHV environments. Great care was taken to ensure as constant a time as possible elapsed between chemical treatment and analysis. Therefore the ability to realise precisely thinner films, with precisely longer etch times would have been seriously undermined by re-growth during chemical treatment which if responsible would have lead to a random distribution of oxide thickness. Figure 4.27 shows a SiO_2 sample etched for 10 mins followed by 10 min immersion in deionised water.

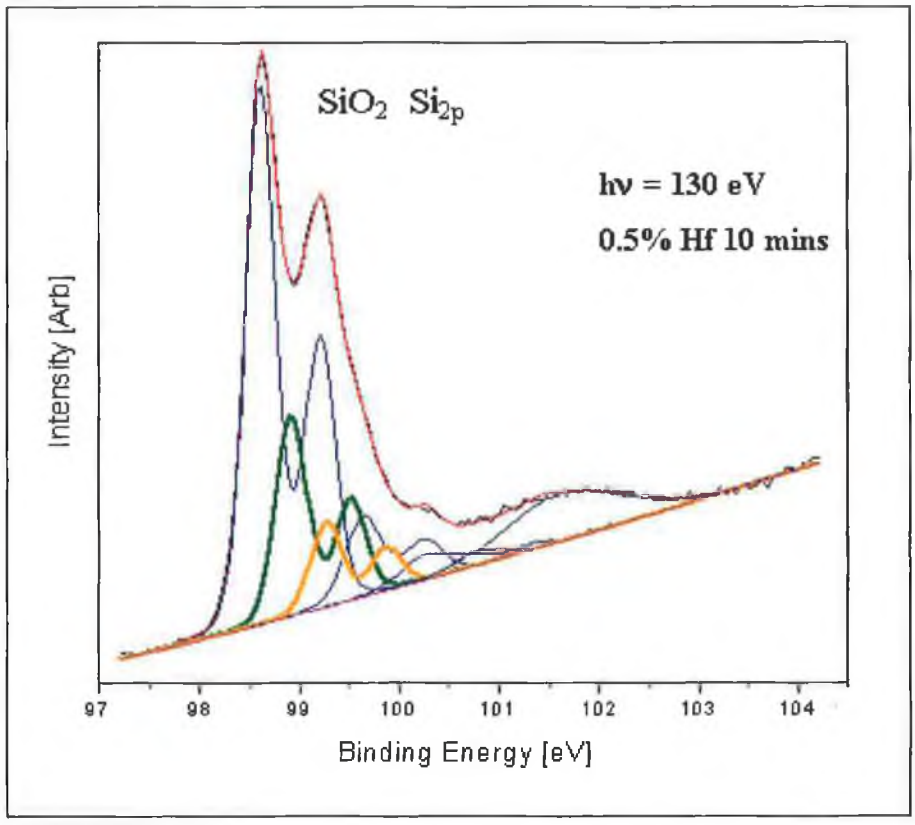

Figure 4.27: SiO_2 Si_{2p} spectrum showing interfacial hydrides in green and orange.

The mono and dihydride peaks are highlighted in green and orange respectively. Effectively no oxide re-growth is evident here eliminating the possibility of the other etched oxides (which were etched for shorter times!) arising from growth during preparation. Also Tay et al [49-52] (see figure 3.4, chapter 3) have successfully performed numerous photoemission studies (both monochromated and synchrotron) of

ultra-thin oxides realised by dilute HF etch back and have not reported the presence of hydrides.

Table 4.5 shows good agreement between our fitting parameters and Himpsel's [10], except for the value of FWHM of the Si substrate peak (Si^{0+}). Other researchers [39] [53] in soft X-ray studies (at the photon energy 130 eV) have mentioned the need to introduce extra peaks near the substrate peak in order to achieve a good fit or the need for a larger FWHM. Keister et al [53] used a value of 0.36 eV, which agrees well with our value of 0.37 eV. Lu et al [40] used a value as large as 0.41 eV. As mentioned earlier, these larger values of FWHM have been associated with strained interfacial silicon below the interface who's spectral contribution cannot be easily resolved from the Si^{0+} peak due to finite resolution and in our case the added presence of overlapping hydrides.

4.6.2 Interface state distribution

In calculating the oxide thickness, the sample was treated (using the overlayer model) as a thin oxide sitting on an infinite substrate and equation 2.19.

$$d = \mathrm{Ln}\left[\frac{I_{SiO_2}}{I_{Si}}\frac{I_0}{I_\infty}+1\right]\lambda_{SiO_2} \qquad \textbf{Equation 2.19}$$

d_{SiO2} is the oxide thickness

I_{SiO2} and I_{Si} are the photoelectron signals from the oxide and substrate respectively

λ_{sio2} is the IEMFP in the oxide

I_0 is the signal from a clean silicon substrate

I_∞ is the signal from an infinitely thick oxide

In order to calculate the density of suboxide species the suboxide region was treated as a thin film of thickness d_{ox} sitting on an infinite substrate. Equation 2.19 was re-arranged to get equation 4.4:

$$\frac{I_{SiO_x}}{I_{Si}} = \left(e^{\frac{d_{SiO_x}}{\lambda_{SiO_x}}} - 1 \right) \frac{I_\infty}{I_0} \qquad \textbf{Equation 4.4}$$

and recalling that:

$$I_\infty = n_{SiO_x} \sigma_{SiO_x} \lambda_{SiO_x} \;\&\; I_0 = n_{Si} \sigma_{Si} \lambda_{Si}$$

n_{Si} is the atomic density in silicon

σ_{Si} is the photoionisation cross section

then for:

$$d_{SiO_x} << \lambda_{SiO_x} \Rightarrow e^{\left(\frac{d_{SiO_x}}{\lambda_{SiO_x}}\right)} - 1 \approx \frac{d_{SiO_x}}{\lambda_{SiO_x}}$$

allowing equation 4.4 to be simplified to calculate the number of Si atoms in intermediate oxidation states per unit area:

$$N_{SiO_x} = n_{SiO_x} d_{SiO_x} = \left(\frac{I_{SiO_x} \sigma_{Si}}{I_{Si} \sigma_{SiO_x}} \right) n_{Si} \lambda_{Si} \qquad \textbf{Equation 4.5}$$

Assuming $\sigma_{Si} / \sigma_{SiOx}=1$, $n_{Si}=5x10^{22}$ cm^{-3}, and $\lambda_{Si}=0.33$ nm, then N_{SiOx} can be calculated from the measured I_{SiOx}/I_{Si} ratio. Suboxide distributions are compared on the basis of normalised (to the substrate) intensities:

$$\frac{I_{SiO_x}}{I_{Si}} \quad \text{or relative intensities} \quad \frac{I^n}{\sum_0^n I^n}$$

or monolayer coverage by considering the ratio of the suboxide density N_{SiOx} to $N_{(100)}$, where $N_{(100)}$ is the two-dimensional density of silicon atoms on the (100) crystalline surface (i.e. $6.8x10^{14}$ atoms/cm^2=a single monolayer).

Before calculating the spatial distribution of the individual oxidation states consideration must be given to two factors, which affect measurements. Firstly, there exists an escape depth effect caused by the fact that higher oxidation states (Si^{4+},Si^{3+}) are believed to exist further away from the interface than lower states (Si^{2+},Si^{1+}). Thus their intensities, when the escape depth is small are enhanced with respect to those of Si^{1+} and Si^{2+}, which lie closer to the interface. For states existing in a number of layers (i.e. Si^{3+}) there is an argument analogous to Shallenberger's (about underestimation/overestimation of distributed N layers, see chapter 3), for the attenuation of the underlying state by the overlying state.

Secondly, Himpsel et al [10] proposed the existence of a shape resonance in the photoionisation cross section of the Si^{3+} oxidation state at a photon energy of 130 eV. The cross section ratios ($\sigma_{SiOx}/\sigma_{Si}$) of each oxidation ($Si^1$, Si^2 , Si^3, Si^4) state relative to that of the substrate (I^0) are 1.0, 1,1, 1.7, 2.2.

In order to address these difficulties, Himpsel considered the oxidation state distribution at a photon energy of 400 eV where the mean free path is significantly large compared to the width of the interface and the individual cross sections are nearly the same, thus reducing the impact of the individual state spatial spread on the distribution. Himpsel considered the ratio of the individual peak intensities to that of $I^{1+}+I^{2+}+I^{3+}$. The results for hν=400 eV were $I^{3+}:I^{2+}:I^{1+}=0.33:0.29:0.38$. Only after dividing the intensities for the corrected cross sections at hν=130 eV did he obtain reasonable agreement $I^{3+}:I^{2+}:I^{1+}=0.36:0.24:0.40$. between the results for both energies.

Sample	Energy	N_{SiOx} (10^{14} atoms cm^{-2})					Total
	hν (eV)	SiH_1	SiH_2	Si^{1+}	Si^{2+}	Si^{3+}	monolayers
Himpsel	130	---	---	3.6	3.8	4.2	1.7
Lu	130	---	---	2.7	2.8	3.8	1.4
Ours	130			2.5	2.6	3.7	1.5
Ours	120			2.6	2.7	3.6	1.6

Table 4.6: Comparison of evolution of individual sub-oxidation state density and total sub-oxidation state from (Himpsel [10]) (Lu [51]) and our own.

However, there has been some disagreement about the correction values. Rochet et al [55] observed an enhancement of the $Si^{4+}$and Si^{3+} states relative to the Si^{1+} state of +45%, +20% respectively compared to Himpsel's values of 120% and 66%. Table 4.6 compares our results for interface suboxide density with Himpsel's and Lu's. Our results are based on the intensities of a 1.3 nm oxide realised by etching our 5.5 nm SiO_2 sample for 2.5 mins in 0.5% HF, see figure 4.24. This is an optimal thickness because for thicker oxides it isn't possible to "see" the substrate peak well enough to fit it and for thinner oxides part of the chemical transition region may be partially removed. In calculating the total sub-oxide density we included the contribution from both hydrides and Himpsel's cross-section corrections. The calculated value of total interface state density obtained was between that of Himpsel's and Lu's. Our results for the "deeper" illumination of 120 eV give a larger value of suboxide density than those at 130 eV. This was attributed to the "escape depth" effect and the possible inaccuracy of Himpsel's correction values for the cross sections at hν=130 eV, as discussed below. Our value of 1.5 monolayers of interface suboxide is relatively small. This is attributed to the post oxidation anneal treatment. Keister et al [53] who investigated the effect of post oxidation anneal temperature on $Si(111)/SiO_2$ suboxide interface state density found a 15% to 20% reduction with anneal temperature from 700°C to 900°C.

Temp °C	N_1 (ML)	N_2 (ML)	N_3 (ML)	ΣN_1 (ML)
300	0.87	0.59	0.38	1.84
700	0.92	0.26	0.42	1.60
800	0.82	0.23	0.58	1.63
900	0.79	0.30	0.46	1.56

Table 4.7: Evolution of individual sub-oxidation oxidation state density and total sub-oxidation state density with post oxidation anneal temperature (Keister [53])

Table 4.7 summarises their results. I^{3+} and I^{1+} remain relatively constant with annealing, however, the non-intrinsic I^{2+} feature is significantly reduced. Keister's final interface state density is 13% lower than Himpsel's.

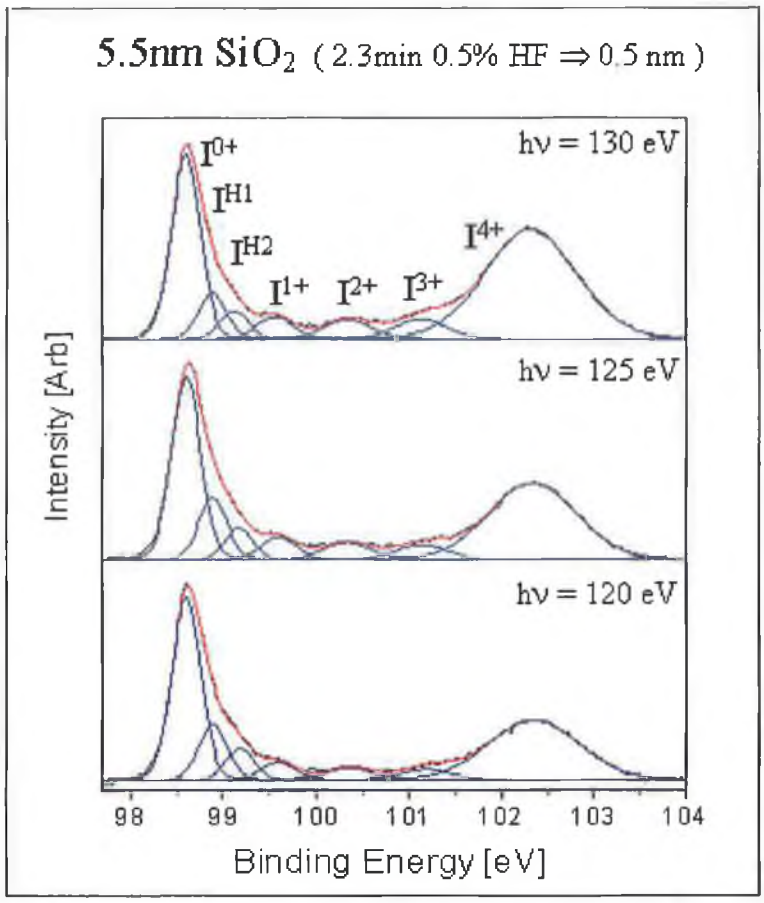

Figure 4.28: $Si_{2p3/2}$ spectra of 0.5nm SiO_2 film at photon energies hν = 130, 125 and 120 eV.

Figure 4.28 shows the $Si_{2p3/2}$ spectra of a 0.5 nm SiO_2 oxide at photon energies of 130, 125 and 120 eV respectively, the sample was etched in 0.5% HF for 3 mins. Table 4.8 summarises the results. The ratio of each oxidation state to the sum of $I_{H1}+I_{H2}+I^{1+}+I^{2+}+I^{3+}$ was considered. In the first set of results the contribution from the hydrides was included in the denominator of the ratio. The absence of the resonance effects in the higher oxidation states coupled with the increased illumination of the "deeper" lying hydrides for the increased sampling depth of the lower photon energies needs to be considered when interpreting the results. The intensities have not been corrected with the cross section corrections. Next in the table are Himpsel's results (also uncorrected for the cross sections) for an ultra thin oxide on Si(111) and Si(100). Finally in the table, for a comparison of the relative intensities, our results without the contribution from the hydrides are included.

An interpretation of the results in terms of the spatial distribution is difficult for the following reasons:

- When illuminating the outer surface using surface sensitive hν=130 eV photon energy, it is tempting to attribute the enhanced signal from the higher oxidation states to their distribution being further away from the interface. However, one must consider the influence of the resonance in the cross section.

- When illuminating deeper into the surface using the more bulk sensitive hν=120 eV photon energy it is tempting to interpret the enhanced hydride signal as arising from the interfacial region and that this signal was underestimated at hν=130 eV.

In order to address this difficulty, Himpsel compared his surface sensitive results with those obtained using the more bulk sensitive photon energy hν=400 eV where the effects of cross section resonance and escape depth are negligible. Having corrected for the cross section he found good agreement for the results at 130 and 400 eV. However, Rochet [55] have found Himpsel's corrections to be overestimated and have even found the photoionisation cross-section resonance to occur at 135 eV instead of 130 eV.

The ratios for our intensities after correction using Himpsel's cross-section values are shown in table 4.8 in red beside the uncorrected values. These data suggest that Himpsel's corrections over estimate the cross sections for the Si^{2+} and Si^{3+} states at hν=130 eV. If the ratios at hν=125 and 120 eV are considered, where the resonance effect is absent, then the Si^{3+} signal is reduced for the deeper illumination of 120 relative to 125 eV. The interpretation of the hydride behaviour is less straightforward. The increased hydride signal with deeper illumination at 120 eV compared to 125 eV and 130 eV could be attributed to the escape depth effect because the hydrides are localised at the interface and so are not fully illuminated at the more surface sensitive photon energies. One would also expect the indigenous Si^{2+} state to show a comparable increase because it is expected to be localised at the interface. It is likely therefore from the hydride intensity behaviour that they are to some extent distributed both below the interface and in the interfacial region.

hν (eV)	$I^{0+}/\sum I^{n+}$	$I^{H1+}/\sum I^{n+}$	$I^{H2+}/\sum I^{n+}$	$I^{1+}/\sum I^{n+}$	$I^{2+}/\sum I^{n+}$	$I^{3+}/\sum I^{n+}$	$I^{4+}/\sum I^{n+}$
	Our's (with hydrides)						
130	1.0 1.2	0.26 0.29	0.16 0.18	0.16 0.18	0.18 0.19	0.19 0.14	2.0 0.27
125	1.0	0.34	0.17	0.16	0.16	0.15	1.3
120	1.2	0.37	0.21	0.14	0.13	0.13	1.2
	Himpsel's						
130 (111)	0.74	---	---	0.31	0.21	0.48	---
120 (111)	0.95	---	---	0.34	0.25	0.41	---
130 (100)	1.1	---	---	0.24	0.28	0.48	---
	Our's (without hydrides)						
130	1.9 2.3	---	---	0.29 0.36	0.33 0.37	0.37 0.27	3.54 1.6
125	2.1	---	---	0.33	0.34	0.33	2.72
120	2.8	---	---	0.34	0.33	0.32	2.97
140	2.3	---	---	0.32	0.34	0.33	2.81

Table 4.8: Comparison of evolution of our oxidation state density (with and with out inclusion of hydrides) with photon energy with (Himpesl's [10])

Also shown are our results for hν=140 eV which are useful because as shown in figure 4.25 the background gradient is severe at low photon energies and the fitting software tends to "sacrifice" peak intensity in order to fit the background which is an unrealistic result. From the inset in figure 4.25 it is apparent that the escape depth at 140 eV is comparable to that at 125 eV but the background is almost horizontal which gives greater confidence in our peak intensities. Himpsel [10] reported variations in I^{1+}:I^{2+}:I^{3+} of ± 10% and up to 30% for I^0. Figure 4.29 shows the $Si_{2p3/2}$ spectra a 5.5 nm SiO_2 samples etched for 2.5, 3.0 and 10 mins respectively in 0.5% HF and illuminated with a photon energy of 130 eV.

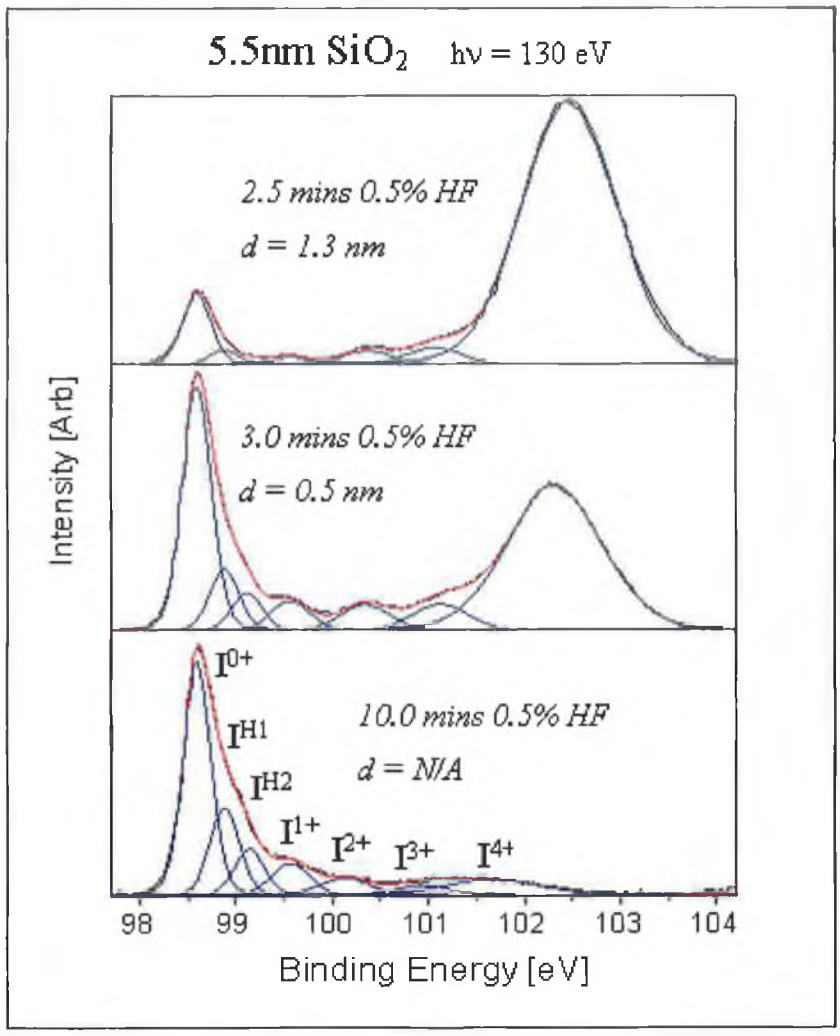

Figure 4.29: $Si_{2p3/2}$ spectra of a 5.5nm SiO_2 oxide etched to thickness of 1.4 nm, 0.5 nm and native oxide thickness, measured at a photon energy hν = 130 eV.

d (nm)	$I^{0+} / \Sigma I^{n+}$	$I^{H1+} / \Sigma I^{n+}$	$I^{H2+} / \Sigma I^{n+}$	$I^{1+} / \Sigma I^{n+}$	$I^{2+} / \Sigma I^{n+}$	$I^{3+} / \Sigma I^{n+}$	$I^{4+} / \Sigma I^{n+}$
1.3	0.92	0.18 20	0.09 6	0.12 13	0.27	0.38	10.5
0.5	1.00	0.26 25	0.16 15	0.16 15	0.18	0.19	2.0
N/A	1.03	0.39 38	0.21 21	0.18 17	0.13	0.08	0.22

Table 4.9: Evolution of individual and total sub-oxidation state density with thickness

It is useful to compare the ratios of the 0.5 nm oxide to that of the relatively thick (1.3 nm oxide) and negligible residual oxide thickness at the same photon energy (hν=130 eV) where the true extent of the resonance (which is unknown) is equally applicable to each spectrum.

The dominance of the Si^{3+} state in the suboxide distribution for the thicker sample is consistent with our expectation that it is localised away from the interface. Also, the Si^{1+} state is more prominent in the thinner oxide. Shown in red in table 4.10 are the hydride intensities as a percentage of the substrate intensity. The increased signal from the hydrides (relative to the substrate) with deeper illumination and for thinner samples, and the change in intensity of the dihydride as a percentage of the mono hydride as shown in table 4.10 was an unexpected resulted as both hydrides were expected to be equally localised near the interface.

d (nm)	Si^{H1} %(Si^{H2})
1.3	22
0.5	54
N/A	62

Table 4.10: Dihydride intensity as a percentage of monohydride intensity.

The data suggests that both hydrides are present at the interface. The dihydride state is strongly localised at the interface because of its role as a passivator of the indigenous dangling bond state. The monohydride is distributed through the suboxide region because of the greater bonding opportunities for a monohydride state. The results obtained are expressed qualitatively below in figure 3.30 where the suboxide layer is sandwiched between an amorphous SiO_2 and crystalline Si layer. Although not supported by the data, a strained layer of SiO_2 is incorporated into figure 4.30. The individual sub oxidation states are identified by colour. Given the complexity of the bonding geometry figure 4.30 is unable to convey micro structural information, instead its purpose is to convey the spatial distribution and population of the various sub oxidation states across the SiO_X region. Therefore, similar to Oh [39] et al (see figure 4.21) it is reasonable to suppose that the SiO_X region is distributed with individual oxidation states populating different layers of the SiO_X region compounding the escape depth effect outlined by Himpsel et al [10].

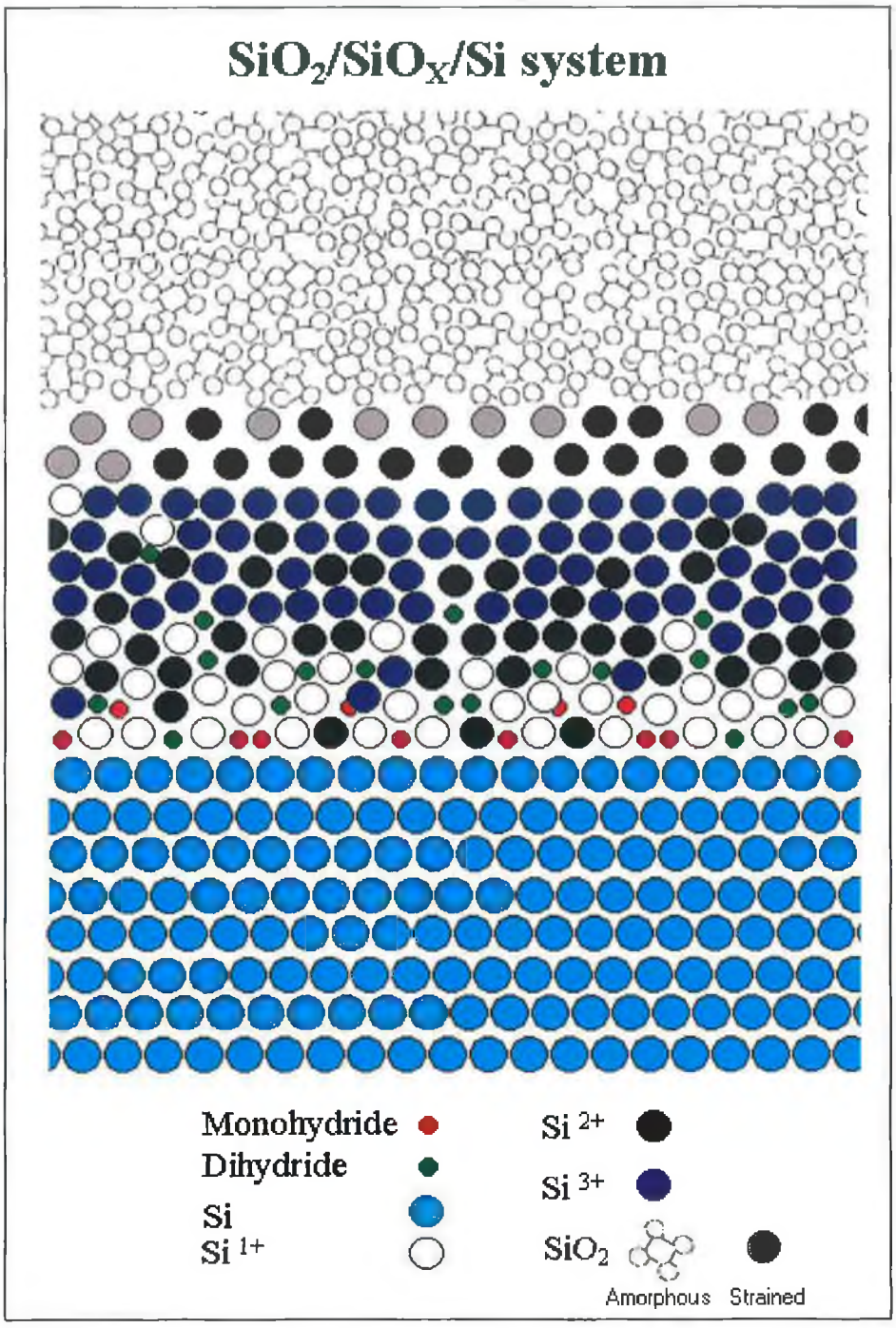

Figure 4.30 A simplified representation of the $SiO_2/SiO_X/Si$ system. A region of intermediary oxidation states exists, sandwiched between an amorphous SiO_2 over layer and crystalline Si under layer. Figure 4.30 is not to scale and seeks only to convey qualitatively the spatial distribution of the various sub oxidation states in the interfacial region.

4.6.3 Discussion of results

The chemical shifts of the intermediate sub-oxidation states and their relative intensities agree very well with the values reported in the literature [10],[51]. The low value of interface suboxide density of 1.5 monolayers affirms the interface quality. Lower values have been achieved experimentally [53]. However, given that the dielectric layers studied in this thesis have undergone post oxidation treatment and given the presence of interfacial hydrides it is reasonable that the interface is more distributed due to this processing. This distribution of suboxide states was investigated by variation of photon energy for a fixed thickness. The Si^{+1}, Si^{+2} states were found to be interface localised and the Si^{3+} was located further out into the oxide. The validity of this result has to be considered in the context of the undermining effects of: overestimation of higher oxidation states due to resonance in photoionisation cross section and escape depth effects. The gradual removal rate of dilute HF acid allowed the interfacial region to be depth profiled without changing the photon energy. The same trend in the localisation of the individual sub-oxidation states as mentioned above adds weight to the view that the interface is not abrupt but is graded as described by Oh et al [39].

Monohydride and dihydride states were consistently fitted in the interfacial region. The behaviour of the hydride peak intensities with thickness in the near interfacial region suggested that the dihydride peak was localised near the interface. Its role at the interface is in quenching the indigenous (two broken bond per surface atom) Si(100) surface state. The monohydride state appears to be more distributed throughout the interfacial region. It is possible that H plays a role in passivating other defects.

The photoemission analysis of the SiO_2/Si(100) interface has provided a template of peak chemical shifts and intensity distributions against which the photoemission results of the SiON/Si(100) results can be compared in order to elucidate the presence of interfacial nitrogen.

4.7 SiON Synchrotron Analysis Overview

In chapter 3, N incorporation into SiO_2 films was considered in terms of process (during oxidation or post oxidation anneal), precursor (NO, N_2O or NH_3) and process type (furnace oxidation (FO) or rapid thermal oxidation (RTO)). From SIMS analysis, nitrogen was found to preferentially pile up near the Si/SiO_2 interface. Annealing in NH_3 resulted in both surface and interface N rich regions. NO resulted in a N pile up on the substrate side of the interface while for an equivalent oxidation with N_2O a more uniform distribution of N in the oxide (although a smaller concentration than NO) was obtained. XPS analysis of the N_{1s} signal originating from the interfacial region (as measured in etched back studies) was found to be Si_3N_4 like (because of it's binding energy 397.9 eV) and without any direct oxygen related bonds. The reduced boron penetration rates observed in MOSFETs gave rise to the interpretation of a "compact" bonding environment were N is bonded to the substrate Si forming interfacial nitrides. In order to better understand the Si/N interfacial bonding relationship, surface sensitive synchrotron studies have been performed for NH_3 adsorption on atomically clean Si surfaces which were subsequently annealed. Table 4.11 summarises the results of Dufour et al [55] who investigated thermal nitridation of silicon surfaces. Figure 4.31 shows the resultant Si_{2p} core level peaks associated with the (111) and (001) surfaces which were attributed to interfacial silicon nitrides. Here silicon singlely bonded to nitrogen is chemically shifted by 0.7 eV. This represents a smaller chemical shift than a Si-O bond (0.9 eV) and is due to nitrogen's lower electronegativity.

120L NH_3	ΔE (eV)	FWHM (eV)	Intensity (%)	Attributed to
Si(001) 1193K	0.0	0.60	27.7	Bulk
	0.72	0.65	7.8	Si^{1+}
	1.50	0.84	5.0	Si^{2+}
	2.58	1.35	59.7	Si^{4+}
Si(111) 1193K	0.0	0.47	22.5	Bulk
	0.6	0.54	3.5	Si^{1+}
	2.59	1.07	74.0	Si^{4+}

Table 4.11: Summary of core level Si_{2p} fitting parameters for nitridation of Si(001) and Si(111) surfaces using NH_3 (Dufour [55])

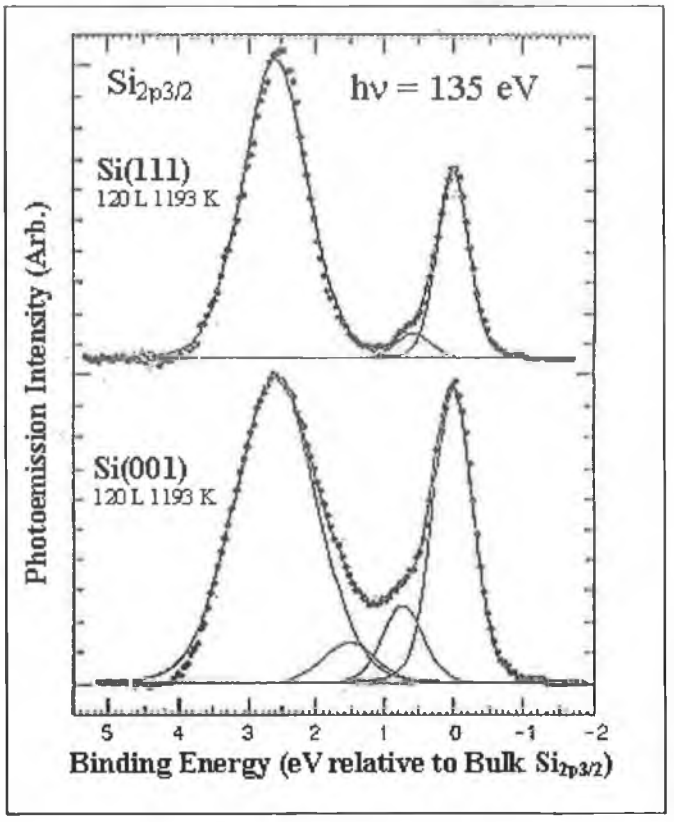

Figure 4.31: $Si_{2p3/2}$ fits for (top) Si(100) and (bottom) Si(111) surfaces after thermal nitridation. Fitting parameters are shown in table 4.11 (Dufour [55])

Similar to the Si/SiO_2 interface the chemical shift of 0.7 eV is considered additive. Dufour [55] considered the interface as bulk crystalline Si connected to a disordered Si_3N_4 lattice. An ideal $Si_3N_4/Si(001)$ interface should exhibit only the Si^{2+} state, the presence of the Si^{1+} state excluded the possibility of an abrupt interface. However, given the presence of the Si^{4+} (stoichiometric silicon nitride Si_3N_4) and Si^{1+} state for the $Si_3N_4/Si(111)$ interface it is closer to the ideal interface. Similar studies were performed by Bishoff et al [56] and Peden et al [57].

These studies are useful in that they provide an expectation of the chemical shifts and intensity distributions associated with nitrogen bonding to the substrate similar to O adsorption studies on clean silicon surfaces. The expectation that interfacial N bonds to the substrate is influenced by SIMS results which reveal the location of nitrogen to be at the interface, and in the case of NO annealed samples below the interface in the substrate silicon as found by Hedge et al [58] and from the XPS N_{1s} binding energy being Si_3N_4 like. Recently Garfunkel et al [59] using MEIS (which offers better spatial

resolution (0.3-0.5 nm) than SIMS (2-3 nm) reported that the nitrogen profile resulting from NO and NO_2 oxidation is located near the interface and not in the substrate. The presence of interfacial silicon nitride bonds can be evaluated in high-resolution surface sensitive soft X-ray analysis of the Si_{2p} core levels. For the oxides in this thesis, nitrogen exists in the oxide matrix (in an unknown bonding environment) through which it migrated during a high temperature anneal. It may also be bonded to the substrate. Recently, in order to better understand the local bonding relationship of nitrogen in oxides researchers have employed along with XPS, extended X-ray absorption fine structure (EXAFS), extended X-ray absorption near edge structure (EXANES) and fourier transform infrared (FTIR) spectroscopy. These techniques offer local microstructural information (i.e. number, distance and bond angle of bonding neighbours). An important consideration for ultra-thin oxides is the nature of the bonding unit in the sub-stoichiometric interfacial region. At the beginning of this chapter the interfacial sub-oxide region at the Si/SiO_2 interface was considered in the context of the RBM and the RMM in order to determine whether SiO_2 segregates into crystalline silicon clusters and SiO_2 as described by the RMM or if there a statistical distribution of sub-oxide tetrahedra $SiO_{x\ (x\ =\ 1,\ 2,\ 3)}$ as described by the RBM. From consideration of the number and distribution of the various sub-oxidation states in synchrotron Si_{2p} spectra the suboxide region was found to be described by the RBM.

At least two different structures can be formed from bonds between Si, O, and N; they are the homogeneous Si-O-N network or the mixture of a-SiO_x and a-SiN_y. Because of the fourfold co-ordination of silicon, amorphous silicon oxynitride films are expected to show a tetrahedral configuration of neighbour atoms around a central silicon. The two models which describe such a structure are;

(1) The RMM, where the structure of amorphous silicon oxynitride is a mixture of SiO_2 and Si_3N_4 separate phases randomly distributed.

(2) The RBM, where the basic structural element is the SiO_xN_y tetrahedron with a central silicon bound to N or O atoms at the edges. The tetrahedrons are labelled $Si_{x,y}$ where x and y donate the numbers of nitrogen and oxygen atoms respectively. The bonding in stoichiometric SiO_xN_y is governed by the Mott rule [60,61] according to which each Si atom is co-ordinated by four O and / or N atoms, each O atom (as in

SiO_2) is co-ordinated by two silicon atoms and each N atom is co-ordinated by three Si (as in Si_3N_4) or O atoms. Each bond between Si and N or O follows a stochastic law and according to Phillips [62] the distribution $H^z(x,y)$ of tetrahedra with stoichiometries Si_z defined by (x+y=z), (x=z, y=4-z) is given by equation 4.6 which is similar to the distribution of SiO_4 tetrahedrons in stoichiometric SiO_2 given by equation 4.0.

$$H^z = \left(\frac{2x}{2x+3y}\right)\left(\frac{3y}{2x+3y}\right)\left(4-z\frac{4!}{z!(4-z)!}\right) \quad \textbf{Equation 4.6}$$

In stoichiometric SiO_xN_y the central silicon atom is fourfold co-ordinated. The two fold co-ordinated oxygen atom bridges two silicon atoms and has a bonding angle that varies between 120° and 180°. This oxygen is the most variable structural element in SiO_xN_y. In a-Si_3N_4, nitrogen is three fold co-ordinated and builds plane triangles with silicon, a more rigid structure compared to the oxygen bridge.

By depositing silicon oxynitride films of various stoichiometries (as discussed above) using techniques such as plasma enhanced chemical vapor deposition (PECVD) and thermal low pressure chemical vapor deposition (LPTCVD) researchers have attempted to characterise the various bond geometries that exist in thin SiO_2 samples after N incorporation in order to better understand the resultant chemical states and their relation with stoichiometric and structural changes.

Behrens et al [63] who studied the whole range of possible compositions of SiO_xN_y films deposited on Si(100) concluded that the bonding network of silicon oxynitrides can be described by a mixture of the RBM and the RMM. For low oxygen contents ($x/(x+y)<0.3$), the geometric structure of the film is almost the structure of a-Si_3N_4, with the oxygen preferably on top of the Si-N_3 triangles building Si_{13} tetrahedrons, which is the basic structural element of Si_2N_2O. As the oxygen concentration increases the O is forced into the triangle and mixed tetrahedrons like $Si_{2,2}$ dominate the structure.

Gritsenko et al [64] using LPCVD deposited a-SiO_xN_y and SiN_x films on Si(100). They considered the partial charge on a central silicon atom in a tetrahedron due to its neighbours using Sanderson electronegativities and the calculated Si_{2p} chemical shift for the various tetrahedral stoichiometries.

They concluded from the agreement between modelled and experimental XPS data that the distribution of a-SiO_xN_y bonding unit is described by the RBM and the distribution of deposited SiN_x stoichiometricies is described by the RMM as SiN_x species dissociate into Si_3N_4 and Si clusters.

Scopel et al [65] characterised SiO_xN_y:H films deposited by PECVD. Using XANES, EXAFS, FTIR and RBS they compared the film's properties to those of reference materials (i.e. a-SiO_2 and βSi_3N_4), and concluded that bonding tetrahedra are best described using the RBM and that for low nitrogen concentrations the films properties are close to those of a-SiO_2.

The local geometric bonding structure of the oxynitrides studied in this thesis is of interest for the following reasons. From XPS analysis nitrogen was shown to exist in the films. From wet chemical depth profiles nitrogen was found in the near surface and interfacial region of the oxide. An asymmetric N_{1s} peak was found. The extent of the asymmetry depended on thickness, which was attributed to a second phase of (Si_3N_4 like) N which is affected by second nearest neighbour oxygens in accordance with the findings of Shallenberger [66] and Bouvet [67]. N-O related bonds were not detected and (as will be discussed below) the interfacial Si-N bonding was not attributed to nitrogen bonded to substrate silicon. These observations suggest the existence of a Si_3N_4 like bonding unit in the oxide for which either the stoichiometry or geometry (i.e. bridging bond angle) or both weakly effects the local bonding environment.

The above experimental results were considered in order to form an explanation of the N bonding structure and bonding state distribution (i.e. SiO_vN_{4-v} for $(v = 0, 1, 2, 3, 4)$ or SiO_2 and Si_3N_4) in ultra thin SiON films. However, these films have been "engineered" through a deposition process where the tetrahedron stoichiometry can be regulated through control of flow rates of ingredient gases. The nitrogen profiles in the oxides considered in this thesis have been realised through a high temperature anneal of an existing oxide with NH_3.

4.7.1 SiON Experimental

The experimental approach adopted for oxynitride analysis was identical to that used for our SiO_2 oxides and also performed on beamline U4A at the NSLS. By etching the as-received oxynitrides (5.5 and 3.3 nm SiON) for suitably long times in dilute 0.5% HF, residual oxide thicknesses were realised where both the oxide and substrate signal could be measured at the surface sensitive photon energy hν=130 eV. All Si_{2p} states were fitted with Voigt functions with 0.1 eV Lorentzian FWHM and different Gaussian FWHM for each Si_{2p} state, which were kept fixed during fitting. A branching ratio of 0.5 and spin-orbit splitting of 0.602 eV were used. After etching samples were rinsed in ultra pure deionised water and immediately transferred via FEL to UHV ($P< 9x10^{-10}$ mbar) within 10 minutes, minimising exposure to surface contamination.

While the approach used to realise interfacial Si_{2p} spectra for both nitrided and non-nitrided oxides has been the same, the interpretation of the nitrided spectra has not been straightforward. On the basis of the earlier consideration of nitrided surfaces and deposition of silicon oxynitride species of various stoichiometries, the expectation of the nitrogen-silicon bonding relationship is unclear. Initially an attempt was made to fit the spectra exclusively with silicon nitrides where the Si_{2p} chemical shift per nitrogen bonding neighbour was 0.7 eV giving shifts of 0.7, 1.50, 2.1 and 2.58 eV for the Si^{N1}, Si^{N2} Si^{N3} and Si^{N4} (taken from Dufour [55]) nitride states respectively as shown in figure 4.32 (a). The experimental data is shown in black and the fit in red. All attempts to fit interfacial nitrides resulted in a poor fit, especially close to the substrate where the spectra seemed more like those found for the SiO_2 samples. In order to address the possibility that there wasn't any nitrogen in the thickness that were being illuminated the spectra were fitted exclusively with SiO_2 parameters as shown in figure 4.32 (b). While the fits were good for the lower oxidation states, it was consistently found the FWHM of the Si^{4+} state at 1.17 eV and the energy position and FWHM of the Si^{3+} were too small. Also not shown, are the attempts to fit both systems together (SiO_x and SiN_x), which were hampered by the finite resolution and the tendency of adjacent peaks to compete. The most consistent and best fit for both oxynitride samples was obtained by using the SiO_2 fitting parameters except for the $Si^{3+}$and Si^{4+} states. The Si^{3+} state was fitted with the chemical shift of Si_3N_4.

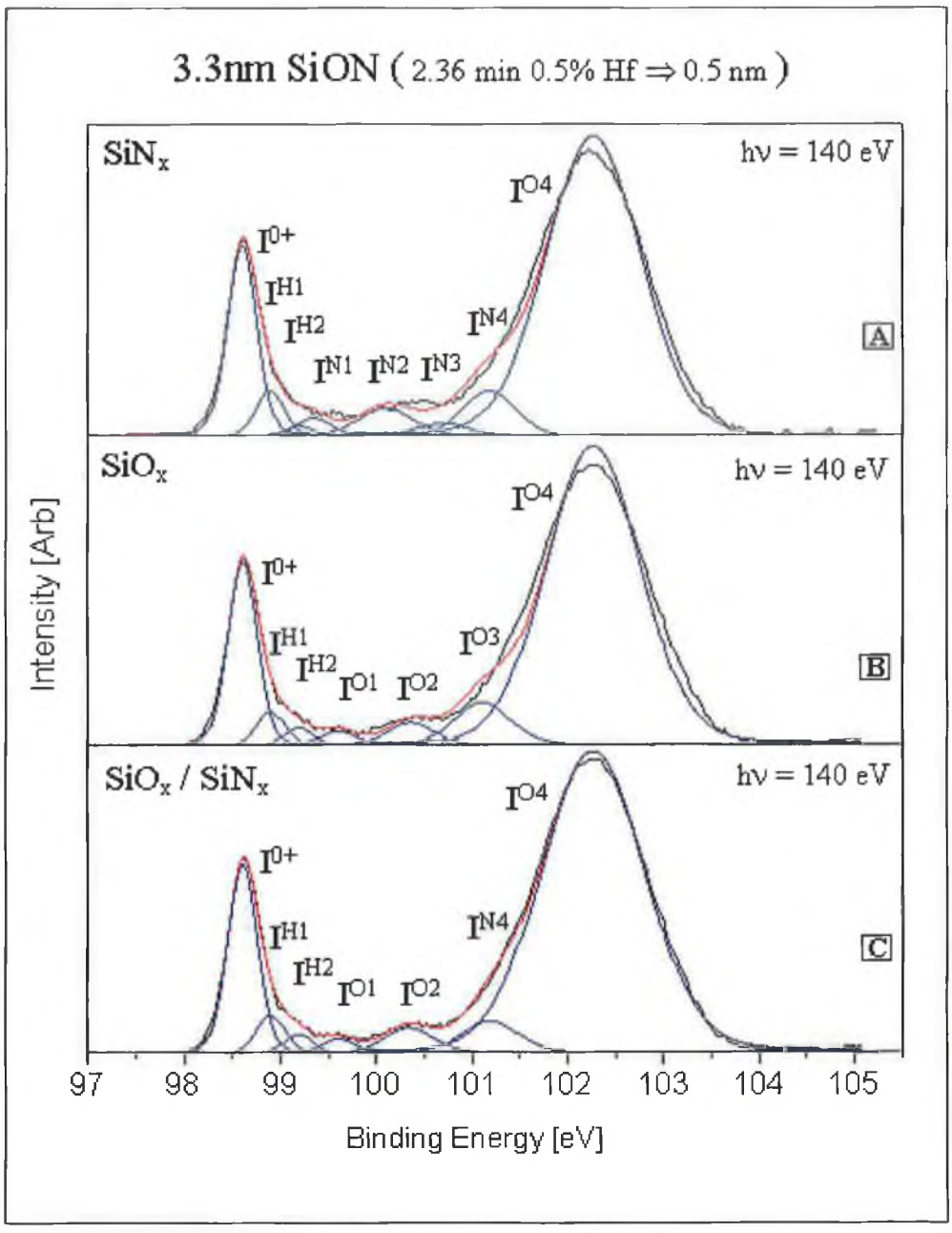

Figure 4.32: Proposed fitting parameters for a 0.5 nm SiON films using a) nitrides except for bulk oxide Si^{4+} peak and b) exclusively SiO_2 parameters c) SiO_2 except for Si^{3+} which was fitted with a Si_3N_4 like state.

This value of chemical shift was taken from Dufour et al [55] (see table 4.11). The FWHM of the Si^{4+} oxide was increased to 1.22 eV. The increase is based on the increased complexity of the bond geometries in the bulk oxide leading to an increase in oxide FWHM. Table 4.12 summarises the fitting parameters. Figure 4.33 shows the Si_{2p} spectra of a 0.13 nm SiO_2 oxide and a 0.12 nm SiON oxide which were realised by dilute HF etch for times of 2.5 and 3.25 mins respectively. Keister et al [53] have found

similar results, figure 4.34 compares two 0.15 nm oxides grown in-situ by Keister with one having been exposed to a He/N plasma for 1.5 mins. Both samples were annealed at 900° C. Keister was unable to converge on a Si_{2p} peak parameter set, which consistently provided a good fit. He attributed the complexity of the interface to the possible co-existence of nitrides and oxides.

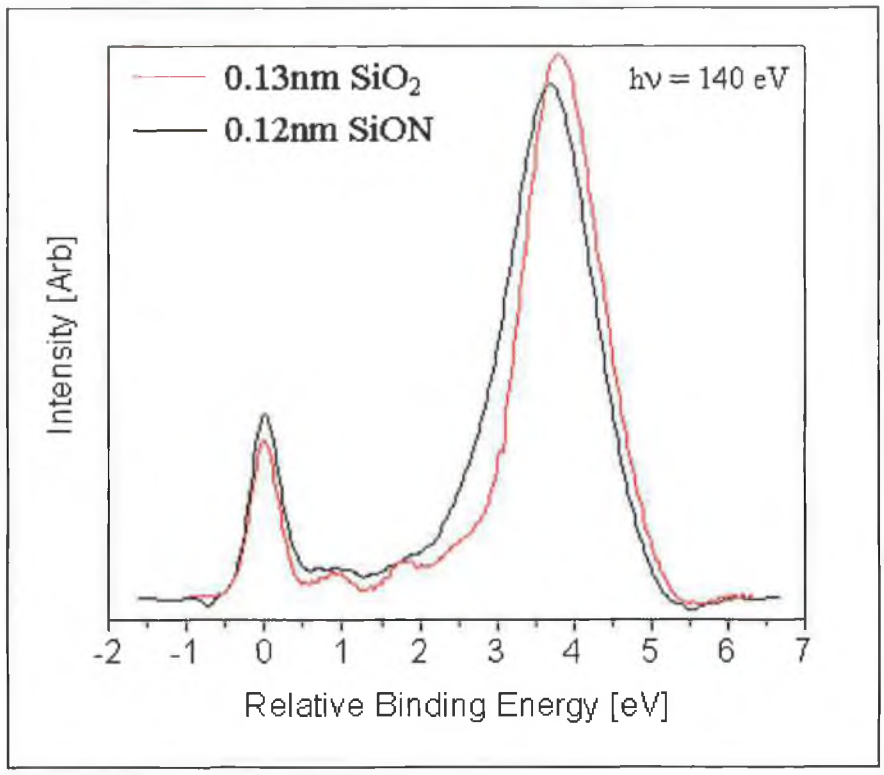

Figure 4.33: Comparison of $Si_{2p3/2}$ spectral envelopes from SiO_2 (red) and SiON (black) oxides of similar thickness. The differences between the spectra are most prominent at higher binding energy.

Chemical State	Chemical Shift ΔE	FWHM
Si^{0+}	0.0	0.37
SiH_1	0.29	0.37
SiH_2	0.57	0.37
Si^{1+}	0.98	0.46
Si^{2+}	1.73	0.59
Si^{3+}	2.58	0.66
Si^{4+}	3.72	1.22

Table 4.12: Summary of Si_{2p} fitting parameters for oxynitride sample.

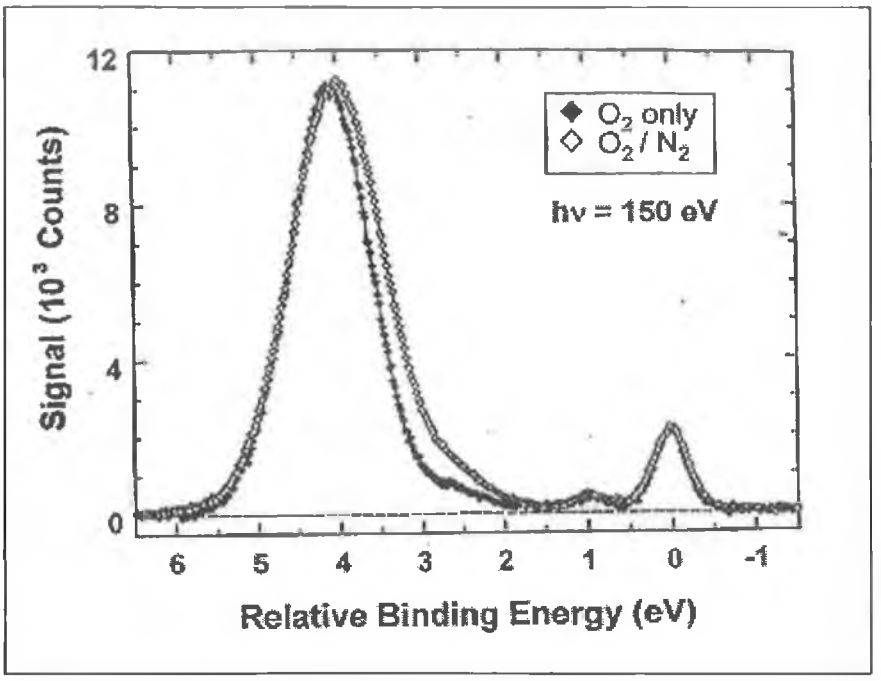

Figure 4.34: Spectral comparison of samples with and without nitrogen incorporated at the SiO_2/Si interface. Both data sets are for ~ 15.3 A total oxide thickness. Peak width and interfacial both increase with N incorporation (Keister [53]).

He found the nitrided spectra to be similar to SiO_2 spectra near the low oxidation states but the peak widths of the higher oxidation states were broader in the nitrided samples.

We sacrificed our Si^{3+} state of the Si/SiO_2 system and assigned the new nitrogen state on the basis of the consistent occurrence of the new state at 2.58 eV from the substrate peak which is the shift of stoichiometric Si_3N_4, and due to Behrens [63] identification for low oxygen concentrations (i.e. $x/(x+y)<0.3$) the Si_3N_4 like state to the Si_2N_2O state which for higher oxygen concentrations shifts in binding energy due to the insertions of an oxygen into the $Si\text{-}N_3$ triangles of the bonding tetrahedra. In order to explain the relaxation of the Si^{4+} FWHM from 1.15 to 1.22 eV, we recall the earlier AFM consideration of the roughening effects of nitrogen incorporation and our detection of a rougher surface in our nitrided samples. The increased Si^{4+} state FWHM is attributed to the roughening of the surface by the local reduced etch rate of the nitrogen rich oxide region. The omission of the Si^{3+} state is harder to justify. However, the results do not propose that the state is absent or quenched by nitrogen incorporation. Rather it was not possible to retain both the Si^{3+} state with and nitrogen state and consistently fit both peaks.

Figure 4.35 shows the Si_{2p} spectra of a 5.5 nm SiON oxide etched in dilute 0.5% HF for times of 3.25, 3.75, and 10 mins, realising thickness of 1.2, 0.3 and N/A nm thickness respectively. As in the XPS analysis the film thickness was calculated using the SiO_2 value of IMFP (λ_{SiO2}) and equation 2.19. Table 4.13 summarises the ratio of each oxidation state to that of the hydrides and sub-oxidation states.

d (nm)	$I^{0+} / \sum I^{n+}$	$I^{H1+} / \sum I^{n+}$	$I^{H2+} / \sum I^{n+}$	$I^{1+} / \sum I^{n+}$	$I^{2+} / \sum I^{n+}$	$I^{3+} / \sum I^{n+}$	$I^{4+} / \sum I^{n+}$
1.2	0.92	0.17 20	0.08 7	0.17 19	0.21	0.36	7.9
0.3	1.32	0.33 25	0.19 14	0.24 18	0.14	0.10	1.37
N/A	1.17	0.34 29	0.25 21	0.27 23	0.11	0.02	0.18

Table 4.13: Individual oxidation state intensity normalised by total sub-oxidation state intensity for different thickness.

Given the uncertainty of peak cross sections and extent of resonance effects coupled with the difficulty of removing the severe background at low photon energies all the spectra at different thickness were compared at a photon energy of 140 eV where the background is easily removed (see figure 4.25) and a reasonable degree of surface sensitivity is maintained. The intensity of the hydrides and Si^{1+} state as a percentage of the substrate Si^{0+} is given in red in table 4.13.

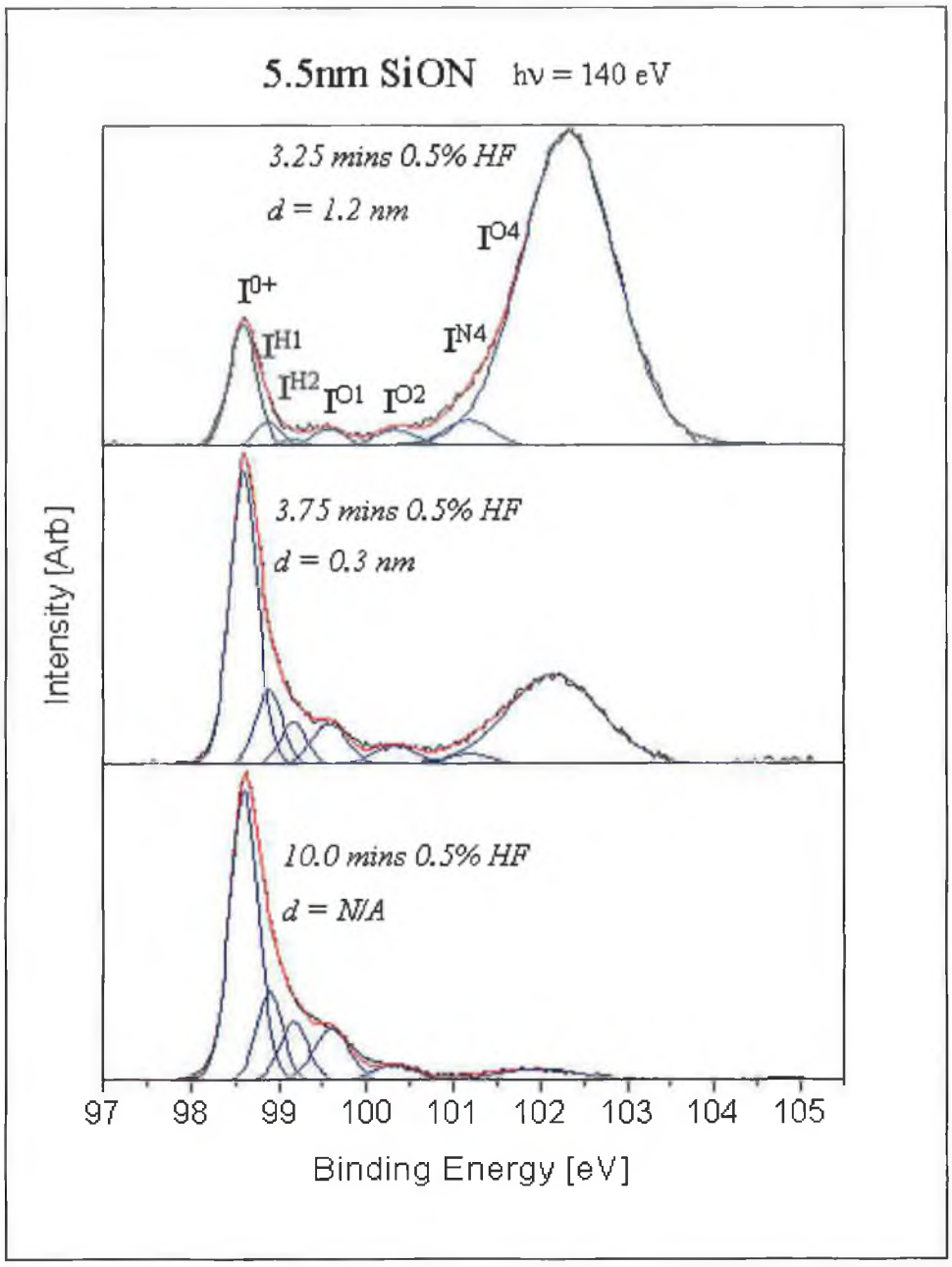

Figure 4.35: $Si_{2p3/2}$ spectra of a 5.5 nm SiON oxide etched to thickness of 1.2 nm, 0.3 nm and native oxide thickness, measured at a photon energy hν=140 eV.

Table 4.14 shows the dihydride intensity as a percentage of the monohydride intensity. The same trend as seen in the Si/SiO_2 interface is evident with the hydrides being interface localised and with the monohydride also being distributed to some extent away from the interface.

d (nm)	Si^{H1} %(Si^{H2})
1.1	22
0.3	54
N/A	62

Table 4.14: Dihydride intensity as a percentage of monohydride intensity for different thickness

From its intensity relative to the other suboxides at each thickness and given that the same photon energy hν=140 eV (which is relatively bulk sensitive) was used it is apparent the Si^{3+} nitride state is localised away from the interface and is not likely arising from bonding with the substrate given its almost non-existence after the 10 min etch.

Figure 4.35 shows the Si_{2p} spectra of the 3.3 nm SiON oxide etched in dilute 0.5% HF for times of 2.0, 2.36, 3.0 and 10 minutes realising thickness of 1.4, 0.9, 0.5 and N/A nm thickness respectively. Table 4.15 summarises our results.

d (nm)	$I^{0+} / \sum I^{n+}$	$I^{H1+} / \sum I^{n+}$	$I^{H2+} / \sum I^{n+}$	$I^{1+} / \sum I^{n+}$	$I^{2+} / \sum I^{n+}$	$I^{3+} / \sum I^{n+}$	$I^{4+} / \sum I^{n+}$
1.4	0.82	0.15 23	0.07 7	0.10 12	0.27	0.38	9.2
0.9	0.94	0.19 23	0.10 10	0.11 12	0.29	0.29	4.9
0.5	1.14	0.36 30	0.20 19	0.13 11	0.19	0.10	2.32
N/A	1.10	0.43 42	0.30 28	0.17 16	0.05	0.03	0.14

Table 4.15: Individual oxidation state intensity normalised by total sub-oxidation state intensity for a 3.3 nm SiON oxide etched to different thickness.

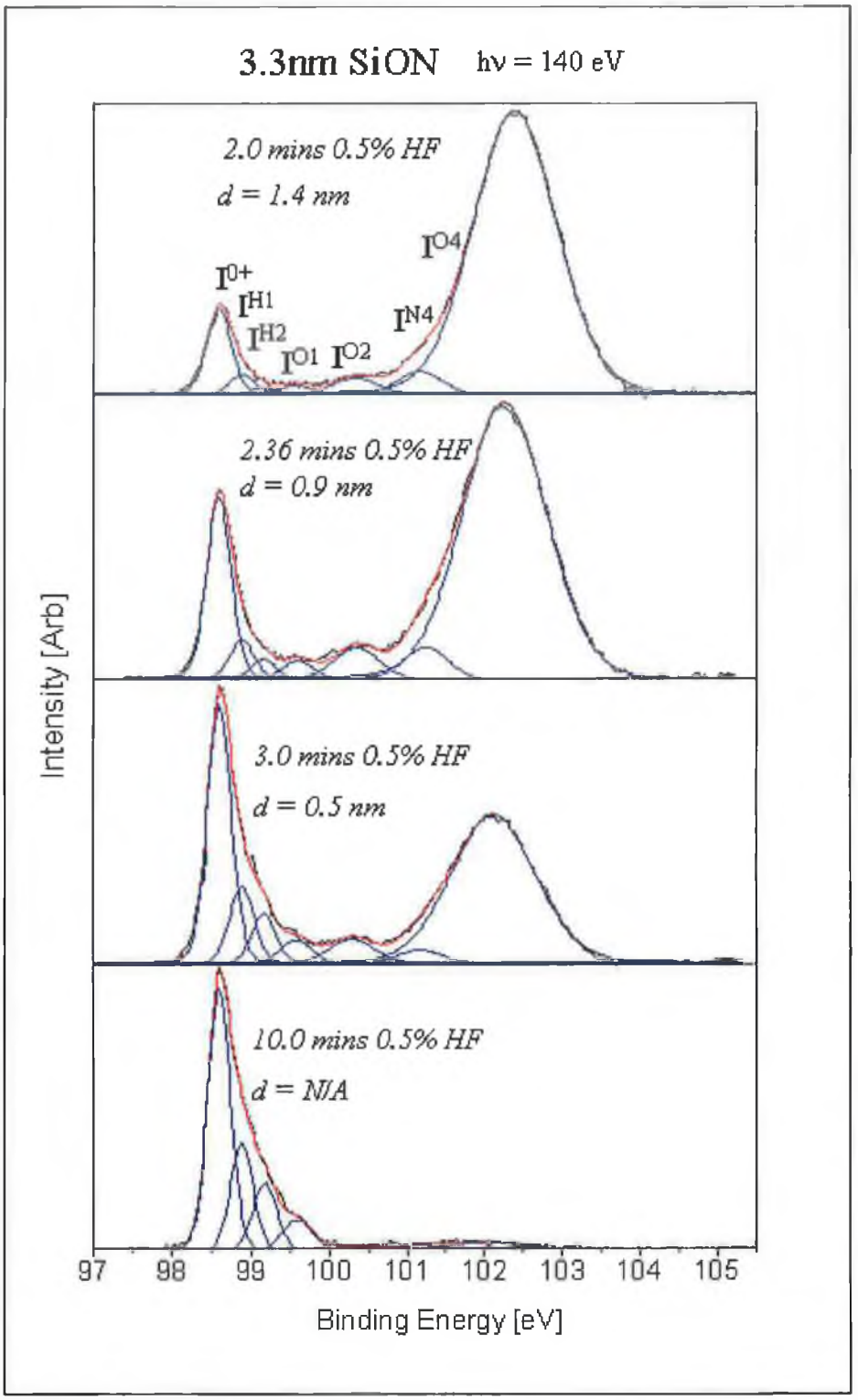

Figure 4.36: $Si_{2p3/2}$ spectra of a 3.3 nm SiON oxide etched to thickness of 1.4 nm, 0.9 nm, 0.5 nm and native oxide thickness, measured at a photon energy hν = 140 eV.

d (nm)	Si^{H1} %(Si^{H2})
1.4	32
0.9	51
0.5	64
N/A	68

Table 4.16: Dihydride intensity as a percentage of monohydride intensity for different thickness

The distribution of states for the 3.3 nm nitrided film like the 5.5 nm film again suggest that the Si^{3+} nitrogen state is localised away from the interface. The growth of the hydride signal with continued removal of the oxide confirms its localisation at the interface. However, having undergone the same 10 min etch as the 5.5 nm SiON film, the hydride signal is a larger percentage of the substrate. Also the amount of residue oxide is smaller. We propose the substrate of the 3.3 nm films has been roughened to a greater extent than the 5.5 nm film due to the longer exposure of the substrate to the etch because it's thinner oxide and therefore would have been removed sooner.

4.7.2 Discussion of results

At comparable values of resolution the Si_{2p} spectra of the SiON samples lack the same degree of spectral structure seen in the SiO_2 samples as shown in figure 4.33. This is attributed to increased bonding complexity due the presence of N and to some extent interface disordering resulting from the nitridation incorporation process.

The interpretation of the SiON Si_{2p} spectra is essentially the same as that of the SiO_2 spectra except for the traditional Si_{2p}^{3+} state being associated with the interfacial Si-N species and the increase FWHM of the Si_{2p}^{4+} oxide peak. The Si_{2p}^{3+} state consistently occurred at a chemical shift of 2.58 eV from the Si_{2p}^{0+} substrate peak which is the expected value [55] for stoichiometric Si_3N_4.

The association of the Si_{2p}^{4+} oxide increased FWHM value to the overlap between the traditional SiO_2 Si_{2p}^{4+} oxide peak and the oxide related phase of the Si_{2p}^{3+} nitrogen species is a tentative one.

This is because the reduced contribution of the oxide related nitrogen phase for thickness less than 1.4 nm should result in a corresponding reduced contribution to the Si_{2p}^{4+} oxide peak, yet no such evolution in the Si_{2p}^{4+} oxide peak FWHM was evident in the SiON samples. However despite this, it is likely that the increased FWHM is in part due to an increased distribution of the interfacial region due to the nitridation process itself.

In terms of evolution of sub-oxidation state intensity with thickness in the near interfacial region, both oxynitride samples show similar behaviour. It is possible that the Si-N bonding species exist in the oxide matrix in that the Si_3N_4 is not due to nitrogen being triply coordinated to silicon at the substrate surface but instead exists in the oxide within 1.6 nm of the substrate. This assertion is supported by the reduced relative contribution of the Si_{2p}^{3+} state to the Si_{2p} spectrum for increased etching. In order to conclude this more conclusively the evolution of the proposed Si-N species would need to be measured for larger thickness. However this possible approach was not pursued because for thickness above ~ 1.5 nm the substrate can not be "seen" through the oxide at the optimal photon energy of 130 eV and so the contribution of the Si-N species would have to be evaluated after de-convolution from the oxide peak.

4.8 Conclusion

The gradual and predictable removal of the oxide by dilute HF etching has allowed the as-received dielectric layers to be profiled to thickness below 2 nm where the chemical state and intensity distribution of interfacial sub-oxidation states has been measured. AFM analyses of the surface microughness suggest the surface is roughened progressively with etch time. The extent of the roughening is not significant enough to undermine the photoemission analysis as evidenced by the stability of the Si^{4+} oxide peak FWHM, which would increase progressively if the surface was severely roughened. In undertaking synchrotron based photoemission measurements we sought to better illuminate the interfacial region in order to see if intermediate sub-oxidation states are present and if present, determine their relative intensity.

As in the XPS analysis in chapter 3, our SiO_2 samples have been prototypical in that the relative intensity and chemical shifts of the suboxides in the SiO_2 layers agree very well with the values in the literature. This result illustrates the point that the chemical state nature of SiO_2/Si interface is "universal" for thermal oxidation because it exists below the oxide and remains when the steady "diffusion limited oxidation growth" stops. The relatively large value of interface sub-oxidation state density measured in this work most likely results from post oxidation treatment of the oxide.

From the behaviour of the N_{1s} peak binding energy position and intensity with etching in chapter 3 the presence of two nitrogen phases, an interfacial Si_3N_4 like and an oxide related shifted phase was established. Comparison of SiO_2 and the SiON Si_{2p} core level spectra suggest a parameter set in which a Si-N chemical state could be consistently fitted, but due to the inability to see the N_{1s} peak could not be conclusively identified. From the consistency in the chemical shift and from the behaviour of the relative intensity of the proposed Si-N state we propose that it exists in a well-defined state (i.e. Si_3N_4) and is distributed in the oxide matrix.

A more quantitative description of the distribution of each sub-oxidation species in the interfacial region would be greatly facilitated by undertaking angular resolved measurements at a fixed photon energy and treating the SiO_x photoelectron signals as arising from different layers, as in a discrete layer model. Such analysis would allow an estimate of the thickness of the SiO_x region which in our approach is not practical to calculate given the distribution of the individual SiO_x states in the SiO_x region and our lack of knowledge of values of inelastic mean free path for individual SiO_x species. However, our aim was not that of an exact value of interface thickness or interface state density. Such absolute values are more worthwhile for comparisons of oxides grown in-situ and without post oxidation treatment.

The usefulness of synchrotron analysis has been in affirming the localisation of the SiO_x region within 1.6 nm of the substrate, the agreement of the SiO_2 results with the literature, the localisation for all samples of hydrides at the interface and the divergence of the nitrated sample results from the non-nitrated sample results on the basis of the presence of an acceptable Si-N related chemical interface state.

4.9 References for Chapter IV

1 D. Vanderbilt, K. Ng, Phys Rev B **59** (1999) 10132

2 A. Pasquarello, M. Hybertson. R. Car, Phys. Rev. Lett. **74** (1995)1024

3 A. Pasquarello, M. Hybertson. R. Car, Phys. Rev. Lett. **68** (1996)625

4 A. Demkov, O. Sankey, Phys. Rev. Lett. **83** (1999) 2038

5 K. Hirose, H. Nohira, T. Hattori, Phys. Rev. B **59** (1999) 5617

6 F. Grunthaner, P. Grunthaner, R. Vasquez, B. Lewis, J. Maserjian, A. Madhukar, Phys Rev. Lett. **43** (1979) 1683

7 K. Hubner, Phys. Status. Solidi **61** (1980) 665

8 E. Martinez, F. Yndurain, Phys. Rev. B **24** (1981) 5718

9 F. Bell, L. Ley, Phys. Rev. B **37** (1998) 8383

10 F. Himpsel, F. McFeely, A. Ibrahimi, J. Yarmoff, G. Hollinger, Phys. Rev. B **38** (1988) 6084

11 B. Holl, F. McFeely, Appl. Phys. Lett. **65** (1994) 1097

12 F. McFeely, K. Zhang, B. Holl, S. Lee, J. Vac. Sci. Tec. B **14** (1996) 2824

13 B. Holl, F. McFeely, Phys. Rev. Letts. **17** (1993) 2441

14 K. Raghavachari, J. Eng, Phys. Rev. Letts. **84** (2000) 935

15 A. Pasquarello, M. Hybertson. R. Car, Phys. Rev. B **53** (1996) 10942

16 M. Weldon et al., Surf. Sci. **500** (2002) 859

17 H. Ubara, T. Imura, A. Hiraki, Sol. State Commun. **50** (1984) 673

18 M. Matsumura, H. Fukidome, J. Electrochem. Soc. **143** (1996) 2683

19 A Crossley, C. Scofield, C. Goff, A. Lake, J. Non-Cryst. Sol. **221** (1995) 187

20 Y Chabal, G. Higashi, K. Raghavachari, J Vac Sci Technol A7 (1989) 2104

21 Y. Morita, H. Tokumoto, J Vac Sci Technol A**14** (1996) 854

22 G. Pietsch, U. Kohler, U. Jusko, M Henzler, Appl Phys Lett **60** (1992) 1321

[23] G. Higashi, K. Y Chabal, W Trucks, K. Raghavachari, Appl Phys Lett **56** (1990) 656

[24] Hattori et al., J. Vac. Sci. Technol B **11** (1993) 1528

[25] K. Ohishi, T. Hattori, Jpn. J. Appl. **33** (1994) L675

[26] T. Hattori, Appl. Surf. Sci. **130-132** (1998) 156

[27] T. Hattori, H. Nohira and K. Takahashi, Microelectronic Engineering **48** (1999) 17

[28] M. Fujimura, K. Inoue, H. Nohira, T. Hattori, Appl. Surf. Sci. **162-163** (2000) 62

[29] J. Sune, I. Placencia, E Farras, N. Barniol, X, Aymerich, Phys. Status Solidi **109** (1998) 496

[30] E. Irene, S. Zafar, Q. Liu, J. Vac. Sci. Technol. A **13** (1995) 47

[31] A. Carim, R. Sinclair, J. Electrochem. Soc. **134** (1987) 741

[32] Q. Liu, J. Wall, E. Irene, J. Vac. Sci. Technol. A **12** (1994) 2625

[33] J. Poler, K. McKay. E. Irene, J. Vac. Sci. Technol. B **12** (1994) 88

[34] M. Hirose, M. hiroshima, T. Yasaka, S. Miyazaki, J. Vac. Sci. Technol. A **12** (1994) 1864

[35] S. Miyazaki, T. Tamura, M. Ogasawara, H. Itokawa, H. Murakami, M. Hirose, Appl. Surf. Sci. **159-160** (2000) 75

[36] G. Tallarida, F. Cazzaniga, B. Crivelli, R. Zonca, J. Non Ctystalline solids **245** (1999) 210

[37] D. Mitchell, K. Clark, J. Bardwell, W. Lennard, G. Massoumi, I. Mitchell, Surf. Intf. Anal. **21** (1994) 44

[38] T. Hattori, K. Hirose, N. Nohira, K. Takahashi, T. Yagi, Appl. Surf. Sci. **144-145** (1999) 297

[39] J. Oh, H. Yeom, Y. Hagimoto, K. Ono, N. Hirashita, A. Kakizaki, Phys. Rev. B**63** (2001) 205310-1

[40] D. Luh, T. Miller, T. Chiang, Phys. Rev. Lett. **79** (1997) 3014

[41] I. Ohdomari, H. Akztsu, Y. Yamakshi, K. Kishimoto, J. Appl. Phys. **62** (1987) 3571

[42] Y. Tu, J. Tersoff, Phys. Rev. Lett. **84** (2000) 4393

[43] R. Buczko, S. Pennycook, S. Pantelides, Phys. Rev. Lett. **84** (2000) 943

[44] R Haight, L Feldman, J. Appl Phys., **53** (1982) 4884

[45] V. Atluri, N. Herbots, D. Dagel, S. Bhagvat, S. Whaley, Nuclear Instruments and Methods in Physics Research B **118** (1996) 144

[46] K. Yamamoto, M. Hasegawa, J. Vav. Sci. Technol. B **12** (1994) 2493

[47] R. Uhrberg, E. Landemark, Y. Chao, J. Elect. Spect. Relt. Phenom. **75** (1995) 197

[48] M. Niwano, H. Katakura, Y. Takeda, Y. Takakuwa, M. Maki, J. Vac. Sci. Technol. A **10** (1992) 339

[49] S. Tay, Z. Lu, T. Miller, J. Appl. Phys. **77** (1995) 4101

[50] S. Tay, Z. Lu, J. McCaffrey,B. Brar, L. Feldman, Appl. Phys. Lett. **71** (1997) 2764

[51] Z. Lu, M. Graham, D. Jiang, Appl. Phys. Lett. **63** (1993) 2941

[52] S. Tay, Z. Lu, R. Cao, P. Pianetta, Appl. Phys. Lett. **67** (1995) 2836

[53] J. Keister, J. Rowe,J. Kolodziej, G. Lucovsky, J. Vac. Sci. Technol. A **17** (1999) 1250

[54] V. Gritsenko, J. Xu, R. Kwok, H, Wong, J. Non crystalline solids **297** (2002) 96

[55] G. Dufour, F. Rochet, H. Roulet, F. Sirotti, Surface Science **304** (1994) 33

[56] J. Bischoff, F. Lutz, D. Bolmont, L. Kubler, Surface Science **251** (1991) 170

[57] C. Peden, J. Rogers, N.Shinn, K. Kidd, K. Tsang, Phys. Rev. B **47** (1993) 15622

[58] R. Hedge, P. Tobin, K. Reid, B. Maiti, S. Ajuria, Appl. Phys. Lett. **66** (1995) 2882

[59] E. Garfunkel, H. Lu, P. Gusev, M. Green, Appl. Phys. Lett. **69** (1996) 2713

[60] V. Gritsenko, J. Xu, R. Kwok, Y. Ng, I. Wilson, Phys. Rev. Lett. **35** (1998) 1293

[61] V. Gritsenko, N. Dikovskaja, K. Mogilnikov, Thin Solid Films **51** (1978) 353

[62] H. Philips, J. Phys. Chem. Sol. **32** (1971) 1936

[63] K. Behrens, E. Klinkenberg, J. Finster, K. Broer, Surf. Sci. **402** (1998) 729

[64] V. Gritsenko, J. Xu, R. Kwok, H, Wong, J. Non Crystalline Solids **297** (2002) 96

[65] W. Scopel, M. Fantini, M. Alayo, I. Pereyra, Thin solid films (2002) Article in Press

[66] J. Shallenberger, S. Novak, D. Cole, J. Vac. Sci. Technol. A **17** (1999) 1086

[67] D. Bouvet et al, J. Appl Phys. **79** (1996) 7114

Chapter 5

X-ray Absorption and Emission spectroscopy of ultra-thin oxides

5.0 Soft X-ray Emission spectroscopy

In photoemission spectroscopy electrons are excited from filled electron states below the Fermi level to empty states above the vacuum level. By measuring the kinetic energy and intensity of the emitted photoelectrons integrated over a large number of emission directions, the binding energy and joint density of states of the occupied electronic states can be determined. Using low energy X-ray radiation the core level states of specific atoms can be measured and from their binding energies their bonding environment determined. By using low energy ultra-violet (UV) photons, the valence band of a material can be investigated. In a photoemission valence band there is information from all the valence band electrons as there is a continuum (see figure 2.1 chapter 2) of final states available. There are, however, some limitations associated with photoemission analysis. Namely that of sample charge up which exist in insulators due to the inability of the photo-hole to decay quickly. Consequently the photoemitted electron in vacuum experiences a Coulomb attraction back to the sample and this alters both the measured energy and momentum. Also the sample cannot be in applied electric or magnetic fields during measurement since these also will alter the energy and momentum of the photoelectrons. Solutions to the above limitations of photoemission are presented to some extent by soft X-ray emission (SXE) spectroscopy.

Figure 5.0 (taken from Iwami [1]) illustrates the SXE process in silicon where an electron is excited from a core state by absorption of an incident photon of energy hν. The atom is de-excited by an electron from a less tightly bound valence band state making a transition into the core hole. The most common mechanism for de-excitation is through an Auger transition. However, there is a finite probability that a core hole will be de-excited by a radiative transition (with the photon energy being equal to the difference in binding energy of the two states involved in the transition) from the valence band. Because the valence band states have a significant energy width, a variety

of photon energies are produced by emission from these states. The transitions are governed by dipole selection rules (only transitions of angular momentum from initial states to final states of ±1 are allowed, for example the photoelectron from a p state may can only be excited to s or d state, also only s or d states may decay into the p core hole).

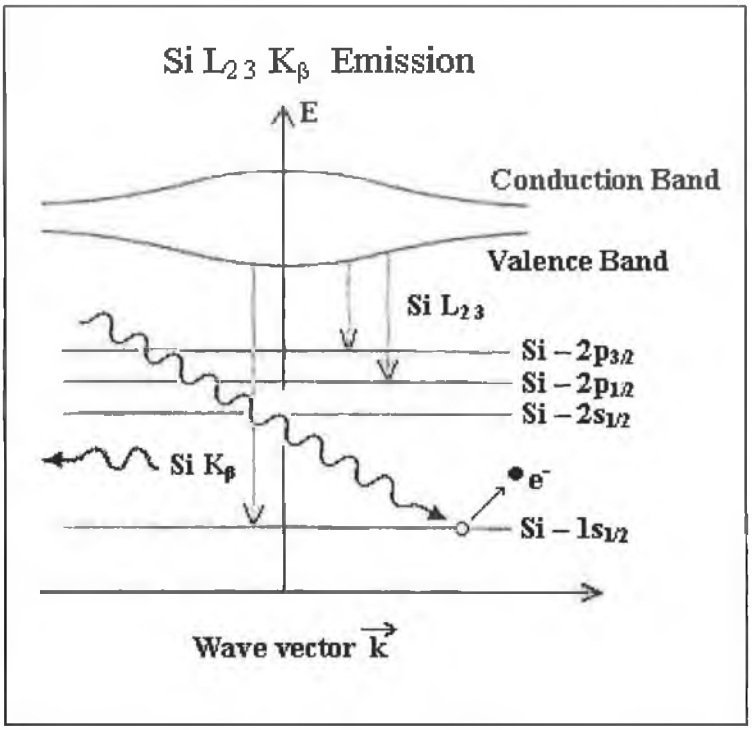

Figure 5.0: A schematic illustration of the mechanism of soft X-ray emission for Si (Iwami [1])

The spectrum obtained by measuring the intensity at each photon energy emitted corresponds to the density of states of the valence band resolved into orbital angular momentum components i.e. the partial density of states PDOS. Since the primary core hole exist only on one discrete level, the transitions are element specific within a multi-element system (i.e. the electronic structure of the valence band that is spatially localised to a region close to the particular excited atom is probed).

However, SXE like photoemission spectroscopy has limitations. The most significant being comparatively low energy resolution. The typical resolution achieved in commercial photoelectron analysers is well below 100 meV, while due to the weak illumination from laboratory X-ray sources, X-ray emission spectra are recorded at a

resolution far worse than in photoemission. Despite this, since a photon is being detected instead of an electron, SXE can measure bulk electronic structure and the charging of insulating samples is irrelevant. An improvement in SXE has been realised through the combined use of grazing incidence diffraction gratings to disperse X-ray emission and a wide area X-ray detector to measure the emission, which can be moved under vacuum to remain at the focal point of the gratings for all energies. This allows energy resolution comparable to that of conventional photoemission [2]. The use of high intensity monochromatic synchrotron radiation as the excitation source allows the selective excitation of individual core levels in a multi-element system. In figure 5.1(a) Rubensson [3] shows the total (or joint) density of states (TDOS) of silicon carbide as measured by photoemission.

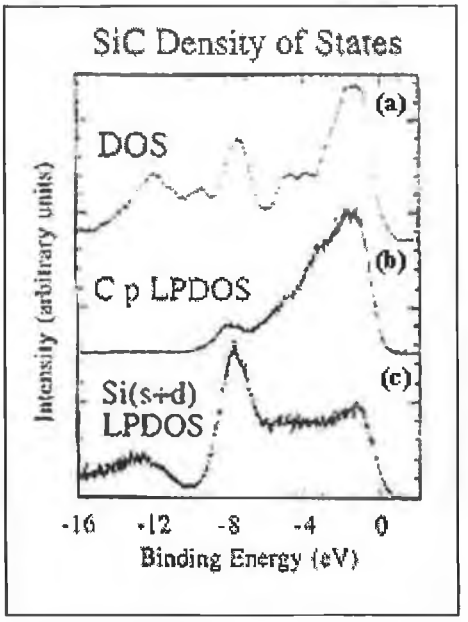

Figure 5.1: Comparison of the total density of DOS states (a) with the C K PDOS (b) and the Si L PDOS (c) emission spectra of cubic silicon The PDOS is reflected in the SXE spectra, whereas the global properties are monitored in PES (Rubensson [3]).

This spectrum is a complex convolution of the contribution of the p, s and d bonding states between Si and C wavefunctions and the continuum of final states. Figure 5.1(b) and (c) shows the local (partial) Cp and Si(s+d) DOS arising from the VB→C_{1S} and the VB→Si_{2p} transitions respectively. Here the valence band intensity is governed by the atomic like nature of the final core hole (i.e. the valence band projection onto local angular momentum symmetries, in accordance with dipole selection rules) and so the local DOS can be seen in isolation.

5.1 Soft X-ray Absorption spectroscopy

Soft X-ray emission spectroscopy gives information about the density of occupied states of the valence band. Soft X-ray absorption spectroscopy (SXA) gives complimentary information to SXE concerning the empty density of states of the conduction band. Figure 5.2 outlines the process by which absorption maybe measured.

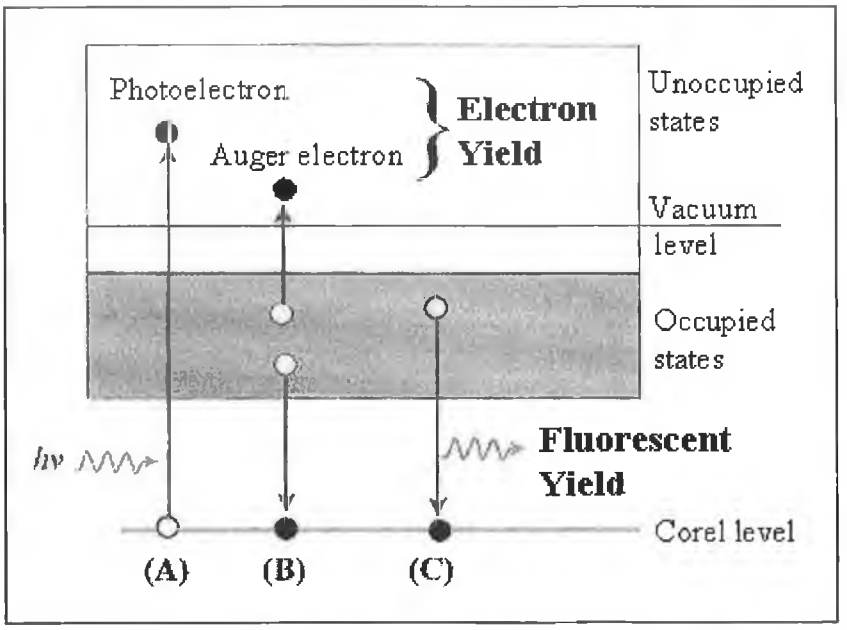

Figure 5.2: By tuning the photon energy through an absorption edge the creation of a core hole can be accompanied with the liberation of; (A) a photoelectron, (B) and Auger electron or in (C) with the emission of a photon of suitable energy.

In figure 5.2 a core hole is created with the absorption of a photon, a compensation current filling the core hole may be recorded. In figure 5.2(B) excited electrons emitted from the sample can be counted with a channeltron (electron yield). In figure 5.2(C) a total count of X-ray emission due to de-exciting electrons filling core holes (fluorescent yield). In SXA the sample is illuminated with monochromatic radiation in the 0.1 to 1 keV range. The photon energy is swept through an X-ray absorption edge and the current through the sample is measured. By sweeping the photon energy through an absorption edge (using synchrotron light), core electrons are excited into the conduction band, and assuming a non-dispersive core state, the current is proportional to the PDOS of the unoccupied conduction band. Figure 5.3 illustrates both SXE and SXA processes.

Figure 5.3(a) shows the dispersion of the crystal momentum of an ideal semiconductor. Core levels are atomically localised and show no momentum dispersion. The density of states is shown by summing through k-space. Absorption spectra may be recorded as either total electron yield (TEY) or by total fluorescent yield (TFY). TEY offers surface sensitive information due to the scattering of low kinetic energy electrons from deep in the solid. Typically the TEY absorption spectra are measured by recording the current flowing into the sample (compensating for ejected electrons) as the photon energy is tuned to the absorption edge of the element of interest.

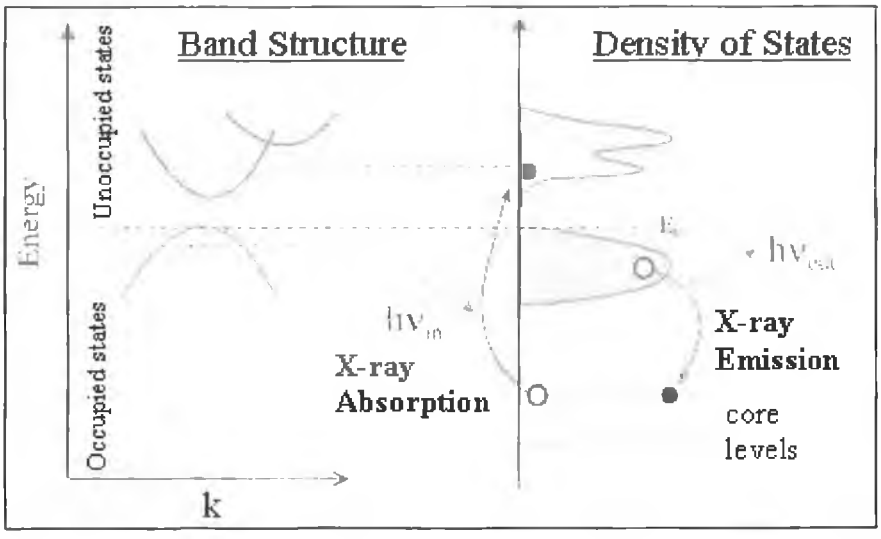

Figure 5.3: Band structure shows dispersion of the crystal momentum of an ideal semiconductor. The core levels are atomically localised and show no dispersion. The density of states is shown by summing throughout k-space. The X-ray emission and absorption process following the creation of a core hole give information about the partial density of states of the unoccupied and occupied bands respectively.

Silicon dioxide is an insulator however and so absorption spectra were measured by monitoring the number of electrons detected from a channeltron multiplier as a function of photon energy. To measure the unoccupied states using the TFY method, the total number of photons emitted from the sample was measured using a soft X-ray emission spectrometer. Due to the low interaction cross-section between X-rays and matter, the TFY technique is bulk sensitive.

5.2 Modification of band structure by nitrogen

Sandwiched between a metallic gate and doped silicon substrate, silicon dioxide's wide bandgap (~8.8 eV) and lack of charge carriers allows it to act as a barrier to charge flow while "permitting" the field applied at the gate to regulate the charge in the silicon substrate. This is its primary function in the basic field effect transistor, which is the fundamental component of modern microprocessors. Figure 5.4 shows the simplified a band diagram of the SiO_2/Si interface.

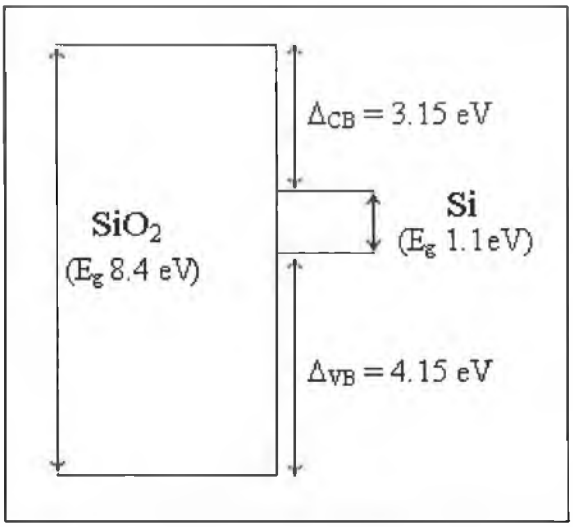

Figure 5.4: A simplified energy band diagram for the SiO_2/Si system showing the valence and conduction band offsets.

The small band gap of silicon (E_g 1.1 eV) relative to the oxide gives rise to band offsets; where the valence band offset is the energy difference between the top of the SiO_2 valence band and the top of the Si valence band (Δ_{VB}=4.15 eV) and the conduction band offset which is the energy difference between the top of the Si conduction band and the SiO_2 conduction band. For the thin (<4 nm) oxide thickness required by current production technologies a significant leakage current exists due to direct quantum mechanical tunnelling across the forbidden barrier presented by the oxide. Lucovsky et al [4] in studying direct and Fowler Nordheim tunnelling currents of electrons through the barrier (presented by the oxide) found that nitrogen incorporation into the oxide through plasma assisted nitridation modified the band structure near the interface in the suboxide region and effected the extent of tunnelling. Figure 5.5 (a) [4] and (b) show

the proposed oxide tunnelling barriers for non-nitrided and nitrided interfacial regions respectively. Included in the diagrams are the suboxide transition regions which define a transition region with an average SiO composition between the Si substrate and the SiO_2 dielectric and who's thickness were estimated to be 0.27 and 0.35 nm wide in the non-nitrided and nitrided oxides respectively.

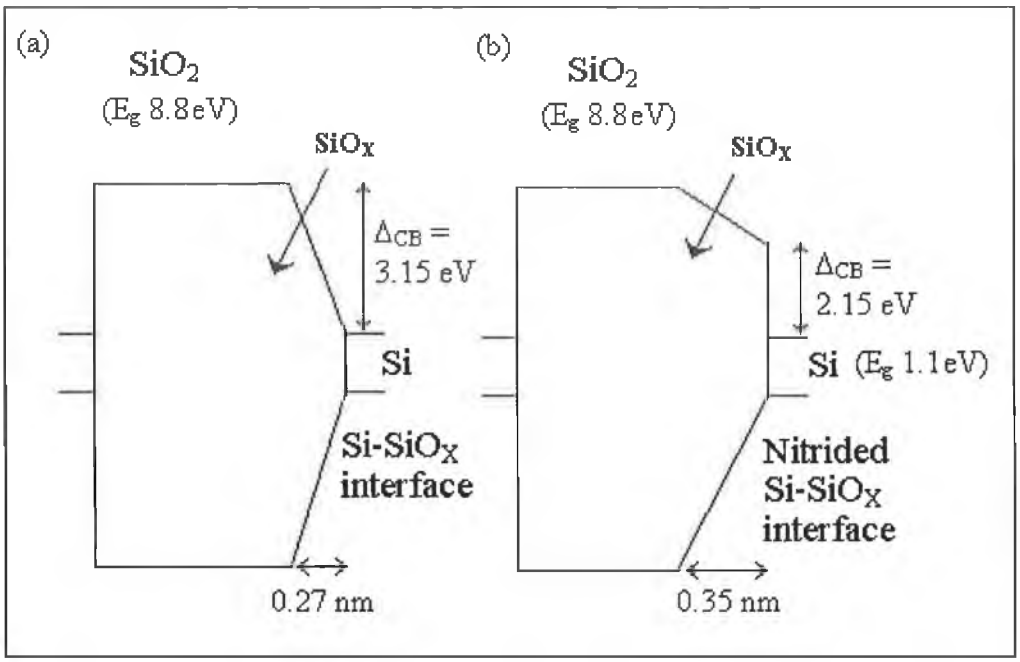

Figure 5.5: Oxide tunnelling barriers with (a) non-nitrided and (b) nitrided suboxide interfacial regions (Lucovsky [4])

Following the results of Maserjian et al [5], Lucovsky assumed a linear variation in the conduction band offset in the suboxide region. A difference in the conduction band offset profiles for the nitrided and non-nitrided interfaces was confirmed from the results of optical second harmonic generation studies. A potential step of 2.15 eV was proposed for the nitrided interface with the remainder of the transition region being represented by a linear variation between the top of the interface step and the SiO_2 conduction band edge. The band structure reduction in direct tunnelling in the nitrided suboxide region relative to the non-nitrided suboxide region was estimated using an analytical expression based on the exact solution of tunnelling through an equivalent rectangular barrier. Lucovsky [4] observed a reduction in direct tunnelling by a factor as much as 8±2.

The Si/SiO_2 band offsets can be inferred using photoemission. Hirose et al [6] using monochromated XPS measured the valence band spectra of ultra thin oxides of thickness of 4.0, 3.7, 3.1, 1.8 nm and also for a H-Si(100) surface. Figure 5.4 shows the spectra. In order to elucidate the oxide bonding structure, the valence band signal from the hydrogen-terminated substrate has been removed from the spectra, which represents Si_{3p} and Si_{3s} bonding orbitals in the bulk. In the energy range 10 to 5 eV the spectrum is due to the anti-bonding O_{2p} line pairs. The O_{2p} lone pair orbital is perpendicular to the Si-O-Si bond plane in the amorphous oxide. From 16.5 to 10 eV the spectrum is a mixture of Si_{3p}-O_{2p} and Si_{3s}-O_{2p} bonding orbitals in the oxide layer with mainly O_{2p} character due to the strong polarity of the Si-O bond [7].

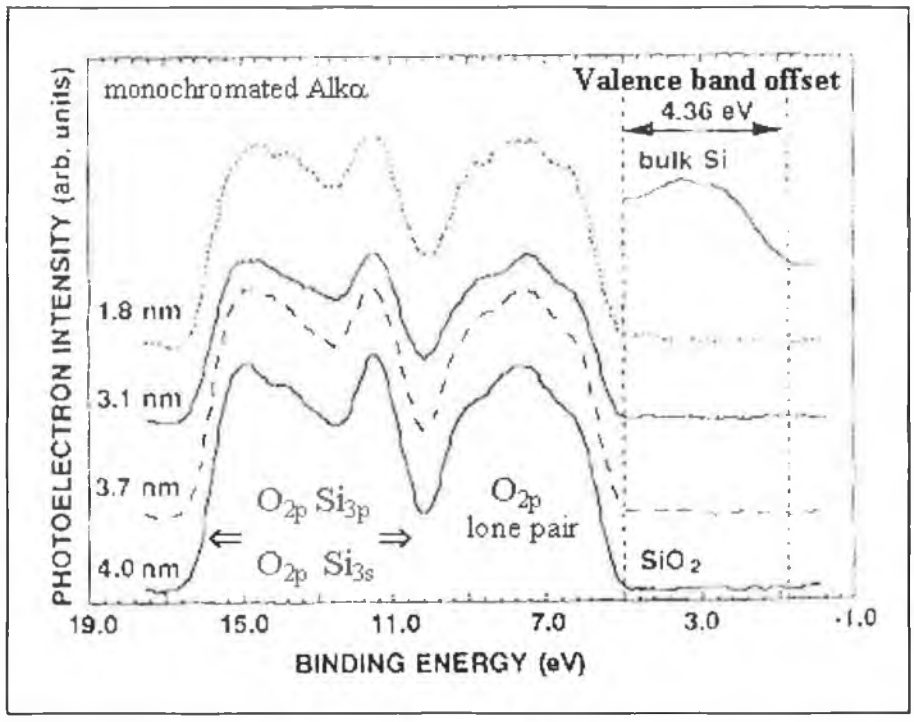

Figure 5.6: Valence band DOS measured for ultra-thin SiO_2 oxides obtained by subtracting the substrate H-Si(100) contribution from the measured valence band DOS (Hirose [6]).

The precise value of the SiO_2/Si valence band offset was obtained by subtracting the charging effect correction in the energy position of the Si valence band top as derived from the position of the Si^{0+} substrate peak. The energy difference between the top of the thin SiO_2 valence band and the top of the bulk Si valence band was found to be 4.35± 0.05 eV for all thickness in the range (1.8 to 3.7 nm) when both the oxide and substrate charging effects were corrected. However, valence band spectra suffer from

differential charging effects as photoelectrons created in the Si bulk can be compensated by other electrons supplied from the sample holder, whereas the photoelectrons emitted from the thin SiO_2 layer are not completely compensated by tunnelling electrons from the substrate. The oxide layer becomes positively charged under X-ray illumination. This positive charge accumulation (Q_{ox}) develops a potential across the oxide layer

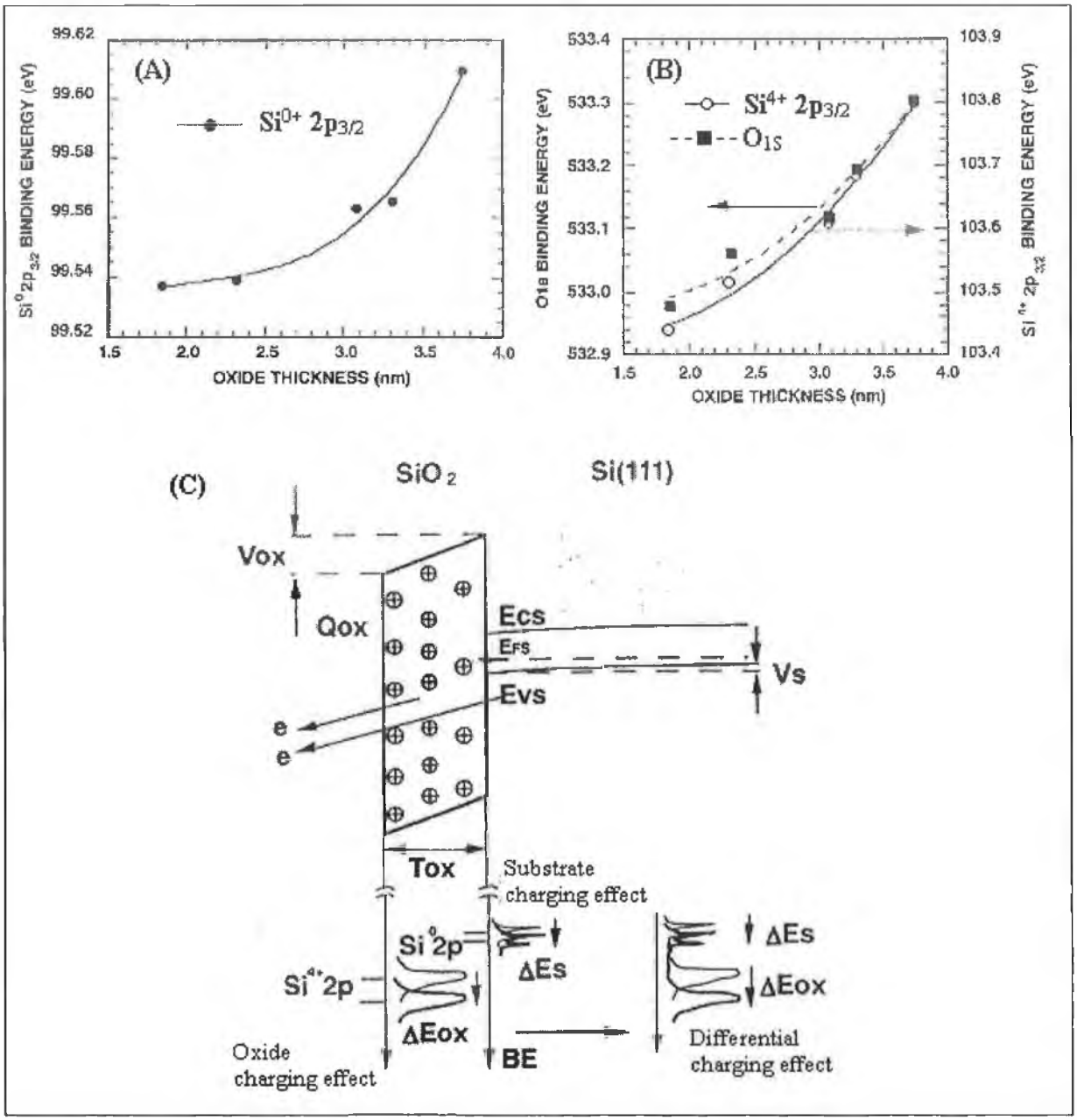

Figure 5.7: (a) $Si2p_{3/2}^{0+}$ binding energy as a function of thickness, (b) $Si2p_{3/2}^{4+}$ and O_{1s} binding energy as a function of thickness and (c) SiO_2/Si interface band diagram indicating differential-charging effect induced on the edge of the valence band and on core-level peaks (Hirose [6]).

(V_{ox}), modifying the energy position of the oxide valence band edge by bending the band downward, and therefore the Si^{4+} and O_{1s} core level binding energies are shifted towards higher energies. Figure 5.7 (a) [6] shows the evolution of the Si^{4+} and O_{1s} binding energies with thickness, both peaks show similar shifts. Figure 5.7 (b) [6] shows the shift of the substrate peak who's shift is a fifth of the Si^{4+} and O_{1s} shift. The p-type valence band in figure 5.7 also exhibits a downward band bending (V_s) due to the oxide charging effect but its value is smaller due to the smooth charge compensation in the Si substrate. The difference in energy shift for Si and SiO_2 leads to the differential charging effect. Given the difficulties of charging, the capabilities of SXE and SXA are better suited to an examination of the band structure in order to elucidate the role of nitrogen in the near interfacial region.

5.3 Experimental Results

SXE and SXA analysis measurements were made on the undulator beamline X1B at the NSLS. Emission spectra were recorded using a Nordgren-type grazing incidence spherical grating spectrometer. The spherical grating had a 5m radius of curvature with 1200 lines/mm. The nitrogen-K edge and oxygen-K edge emissions were recorded in first order diffraction with total energy resolutions of 0.4 and 0.6 eV respectively. For the SXA spectra the energy resolution of the monochromator was set to 0.20 eV. In order to obtain reasonable statistical accuracy in the SXE spectra, the data was acquired for 60-90 min per spectrum. The lower resolution in SXE arises from the need to compensate for the lower count rate (by opening the exit slits) due to the weak process of SXE compared to non-radiative de-excitation processes. The base pressure of the analysis chamber was below $5x10^{-9}$ Torr. Absorption spectra were recorded by both the sample drain current technique to obtain total electron yield (TEY) and by measuring the total fluorescence yield (TFY). A 5.5 nm SiON film was thinned to a thickness of approximately 1.7 nm (determined by XPS) by etching it in dilute 0.5% HF for 2.5 mins followed by a rinse in deionised water before insertion into the vacuum system.

Figure 5.8(a) shows the oxygen K_α SXE and SXA spectra taken from an etched SiON and a SiO_2 sample. The SXE spectrum reflects transitions of O_{2p} electrons from the valence band to holes created on the O_{1s} level, and thus measures the O_{2p} valence band

partial density of states. The excitation energy used to create the O_{1s} core hole was 562 eV in both cases. The SXA spectrum was simultaneously measured by two methods mentioned above TEY and TFY. SXE spectroscopy can be used as a probe of bulk density of states [8,9], and also as a probe of the electronic structure of buried interfaces [10,11]. Similar results are expected from both methods for the nitrated and non-nitrided samples as the oxygen signal from the 1.7 nm oxide thickness is within the sampling depth of the total electron yield method. Because the SXE and SXA spectra were acquired separately, a calibration procedure was used to reference the SXE energy scale to the SXA scale in order to determine the energy gap between the O_{2p} PDOS which contribute to the SiON valence and conduction bands.

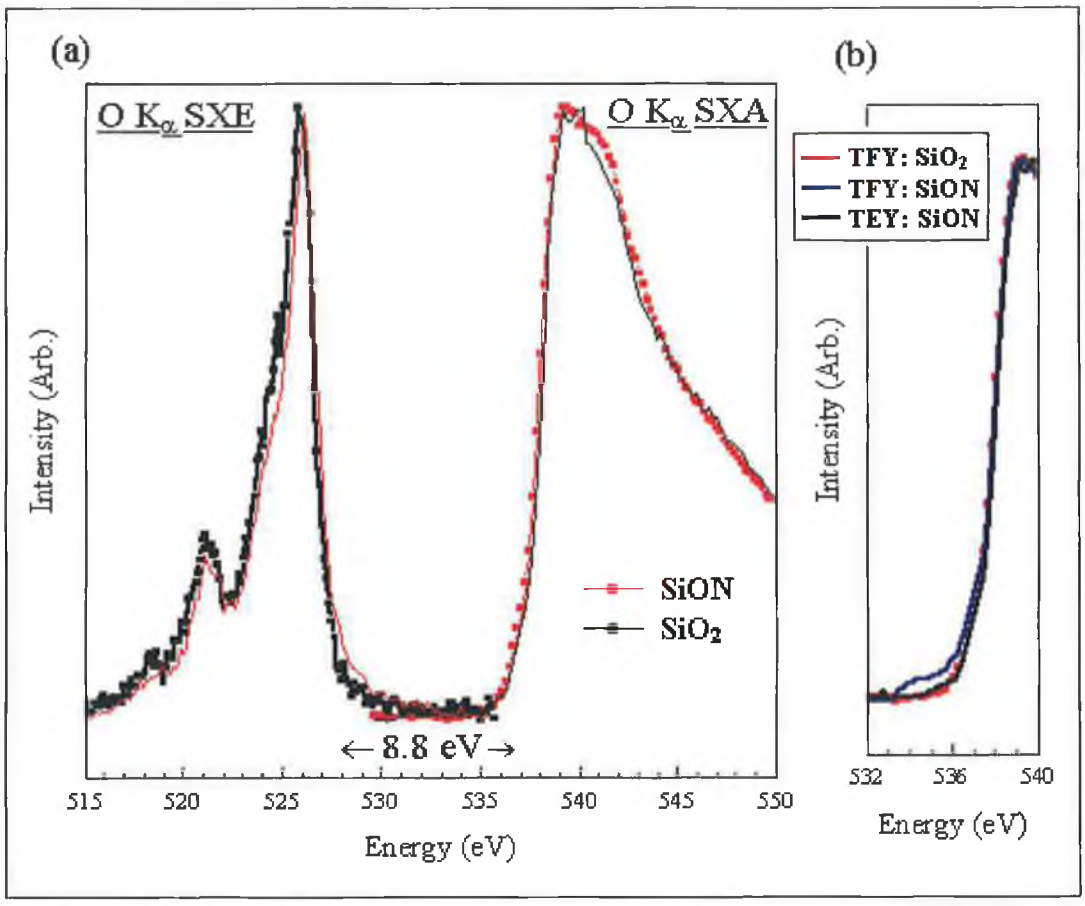

Figure 5.8: (a) O K edge SXE and SXA spectra from both the SiON sample (line with squares) and the SiO_2 sample (solid line). The SXE spectra were obtained with an excitation energy of 562 eV. (b) The O K edge SXA spectra of SiON obtained in both TEY and TFY mode are compared with that of SiO_2 obtained in TFY mode. The SiON TFY (shown in black) spectrum shows a step extending from the conduction band edge by 3eV not observed in the SiO_2 spectrum.

This was performed by detecting the elastically scattered incident photons for both absorption and emission spectra, which are then effectively referenced to the energy calibration of the beamline monochromator. The value measured for the bandgap from the O_{1s} PDOS was 8.8 eV, which closely approximates to the bulk SiO_2 bandgap [12]. For comparison the O K_α SXA and SXE spectra of SiO_2 are included in figure 5.8(a) and are essentially the same as that obtained from the SiON film though the O_{2p}. PDOS from the SiON film shows minor differences. Figure 5.8(b) shows a clear difference when comparing the measured SXA spectrum obtained in the TFY mode (bulk sensitive) between the SiO_2 and the SiON spectra with a visible step extending downwards from the conduction band edge by about 3 eV.

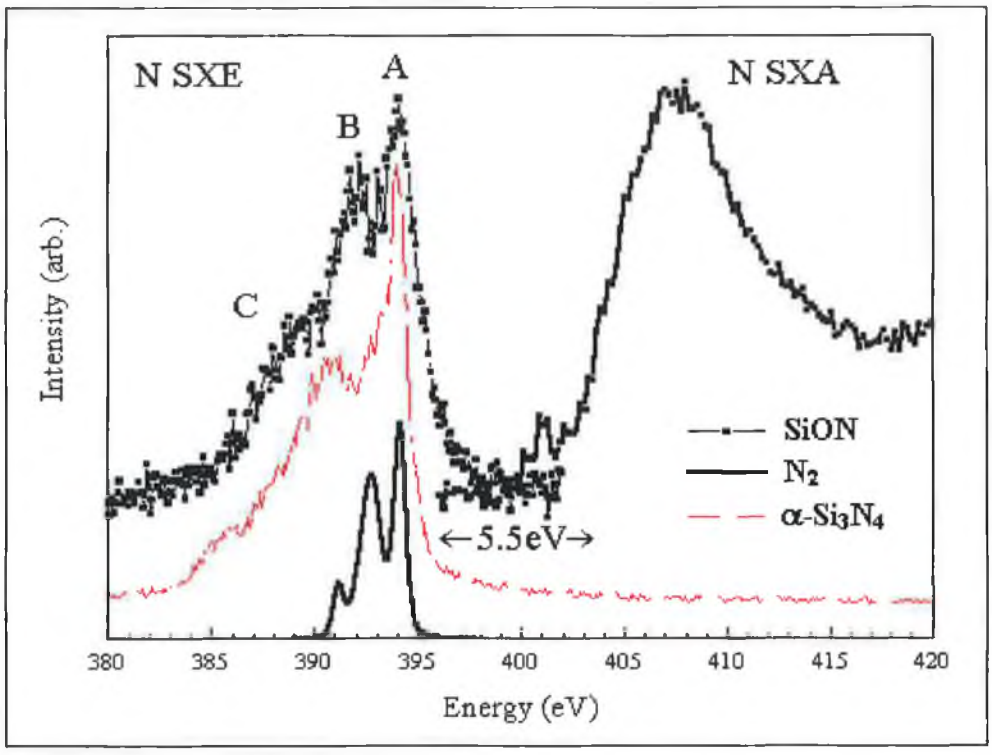

Figure 5.9: N K edge SXE and SXA spectra from the SiON sample (top). The SXA spectrum was obtained with an excitation energy of 440eV. The N K edge SXE spectrum obtained from α-Si_3N_4 is shown (middle) as well as that of molecular N_2 (bottom).

A similar reduction of 3 eV in the conduction band onset has been observed by Muller et al [13] through EELS measurements on interfacial oxides at the interface between Si and SiO_2 and has been attributed to induced gap states predicted to be present at all Si/SiO_2 interfaces. In figure 5.8(b) however, the step is not observed in SiO_2 but is in the TFY obtained from the oxynitride sample and must therefore be a feature of the

Si/SiON interface. Figure 5.9 shows the N_{1s} SXA and SXE spectra measured from the same SiON sample, from a α-Si_3N_4 and from molecular N_2.

The SXA and SXE spectra, which are measures of the unoccupied and occupied N_{2p} PDOS respectively, indicate that the energy bandgap is of the order of 5 eV. This bandgap approximates that of Si_3N_4. The excitation energy used to create the N_{1s} core hole was 435 eV. Finally figure 5.10 shows two separate N_{1s} SXE spectra, one taken at threshold at an excitation energy of 402 eV, the second was obtained at an excitation energy of 435 eV. A shift was observed between the leading edge of the emission spectra, but also a change in the energy spacing of the peaks between the two spectra can be observed.

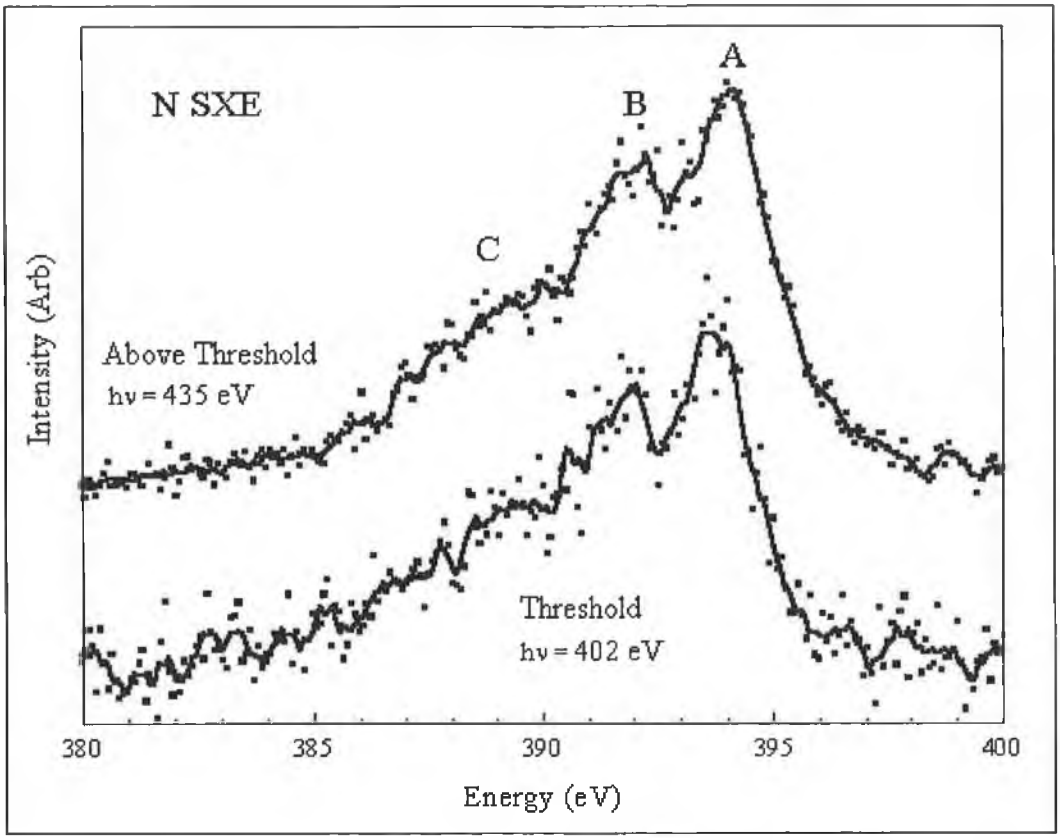

Figure 5.10: N K edge SXE spectrum of SiON sample obtained above threshold (solid line - top) and at threshold (dashed line - bottom). The lines represent 3pt moving averages of the data to guide the eye.

5.4 Discussion of results

A number of band structure calculations are available for Si_3N_4 and also for Si_2N_2O whereas at present few calculations exist for silicon oxynitride systems with more dilute nitrogen concentrations such as those found in industrial device grade material [14,16]. Ance et al [17] have undertaken theoretical calculations for a unique disordered SiO_xN_y phase with a random distribution of Si-O and Si-N bonds the probability of which is determined by the relative oxygen and nitrogen concentration. Their calculations have indicated that for low nitrogen concentrations, the width of the N_{2p} lone-pairs which form the top of the valence band decrease rapidly while the bottom of the conduction band is a combination of Si_{3p}, N_{2p} and O_{2p} antibonding states.

Their results show that the optical absorption edge changes from approximately 5.5 eV for the nitrogen rich material (Si_3N_4 like) to approximately 9 eV for SiO_2. Also the shape of the optical absorption has a step like feature similar to that in our TFY SXA spectrum in figure 5.9 where the step extends from the conduction band edge some 2-3 eV for O/(O+N) ratios in the range of 0.8-0.98, where our bulk O/(O+N) ratio was approximately 0.95.

Wiech et al [18] and Glans et al [19] have undertaken SXE spectroscopy on α-Si_3N_4 and molecular N_2 respectively. It is possible to directly compare our results for the N_{2p} SXE from the SiON with these reference spectra (see figure 5.9). A difference in the position of the valence band maximum of ~0.4 eV between our SiON spectrum and the α-Si_3N_4 spectrum taking into account instrumental broadening was found. The main peak of emission is coincident with that of Si_3N_4 and that of molecular N_2. The N_{2p} valence bandwidth was comparable to that of α-Si_3N_4 and was ~10 eV. The strongest peaks in the emission had an energy difference of 2.3 eV for SiON, 3.09 eV for Si_3N_4 and 1.4 eV for N_2. In analysing the SXE spectra of α-Si_3N_4 Wiech [18] identified the origin of the three peaks denoted A, B and C in figure 5.9 by comparison to calculations of the partial density of states. He determined peak A to be a mixture of Si_{3s}, Si_{3d} and N_{2p} components, peak B to be a mixture of Si_{3p} and N_{2p} and peak C to be mainly due to Si_{3s}. Band structure calculations by Xu et al [16] of the Si_2N_2O result in a sharper partial density of states closer to the valence band maximum in broad agreement with that

observed in this study. Figure 5.10 shows the N_{2p} SXE spectra recorded with a photon excitation energy close to the N_{1s} absorption threshold (403 eV) and far above the threshold at 435 eV. The latter spectrum was the same as presented in figure 5.7 and reflects the N_{2p} PDOS. Clear differences between the positions of the peaks in the emission spectra can be seen for the above threshold spectrum and the threshold spectrum in figure 5.8. The peak designated A has shifted by –0.35 eV in the threshold spectrum relative to the above threshold spectrum, peak B has shifted by –0.15 eV and peak C has not shifted. Such a change in profile on resonant excitation is an indication of the probing of different N sites in the SiON layer, the existence of which have previously been indicated by photoemission as being $N\text{-}Si_3$ and $N\text{-}Si_2$ bonding environments in a dilute nitrogen SiO_xN_y sample. Our photoemission results indicated that nitrogen exists near the interface and is bonded to silicon. It is in this region that the narrowing of the bandgap would contribute to the reducing of the band offsets between Si and SiO_2. This is agreement with the results reported by Lucovsky et al [4] for nitrogen having an influence on the oxide bandgap in the interfacial region of nitrided oxides.

5.5 Conclusion

The experimental findings to date suggest that the distribution of nitrogen in ultra thin SiON films is, both process dependent and interface dependent. The picture, which emerges from these studies, is that the ammonia based nitridation of the SiO_2 layer of the SiO_2 dielectric layer results in the build up of nitrogen at the $Si\text{-}SiO_2$ interface and in the near surface region of the oxide. The photoemission data is consistent with the nitrogen bonding in a $N(\text{-}Si_3)$ bonding environment at the interface. The SXE and SXA data indicate that the contribution of the N_{2p} occupied and unoccupied states to the conduction and valence bands respectively, generate an interfacial bandgap of 5 eV which would significantly modify the band offset between Si and it's oxide.

5.6 References for Chapter V

1 M. Iwami, Appl. Surf. Sci. **113/114** (1997) 377

2 K. Smith, submitted for publication

3 J. Rubensson, J. Electron Spectrosc. Relat. Phenom **92** (1998) 189

4 G. Lucovsky, J. Keister, J. Rowe, Hiro Nimmi, Appl. Surf. Sci. **166** (2000) 485

5 J. Maserjian, N. Zamani, J. Appl. Phys. **53** (1982) 559

6 M. Hirose, J Alay, T. Yoshida, The Physics and Chemistry of SiO_2 and the Si-SiO_2 interface –3 H. Massoud Proc. Vol. 96-1 p. 485

7 F. Bell, L. Ley, Phys. Rev. B **37** (1988) 8383

8 C. Stagarescu, L. Duda, K. Smith, et al, Phys Rev B**54** (1996) R17335

9 K. Smith, L. Duda, et al, J. Vac. Sci. Tech. B **16** (1998) 2250

10 P. Nilsson, J. Kanski, J. Thordson, et al, Phys. Rev. B**52** (1995) R8643

11 P. Nilsson, S. Mankefors, E. Lundgren, J. of Alloys and Compounds **286** (1999) 31

12 S. Sze, Physics of Semiconductor Devices. Wiley 1981 2nd Ed.

13 D. Muller, T. Sorsch, S. Moccio, F. Baumann, K. Evans, G. Timp, Nature **399** (1999) 758

14 A. Ivanovskii, N. Medvedeva, O. Kontsevoi, Physica Status Solidi B **221** (2000) 647

15 G. Pacchioni, D. Erbetta, Phys Rev B **60** (1999) 12617

16 Y. Xu, W. Ching, Phys. Rev. B **51** (1995) 17379

17 C. Ance, F. de Chelle, J. Ferraton, Appl. Phys. Lett. **60** (1992) 1399

18 G. Wiech, A. Simunek, Phys. Rev. B **49**, (1994) 5398

19 P. Glans, P. Skytt, K. Gunnelin, J. Electron Spectrosc. Relat. Phenom. **82** (1996) 193

Chapter 6

Core–level photoemission studies of the sulphur terminated Si(100) and Ge(100) surfaces

6.0 Introduction

The reduced size of semiconductor devices resulting from the drive towards increased device density in modern IC technology has inevitably resulted in the increased role of the surface and it's properties in shaping the electronic properties of these devices. The surface structure of the (100) and (111) surfaces of germanium and silicon represent prototype systems for the investigation of surface bonding involving double and single dangling bonds, respectively. Several studies have investigated the possibility of terminating the (100) surfaces of these semiconductors by an adsorbed monolayer of the group VI element, sulphur. This structure has the potential to eliminate all surface dangling bonds, producing an ideal bulk (1x1) termination of very low chemical reactivity suitable for subsequent hetroepitaxial growth. An ideal sulphur monolayer–terminated surface would also be of significant technological importance if it were a perfect surface termination. This is especially true if it proved to be atomically abrupt, a level of perfection that cannot be achieved with the Si/SiO_2 interface. It would be an ideal surface for the subsequent deposition of high dielectric constant materials in nanoscale transistor fabrication as the surface dangling bond density would be extremely low.

6.1 Si(100) bulk and surface structure

Silicon is a group IV element. It crystallises in the diamond structure where it is co-ordinated tetrahedraly to four other silicon atoms through bond angles of $109^0\ 28'$ (see figure 6.0) [1]. Unlike its oxide there is long range order in the bulk crystal structure due to the absence of the flexible Si-O-Si inter tetrahedral bridge bond.

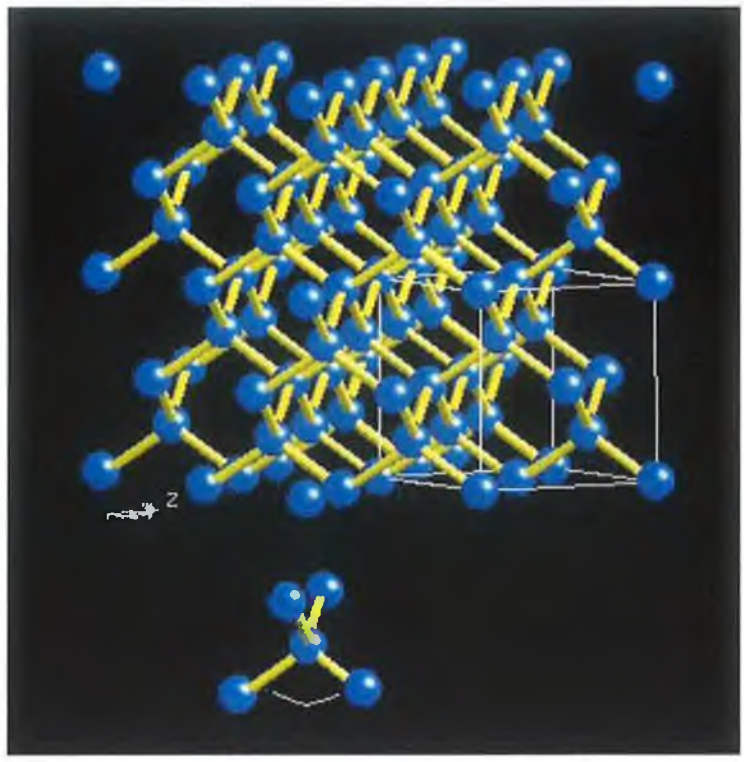

Figure 6.0: A ball and stick model of crystalline silicon in the diamond structure [1]

Silicon's ground state electron configuration of the outer orbitals is [Neon-like]–$3s^2 3p^2$ as shown in figure 6.1 [2]. In order for Si to form four bonds (given that two of its valence electrons are already paired and only two unpaired) a 3s electron is promoted to a 3p orbital, the resulting s-p wavefunction combination is known as a sp^3 hybrid. In forming tetrahedral bonds each of the four equivalent sp^3 hybrid orbitals has two lobes of different phase like a "p" orbital, but with one of the lobes larger than the other and with the four larger lobes orientated towards the four corners of the tetrahedron as shown in figure 6.1. In a molecular bonding approximation the system is equivalent to a collection of diatomic molecules with bonding (+) and antibonding (-) energy levels [3].

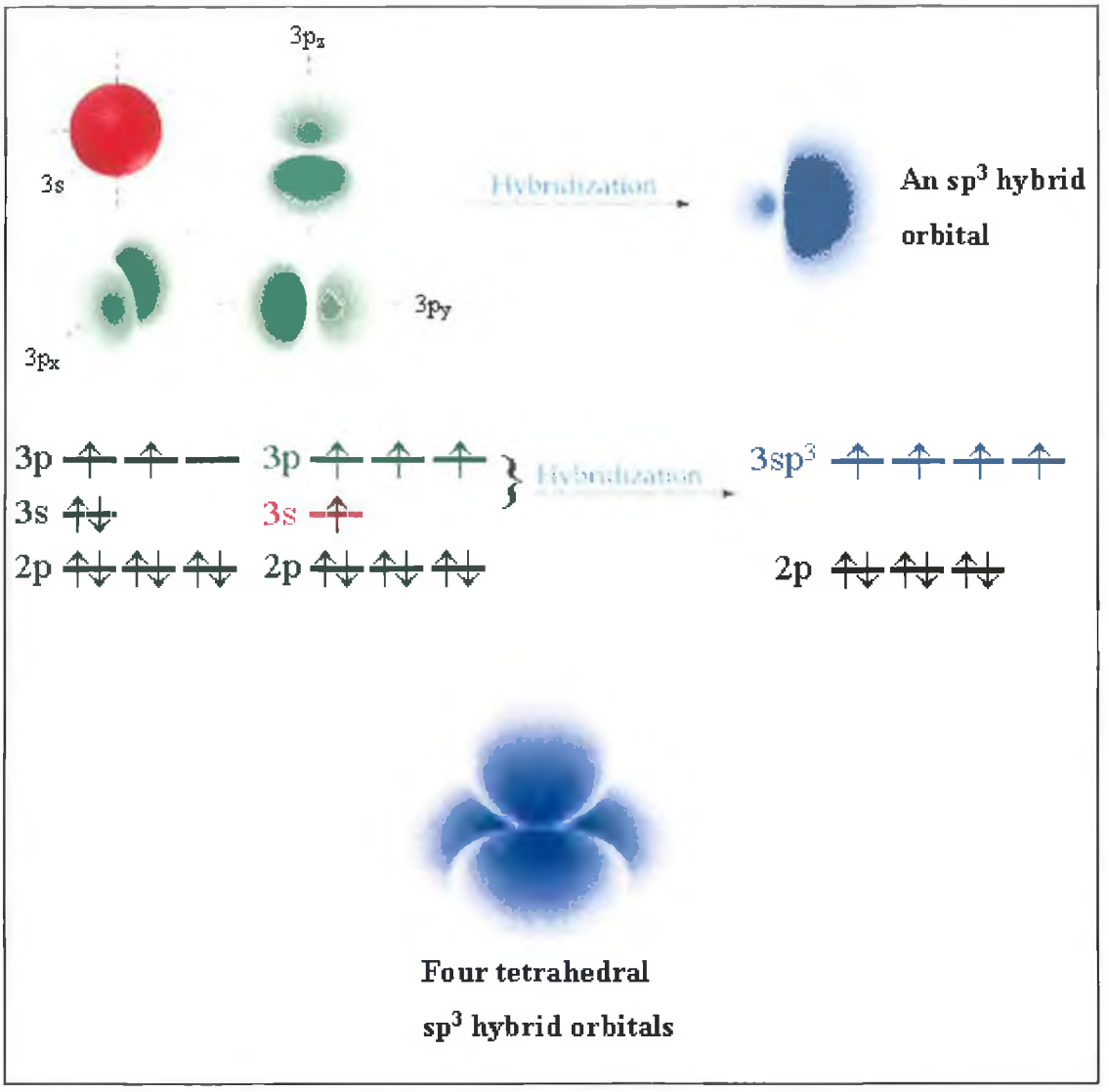

Figure 6.1: Formation of four sp^3 hybrid orbitals by combination of an s atomic orbitals with three p orbitals. Each sp^3 hybrid orbital has two lobes, one of which is larger than the other. For the covalent bonding in crystalline silicon the four larger lobes are orientated toward the corners of a tetrahedron at a angles of 109.5° [2].

In the condensed crystalline environment where the valence wavefunctions of neighbouring atoms overlap the silicon valence ($(3s)^2(3p)^2$ orbitals from sp^3 hybrid) orbitals split into bonding and anti bonding orbitals where the electrons accommodated in the bonding level are much more stable than the initial state of the isolated atom. Due to the directionality of the covalent bonding and the periodicity in the crystal, the bonding and anti bonding levels are broadened into valence and conduction bands respectively separated by a band gap. However, at the surface, silicon atoms have a reduced coordination number and unpaired electrons are left dangling into vacuum. In the absence of any re-bonding, a partially occupied orbital results. The surface energy

and symmetry can be reduced by a rearrangement of the outer surface atoms, which causes the occupied orbital to split into a (higher) unoccupied (antibonding) orbital and a (lower) doubly occupied (bonding) orbital. The trade off between the gain in electronic energy versus the energetic cost of the atomic arrangement decides whether such a surface reconstruction occurs. Duke [4] has outlined three general principles, which help decide whether or not a surface reconstructs:

- The first is the tendency for atoms on the surface of tetrahedraly coordinated semiconductors to "reconstruct" or rearrange so as to either "saturate" (satisfy the valence) the surface atom's "dangling" (broken) tetrahedral bonds that would occur if the surface were to retain its truncated bulk geometry, or to convert them into non bonding electronic states.

- The second principle of semiconductor surface reconstruction is that in many cases, surfaces can lower their energies by atomic reconstruction that opens an energy gap between the highest occupied and lowest unoccupied surface states, giving rise to an insulating or semiconducting surface as opposed to a metallic surface.

- The third principle of surface reconstruction helps to distinguish between activated and activationless surface reconstructions. Activated surface reconstructions have energetic barriers that must be overcome in order to obtain them, whereas activationless surface reconstruction have little or no barrier to obtain them. The surface reconstruction observed will be the lowest structure kinetically accessible under the preparation conditions.

Figure 6.2 (a) [5] shows the truncated Si(100) surface. There are two dangling bonds sp^3 hybrid orbitals per surface atom, which appear like "rabbit ears" on the outer most surface atom (shown in white). This surface geometry is unstable and the surface reconstructs in such a way as to saturate surface dangling bonds (as predicted by the first principle above), and to produce an insulating surface (as predicted by the second principle above) while minimising the elastic energy associated with the distortion of the tetrahedral bond angles away from their bulk values.

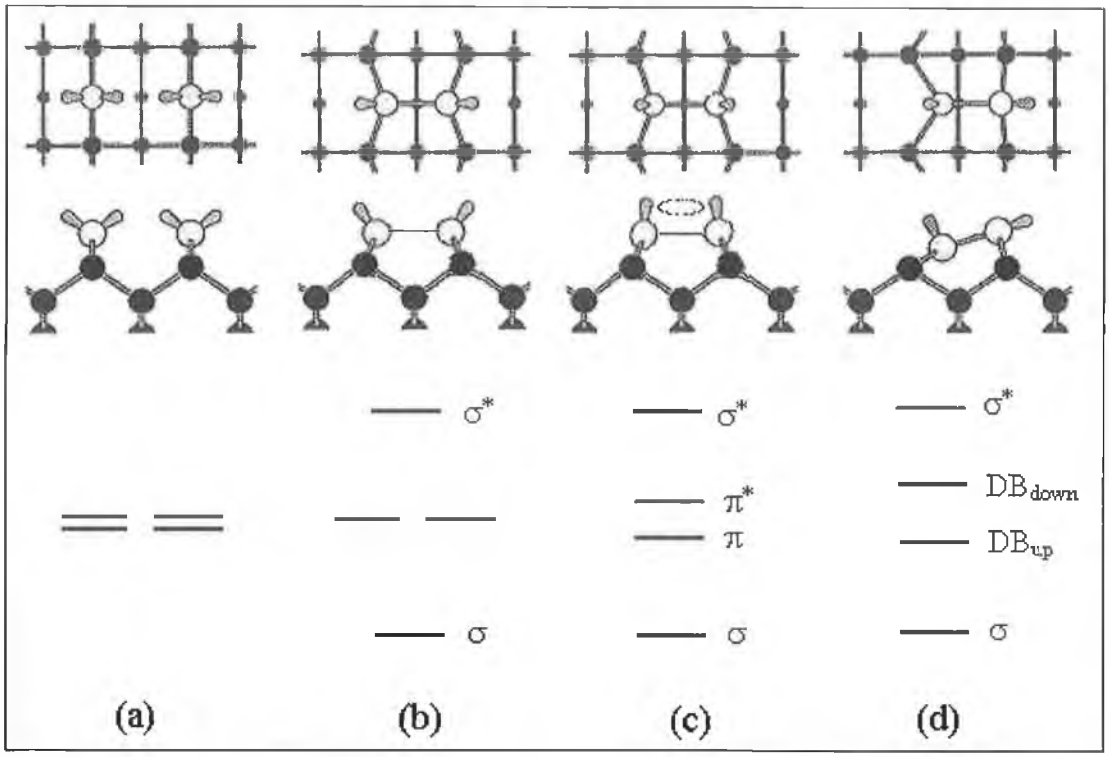

Figure 6.2: a),b),c) and d) (Top panel [5]) shows the ball and stick models of bonding between un-terminated surface bonds for the unreconstructed and reconstructed Si(100) surface [5]. a),b),c) and d) (Bottom panel) show the energy level diagrams with the bonding and anti-bonding states formed associated with surface geometries shown in the ball and stick models (top panel [35]).

Surface dimers (figure 6.2 (b)) are formed when the atoms of the truncated bulk re-bond pairwise to reduce the number of surface dangling bonds per atom to one for the reconstructed surface from two for the unreconstructed surface. In the dimer, sigma (σ) bonding results with pairs of sp^3 orbitals directed along the bond. A weaker form of bonding called pi (π) bonding can occur, which is purely between p orbitals whose axis is perpendicular to the bond. Dimer formation lifts the four-fold degeneracy with adjacent sigma pairing resulting in bonding (σ) and anti bonding (σ^*) sigma states. Pi bonding between the remaining two dangling bonds (figure 6.2 (c)) splits the remaining degeneracy into bonding (π) and anti bonding (π^*) pi states. These states spread into the nearly one-dimensional surface bands along rows formed by dimer pairs resulting in a metallic surface. However for many years there has been disagreement among experimentalists about the nature of the surface reconstruction of Si(100). The symmetric dimer model is supported by the observation of a double domain (2x1) LEED [6] pattern from clean surfaces with monatomic steps. Also, room temperature STM images reveal symmetric dimers [7,8]. Angular resolved photoemission studies,

however, which map the electronic surface band structure of the surface find a band gap [9]. Also (as discussed later) surface sensitive photoemission studies of the surface core level shifts have been in disagreement with the symmetric dimer model. Figure 6.2 (d) shows the symmetry of the dimer is changed with the dimer bond angle making an angle of ~ 20^{o} with the surface. This distortion is driven by rehybridization, which means that after buckling, the orbitals occupied by electrons unused in bonds become more 's' like. The "down or DB_{down} " atom (see figure 6.2 (d)) moves closer to the plane of it's three nearest neighbours, so that it's orbit becomes more sp^2 like. It's "dangling" orbital acquires more 'p' character; its energy increases, that is, it's electronegativity decreases. The opposite happens to the "up" atom. The two electrons in the two "dangling" orbitals buckle the dimer in an attempt to stay longer on the up atom. While symmetric dimers are metallic (due to partial overlap of π and π^* bands), buckling opens a gap ~0.5 eV between the π band (completely occupied) and the π^* band (completely empty) surface states resulting in an semiconducting surface [10]. At room temperature the dimers flip from the up to down at a rate faster than can be followed by an STM tip.

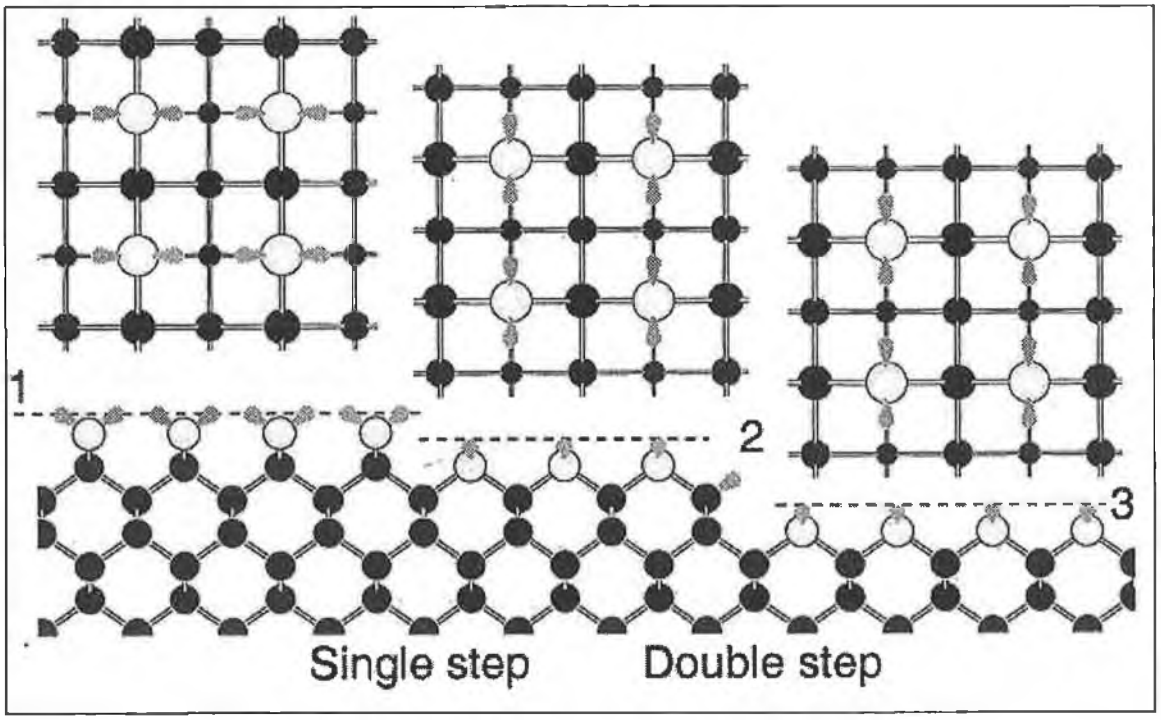

Figure 6.3: A monatomic step on the Si(100) surface results in 90^{o} rotation in the surface bond symmetry, a double step returns the original surface bond symmetry [5].

Figure 6.3 [5] shows a top and side view of the truncated Si(100) surface with a single and double step. Removing a single monolayer of atoms (a single step) uncovers a 90° rotation in the surface orientation, which after a double step is returned to the original. Thus for the reconstructed surface dimer rows run perpendicular to each other on atomic planes separated by single steps. Figure 6.4(a) [11] shows a room temperature (0.2μm x 0.2μm) STM image of a clean Si(100) which has single atomic steeps.

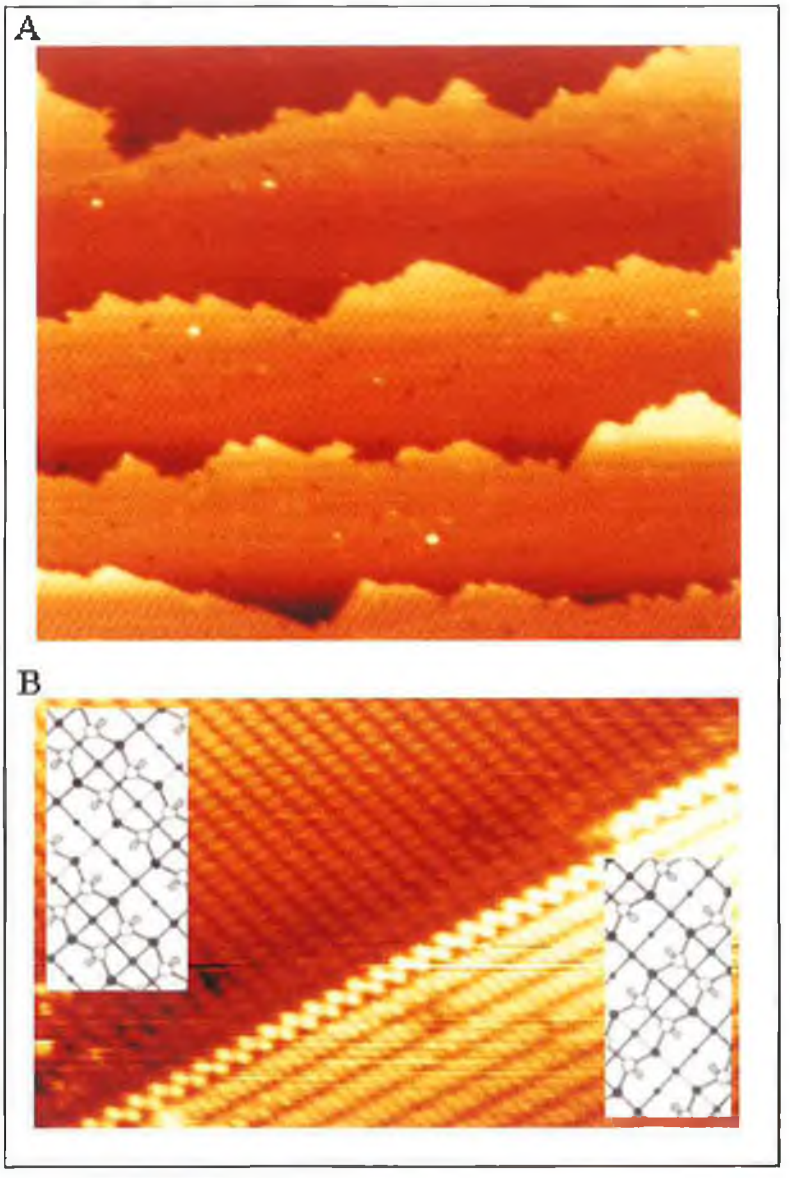

Figure 6.4: UHV STM images of atomically clean Si(100). a) A large area 0.2 x 0.2 μm scan showing monatomic steps. a) A high-resolution 10 x 10 nm scan across a monatomic step. The mutually perpendicular directions of the (1x2) and (2x1) dimer domains on the surfaces is visible in the images an is highlighted in the insets [11].

Figure 6.4 (b) shows a magnified (10 nm x 10 nm) view of the boundary of a monatomic step. The different orientations of the dimer rows are visible in the image and are illustrated in the insets.

6.2 LEED Structure

In order to appreciate some of the above results it is useful to consider the surface periodicity. The periodicity of bulk solids can be investigated with X-rays. A diffracted beam of X-rays will emerge from a bulk crystal whenever constructive interference occurs between successive planes of atoms in the real space lattice. The diffraction condition is more easily determined in reciprocal space where within the Ewald sphere the change in momentum (only direction is changed) on being elastically scattered is equal to a reciprocal lattice vector. The position of the diffracted beams offers information about the crystal lattice size and symmetry. Analysis of the intensity gives information about the arrangement of atoms within the lattice (the crystal basis).

We cannot use X-ray beams in order to probe the periodicity of the surface however because of the small scattering interaction between X-rays and the charge distribution on atoms which results predominately in bulk information which would dominate the smaller surface signal. Low energy electrons however have a very strong interaction with matter and have a short mean free path (for $E < 150$ eV). Also, the wavelength of such electrons is slightly smaller (a few angstroms) than typically interatomic spacing and therefore suitable for diffraction experiments. In a LEED experiment a beam of monochromatic low energy electrons is incident on the clean surface. The electrons are backscattered from the sample surface onto a system of grids. Only the elastically scattered electrons form the LEED pattern and are accelerated towards a fluorescent screen where a pattern of bright spots is seen. The inelastically scattered electrons are rejected by the negative potential of the other two grids.

Figure 6.5 (a) shows the ball and stick model of the truncated Si(100) surface, the green grid show the real space representation and shown in black, the resulting (reciprocal space) LEED pattern. Figs 6.5 (b) and (c) show the (1x2) and (2x1) reconstructions respectively and their corresponding LEED patterns. However as mentioned above the

LEED pattern observed experimentally is a double domain (2x1) where there are contributions from the (1x2) and (2x1) reconstructions separated by atomic steps.

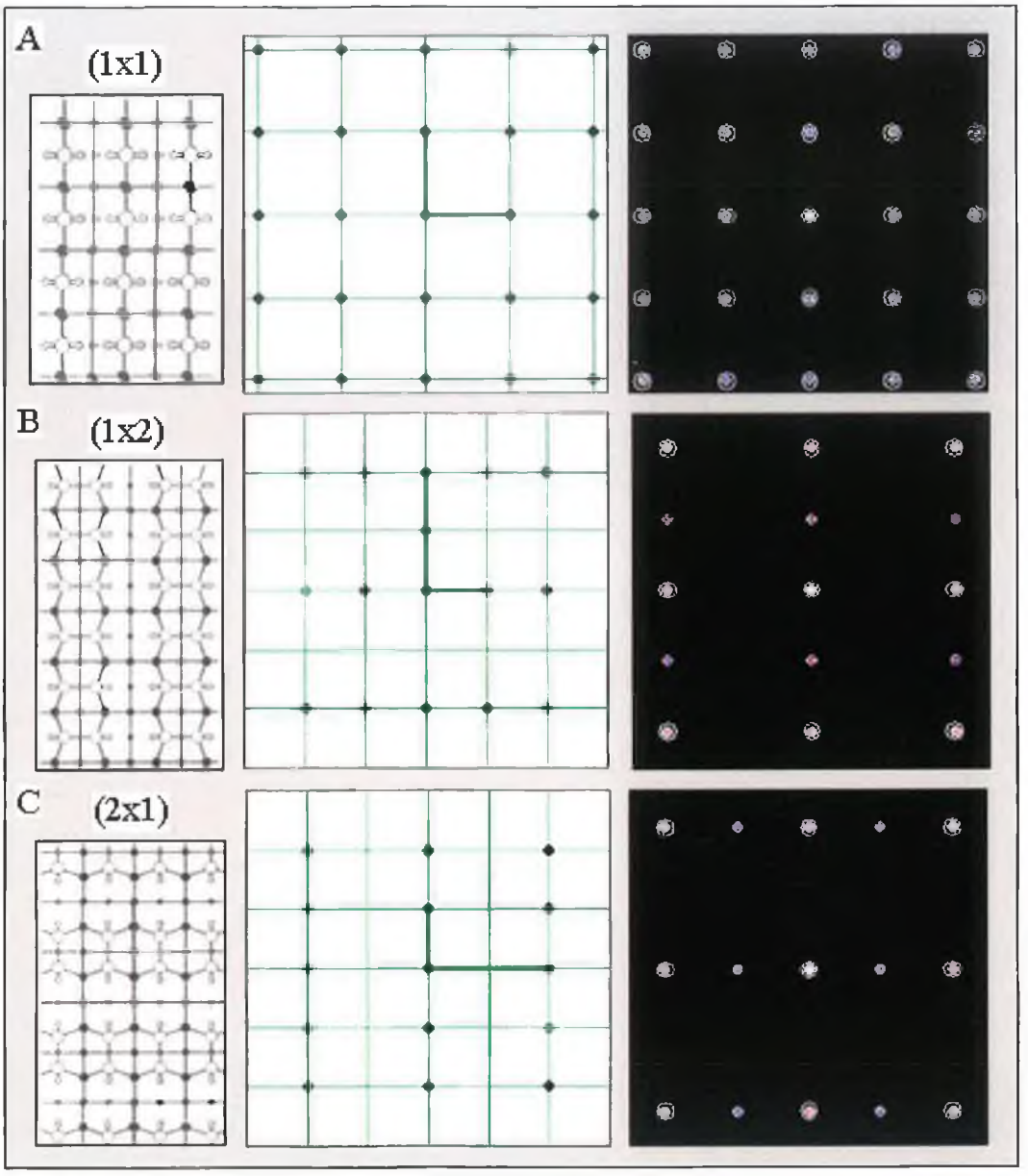

Figure 6.5: a) Si(100) (1x1), b) Si(100)-(2x1) and c) Si(100)-(1x2). Left ball and stick representation of dimers, middle real space representation of surface reconstruction, LEED pattern representing the inverse representation of the surface reconstruction.

Figure 6.6 [11] shows a double domain (2x1) LEED pattern as seen on the florescence screen.

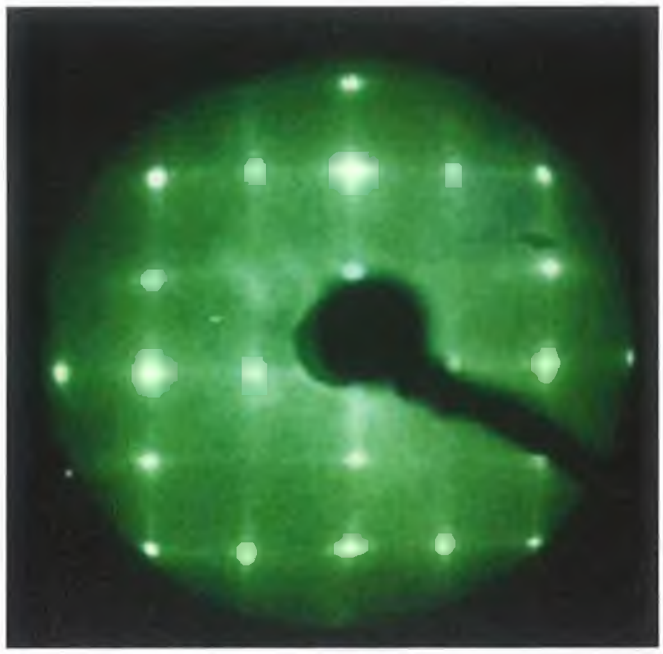

Figure 6.6: Double domain (2x1) experimental LEED image from clean Si(100) (2x1) [11]

6.3 Photoemission

In chapter 4, the surface sensitivity and resolution of soft X-ray synchrotron radiation was used to exclusively illuminate and resolve the chemical states of silicon in the interfacial region of its oxide. Similarly using soft X-ray synchrotron radiation, the chemical state of silicon atoms in the outer atomic layers of clean Si(100) (surface core level shifts) have been investigated. Figure 6.7 (a) shows the geometric bonding environment of the first three atomic layers of the clean Si(100). Figure 6.7(b) shows the soft X-ray photoemission results of Uhrberg et al [12] who de-convoluted the Si_{2p} spectrum into five components corresponding to five unique chemical environments.

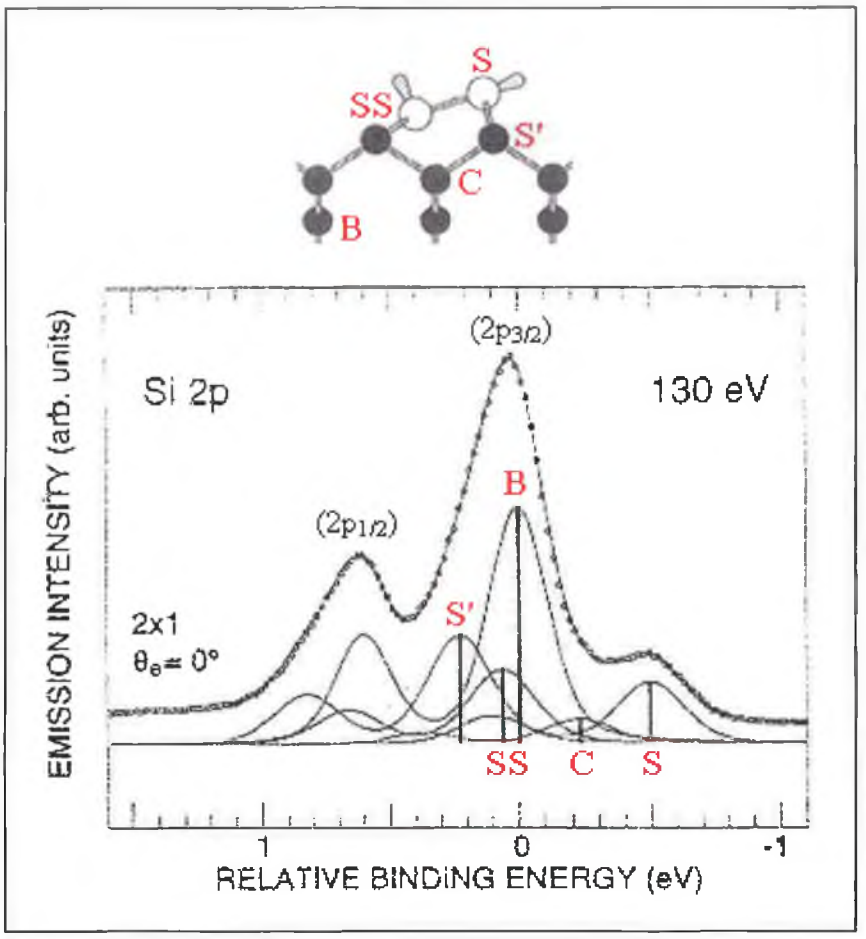

Figure 6.7: (Top) the geometric structure of first four layer of silicon atoms. (Bottom) the surface core level shifts in the Si_{2p} spectrum of the outer atomic layers at hν = 130 eV. Charge transfer from the up to down dimer atom results in the states (S) and (SS) respectively. (S') is associated with emission from the second layer of atoms and (C) is associated with half a monolayer of the third layer (Uhrberg [12]).

The surface core level shifts (SCLS) are referenced to the chemical state of silicon atoms in the bulk. In the first layer of atoms the dimer bond makes an angle of 21° with respect to the surface. Chadi et al [9] proposed that charge transfer occurred within the dimers due to bulking, resulting in a split of ~ 550 meV between the up and down state. As mentioned earlier the "up" dimer atoms experienced a reduced energy in moving away from the plane of it's neighbours, it's dangling bond becomes more 's' like and becomes more electronegative. It is bound less tightly than silicon atoms in the bulk and so it is chemically shifted to a binding energy lower than that of the bulk silicon (B) by –485 meV giving the state (S). The "down" dimer atom (SS) moves closer to the plane of it's three nearest neighbours, its energy increases, it's dangling bond orbital becomes more 'p' like.

The electronegativity of this down atom decreases and the peak is difficult to assign as it almost "sits" directly underneath the bulk core level peak shifted by only 62 meV. The state (S') has a shift of 220 meV and is associated with photoemission from atoms in the second layer. A possible interpretation for the component (C) shifted by –205 meV suggested by Uhrberg [12] was that of emission from half the third layer.

6.4 Group IV Semiconductor Surface passivation

From earlier considerations it is apparent that the surface of clean Si(100) reconstructs from the bulk (1x1) periodicity to a (2x1) as described by the asymmetric dimer model. In doing so the dangling bond density per surface atom is reduced from two to one. However the resultant surface still has unteriminated bonds and is thus chemically reactive.

Adsorption of adatoms can change the surface reconstruction in many ways by formation of new bonds. It has been shown (Bringans [13], Olmstead [14] and Uhrberg et al [15]) that unreconstructed Si(111) and Ge(111) surfaces can be obtained if the surface layer of Si or Ge is replaced by As atoms. This occurs because As atoms have one extra valence electron compared to Si or Ge atoms, and thus the occupied surface orbitals for the clean surface are replaced by a fully occupied or lone pair orbital. A monlayer of arsenic atoms has been shown by Uhrberg et al [16] to provide a passivated coverage on the Si(100) surface. Here the Si-Si dimers of the clean surface reconstruction are broken and the As-As dimer are added on top. The extra valence electron on each As atom again leads to fully co-ordinated atoms.

Adsorption of sulphur and selenium shows particular interesting structural properties in that a monolayer of these adatoms could completely remove the surface reconstruction. However, initially this possibility was only a theoretical one. For S on Ge(100) Weser et al [17] reported the preparation of a well ordered Ge(100)-(1x1) configuration. Using core level spectroscopy, photoemission measurements and total energy minimisation calculations Weser et al [17] identified a bond geometry with S atoms residing in bridge positions above Ge atoms of the topmost layer. For S or Se monolayers on Si(100) that particular configuration has not been observed until recently. Also, there exists

disagreement about the ideal termination of Si(100) by S adsorption which shall be discuss shortly.

It is useful when considering a likely elemental candidate (S or Se) to passivate the surface dangling bonds and restore the surface periodicity to the bulk value to examine the implications of the valency and atomic radius of the potential adatom. Kaxiras [18] has outlined a set of empirical criteria for evaluating surface-adsorbate combinations that can lead to semiconductor surface restoration.

The first criterion is: with respect to a given substrate, the adsorbate atom must be either of a lower valence, such that the occupancy of broken bonds is eliminated, or of a higher valence, such that broken bonds are reduced to fully occupied nonbonding states. For silicon (valence 4), a bulk terminated Si(111) plane consists of threefold bonded atoms with one broken covalent bond, containing a single unpaired electron on each surface atom. Replacing the surface Si atoms by adsorbates of valence either 3, which would eliminate unpaired electrons, or 5, which would create a pair of non-bonding electrons.

However, because of differences in bulk phase between the adsorbate and substrate the first criterion alone doesn't guarantee the resulting surface restoration is stable. For example the bulk phase (a layered structure where every atom has three close neighbours bonded through sp hybrids [19]) of group V elements (e.g. P or As) is similar to that of Si(111) and leads to the restoration of Si(111) surface. However the bulk phase of group III elements (eg. Al, Ga, In) is different (a metallic close packed structure with the number of neighbours varying from 12 (Al) to 4 (In) [10]) and results in complicated surface reconstruction without restoring the Si(111) bulk terminated geometry. Thus the second criterion is that the adsorbate must exist in a bulk phase with the same local bonding geometry as in the restored surface.

A third criterion arises from consideration of the implications of differences in atomic radii between the adsorbate and substrate [20]. The third criterion says that it is necessary to discriminate between elements of different atomic sizes due to the possibility of adsorbate-induced surface stress. Also the differences between bond angles of the adsorbate in its bulk phase and in its restored surface geometry. When the

covalent radii of the adsorbate and substrate atoms are similar to within a few percent, the prospects for stability increase, since the substrate-adsorbate bonds in the restored surface will have a bond length comparable with both constituents, which tends to reduce the stress.

A fourth criterion concerns the adverse effect of chemical reactivity on surface restoration. It is possible that the adsorbate reacts strongly with the substrate forming volatile molecules. The net result might be a continuous etching of the surface, rather than the formation of a stable adsorbed layer. Alternatively it might be difficult to deposit a suitable elemental adsorbate if its molecular compounds do not decompose on the surface under normal adsorption conditions.

On the basis of the first criterion elements with a valence of 2 or 6 are a natural choice. From the second criterion, group VI elements (O, S, Se, Te) are more promising because they tend to form structures with two fold coordination and sp^3–bonding hybrids as required for the restoration of Si(100). Te is eliminated by the third criterion since it's average bulk bond length differs from that of Si by +22%. For oxygen the Si-O bond length is much shorter than Si-Si bonds (so the third criterion is not satisfied) and the Si-O bond is energetically much stronger than Si-Si, making the formation of a stable O overlayer on Si(100) unlikely. S and Se are likely candidates as they satisfy the four criteria although their average bulk bond lengths differ from that of bulk Si. However, the S-Si bond energy is larger than that of Si-Si and so Kaxiras concluded that both chemical reactivity and induced stress would tend to inhibit the formation of an ordered S monolayer on Si(100) where as the restoration of Si(100) by Se would be more likely. On the basis of the above considerations the core level results for the clean and sulphur terminated Si(100) surface are presented.

6.5 Si(100) Experimental

As in the oxynitride analysis, soft X-ray photoemission analysis was performed on beamline U4A at the NSLS. A UHV compatible electrochemical S cell was mounted onto the system via a 4-inch knife edge flange allowing line of sight effusion of S onto the sample. After a 12-hour bake at 120 °C with subsequent degassing cycles a base

pressure of $8x10^{-10}$ mbar was realised in the analysis chamber. The residual gas in the vacuum vessel at the base pressure was monitored by a mass spectrometer attached to the system. The native oxide of the sample was removed through short cycles of high temperature e-beam heating (as described below) until a clear (2x1) LEED pattern was obtained. The surface core level bonding state was probed at the surface sensitive photon energy (hν = 130 eV) at a combined resolution of 120 meV. The Si_{2p} spectrum was fitted using Viogt functions (with 0.1eV Lorentzian FWHM and different Gaussian FWHM taken from the literature) after removing a fourth order polynomial background.

6.51 Electron beam heat cleaning

Using a high voltage source the sample was held at a positive potential of a few hundred volts with respect to ground which was sufficient to strip and accelerate energetic thermionic electrons emitted from a white hot tungsten filament in close proximity (~5 mm) to the back of the sample. Figure 6.8 shows a simplified representation of the sample heating set-up.

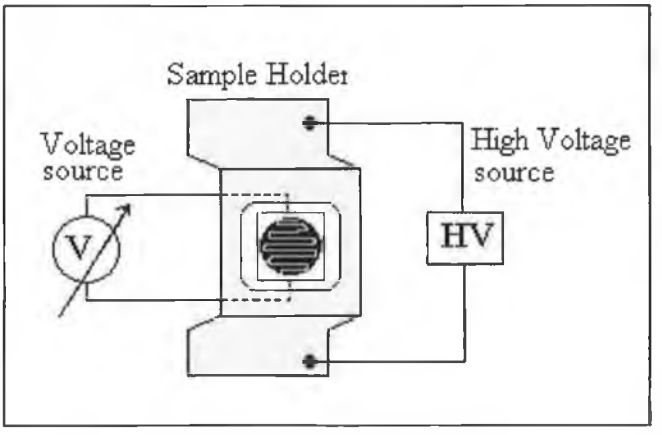

Figure 6.8: simplified representation of the sample heating stage where a higher voltage applied to the sample accelerates electrons from a near by hot tungsten filament which is electrically isolated from the sample using ceramics.

The sample holder shown in grey was isolated electrically from the (using ceramics) tungsten filament (shown in orange) which sits underneath the sample. The temperature of the sample could be regulated by changing the current through the tungsten filament and the resulting sample temperature was measured using an optical

pyrometer. At a potential of 600 V, ramping the filament current to and holding it (for 10 second intervals) at 6 Amps caused the sample to glow white-hot and realised a temperature of ~1130 C^{o}. At this temperature the native oxide is desorbed along with hydrocarbon contamination. The base pressure during heat cleaning cycles was only ever allowed to rise to $8x10^{-8}$ mbar. After a series of heat cleaning cycles the oxide was removed and a well ordered (2x1) LEED pattern was obtained.

6.52 Sulphur Cell [21]

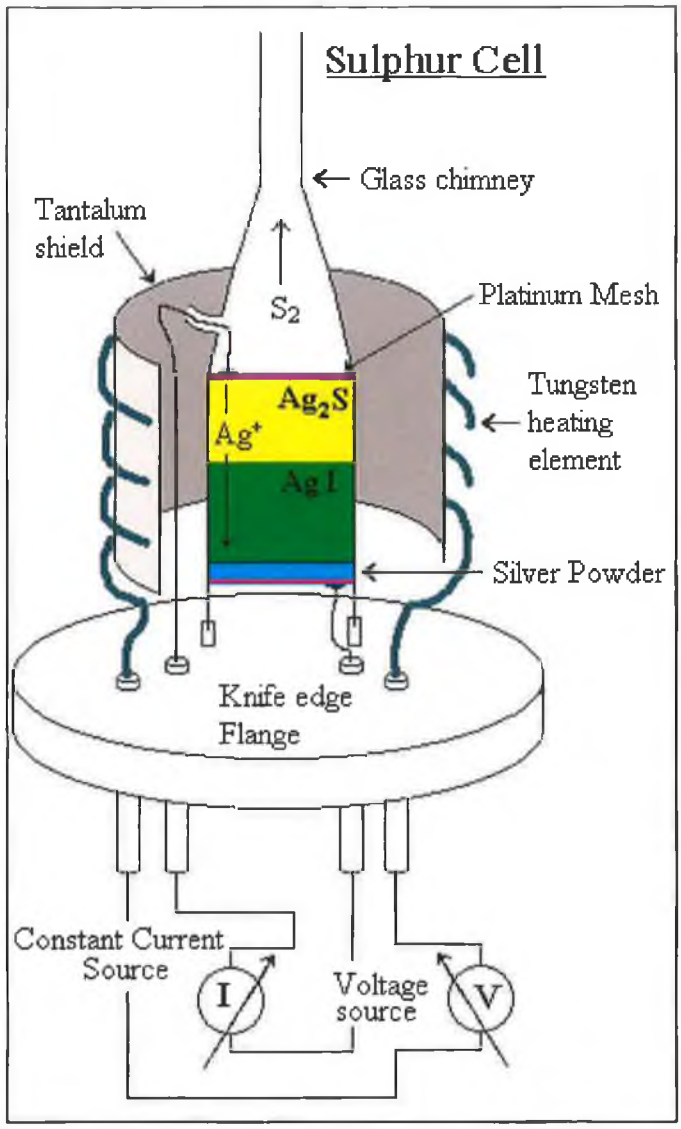

Figure 6.9: A schematic illustration of the electrochemical sulphur source

Figure 6.9 shows a diagram of the sulphur cell mounted on a knife-edge flange with electrical feedthroughs. The cell was made from a compressed pellet by pressing powders of silver (Ag), silver iodide (AgI) and silver sulphide (AgS_2) together between two sheets of platinum mesh. The pellet sits into the glass chimney with electrical contacts made to the front and back end of the pellet. The chimney is surrounded by a sheet of tantalum, which is heated radiativity by passing a suitable current (~ 6 A) through the exterior tungsten wire which is wrapped into a helical coil. The hot tantalum sheet then uniformly heats the pellet. When heated to approximately 200 °C an electrical potential of 200 meV exists across the cell. By applying a suitable bias to the cell a constant current (20 μA) is established by a constant current source. This current is facilitated by the silver sulphide acting as a ionic conductor, with Ag^+ ions flowing towards the silver iodide pellet. Molecular sulphur effuses from the throat of the chimney given the local concentration of sulphur. The clean surface is located (in line of sight) a few cm away from the top of the chimney. Figure 6.10 shows a photograph of the inside of the analysis chamber as seen during S deposition.

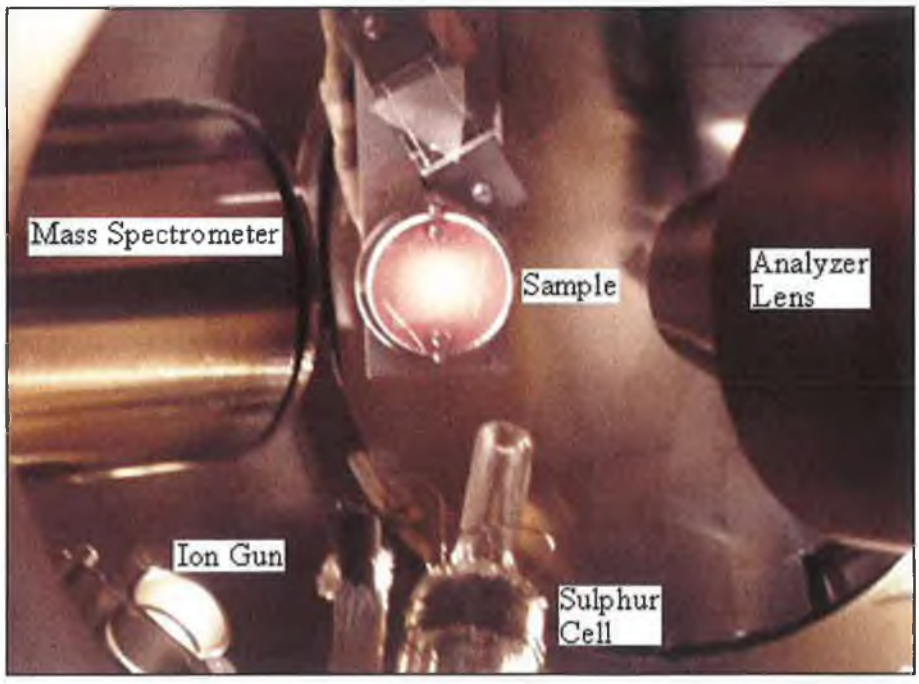

Figure 6.10: A photograph of the inside of the analysis chamber

The silicon sample has been mounted onto the substrate heater with tantalum clips and is visibly hot. On the left is the mass spectrometer head. On the right is the lens of the

analyser. The LEED system is in the background and is protected by its shutter. Finally the glass chimney of the sulphur cell is visible protruding from below.

6.53 Clean Si(100)

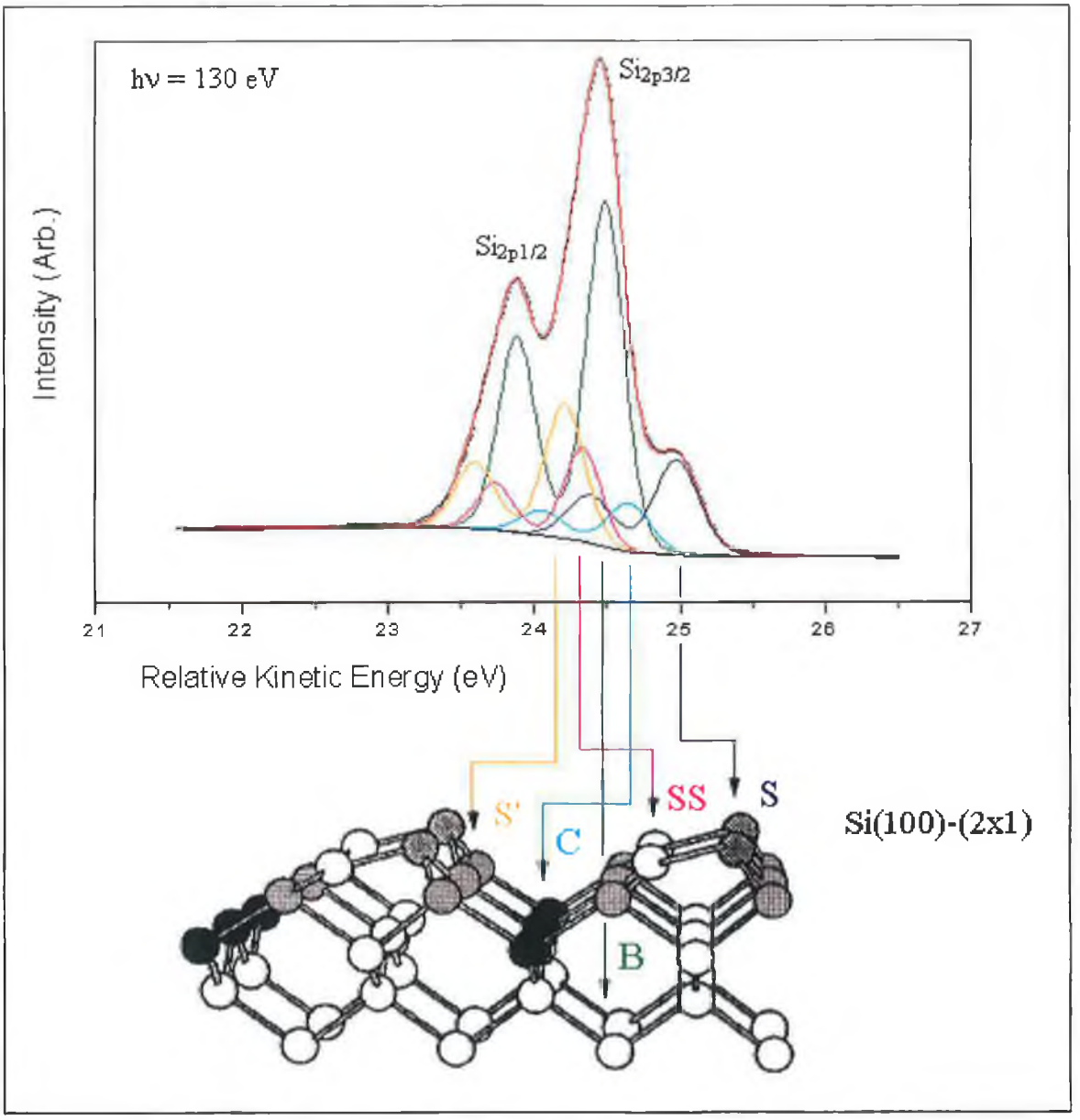

Figure 6.11: (Top) surface core level shifts in Si_{2p} spectrum at hν = 130 eV. (Bottom [22]) ball and stick representation of outer surface geometric surface.

Having "burned off" the native oxide and established a well ordered (2x1) LEED pattern, the Si_{2p} core-level spectrum was measured at a photon energy of 130 eV. Figure

6.11 shows the resulting spectrum. The experimental data is shown in black and the fit in red. The spectrum was fitted using a least squares fitting routine with five Voigt peaks who's Lorentzian width was fixed at 100 meV, a value of 250 meV was used for the Gaussian FWHM (as used by Landemark et al [22] and Pi et al [23]). A branching ratio of 2 and spin-orbit split of –0.6 eV were consistently found to provide the best fit. The background was fitted with a Shirley background. The magnitude of the chemical shifts to higher (two components) and lower (two components) kinetic energy relative to the substrate component were found to be +161 meV (peak C), + 591 meV (peak S) and –155 meV (peak SS), -289 meV (peak S'). Resolution limitations prevented us from distinguishing between the precise assignments of these components as proposed by Landemark [22] and Pi [23].

6.54 Sulphur Deposition

The sample temperature was brought to 1130 K by slowly increasing the current in the heating filament while the sample was held at a potential of +600V. With the sample facing away from the sulphur cell, the cell was heated to 200 ^{o}C and when the cell potential was established a current of 20 μA was passed through it. The pressure in the main chamber rose to 5 x 10^{-7} mbar, a large sulphur signal was evident from the mass spectrometer display and was the dominant contributor to the pressure increase. Next the sample was turned to face into the sulphur flux for 5 mins. The sample temperature was gradually reduced and allowed to cool in the sulphur flux. Figure 6.12 shows the Si_{2p} core level spectrum taken from the sample at a photon energy of 130 eV at normal incidence and at 60^{o} off normal respectively. The spectra of the sulphur treated surface could be consistently fitted with one bulk and two chemically shifted surface components of approximately equal magnitude shifted by 0.53 and 1.2 eV to higher binding energy. These chemical shifts were assumed to correspond to silicon atoms at the surface in the +1 and +2 oxidation state. While the chemically shift associated with the +2 oxidation state at 1.2 eV was consistent with that reported by Weser et al [24], the +1 oxidation state had a lower chemical shift. This however could be due to strain effects in the local surface structure resulting in a modification of the electronic structure as their method of surface preparation is different from ours.

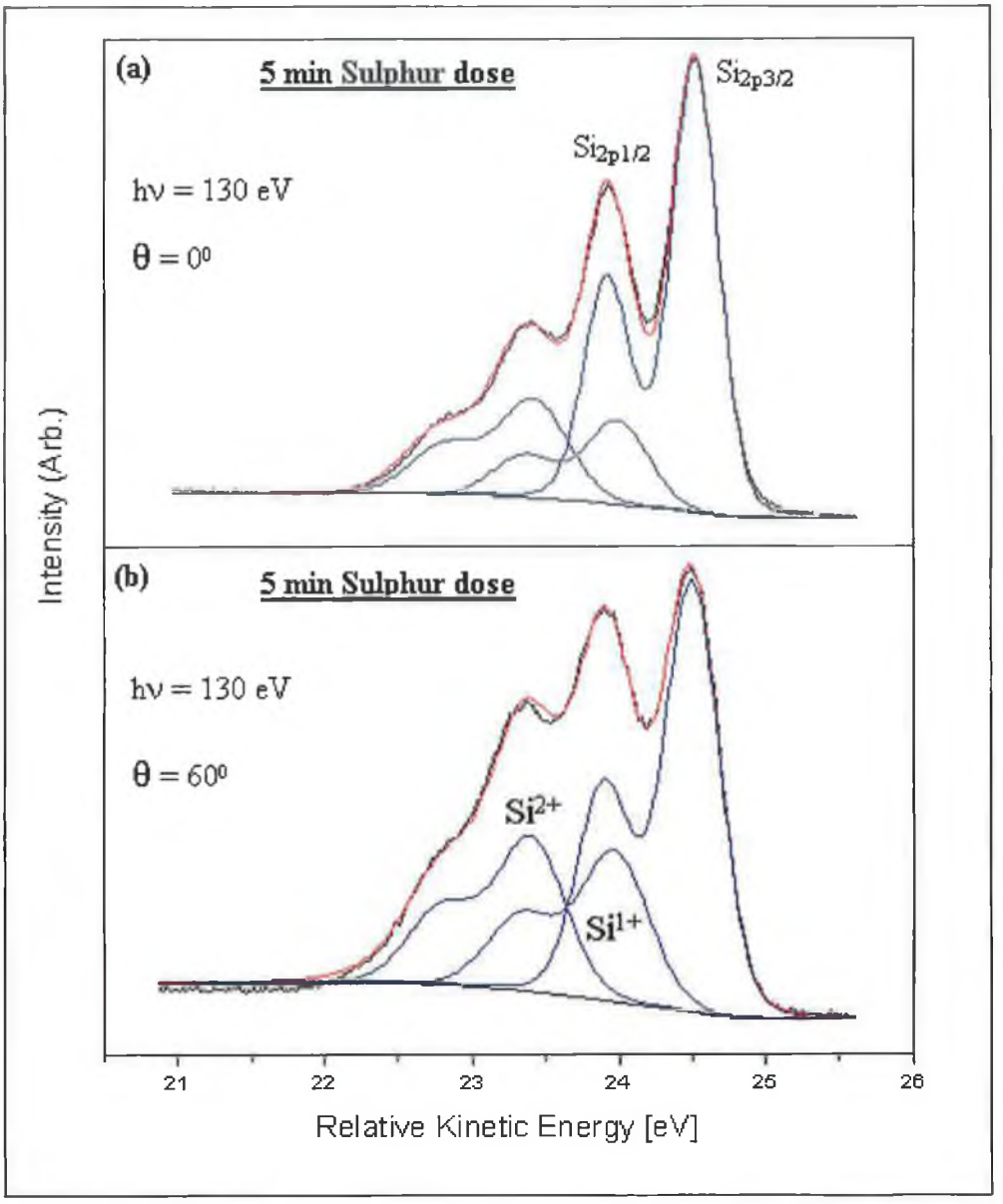

Figure 6.12: De-convolution of Si_{2p} oxidation states for the sulphur treated (5 min dose) surface at hν=130 eV for (a) normal emission and (b) 60° off normal on Si(100).

Take-off Angle (θ)	Si^{1+} % Bulk	Si^{2+} % Bulk	Si^{1+} % Si^{2+}
0	25.5	36.5	89
60	42.3	64	85

Table 6.0: Si_{2p} peak intensities for normal and 60 off angle scans.

Table 6.0 summarises the peak intensities for the normal and 60° off normal scans. The relative intensities of the two oxidation states is independent of angle suggesting that

both components are located in the same surface plane and exist in the outer most plane. LEED analysis of the surface indicates that the surface displays a bulk like (1x1) surface termination. The lifting of the (2x1) surface structure suggests that the surface dimers have been broken.

Figure 6.13 shows the sulphur 2p core level spectrum taken at normal incidence at a photon energy of 190 eV. The peak was fitted using a branching ratio of two, a Gaussian FWHM of 0.47 eV and a spin-orbit split of 1.15 eV.

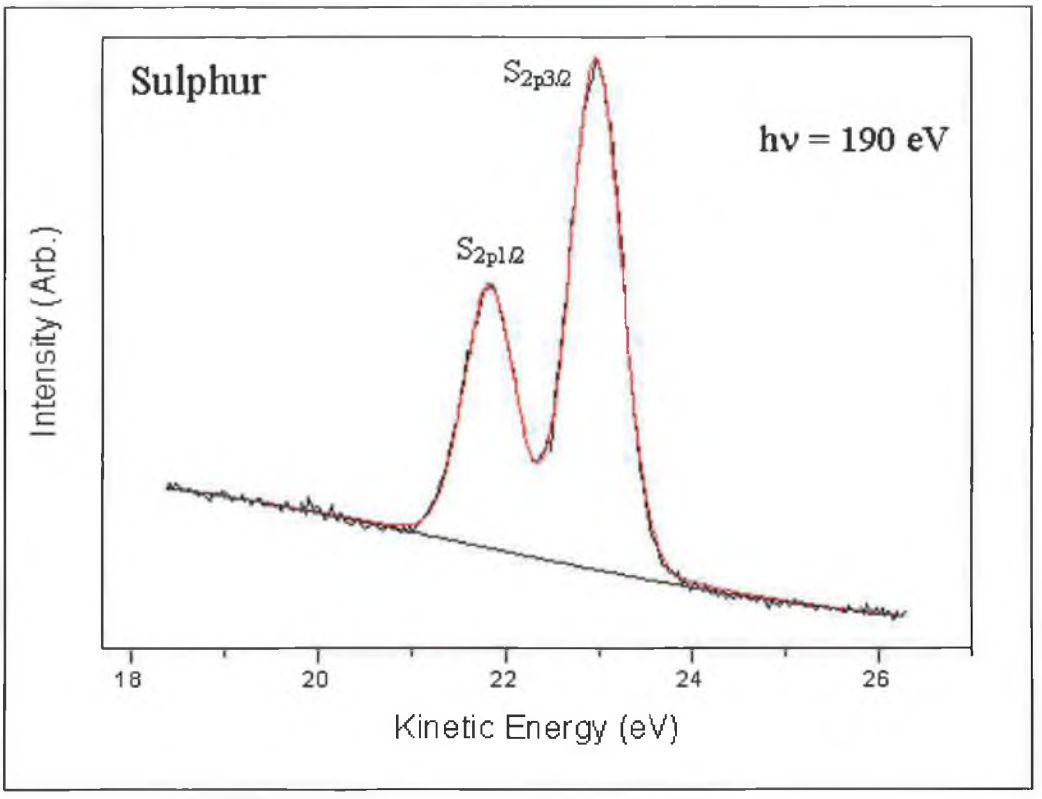

Figure 6.13: Core-level photoemission spectrum of the S_{2p} peak from the sulphur treated (5 min dose) surface at hν=190 eV on Si(100) (1x1).

A good fit could only be obtained using a single peak which was identical to that obtained at 60° off normal. This suggested that sulphur existed in a unique chemical environment at the surface. Our fitting parameters were similar to those reported by Mullins et al [25] for the interaction of sulphur with the tungsten surface in which the sulphur resides in a single chemical phase for coverages of less than half a monolayer. In order to properly interpret the surface termination the existence of sulphur in a single chemically shifted component while the silicon substrate spectra displays two

chemically shifted interface peaks of approximately equal intensity needs to be resolved.

6.55 Discussion of results

It is useful to precede our interpretation of the above results by first comparing them with those of others in the literature. Earlier it was mentioned that the restoration of the (1x1) bulk periodicity and passivation of the Si(100) surface with sulphur was until recently only a theoretical possibility. Papageorgopoulos et al [26] reported the successful room temperature deposition of elemental sulphur on Si(100) restoring the surface (2x1) periodicity back to a (1x1). Previously Weser investigating the behaviour of S on Si(100) had not been able to observe an ordered overlayer. Moriarty et al [27] reported that room temperature adsorption of sulphur on silicon resulted in the formation of an overlayer with the underlying Si(100) retaining the (2x1) reconstruction. On annealing the S/Si(100)2x1 surface to 325 ^{o}C desorption of the sulphur overlayer occurred with the appearance of a coexisting c(4x4) and (2x1) surface reconstructions.

Papageorgopoulos [26] proposed, from consideration of the change in slope of the S Auger peak-to-peak heights as a function of the number of sulphur doses and from LEED analysis that for low sulphur does, S adatoms initially reside on the dimers in bridge sites with each S atom bonded through the dangling bonds forming a half monolayer (2x1) coverage as shown in Figure 6.14 (B). Figure 6.14 (A) shows the clean reconstructed Si(100)2x1surface. For coverages above ½ a monolayer the Si dimers are broken providing bonding for the sulphur atoms. The silicon atoms are displaced resulting in the restoration of the (1x1) bulk termination. The sulphur adatoms remain in bridge sites and are bound to neighbouring Si atoms as shown in Figure 6.14 (C). For coverages between 1 and 2 monolayers sulphur is embedded into the Si substrate through diffusion as shown in Figure 6.14 (D).

However Hahn et al [28,29] reported that they were unable to reproduce the results of Papageorgopoulos but did however obtain a Si(100)-(1x1) termination by exposing the surface to a beam of sulphur at elevated temperatures in a method similar to ours.

Bringans and Olmstead [30,31] reported results of a photoemission study of selenium and ZnSe interactions with the Si(100) surface in an investigation of heteroepitaxial growth on elemental semiconductors.

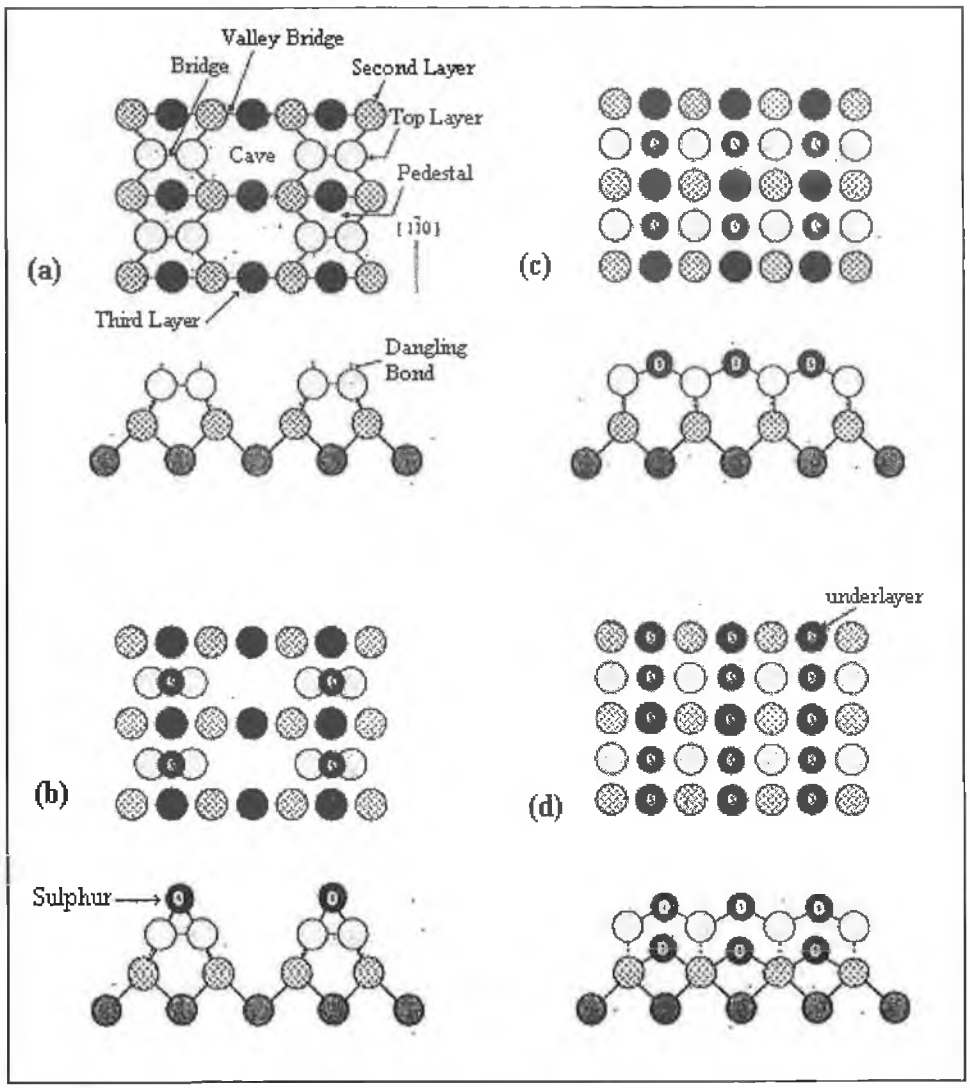

Figure 6.14: (a) clean reconstructed Si(100)2x1, b) the S-(2x1) (hemisulfide) structure on the Si(100)2x1 surface, c) the S-(1x1) (monosulfide) structure on a Si(100)1x1 surface and d) the diffused second S layer into the bulk of Si(100)1x1 (Papageorgopoulos [26]).

They concluded from their core level spectra that only a half of the topmost silicon atoms are bonded to two Se atoms, with the other half bonded to one Se atom. This indicated that the surface coverage of Se corresponded to 3/4 monolayer of Se atoms in the bridge position. What is interesting about this submonolayer-covered surface, in the

context of our results is that it resulted in the surface displaying a (1x1) surface reconstruction without achieving ideal termination.

In theoretical studies of the structural and electronic properties of both sulphur and selenium terminated Si(100) surfaces, Kruger and Pollmann [32] concluded that a restoration of the ideal bulk terminated geometry was energetically favourable.

Consideration was given earlier to the empirical criteria of Kaxiras [18] for evaluating surface-adsorbate combinations that can lead to semiconductor surface restoration. In a theoretical study similar to that of Kruger and Pollmann Kaxiras concluded that since the S-Si bond energy is larger than the Si-Si bond energy, volatile Si_nS_m molecules could form, inhibiting the formation of a Si(100):S termination. His calculations also suggested that the compressive stress along the Si-S-Si chains could be relieved by the creation of vacancies along the chain, which would result in optimal Si-S-Si bond angles. In order to calculate the S coverage in monolayers of our surface the continuum model of McFeely et al [33] was used. The model relates the ratio R (of total surface core level intensity to that of the bulk) to the coverage θ (in monolayers) through the equation:

$$R = 1 - e^{\frac{\theta d_\perp}{\lambda}} \qquad \textbf{Equation 6.0}$$

where $d_\perp$ is the layer spacing in the crystal perpendicular to the surface and λ is the inelastic mean free path of the photoelectron in silicon. Using $d_\perp(100) = 1.36$ A and λ_{Si} =3.3 A, from Himpsel et al [34] we calculated a surface coverage of approximately 0.75 monolayers.

Using their results for the Se-terminated Si(100) surface mentioned earlier Bringans and Olmstead [30,31] outlined how a complete monolayer coverage would give exclusively +2 oxidation states on the silicon substrate, while ¾ of a monolayer would give rise to equal concentrations of +1 and +2 oxidation states. As illustrated in Figure 6.15 this configuration results in the group VI element always bonded to two surface atoms and therefore exists in a unique chemical environment, while the silicon atoms at the surface are in two distinct chemical states.

The appearance of a (1x1) LEED pattern from a surface covered by approximately ¾ monolayer indicates that the sulphur layer contains no long-range order and that the pattern must arise from the bulk periodicity. Therefore we conclude that the (1x1) surface reconstruction observed does not result from ideal monolayer coverage of the Si(100) surface.

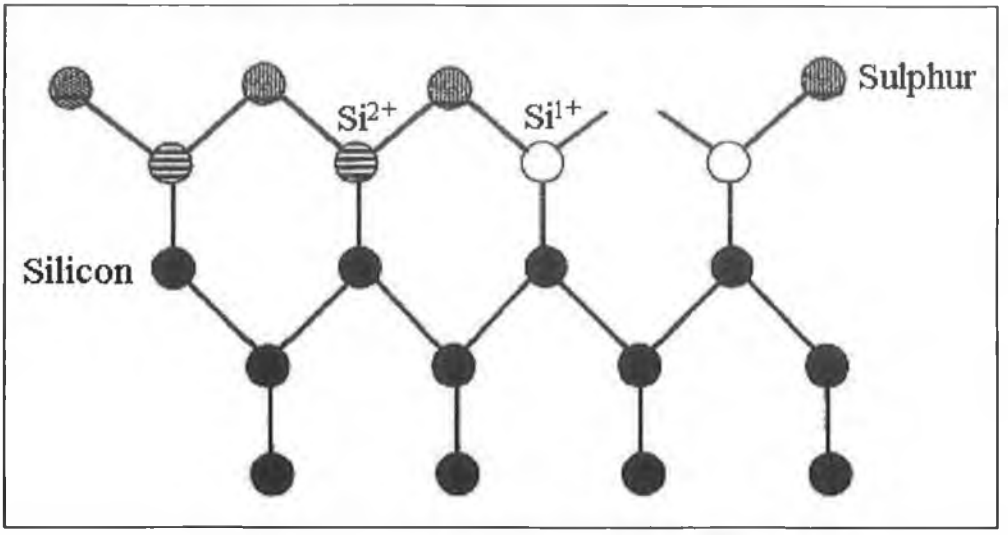

Figure 6.15: Schematic diagram showing the submonolayer coverage of sulphur (shaded circles). Solid circles correspond to silicon atoms in a bulk chemical environment, open circles and hatched circles correspond to silicon atoms in the +1 and +2 oxidation states, respectively.

6.6 Germanium (100) Overview

[35] Due to the relative technological interest in the two surfaces, germanium surfaces have not been investigated to the same extent as silicon surfaces. Intrinsic room temperature germanium has higher electron (3900 $cm^2/V.s$) and hole (1900 $cm^2/V.s$) mobilities than intrinsic silicon which has a room temperature electron and hole mobilities of 1350 $cm^2/V.s$ and 480 $cm^2/V.s$ respectively. However the oxide, which forms on germanium, is water soluble, in contrast to that which forms on silicon, rendering germanium less useful from a technological perspective. Like silicon germanium crystallises in the diamond structure where it is covalently bonded to four nearest neighbours in a tetrahedron. A germanium crystal cleaved to expose a clean (100) surface leaves each surface atom with two dangling-bond sp^3-hybrid orbitals per surface atom as shown in Figure 6.16 [34]. Like the Si(100) surface, the Ge(100)

surface reconstructs through the pairing of surface atoms to form rows of asymmetric dimers along the [110] crystallographic directions. In STM studies [36] the orientation of the reconstruction was found to rotate through 90° between (2x1) terraces that were separated by monatomic step heights as expected for the rotation of the tetrahedral dangling bonds by 90° between terrace domains.

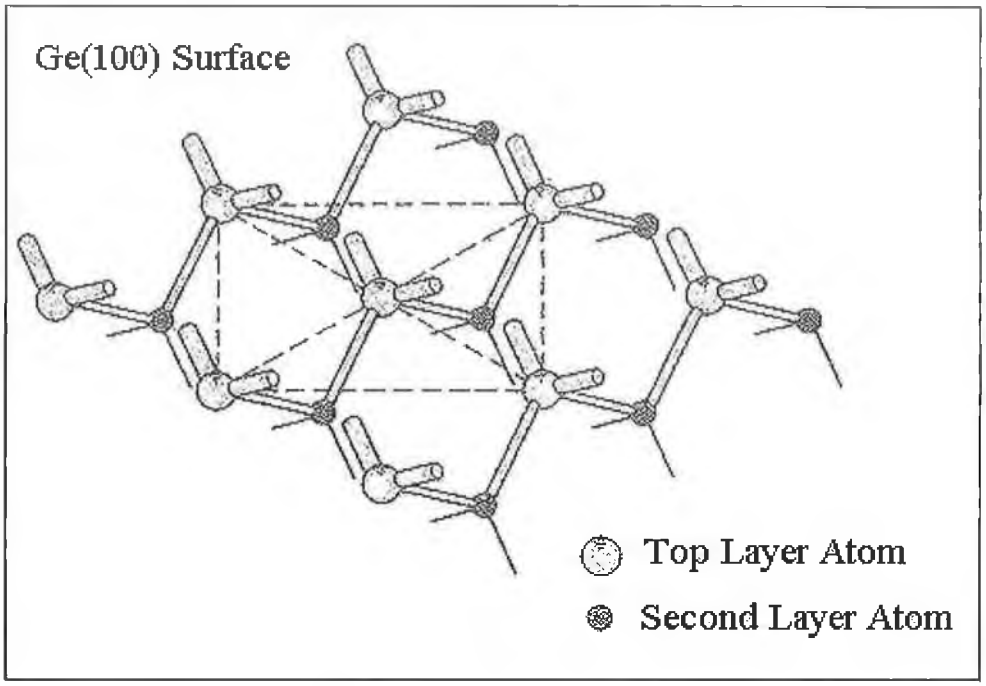

Figure 6.16: Plan view of the bulk terminated (100) surface. Each surface atom is left with two dangling-bond orbitals. The tetrahedral dangling-bonds on the second layer atoms are rotated by 90° with respect to the surface normal from the top layer of tetrahedral bonds. This bond rotation leads to a surface with two domains, after undergoing a (2x1) pairing reconstruction, where the two domains are separated by monatomic height steps [34].

This multi-domain structure gives rise to the (2x1) LEED pattern like silicon and it minimises the elastic energy in the substrate. In addition to the half order LEED spots expected for the two-domain (2x1) dimer reconstruction, weak quarter-order spots have also been observed in room temperature measurements by Fernandez et al [37] of the surface indicating the existence of higher order domains (ie (4x2)). The first room temperature STM images by Kubby et al [35] of Ge(100) found it to be composed of asymmetric dimers that did not require defects to quench the surface dynamics in contrast to the room temperature Si(100) surface.

6.61 Clean Ge(100)-(2x1) SCLS

In investigating the surface core level shift of the Si(100)-(2x1) surface Landemark et al [22] enjoyed an excellent resolution of 70 meV facilitating the identification of 4 chemical states corresponding to the up dimer atoms (S), the down dimer atoms (SS), the atoms in the second layer (S') and half of the third layer atoms (C). Despite this, their convergence on a final consistent peak parameter set was only made after detailed analysis of the stability of the bulk peak position while fitting with three surface peaks (in order to elucidate the presence of the fourth) as not all peaks are apparent from the spectrum envelope. The experimental resolution obtained for the Ge(100) 3d core-level spectra has been lower than that obtained for Si(100) 2p data and there is no general consensus about how many surface related components are present in the Ge 3d core level photoemission spectra. Schnell et al [38] fitted the Ge(100) spectrum using only one surface component, shifted by ~ –0.45 eV with respect to the bulk component, due to one monolayer of both up and down dimer atoms. Chen et al [39] also used only one surface component but argued that two separate components should be expected because of the charge transfer from the down atom to the up atom in the same dimer. He associated the observed surface core level shift with ½ a monolayer of up atoms, while the down atom component was assumed to overlap the bulk contribution. LeyLay et al [40] and others [41,42] have used two surface components, besides the lower binding energy doublet at –0.54 eV with respect to the bulk they found a second core level shifted by –0.19 eV. However, the dimer bonding is interpreted as covalent and the second component is attributed to emission from the subsurface layer. In the ionic model of Chen [39] the second component is attributed to charge transfer from the down atom emission.

In order to elucidate the number of surface core level peaks Goldoni et al [43] have undertaken difference spectra analysis of the Ge3d spectrum in order to remove a suitable weighted bulk component numerical, from a surface sensitive spectrum, thus leaving the surface core level shifts. Figure 6.17(a) shows the Ge_{3d} spectra taken at photon energies of 45 eV (at normal emission) and 70 eV (at 70^{o} off normal) which yield bulk and surface sensitive information respectively. Figure 6.17(b) shows the spectra after background subtraction and having been normalised to the same area.

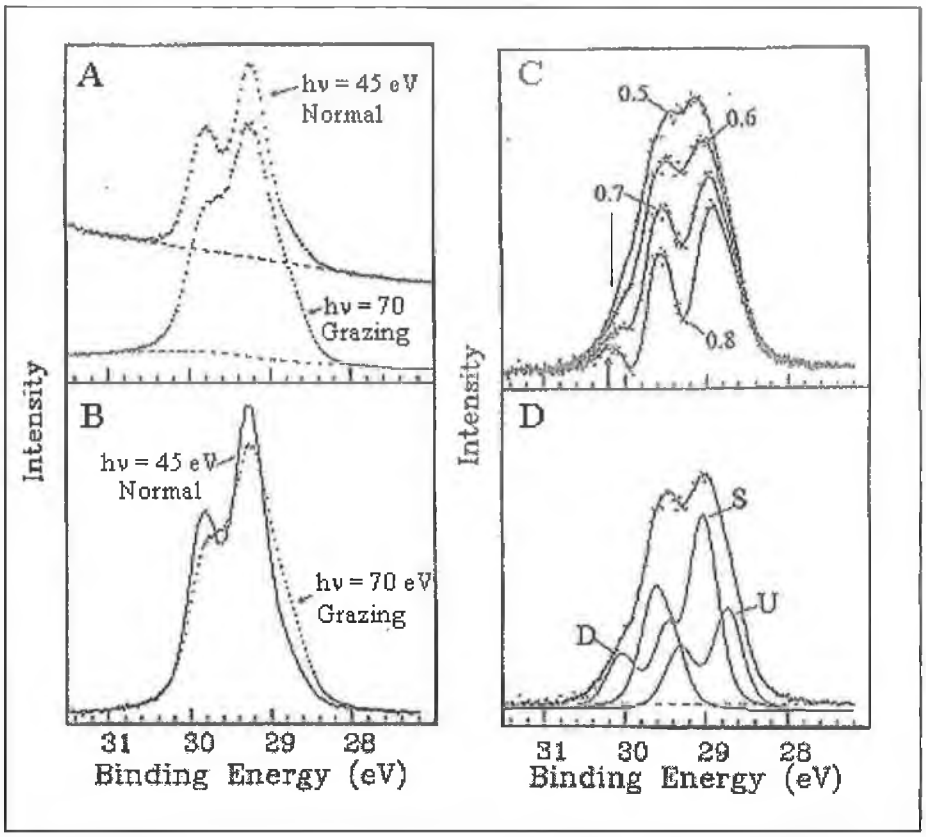

Figure 6.17: (a) bulk and surface sensitive Ge_{3d} spectra of the clean Ge(100)-(2x1) surface, b) both spectra are normalized to the same area after background removal, c) difference spectra fits with different spectral weights and d) the best fit was obtained using three surface core-level shifts and a spectral weight of 0.6 (Goldoni [43]).

Figure 6.17(c) show the difference spectra that result when the weighted bulk Ge peak (taken from the bulk sensitive scan) is subtracted from the surface sensitive spectrum. The numbers beside the curves represent the scaling coefficient (or weight) on the bulk. For a weight of 0.6, a spin orbit splitting of 0.66 eV an intensity ratio of 0.59 and a Gaussian FWHM for the bulk peak of 0.35 eV, is shown in Figure 6.17(d).

SCLS	FWHM (eV)	E_B (w.r.t) bulk (eV)
S	0.35	-0.24
U	0.35	-0.53
D	0.35	+0.19

Table 6.1: Fitting parameters for Ge(100) SCLS (Goldoni [43]).

The spectrum was fitted with three surface core level shifts S, U and D whose peak parameters are summarised in Table 6.1. These peak parameters were found to consistently give the best fit. Figure 6.18 shows the fits obtained for bulk and surface sensitive spectra, the goodness of the fit is evident from the fit residuals shown under each spectrum. The states U and D are associated with the up and down dimer atoms respectively while the state S is associated with subsurface atoms.

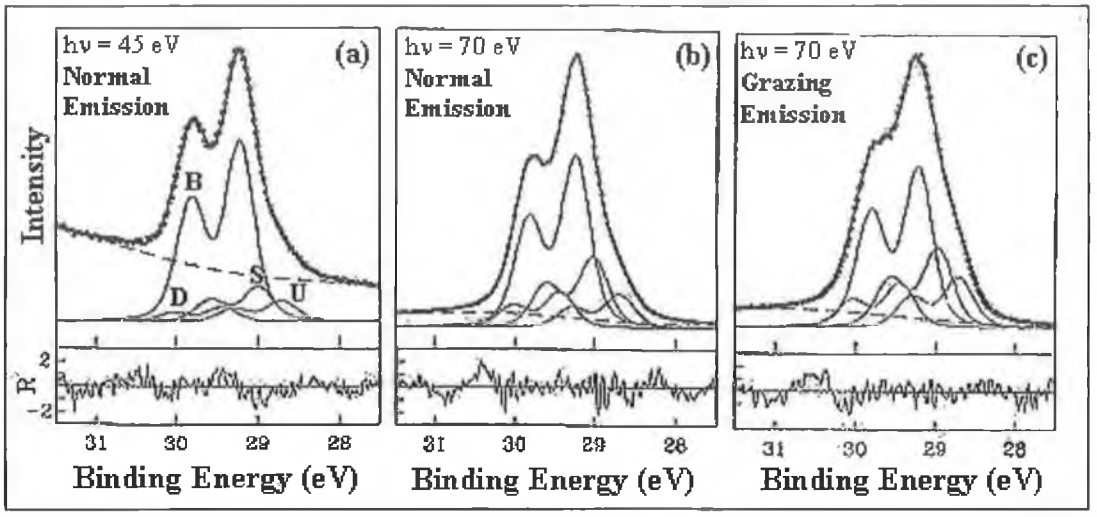

Figure 6.18: De-convolution of the Ge_{3d} spectrum from the clean Ge(100)-(2x1) surface using the three SCLS of Figure 6.17(d). a), b) and c) represent different degrees of surface sensitivity. The universal applicability of the fitting parameters is evidenced by the goodness of the fit (bottom panel in fits) in each spectrum (Goldoni [43]).

It is apparent from the literature that the assignments of surface core level shifts for Ge(100) have been less conclusive than for Si(100). Theoretical calculations have been made for the binding energies of the surface core levels but a spread in the energies resulted as calculations made in the Initial state (no screening of core hole) and final state (complete static screening) regimes give different shifts. Goldoni's [43] estimated values for the binding energies for D and U were between those found by initial and final state calculations in the literature.

6.62 S Passivation of Ge(100)

In this thesis sulphur passivation has been investigated by deposition of molecular S using the flux from an electrochemical cell. Sulphur has also been deposited in-suitu using HS_2 gas and ex situ wet chemically using NHS_4. H_2S adsorption on Si(100) is believed to be dissociative and leads to co-adsorption of H_2S H and S [44]. Kuhr and Ranke [45] investigating the adsorption of H_2S on Ge(100) found it to be dissociative, they identified SH and S using photoemission. Leung et al [46], by monitoring the Ge/S auger intensity achieved a S saturation coverage of Ge(100) after successive cycles of dosing and annealing at 350°C. They concluded from the disappearance of Ge-H and S-H related peaks in separate electron energy loss spectroscopy measurements, that annealing at 350°C leads to the desorption of H leaving S on the surface. They proposed that S starts to desorb at 370°C. However, despite this there is uncertainty about the temperature at which S desorbs and also it has been proposed that H cannot be removed selectively [17]. In chapter 4 the wet chemical passivation of Si was considered by the removal of it's native oxide and the termination of its dangling bonds with hydrogen using HF. Urhberg et al [47] have undertaken soft X-ray synchrotron photoemission analysis of the hydrogen terminated surface and concluded that the adsorbed H bonds to the surface dangling bonds resulting in a symmetric dimer reconstruction. Similarly Anderson et al [48] have investigated the S passivation of Ge wet chemically using aqueous ammonium sulphide $(NH_4)_2S$. Others have sought to engineer a flux of elemental S insitu using by evaporating sulphur from a tungsten filament [23] or by molecular beam epitaixy. An electrochemical cell performs well as a source of a large flux of molecular sulphur but as pointed out by Gothelid [47] can behave non-uniform in its delivery over the course of sample dosing.

In a theoretical study of the structural and electronic properties of sulphur terminated Ge(100), Kruger and Pollmann [49] concluded that a restoration of the ideal bulk terminated geometry was energetically favourable with the sulphur atoms occupying bridge bond sites between neighbouring surface Ge atoms. Weser and Bogen [17] investigated room temperature deposition of molecular sulphur using core level photoemission, Auger electron spectroscopy and LEED. Using an electrochemical cell they reported the "ideal monolayer termination" of Ge(100)-(2x1) surface at room temperature with the restoration of the (1x1) bulk termination. Figure 6.19(a) shows the

bulk and SCLS of the clean Ge(100) surface ($3d_{3/2}$ component of the Ge_{3d} spectrum has been numerically removed leaving the $3d_{5/2}$ component).

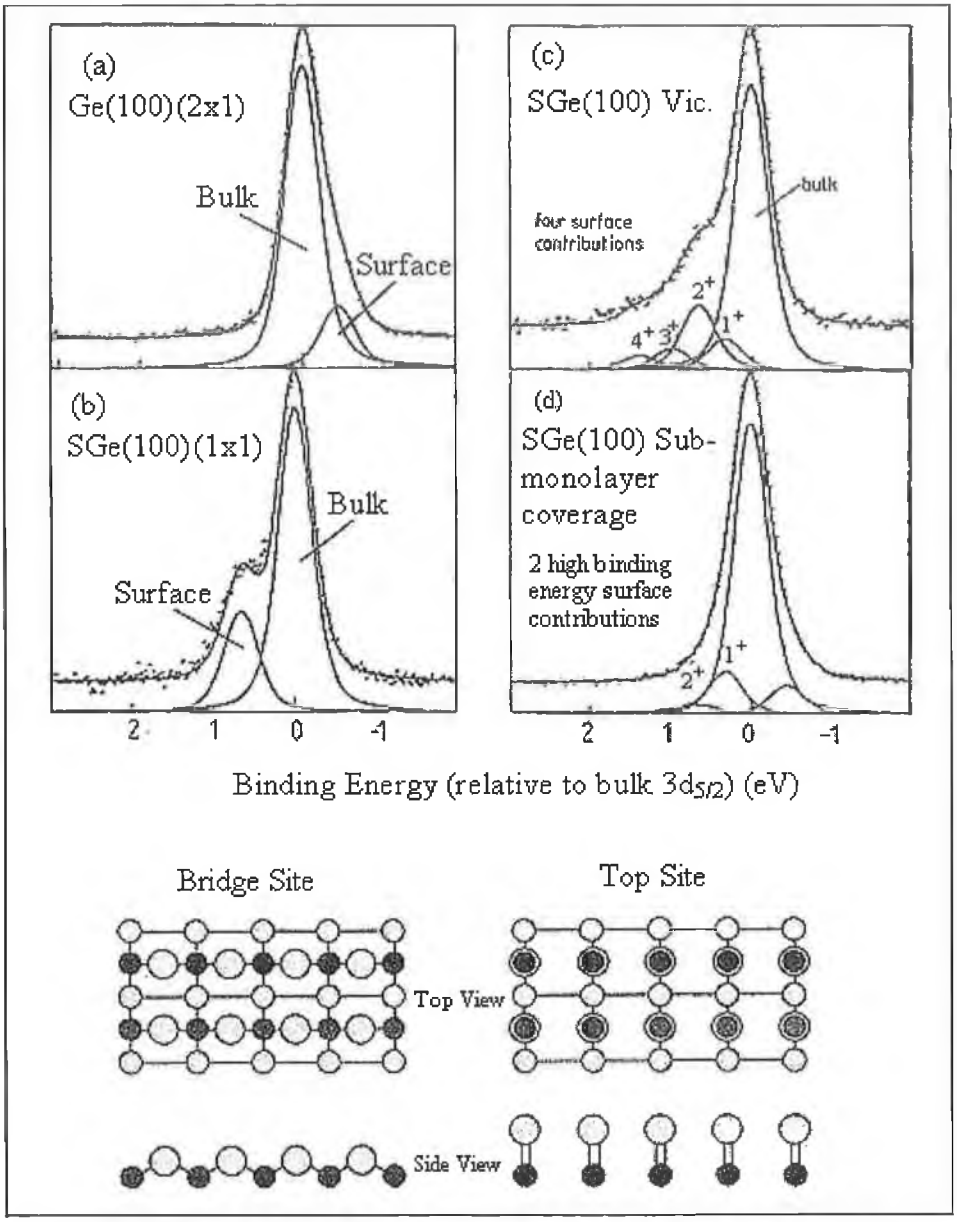

Figure 6.19: Ge3d photoemission results for a) clean Ge(100)-(2x1), b) ideal sulphur termination, c) sulphur states at step edges, d) submonolayer sulphur coverage. (Bottom) two possible adsorption geometries for sulphur (Weser [17]).

From the single germanium oxidation state Si^{2+} in figure 6.19(b), Weser concluded that all the Ge surface atoms are bonded to the same number of sulphur atoms, which was identified as the 2^+ state (which corresponds to a sulphur coverage of one atom per Ge surface atom). Figure 6.19(c) shows sulphur-bonding states at the step edges of a sulphur covered vicinal surface where all oxidation states are possible. Figure 6.19(e)

show the two possible bonding geometries for sulphur. As the bridge site corresponds to single bonds (S-Ge) and the top site corresponds to double bonds (S=Ge), the two different bond models were distinguished by Weser from investigation of low S coverages. Namely in the absence of island formation, two oxidation states (1+ and 2+) are expected for bridge adsorption and only one oxidation state (+2) for top site adsorption. Figure 6.19(d) shows the spectrum for room temperature low S coverages, which show two surface contributions, dominated by the 1+ oxidation state suggesting that S is bridge bonded with no large sulphur islands formed.

6.63 S/Ge(100) Experimental

Soft X-ray photoemission analysis was performed on beamline U4A at the NSLS. Germanium (100) substrates (p type 1-2 Ωcm) were used. A flux of molecular sulphur was realised as described earlier using a UHV compatible electrochemical S cell. The germanium lattice cannot sustain the same degree of aggressive heating which is used to clean Si and so successive cycles of mild (0.6–0.8 keV) Ar^+ ion sputtering and annealing at 600 °C were used until a well ordered (2x1) LEED pattern was obtained. The core level bonding states of the surface were probed at the surface sensitive photon energy (hν=70 eV) at a combined resolution (monochromator + analyzer) of 200 meV. The Ge_{3d} spectrum was fitted using Voigt functions (with 0.1 eV Lorentzian FWHM and different Gaussian FWHM). The fitting parameters are based on those used by Goldini [43] as described earlier. Figure 6.20 shows our fit for the clean Ge(100)-(2x1) surface. The raw data is shown in red and the fit in black. Table 6.2 summarises the fitting parameters.

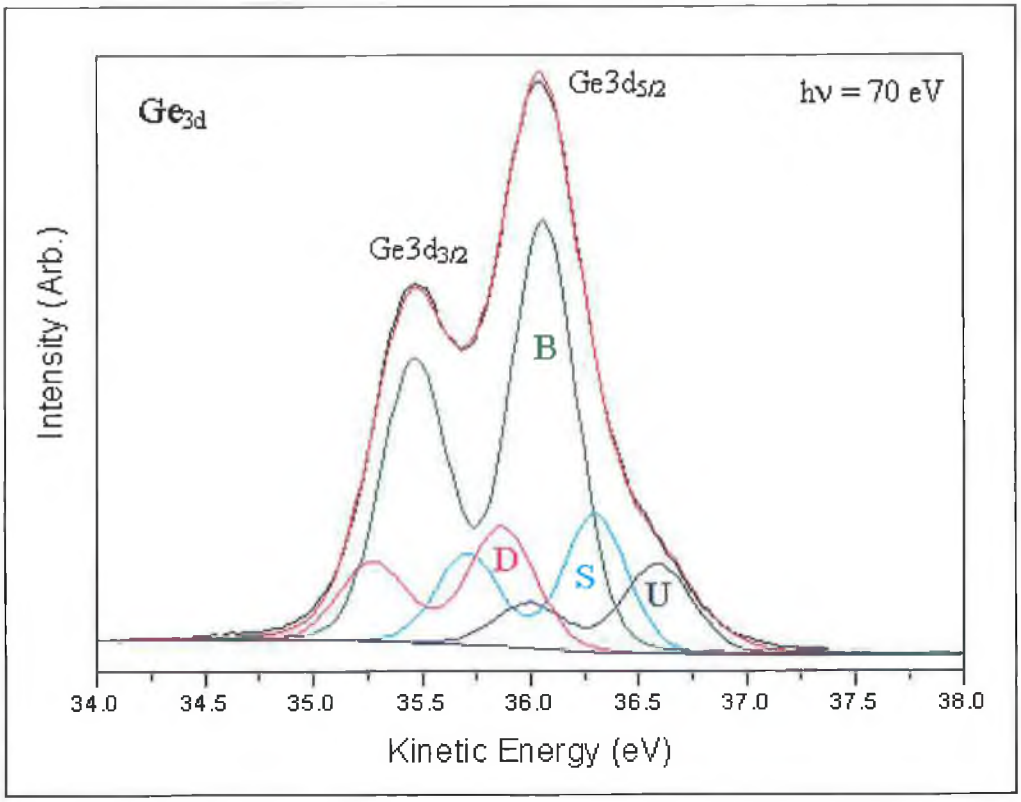

Figure 6.20: De-convolution of the clean Ge(100)-(2x1) Ge_{3d} spectrum using three SCLS U, D and S which are associated with emission from the up atom, down atom and subsurface atoms respectively.

Peak	FWHM (eV)	ΔE_B w.r.t Bulk (eV)
B	0.39	0
U	0.36	-0.52
S	0.36	-0.24
D	0.36	0.18

Table 6.2: Ge_{3d} peak fitting parameters.

6.64 Sulphur deposition

The Ge(100)-(2x1) substrate was dosed at room temperature in the sulphur flux for 20 mins as described for silicon. Figure 6.21(a) shows the resulting Ge_{3d} spectrum obtained at a photon energy of 70 eV. The spectra were consistently fitted with one bulk and four chemically shifted interface components shifted by multiples of 0.40 eV to lower kinetic energy.

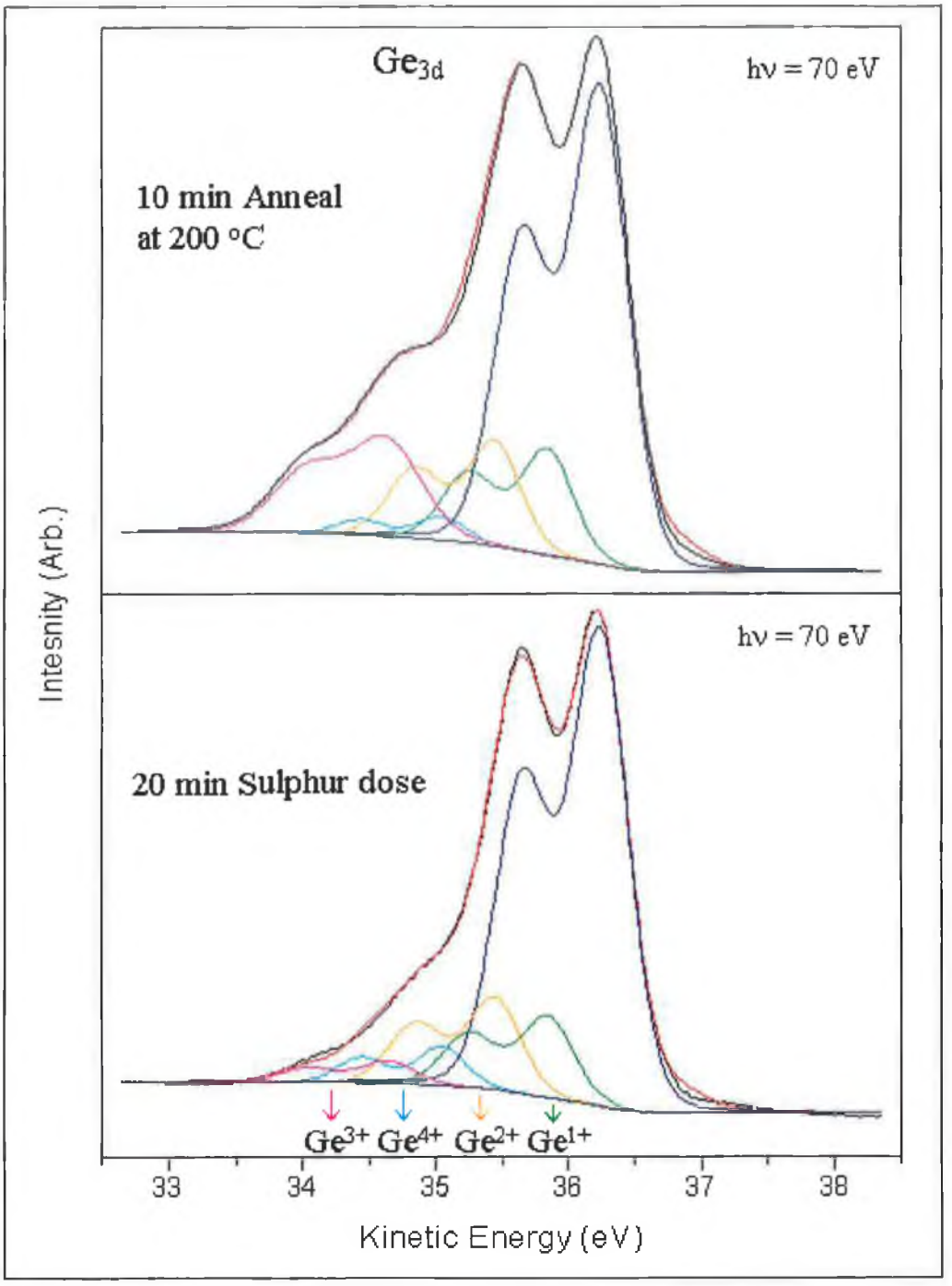

Figure 6.21: (a) De-convolution of Ge_{3d} spectrum from sulphur treated Ge(100) surface into four oxidation states. b) A 10 min anneal at 200°C results in an enhancement of the higher oxidation states.

These chemically shifted components are interpreted as germanium atoms at the surface existing in oxidation states from +1 to +4. The magnitude of the chemical shift per oxidation state is the same as that reported by Gothelid et al [50]. The component peaks were fitted using Gaussian widths of 0.37-0.45 eV with higher values allowed for the +4 oxidation state. A saturation coverage of sulphur was reached after a 10 minute

exposure to sulphur from the electrochemical cell after which a bulk like (1x1) LEED pattern was observed. The lifting of the (2x1) surface structure following sulphur treatment is consistent with the breaking of the surface dimers. However unlike Weser et al [17] we observed all four oxidation states as opposed to just the +2 characteristic of the ideal termination by a monolayer of sulphur atoms occupying bridge positions. Gothelid et al [50] reported that at saturation coverage (which they estimated to be above one monolayer) there are contributions from all four oxidation states. They explained the presence of higher oxidation states by the fact that sulphur etches the surface to produce a stripped character with a high density of monatomic steps, as seen in STM analysis by his group. The ratio of the intensity of the chemically shifted components to the bulk substrate peak 38:62 indicate that the saturation coverage was in excess of a monolayer in agreement with Gothelid. From analysis of the relative intensities, the +2 oxidation state intensity was found to dominate, which corresponds to adsorbed sulphur atoms occupying bridge sites between neighbouring atoms. The above experimental observations suggest that the (1x1) LEED pattern observed for the sulphur covered surface originated from the underlying bulk structure and not from an ordered S overlayer.

Figure 6.22 shows the evolution of the S2p spectrum with sulphur dose and final anneal as reported by Gothelid [50] . He attributed the high binding energy (low kinetic energy) component A_2 to a non-reacted surface component, which disappeared upon annealing. Figure 6.23 (a) and (b) shows our S_{2p} spectra after 10 min deposition and subsequent anneal at 200°C respectively. We also attribute the low kinetic energy component to a non-reacted S component, which de-absorbs after annealing the surface. Annealing of our sulphur treated surface at 200°C for 10 minutes resulted in a significant increase in the intensity of the Ge +4 oxidation state (see Figure 6.21(b)) and a corresponding increase in the ratio of surface to substrate intensity from 38:62 to 47:53. This increase was most likely caused by the incorporation of some of the non-reacted sulphur on the surface and is consistent with the formation of a thicker reacted phase layer between the sulphur and germanium, possibly a GeS_2 reacted layer. Similar changes were reported in the distribution of oxidation states following the annealing of the oxygen covered surface by Himpsel et al [51]. Bringans and Olmstead [30] also reported the presence of 4 oxidation states following the thermal annealing of a deposited selenium layer on the Si(100) surface, with the +4 state being the dominant

component. They interpreted the result as indicating the formation of a $SiSe_2$ layer at the surface.

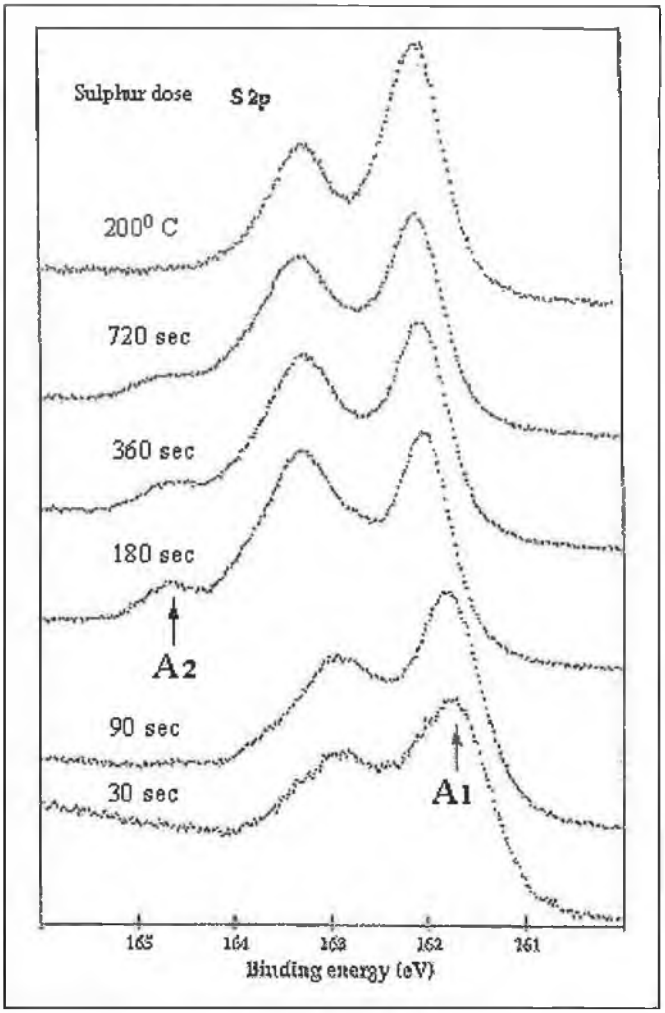

Figure 6.22: S_{2p} spectra following room temperature sulphur deposition and annealing of the Ge(100) substrate. Two contributions were observed, A1 and A2. (Gothelid [50])

The presence of +3 and +4 oxidation states following room temperature adsorption is indicative of sulphur bonding to surface steps and imperfections, the number of which can depend on the surface preparation procedure. After annealing the sulphur covered surface to temperatures higher than 200 °C a reduction of the intensity of the chemically shifted components was observed and ultimately the complete removal of the adsorbed sulphur layer and the re-establishment of the clean surface (2x1) reconstruction. The S_{2p} spectrum, following the 200 °C anneal in Figure 6.23 was significantly broader than the corresponding spectrum for the same peak observed on the sulphur terminated Si(100) surface.

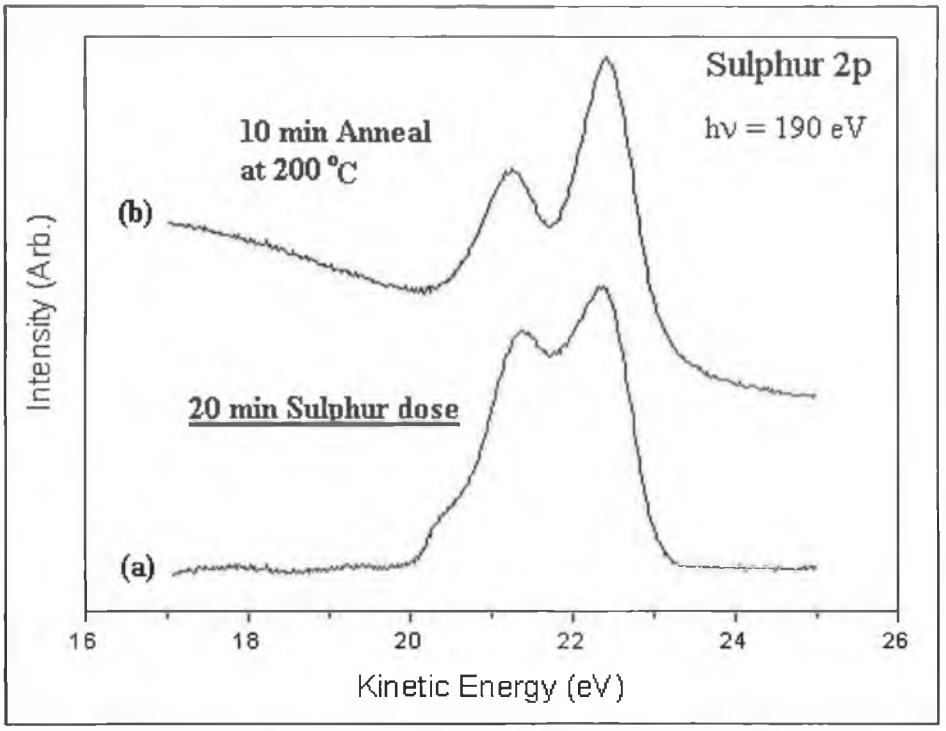

Figure 6.23: (a) S_{2p} spectrum after 20 min dose, there sulphur is in a multi-bonding environment (b) the low kinetic energy S contribution has been removed following a 10 min anneal at 200 °C

This is reasonable given that the analogous Ge_{3d} spectrum still contained 4 oxidation states, indicating that the near surface germanium atoms were in a range of different chemical environments. Recent STM and thermal desorption studies [52] support the assertion by Gothelid [50] that the thermal annealing of the sulphur covered surfaces leads to the desorption of surface germanium atoms in an etching process. These results are consistent with our experimental observations of preferential compound formation following thermal annealing.

6.65 Discussion of results

The deposition of sulphur onto the Ge(100) surface at room temperature lead to the breaking of the surface dimers and the termination of the surface in a chemically reacted S-Ge layer of one to two monolayers thick. Following an anneal at 200^0C, this reacted phase predominately consisted of GeS_2. The surface termination was therefore non-ideal and the (1x1) LEED pattern was ascribed to the bulk structure being observed through a

disordered layer. Annealing at higher temperatures resulted in the desorption of sulphur, restoring the clean (2x1) surface reconstruction.

6.7 Conclusion

From consideration of the results of the literature and our own attempts to realise an ideal monolayer termination of the surfaces of Si(100) and Ge(100) with sulphur it is apparent that the passivation of these surfaces with a single monolayer is possibly unattainable. The body of work in the literature is finite and diverse in that a wide variety of passivation procedures have been tried, but are not exhaustive. The point is borne out by the SiO_2 core level findings of chapter 4 where despite 20 years of dedicated optimisation the non-idealness of the SiO_2 interface, manifested by the existence of an interfacial SiO_x, is inherent in the oxidation process.

Theoretical studies in deciding the suitability of sulphur as a candidate for passivation Si(100) and Ge(100) surfaces are encouraging except in respect of the larger bond length and energies for S-Si bonds compared to Si-Si bonds and the volatile bonding interaction of S and germanium. It is on this theoretical basis that the co-existence of the single S_{2p} phase with the two oxidation states of silicon was reconciled. In other words the adsorbate induced strain is relaxed through the formation of optimal Si-S bond angles which is facilitated by vacancies in the surface S coverage. Analogously for Ge(100) the increased complexity of the surface structure manifested by the presence of all four oxidation states is attributed to the volatile S-Ge bonding interaction resulting in the surface being etched.

Synchrotron radiation has played a valuable role in investigating both the bonding chemistry and geometry of the outer surface through the surface core level shifts. However, from the literature and our analysis of the Si/SiO_2 system we are mindful of the need to characterise photoemission results in the context of a samples history, which for surface passivation starts, with the engineering of the clean surface. Therefore for future work where Si(100) and Ge(100) surfaces are passivated through a more optimised procedure, complementary techniques such as FTIR and STM could be employed along with synchrotron radiation analysis facilitating a more complete characterisation.

6.8 References for Chapter VI

1 Taken from the web elements online book store http://www.webelements.com/

2 Chemistry, 3rd Ed, Mc Murry (Prentice Hall) page 275

3 S. Hasegawa, X. Tong, S. Takeda, N. Sato, Prog. Surf. Sci. **60** (1999) 89

4 C. Duke, Appl. Surf. Sci. **65/66** (1993) 543, Also C. Duke, Scanning Micros. **8**(1994) 743

5 Silicon Surfaces and formation of interfaces, J. Dabrowski, H. J. Mussig World scientificpage 90

6 H. Farnsworth, R. Schlier, T. George, R. Burger, J. Appl. Phys. **29** (1958) 1150

7 R. Tromp, R. Hamers, J. Demuth, Phys. Rev. Letts **55**, (1985) 1303

8 J. Dabrowski, M. Scheffler, Appl. Surf. Sci. **56** (1992) 15

9 M. Rohlfing, P. Kruger, J. Pollmann, Phys Rev B **52** (1995) 13753

10 D. Chadi , Phys Rev Lett, **43** (1979) 43

11 Courtesy of the G. Hughes A. Coffola, D. Carty, P Gauano, Surface science group, DCU

12 R. Uhrberg, E. Landemark, Y. Chao, J. Elect. Spect. Relt. Phen. **75** (1995) 197

13 R. Bringans, R. Uhrberg, R. Bachrach, J. Northrup, Phys. Rev. Lett. **55**(1985) 533

14 M. Olmstead , R. Bringans, R. Uhrberg, R. Bachrach, Phys. Rev. B **34** 6041 (1986) 6041

15 R. Uhrberg, R. Bringans, M. Olmstead, Phys. Rev. B **35** (1987) 3945

16 R. Uhrberg, R. Bringans , R. Bachrach, J. Northrup, Phys. Rev. Lett. **56** (1986) 520

17 T. Weser, A. Bogen, B. Konrad, R. Schnell, C Schung, Surf. Sci. **201**, (1988) 245

18 E. Kaxiras, Phys. Rev. B **43** (1991) 6824

19 R. Wyckoff, Crystal Structures, 2nd Ed. Interscience New York 1963 Vol 1

20 D. Vanderbilt, Phys. Rev. Lett. **63** (1989) 1404

21 W. Heegemann, K. Meister, E. Bechtold, K. Hayek, Surf. **49** (1975) 161

[22] E. Landemark, C. Karlsson, Y. Chao, R. Uhrberg, Phys. Rev. Lett. **69** (1992) 1588

[23] T. Pi, C. Cheng, H. Hong, Surf. Sci. **430** (1999) 126

[24] T. Weser, A. Bogen, B. Konrad, R. Schnell, C. Schug, W. Steinmann, in: O. Engstrom (Ed.) Proc. 18th Int. Conf. Physics of Semiconductors, World Scientific, Singapore, 1987, p. 97

[25] D. Mullins, P. Lyman, S. Overbury, Surf. Sci. **277** (1992) 64

[26] A. Papageorgopoulos, A. Corner, M. Kamaratos, A. Papageorgopoulos, Phys. Rev. B **55** (1997) 4435

[27] P. Moriarty, L. Koenders, G. Hughes, Phys. Rev. B **47** (1993) 950

[28] H. Metzner, T. Hahn, J. Bremer, Surf. Sci. **377** (1997) 71

[29] T. Hahn, H. Metzner, B. Plikat, M. Seibt, Appl. Phys. Lett. **72** (1998) 2733

[30] R. Bringans, M. Olmstead, J. Vac. Sci. Technol. B **7** (1989) 1323

[31] R. Bringans, M. Olmstead, Phys. Rev. B **39** (1989) 12985

[32] P. Kruger, J. Pollmann, Phys. Rev. B **47** (1993) 1898

[33] F. McFeely, J. Morar, N. Shinn, G. Landgren, F. Himpsel, Phys. Rev. B **30** (1984) 764

[34] F. Himpsel, F. McFeely, A. Ibrahimi, J. Yarmoff, G. Hollinger, Phys Rev. B **38** (1988) 6084

[35] J. Kubby, J. Boldand, Surf. Sci. Repts. **26** (1996) 61

[36] J. Kubby, J. Griffith, R. Becker, J. Vickers, Phys. Rev.B **36** (1987) 6097

[37] J. Fernandez, W. Yang, H. Shih, F. Jona, D. Jespen, P. Marcus, J. Phys. C **14**(1981) L55

[38] R. Schnell, F. Himpsel, A. Bogen, D. Riger, W. Steinmann, Phys. Rev. B **32** (1985) 8052

[39] X. Chen, W. Ranke, Surf. Sci. **262** (1992) 294

[40] G. LeyLay, J. Kanski, P. Nilsson, U. Karlsson, H. Hricovini, Phys. Rev. B **45** (1992) 6692

[41] D. Lin, T. Miller, T. Chiang, Phys. Rev. Lett. **67** (1991) 2187

[42] R. Cao, X. Yang, J. Terry, P. Pianetta, Phys. Rev. B **45** (1992) 749

[43] A. Goldoni, S. Modesti, V. Dhanak, M. Sancrotti, A. Santoni, Phys. Rev. B **54** (1996) 11340

[44] M. Cakmak, G. Srivastava, Phys. Rev. B **60** (1999) 5497

[45] H. Kuhr, W. Ranke, Surf. Sci, **189/190** (1987) 87

[46] K. Leung, L. Terminello, Z. Hussain, x. Zhang, T. Hayashi, D. Shirley, Phys. Rev. B **38** (1998) 8241

[47] R. Uhrberg, E. Landemark, Y. Chao, J. Electron Sprctros. Relt. Phen. **75** (1995) 197

[48] G. Anderson, M. Hanf, P. Norton, Z. Lu, M. Graham, Appl. Phys. Letts, **66** (1995) 1123 Also, P. Ma, G. Anderson, P. Norton, surf. Sci. **420** (1999) 134

[49] P. Kruger, J. Pollmann, Phys. Rev. Letts. **64** (1990) 1808

[50] M. Gothelid, G. Ley, C. Wigreg, M. Bjorkqvist, M. Rad. U. Karlsson, Appl.

[51] F. Himpel, D. Lapiano, J. Morar, The Physics and Chemistry of SiO_2 and the Si-SiO_2 interface 2 Ed C. Helms and B. Deal, Plenum Press 1993 page 237

[52] L. Nelen, K. Fuller, C. Greenlief, Appl. Surf. Sci. **150** (1999) 65

Chapter 7

Comparisons, Conclusions and Further Work

7.0 Overview of thesis

This thesis is concerned with the characterisation of ultra-thin oxide and oxynitride dielectric layers grown in an industrial environment on Si(100). The investigation of the oxidation of Si(100) and the oxide formed has been on going for a long time using a diversity of experimental techniques and resulting in a richness of results. The drive toward increased device scaling to realise faster, cheaper technologies has resulted in the refinement and optimisation of oxide technologies to the extent that a dielectric layer with a thickness variation less than 1 nm can be achieved across an 8-inch production oxide. Device scaling cannot continue indefinitely. In its basic operation a MOSFET acts as an electronic switch. By the application of a suitable voltage at the gate terminal the current flowing from source to drain terminals can be switched on or off. The SiO_2/Si system plays a key role here in allowing the field resulting from the gate potential to switch on or off a conducting channel in the substrate without allowing current flow across the dielectric layer. A drain source voltage results in a channel current whose conductance is give by equation 7.0.

$$g = \frac{I_{ds}}{V_{ds}} = \left(\frac{\varepsilon_{oxide}\mu A}{L^2 d}\right)\left(V_g - V_t\right) \qquad \textbf{Equation 7.0}$$

V_{ds} drain to source voltage
I_{ds} drain to source current
ε_{oxide} is the permitivity of the oxide
μ is the carrier mobility in the channel
A is the area
L is the source to drain distance
d is the oxide thickness
V_g is the gate voltage
V_t is the threshold voltage

Thus, the gate voltage acts to control the drain source current. The transistor is switched "on" for voltages above the threshold voltage V_t and switched "off" for voltages below V_t. The above description assumes the oxide can act as a perfect dielectric and therefore support an arbitrary large voltage without a current flowing through it. For ultra-thin oxides (d<5 nm), leakage current exists due to the quantum mechanical tunnelling of electrons across the oxide and the oxide can support a maximum electric field before the device fails through dielectric breakdown. These effects pose practical limitations for future technology and make the physical dimensions (L, d and A) and electrical quantities in equation 7.0 interdependent [1]. For a maximum voltage available as a gate voltage V_g, limiting the electric field supported by the gate oxide imposes a limit on the oxide thickness, and thereby determines the minimum values of L and A; therefore the breakdown behaviour of the oxide film may limit the size of individual devices.

The limitations for device scaling inherent in equation 7.0 have been delayed to some extent by chemical and electrical research of the SiO_2/Si(100) system. The effects of leakage current in both Fowler Nordheim [2,3] and direct tunnelling [4] regimes has allowed the dielectric breakdown process to be separated into soft and hard breakdown regimes and established statistical parameters from which pre and post breakdown behaviour of the MOS device can be evaluated. At the same time the use of an oxide with a higher dielectric constant k value [5,6] has allowed the oxide thickness to be increase while maintaining the same effective capacitance, which given the exponential dependence of tunnelling current on thickness greatly reduces the leakage problem. Suggested alternative high k dielectric materials are (Ta_2O_5, TiO_2, Y_2O_3, CeO_2 and Al_2O_3) [7]. A number of these materials are not thermally stable on silicon. Also for most of these high-k materials, the band gap is inversely proportional to the dielectric constant [8]. Even if there is a reduction of leakage current due to the increased thickness, this may be nullified by the reduction of the barrier height. Both the thickness and barrier height have an exponential influence on tunnelling current. So far nitridation of the oxide has proved successful in reducing the above-mentioned problems, as discussed in the previous chapters of this thesis.

It is necessary to say that the above mentioned results and studies are only a few of the many oxide related studies chosen in order to contextualise the oxide layers studied in this thesis in terms of their role in MOS device operation and the future of such devices.

This highlights an important reality for this thesis and its scope. This thesis seeks a characterisation method using photoemission, which can assure the consistency and quality of a production grade oxide. To this end the quality of the oxide layers has been identified through the consistency of the values of thickness, elemental composition and stoichiometry in the as-received samples. The unsuitability and suitability of inert ion bombardment and Wet chemical acid etching for depth profiling the dielectric layers were identified. The presence of N in the oxynitride layers was identified. From wet chemical depth profiling and angular resolved measurements both surface and N interface layers were identified. The existence of both an interfacial and oxide related N phase is not conclusive from our analysis but it is reasonable given the N peak position and shape behaviour with take-off angle and depth. Synchrotron based photoemission, XES and XAS analysis has allowed the role of interfacial nitrogen in terms of Si-N bonding chemical state and its effects on the band structure to be identified.

Many of the conclusions in this thesis are inconclusive and have been shaped or guided by the results of others in the literature. It is noteworthy that photoemission has offered a wealth of information (thickness, elemental composition and chemical state) across a range of thickness where other techniques (ellipsometry, SIMS, MEIS, NRA & AES etc.) are more specialised in the information they deliver. Therefore in a manner analogous to oxide production, perhaps oxide characterisation is approaching its own limitations which could be reduced or overcome by incorporating a range of techniques into oxide characterisation where the combined results allow more conclusive quantitative conclusions to be obtained.

Finally, in investigating the potential of sulphur to terminate the surfaces of Si(100) and Ge(100) we enjoyed an opportunity to direct photoemission away from characterisation and towards a first principle examination of silicon. That is to say at the foundation (100) surface on which it is grown and where it's oxide interface is formed.

Unfortunately, due to the limited accessibility of synchrotron radiation sources and the complexity of the deposition procedure we were unable to draw our conclusions in respect of S passivation from as large a data set as was used for oxide characterisation. Also our experimental inability to deposit sulphur with the same degree of precession as is achieved in industrial oxide growth means that our results have to be considered

against those of others in the literature. As mentioned in chapter 6, a diversity of experimental procedures and results exists. We feel an ideal termination by sulphur is limited for Si(100) due to the large bond length and energy, and for Ge(100) due to the volatile bond interaction. Our understanding would benefit from further experimental photoemission studies of both surfaces.

7.1 References for Chapter VII

1 F. Feigl, Physics Today, Oct. (1986) 47

2 S. Zafar, Q. Liu, E. Irene, J. Vac. Sci. Technol. A**13** (1995) 47

3 J. Poler, K. McKay, E. Irene, J. Vac. Sci. Technol. B**12** (1994) 86

4 G. Lucovsky, H. Niimi, H. Yang, J. Keister, J. Rowe, Appl. Surf. Sci. **166** (2000) 458

5 G. Lucovsky, H. Yang, Y. Wu, H. Niimi, Thin solid films **374** (2000) 217

6 G. Lucovsky, H. Yang, Y. Wu, H. Niimi, Appl. Surf. Sci. **159** (2000) 50

7 D. Buchanan, IBM J. Res. Develop. **43** (1999) 245

8 S. Campbell, D. Gilmer, X. Wang, M. Hsieh, IEEE Trans. Electron Devices **44** (1997) 104